Universidad de Granada

Grupo de Investigación de Dinámica de Flujos Ambientales

Departamento de Mecánica de Estructura e Ingeniería Hidráulica

Circulation of the Rules Reservoir induced by atmospheric forcing

Tesis doctoral realizada por:

Christian Mans

Directores:

Miguel Ángel Losada Rodríguez

Asunción Baquerizo Azofra

Granada, Diciembre 2008

Editor: Editorial de la Universidad de Granada
Autor: Christian Mans
D.L.: GR. 2751-2008
ISBN: 978-84-691-8253-6

To Simona

Acknowledgments

I would like to thank my supervisors Miguel Losada and Asunción Baquerizo for their time and patience in sharing their knowledge and experience with me.

To the people of the Grupo de Puertos y Costas and the Grupo de Viento, in particular to Todd Cowen for his help in teaching the LDV system; and Alex and David for their help with the field campaign. Special thanks to Monica and Javier for always freely giving your time and assistance.

Finally, to my family and Simona for your support through the tough times.

Abstract

This doctoral thesis investigates the influence of the surrounding local topographical features on the free surface oscillation of a small reservoir in complex terrain. The study shows the high frequency micro-scale atmospheric forcing components (<10min) can produce resonant excitation of the free surface. The high frequency harmonics in the atmospheric forcing are believed to be due to local topography effects and from flow separation off the dam structure.

The water free surface response to the atmospheric forcing is studied in detail with a two-dimensional, depth-averaged, hydrodynamic numerical model developed from the linearized shallow water equations.

The high frequency atmospheric forcing variation (barometric pressure and wind shear stress) and the free surface response are presented from field measurements of a small reservoir located in complex terrain (Rules Reservoir, Granada). At certain times, harmonics in the measured atmospheric forcing are observed in the field measurements, ranging between periods of 200-500 seconds. Surface seiches are generated when the harmonic forcing matches the reservoir eigenmodes, even for low wind speeds.

The spatial variation of the atmospheric forcing on the reservoir water surface is studied from simulations in a boundary layer wind tunnel. The surrounding topographical features are modeled at a scale of 1:3000 for a single wind direction which coincided with the orientation of the principal axis of the reservoir and the local wind directionality above the reservoir. The wind tunnel simulation provides a high resolution map of the mean wind speed and directionality variation over the water surface, along with variations in the water surface pressure distribution.

The measurements from the field study and the wind tunnel simulation are merged together to provide a high resolution map of the spatial and temporal variability of the atmospheric forcing, which are included as loading conditions in the numerical model of the free surface response. The model is shown to accurately simulate the free surface oscillations measured during the field campaign with the reservoir at its current water level.

The atmospheric forcing is also applied to simulations of the reservoir with higher water levels, predicting the response of the free surface when it is at full capacity and at intermediate levels. The model demonstrates how different eigenmodes contribute to the response of the free surface at different water levels, modifying the magnitude and location of the maximum oscillations.

Resumen

Los procesos hidrodinámicos que ocurren en un embalse se deben a la compleja interacción de un cierto número de factores naturales y humanos, que incluyen: (a) las condiciones hidráulicas del embalse en la zona de captación, (b) el clima, (c) la morfología del embalse, (d) la operatividad de la presa,(e) la limnología y (f) las variaciones estacionales (Wetzel, 2001). La comprensión de los procesos físicos involucrados en la hidrodinámica de un embalse puede ayudar en las fases de gestión del mismo.

Generalmente, la circulación de agua en un embalse, o en cualquier cuerpo cerrado de agua, está dominada por los agentes forzadores atmosféricos (esfuerzo de corte del viento y presión barométrica). El embalse responde a estos agentes produciendo una serie de oscilaciones periódicas, tanto en la superficie de agua (sobrelevación) como internamente (ondas internas). Este proceso a su vez induce la generación de celdas de circulación a lo largo de toda la columna de agua, regulando el transporte de sedimentos, nutrientes, materia orgánica, gases disueltos y la distribución de la temperatura y de la densidad de agua. Dichos factores influyen tanto en la expectativa de vida útil del embalse como en la de los organismos biológicos que viven en el mismo.

Las oscilaciones periódicas estacionarias en un embalse se pueden desarrollar por diversas condiciones forzadoras. La amplitud de la oscilación estacionaria depende de la geometría del lago y de la magnitud del forzamiento atmosférico. En el caso de pequeños lagos, la amplitud puede ser del orden de mm, o cm con condiciones meteorológicas inusuales, aumentando hasta el orden de metros en el caso de grandes lagos (p.ej. la oscilación de 1.83m en el lago de Ginebra, Suiza).

Aunque las oscilaciones en los embalses suelen ser relativamente pequeñas, estas pueden producir una oscilación significante en la vertical y promover la mezcla a lo largo de toda la columna de agua. En consecuencia, el movimiento periódico de las ondas internas puede inducir una elevada tasa de transporte de material orgánico e inorgánico a lo largo del embalse. En particular, este oleaje estacionario induce una capa límite cerca del lecho, donde se verifican los procesos de mezcla más significantes (Bramato et. al., 2007).

Las oscilaciones de la superficie libre ocurren con frecuencia en cuerpo cerrado de agua durante condiciones moderadas de viento. Por ejemplo, durante el paso de un sistema frontal, el incremento repentino de la velocidad de viento, acoplado con la variación de la presión barométrica, puede inducir unas oscilaciones significativas de la superficie de agua (Ward, 1979; Hutter, Raggio, Bucher, & Salvade, 1982; Horn, Mortimer, & Schwab, 1986). La frecuencia de ocurrencia de dichos eventos depende de la meteorológica local de la región. En zonas tropicales, estos eventos ocurren casi a diario durante los meses de verano debido al paso de las tormentas extra-tropicales en las horas de la tarde.

La excitación resonante de las oscilaciones en la superficie libre puede verificarse si la frecuencia de los forzadores atmosféricos coincide con la frecuencia de uno de los modos propios de la oscilación. El Mar Báltico es un buen ejemplo de este acoplamiento, donde se verifica que la frecuencia del primer modo es aproximadamente de unas 24 horas, coincidiendo con el ciclo diario de las oscilaciones atmosféricas. Este fenómeno induce una oscilación casi constante del mar en su modo principal.

Sin embargo, en el caso de pequeños lagos, el periodo de los modos dominantes es mucho más pequeño, típicamente del orden de minutos, donde no se verifican picos naturales en el espectro meso escalar meteorológico de distribución de energía. Las formaciones topográficas de elevadas dimensiones pueden inducir armónicos que fuercen el cuerpo de agua debido a (a) la formación de vórtices turbulentos en superficie cuando el flujo de aire pasa alrededor de una montaña o la estructura de la presa y (b) ondas de montaña. Si la frecuencia de la oscilación de los forzamientos atmosféricos coincide con la frecuencia de uno de los modos del embalse, las ondas superficiales y internas generalmente se pueden producir y perdurar en escala casi diaria, dominado completamente la circulación de agua y los procesos de mezcla en el embalse.

Estudios recientes en la playa de Carchuna han demostrado cómo la presencia de formaciones topográficas en la playa puede contribuir a reforzar las formaciones morfológicas en la línea de costa debido a fenómenos de separación de flujo (*vortex shedding*) alrededor de un obstáculo geográfico de elevada dimensión ubicado en un extremo de la playa y la generación de vórtices turbulentos en la superficie de agua que se acoplan con la hidrodinámica cerca de la costa (Ortega-Sánchez, Bramato, Quevedo, Mans, & Losada, 2008).

Típicamente, en los modelos hidrodinámicos de un embalse, las condiciones atmosféricas se registran como valores promedios sobre 10 minutos, eliminando así las oscilaciones de elevadas frecuencias de los datos registrados, lo cual representa un tipo de medida estándar para redes meteorológicas y aeropuertos. Sin embargo, en el caso de lagos pequeños, las oscilaciones de alta frecuencia de los forzamientos atmosféricos son importantes porque se encuentran dentro del rango de las frecuencias modales de las oscilaciones de las superficie libre de agua. Por este motivo, en el caso de pequeños embalses sería razonable incluir en los modelos hidrodinámicos de circulación dentro del embalse las oscilaciones de alta frecuencia en las condiciones atmosféricas (frecuencias mayores que 10 min).

Además, no es usual considerar la variación espacial de los forzamientos atmosféricos. Generalmente, las condiciones atmosféricas se miden en una única ubicación, cerca del embalse, y son aplicadas uniformemente a lo largo de la superficie libre. Mientras que dicha hipótesis puede ser válida en embalses ubicados en terrenos expuestos, no describirá con precisión la variabilidad de los forzamientos atmosféricos dentro de lagos circundados por formaciones topográficas complejas, donde es de esperar algunos efectos locales de protección ofrecida por la topografía circundante. Esta simplificación puede inducir errores significantes en embalses ubicados en los valles, donde existe una

elevada variabilidad de la velocidad, dirección de viento y presión barométrica en el tiempo y en el espacio a lo largo de la superficie libre del embalse.

La presente investigación considera dichos aspectos, mediante el estudio de los parámetros hidrodinámicos de un pequeño embalse ubicado en terreno complejo, empleando una elevada resolución en la descripción de la variación de los forzadores atmosféricos en el espacio y en el tiempo. La respuesta de la superficie libre se simula en detalle empleando un modelo numérico hidrodinámico bidimensional, promediado en la vertical y desarrollado a partir de las ecuaciones lineales de aguas someras. Antes de su aplicación al embalse, el modelo se valida comparando la solución numérica con un cierto número de soluciones analíticas exactas con un embalse simplificado en 1D. El modelo se aplica al embalse de Rules, ubicado en un valle distante unos 20 km del mar Mediterráneo, en la costa sur de España. El embalse es un caso interesante de estudio, porque se encuentra en una región de topografía extremamente compleja que puede generar unos patrones de circulación atmosférica extremadamente variados. Con la condición de llenado actual, la geometría del embalse es relativamente simple, siendo aproximadamente de forma rectangular, con una longitud mayor orientada a lo largo del eje identificado por la dirección dominante del viento. El modelo permite claramente definir cada respuesta hidrodinámica forzada por los agentes atmosféricos. A medida que aumenta la profundidad la geometría empieza a ser más compleja, con un valle que se separa en dos ramas distintas. Este conduce a una geometría inusual con tres cuerpos de agua de casi la misma longitud, que se juntan en un punto central.

La variación de alta frecuencia de los agentes atmosféricos forzadores (presión barométrica y esfuerzo de corte del viento) y de la respuesta hidrodinámica (sobrelevación de la superficie y perfiles de corriente) se obtienen gracias a medidas de campo en el embalse de Rules. Cuando las frecuencias de los armónicos observadas en los espectros de los agentes atmosféricos coinciden con las frecuencias modales del embalse, se generan oscilaciones de la superficie libre con contribuciones hasta el sexto modo. Los armónicos de alta frecuencia en los agentes atmosféricos se generan a causa de la separación del flujo sotavento de la presa y por efectos de la topografía circundante al embalse.

La variación espacial de los agentes atmosféricos que actúan como forzadores en la superficie libre del embalse, se ha obtenido a partir de simulaciones en un túnel de viento de capa límite. Las simulaciones en el túnel de viento de capa limite representan una técnica novedosa para incrementar la variación espacial de los parámetros atmosféricos en la superficie del embalse. Las características topográficas que rodean el embalse se han modelado a escala 1:3000, simulando una dirección de viento que coincide con la orientación del eje principal del embalse y con la direccionalidad de viento local sobre el mismo. La simulación en el túnel de viento proporciona un mapa de elevada resolución de velocidad media y direccionalidad de viento sobre la superficie de agua, junto con la variación superficial de la distribución de la presión barométrica.

Las medidas de campo y la simulación en el túnel de viento se combinan para proporcionar un mapa detallado de alta resolución espacial y temporal de la variabilidad

de los parámetros atmosféricos, que se emplean como condiciones de entrada en el modelo numérico para simular la respuesta de la superficie libre. La comparación entre las oscilaciones de la superficie libre obtenidas numéricamente y las oscilaciones medidas en el campo evidencia el buen funcionamiento del modelo. El modelo es capaz de predecir no solo cuál es el modo dominante en el embalse sino también dónde se verifica el máximo desplazamiento vertical.

Además se ha simulado numéricamente la respuesta del embalse con profundidades más elevadas bajo el mismo forzamiento atmosférico, para predecir su comportamiento en condiciones de llenado total e intermedio.

Las observaciones no se limitan solo a las situaciones de terreno complejo, sino que pueden ser relevantes en pequeños lagos, embalses y dársenas de puertos ubicados en zonas urbanas, donde fenómenos de separación de flujo y armónicos de alta frecuencia se pueden generar por efecto de los edificios circundantes o de estructuras construidas por el hombre.

Table of Contents

List of Figures

List of Tables

List of Symbols

a	width of idealized moving pulse atmospheric forcing (m)
a_r	Rossby radius
A	amplitude of surface seiche (m)
C_{A-C}	linear weighting coefficient of atmospheric forcing
C_p	mean surface pressure coefficient
C_u	horizontal mean wind speed coefficient
C_v	vertical mean wind speed coefficient
f_c	coriolis force
F	atmospheric forcing (m^2/s^2)
F_{A-C}	atmospheric forcing measured at anemometer station A-C
F_h	LDV horizontal alignment factor
F_v	LDV vertical alignment factor
F_s	wind tunnel reference factor
g	acceleration of gravity (m/s^2)
h	water depth (m)
h_b	Characteristic basin depth (m)
H	Heaviside function
I_u	horizontal wind turbulence intensity
k	Von Karman constant
L	basin length (m)
L_b	Characteristic basin length (m)
n	n^{th} surface seiche mode
P_{corr}	wind tunnel pressure coefficient correction factor
P_s	atmospheric surface pressure (Pa)
P_{st}	wind tunnel static pressure
P_i	wind tunnel dynamic pressure, at point 'i'
q	depth averaged flow velocity
T_b	Characteristic surface seiche period (sec)
u	horizontal component of water current (m/s)
U	horizontal wind speed (m/s)
$\overline{U}$	mean horizontal wind speed (m/s)
$\overline{U}_{grad}$	mean wind speed at gradient height (m/s)

v	vertical component of water current (m/s)
V	Vertical mean wind speed (m/s)
V_p	velocity of idealized moving pulse atmospheric forcing (m/s)
z	height above ground (m)
z_0	roughness length (m)
β	basin eigenvalue of free surface response
γ	$\lambda/2$
η	free surface elevation (m)
λ	surface friction factor
ν	air viscosity
ρ	density of water (kg/m^3)
ρ_a	density of air (kg/m^3)
σ_u	standard deviation of wind longitudinal turbulence
τ_b	bed shear stress (m^2/s^2)
τ_s	surface wind shear stress (m^2/s^2)
u_*	friction velocity (m/s)
ω	basin eigenfrequency of free surface response
$\hat{f}$	modal coefficient of basin eigenfunction
χ	basin eigenfunction of free surface response

1 Introduction

1.1 Motivation

Reservoir hydrodynamics is the complex interaction of a number of natural and man-made factors, including: (a) hydraulic conditions of the reservoir and of the catchment area; (b) climate; (c) reservoir morphology; (d) dam operation; (e) limnology; and (f) seasonal variations (Wetzel, 2001). Understanding the physical processes involved in the reservoir hydrodynamics can help the management process.

Typically, the water circulation in a reservoir, or any closed water body, is dominated by the atmospheric forcing (wind shear and barometric pressure). The reservoir responds to the forcing by producing a series of periodic oscillations, both on the water surface (surface seiches) and internally (internal waves). This in turn produces circulation cells throughout the depth of the water body, promoting the movement and distribution of sediments, nutrients, organic matter, dissolved gases, water temperature and water density. These factors affect both the life expectancy of the reservoir and the biological elements within.

Periodic oscillations in a reservoir can be developed through a variety of means. If the reservoir is subjected to a constant wind forcing, the water will build-up at the downstream end of the reservoir. When the wind speed reduces, the displaced volume of water will quickly try to balance itself back into equilibrium through gravitational forcing, leading to the formation of a standing wave at the free surface and internally at the isothermal depth. The amplitude of the standing wave is dependent on the geometry of the lake and the magnitude of the atmospheric forcing. For small lakes, the amplitude of the free surface oscillation may be in the order of mm, or cm in the case of unusual meteorological conditions, increasing up to scales of metres for large lakes (i.e 1.83m oscillation at Lake Geneva, Switzerland).

Although the oscillation may be relatively small in reservoirs, they still produce significant vertical motion and mixing throughout the depth of the lake. For stratified lakes, the surface seiche can generate an internal wave, resulting in the movement of the entire water body, completely mixing the water throughout the depth of the lake. Consequently, the periodic movement of internal waves forms the greatest transport of

organic and inorganic material throughout the reservoir. In particular, the oscillatory motion of the bottom boundary layer can create significant mixing. As sediment deposits in reservoirs usually contain very fine particles, sediment re-suspension within the reservoir is particularly susceptible to weak forcing conditions.

Surface seiches regularly occur in closed water basins during moderate wind conditions. For example, during the passage of a frontal system, the sudden increase in wind speed, coupled with the variation in barometric pressure, can lead to significant oscillations of the water surface (Ward, 1979; Hutter, Raggio, Bucher, & Salvade, 1982; Horn, Mortimer, & Schwab, 1986). The frequency of occurrence of these events depends on the local meteorology of the region. In tropical zones, this may occur almost daily in summer months due to the passing of extra-tropical thunderstorms during the evening hours.

Resonant excitation of the surface seiches may also occur if the frequency of the atmospheric forcing matches the frequency of one of the seiche modes. The Baltic Sea is a good example, where the frequency of the first mode is approximately 24 hours, matching the daily cycle of the atmospheric variation. This results in an almost constant oscillation of the sea in its fundamental mode. Recent studies at Carchuna Beach have showed local topographical features may contribute to the formation of beach embayments due to wind vortex shedding off coastal headlands coupling with the downstream coastal hydrodynamics (Ortega-Sánchez, Bramato, Quevedo, Mans, & Losada, 2008).

For small lakes, however, the periods of the dominant eigenmodes are much smaller, typically in the order of minutes, where there is no naturally occurring peak in the meso-scale meteorological spectral energy distribution. However, the atmospheric forcing may still contain some regular harmonic component. For example, large topographical features may create harmonic forcing on the water body through (a) the formation of eddies in the wake of the mountain or the dam structure, and (b) mountain waves. If the oscillating frequency of the local atmospheric disturbances were to match the frequency of one of the reservoir modes, surface seiches or internal waves may develop on an almost daily basis, completely dominating the water circulation and mixing processes in the reservoir.

In typical reservoir hydrodynamic models, the high frequency range of atmospheric forcing is not considered. Instead, the atmospheric conditions are recorded as a 10 minute average, which is the standard for meteorological networks and airports, thereby removing the high frequency variations from the recorded data set. However, for small lakes, it is the high frequency variation in the atmospheric forcing that is within the range of the modal frequencies of the water free surface oscillation. Therefore, at least for small reservoirs, it seems reasonable to consider the high frequency variations in the local atmospheric conditions (frequencies greater than 10min) in hydrodynamic models of reservoir circulation patterns.

In addition, the spatial variation of the atmospheric loading is not always considered. Typically, the atmospheric conditions are usually measured at a single location, close to

the reservoir, and applied uniformly across the water surface. While this assumption may hold for reservoirs located in relatively exposed conditions, it will not accurately describe the forcing variability of lakes surrounded by topographical features, where some local sheltering is expected. This simplification may become significant for valley reservoirs, where large temporal and spatial variations in the wind speed, direction and barometric pressure will be expected over the reservoir water surface.

This investigation seeks to address these two issues by studying the hydrodynamics of a small reservoir in complex terrain, with a high resolution description of the spatial and temporal variation of the atmospheric forcing. A two-dimensional, depth-averaged, model of the reservoir is developed from the linearized shallow water equations to describe the free surface movement due to the combined effects of the atmospheric pressure and the wind shear forcing terms. The model is applied to Rules Reservoir, a valley reservoir located approximately 20km inland from the Mediterranean Sea on the southern Spanish coast. The reservoir is an ideal test case, as it located in a region of extremely complex topography which can create a wide variety of atmospheric flow patterns. At its current water level the geometry of the reservoir is relatively simple, being roughly rectangular in shape, with its larger length orientated along the axis of the dominant wind direction. Therefore, any hydrodynamic response to the atmospheric forcing can be readily defined. At greater water depths, the geometry becomes more complicated as the valley separates into two separate branches, leading to an unusual geometry of three long basins of almost equal length, connected at a central junction.

The temporal and spatial variation of the atmospheric forcing and the response of the water free surface are studied with three methods:

- High frequency **field measurements** of the atmospheric forcing (barometric pressure and wind velocity) and the hydrodynamic response (free surface elevation and water current profiles) are studied at three locations along the length of the reservoir.

- **Wind tunnel simulations** in a boundary layer wind tunnel are a novel technique for capturing the spatial variation of the atmospheric forcing on the reservoir surface. The simulation measures the wind velocity and pressure variation at multiple locations over the water surface of a scaled model of the reservoir, which includes all surrounding local topography.

- The free surface response of the reservoir is modeled with a **2D numerical model**. The atmospheric forcing captured from the field measurements are merged together with the wind tunnel information to provide a detailed temporal and spatial loading variation.

1.2 Objectives

The study involves the application of a two-dimensional hydrodynamic model of a closed basin with detailed spatial and temporal variation of the atmospheric forcing over the water surface.

The principal objectives of the study can be summarized as follows:

- *Develop a two-dimensional, depth-averaged, hydrodynamic numerical model of a closed basin using the linearized shallow water equations. The atmospheric forcing terms include the combined action of the atmospheric pressure and wind shear. Before application to a reservoir, the model is validated by comparing the numerical solution with a number of exact analytical solutions for a simplified 1D basin.*

- *Capture, through on-site measurements, the high frequency temporal and spatial variation of the atmospheric forcing on a reservoir situated in complex terrain (Rules Reservoir, Granada). The coupling between the atmospheric forcing and the free surface response of the reservoir is investigated.*

- *Study the wind field above the reservoir and the effects of the local topography through a detailed wind tunnel simulation in a boundary layer wind tunnel. The wind tunnel simulation provides an understanding of the local atmospheric behavior throughout the complete depth of the boundary layer above the reservoir, including the wind speed and directional variation and the pressure distribution on the water surface.*

- *Apply the two-dimensional hydrodynamic model to Rules Reservoir, by merging the temporal and spatial structure of the atmospheric forcing provided by the field and wind tunnel information. The model investigates the influence of the high frequency atmospheric variation on the free surface oscillations. The model is extended to include the response of the reservoir to a range of reservoir water levels to determine if resonant excitation may also occur at full capacity and at an intermediate depth.*

1.3 Organization

The thesis is organized into six principal chapters. The following section provides a brief description of each chapter.

Chapter 2 provides a brief introduction to the problem, describing (a) the atmospheric forcing and its spectral distribution; and (b) the free surface response of a lake/reservoir to atmospheric forcing.

Chapter 3 describes the formulation of the two-dimensional, depth averaged, numerical model. The model is derived from the linearized shallow water equations, focusing on simulating the contributions of the atmospheric forcing (wind shear and barometric pressure) on a closed basin.

Chapter 4 introduces Rules Reservoir, which is the focus of the current study. A description of the reservoir and the atmospheric conditions of the region is provided, followed by an eigenvalue analysis of the reservoir free surface response. A summary of the field campaign is given, where measurements of the local atmospheric conditions and the response of the reservoir are recorded simultaneously over a two week period. A discussion of the observed coupling between the high frequency atmospheric forcing and the free surface oscillations is provided, identified by two short duration storm events which occurred during the measurement period.

Chapter 5 provides a description of the wind tunnel simulation of the wind field above the reservoir. The simulation models the local topography of the region, between the Mediterranean Sea and the reservoir, for one of the dominant wind directions of the region. The wind field above the reservoir and the effects of the local topography is discussed, along with a description of the wind velocity and pressure variation over the reservoir water surface.

Chapter 6 applies the two dimensional numerical model to Rules Reservoir, Granada. The spatial and temporal distribution of the atmospheric forcing obtained from the field measurements and the wind tunnel simulations are both incorporated into the numerical model. The model is applied to a variety of loading conditions and water depths, including two short duration storm events recorded during the field campaign.

Chapter 7 presents the principal conclusions of the study, highlighting the implications of the observed coupling between the high frequency atmospheric forcing and the reservoir response, in relation to the mixing processes, sediment transport and re-suspension and water quality of a small reservoir.

The results presented in this thesis and related studies can be found in the following publications:

- Ortega-Sánchez, M. Bramato, S., Quevedo, E., Mans, C. and Losada, M.A. (2008), Field evidence of atmospheric-hydrodynamic coupling in the nearshore. Geophysical Research Letter, 2008GL036043.

- Mans,C., Cuesta, J.A., Terrés, J.M. and Losada, M.A. (2007) Estudio del campo de viento local en el embalse de rules, Granada. IX Jornadas Españolas de Ingeniería de costas y puertos. San Sebastian, Spain.
- Bramato, S., Mans, C., Sánchez-Badorrey, E. and Losada, M.A. (2007), High resolution LDV measurements of BBL velocities under standing monochromatic oscillating flows: uncertainty analysis. Proc. Hydraulic Measurements & Experimental Methods Conference, Lake Placid, NY, U.S.A., pp. 437-442.

2 Literature review

The present chapter provides a background to atmospheric forcing conditions relevant to small reservoirs in complex terrain and the free surface response to atmospheric forcing.

2.1 Atmospheric forcing

The atmospheric loading (wind shear and atmospheric pressure) on a closed water basin is the principal forcing mechanism that promotes circulation in a small reservoir. The wind field at any site can be generated through a variety of forms, from synoptic winds generated from low pressure systems, tropical cyclones or hurricanes, to thunderstorm downbursts and frontal systems.

The temporal variation of atmospheric forcing is best described by the work of Van der Hoven (1957), who separated the wind speed spectrum into two components, the macro-meteorological spectrum and the micro-meteorological spectrum, with a spectral gap between the two (Figure 2.1). The macro-scale component includes the low frequency variation of the atmospheric forcing, including annual variations, the passing of pressure systems (every 100 hours), daily variations (24 hours) and diurnal variations (12 hours). The micro-scale component includes the gust components generated by local turbulence in the atmosphere, centered around the range of 60 seconds (0.02 hours). A spectral gap sits between the two peaks, between 5 minutes and 5 hours. Thus, it is assumed that any averaging period that lies within the spectral gap can remove the micro-scale component while retaining all the information of the macro-scale component. This is the fundamental reason why meteorological data from weather stations are presented as 10 minute or hourly mean values.

Each peak in the macro-scale and micro-scale spectra represents a different type of atmospherical forcing condition, each of which will affect the reservoir circulation. The following section will provide a brief overview of the relevant types of atmospheric forcing which occur in nature and their spatial and temporal scales.

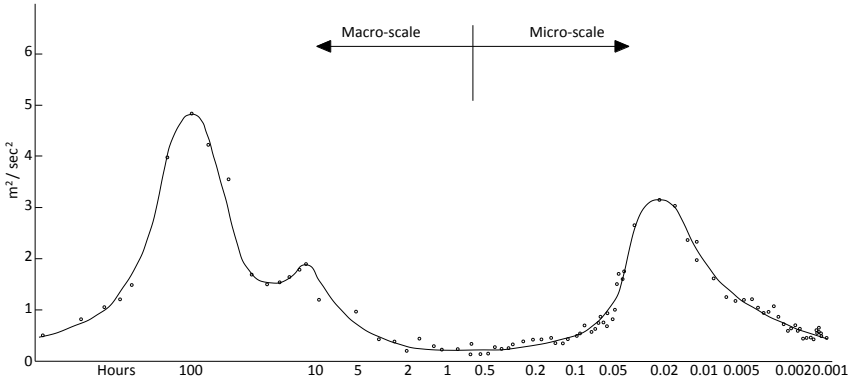

Figure 2.1 Horizontal wind speed spectrum (Adapted from (Van der Hoven, 1957))

2.1.1 Synoptic winds

Synoptic winds are strong and prolonged winds generated by low pressure systems. In general, the winds generated by pressure systems last for of up to three or four days and present the largest peak in the wind speed spectrum of Figure 2.1. The length scales of the systems are in the order of 1000km. With this temporal and spatial scale, the winds contain a completely developed boundary layer and maintain a relatively constant direction over large periods of time, generating high levels of turbulence close to the ground surface (Holmes, 2001).

It is possible to mathematically describe the atmospheric boundary layer profile due to synoptic winds according to the Log Law, where the wind speed is a function of the height above the ground, z. Ignoring the effect of the earth's rotation and the molecular viscosity of air, the variation of the mean wind velocity with height is defined as:

$$\overline{U}(z) = \frac{u_*}{k} log_e\left(\frac{z}{z_0}\right) \qquad (2.1)$$

where k is the Von Karman constant and equal to 0.4, z_o is the the roughness length and represents a measure of the size of the turbulence eddies close the ground, u_* is the friction velocity.

The roughness length, z_o, and the friction velocity, u_*, vary in function with the ground surface roughness and influence the slope and the depth of the atmospheric boundary layer. Table 2.1 presents a guide of the typical roughness lengths for different terrain types.

Figure 2.2 presents the corresponding boundary layer profiles according to the Log Law. The figure shows how an increase in the surface roughness reduces the mean wind speed, in particular within the region close the ground surface. High surface roughness values also increase the depth of the boundary layer.

Table 2.1 Roughness length, z_o, for various terrain types

Terrain	Surface roughness length, z_o (m)
Open sea (snow, desert)	0.001-0.005
Open country (grassland, few trees)	0.01-0.05
Suburban (Buildings up to 3-5m)	0.1-0.5
Dense urban (Buildings up to 10-30m)	1-5

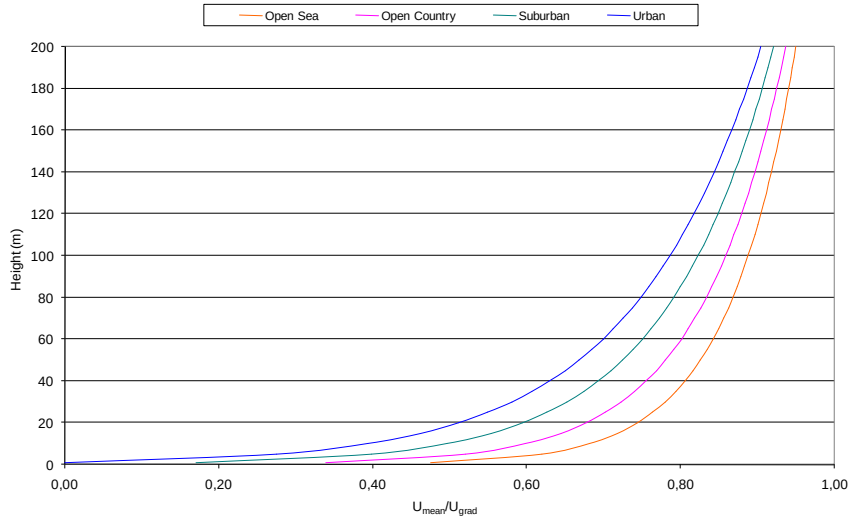

Figure 2.2 Surface roughness effects on the boundary layer profile

2.1.2 Diurnal and semi-diurnal winds

Diurnal and semi-diurnal winds originate from local temperature variations in the atmosphere leading to localized sea-breeze and land-breeze circulation cells. The circulation cells are most intense in coastal regions, where the temperature variations in the atmosphere above the water and the land create a sea-breeze during the afternoon hours. During the evening, the circulation changes direction to a land-breeze as the temperature differences are inverted, although the wind speeds are typically less intense.

As the winds originate through local differences in temperature, the variation of the wind velocity with height does not necessarily follow a logarithmic profile as with synoptic winds. As shown in Figure 2.3, the boundary layer profile varies during the day, due to changes in the atmospheric stability. During the morning hours the surface wind speeds are dominated by a shallow mixing layer, which presents an almost linear variation with height within the lower atmospheric layer (9AM). By the afternoon, the

land surface temperature has increased and the depth of the mixing layer has grown, presenting an almost uniform wind speed with height throughout the full depth of the atmospheric boundary layer (3PM). This is due to the high degree of turbulence contained within the wind mixing the thermal differences throughout the depth of the atmospheric boundary layer. During the evening, the surface temperature decreases, along with the wind turbulence intensity. Because of this, the drag from the land surface slows the winds close to the surface, but does not affect the winds within the atmosphere, which accelerate and may even result in being greater than the geostrophic wind speeds (9PM – 3AM).

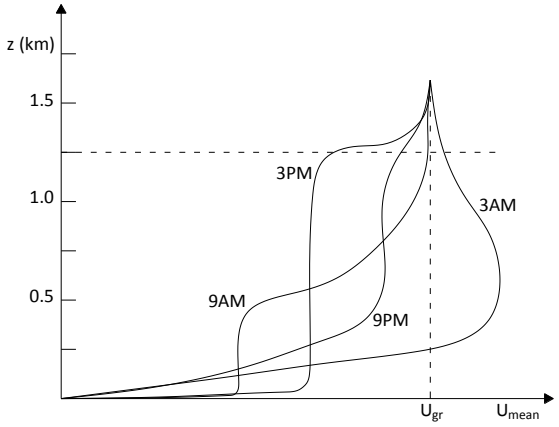

Figure 2.3 Diurnal wind speed variation within the ABL (Adapted from (Stull, 2000))

Within the surface layer (z<50m), the wind profile varies according to the atmospheric stability. During neutral conditions (synoptic winds) the profile follows the logarithmic profile described in Figure 2.2. During stable conditions (evening hours), the profile increases roughly linearly with height and during unstable conditions (daylight hours), the profile follows more of an exponential relationship. The three profiles are represented in Figure 2.4.

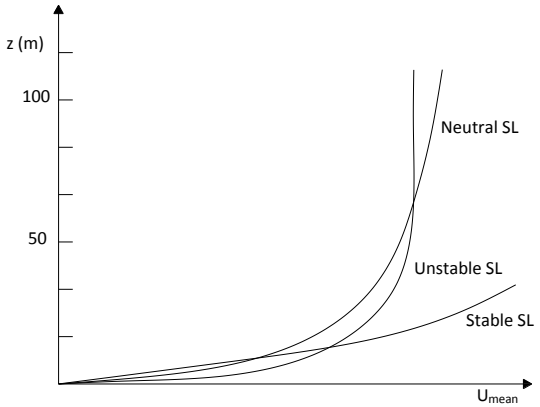

Figure 2.4 Wind speed profiles in the surface layer (Adapted from (Stull, 2000))

2.1.3 Thunderstorms

Compared with synoptic winds, thunderstorms are geometrically much smaller events, but can generate winds of greater magnitude than synoptic winds. They generate their energy through heat, where warm humid air rises to the upper layers of the atmosphere at which point the humidity evaporates, rapidly cooling the air mass. When the air is sufficiently cool, it descends to the ground surface and disperses laterally after impacting with the ground, provoking intense three dimensional and highly turbulent winds. The duration of the storm is typically very short, normally less than 10min, but can travel for up to 3 to 15km. Due to its rapid development and decay, the storm does not have sufficient time to develop a boundary layer profile, but presents a bell shaped profile where the maximum wind speed occurs at a height of around 100m.

Numerous investigators have studied the structure of the thunderstorm through scaled physical models, simulating the wind outflow as a vertical jet of air impacting on a horizontal surface. Figure 2.5 presents the mean horizontal wind speed profile of a physical thunderstorm downburst simulation. The figure shows the maximum wind speed occurs at a height H/D of 0.05, or 100m in full scale, reducing rapidly with height (Letchford & Mans, 2001).

Unlike synoptic and diurnal winds, thunderstorm winds generally exhibit a strong vertical component, in particular at the leading nose of the downburst. In terms of reservoir hydrodynamics, this can produce significant vertical forcing and agitation on the water surface.

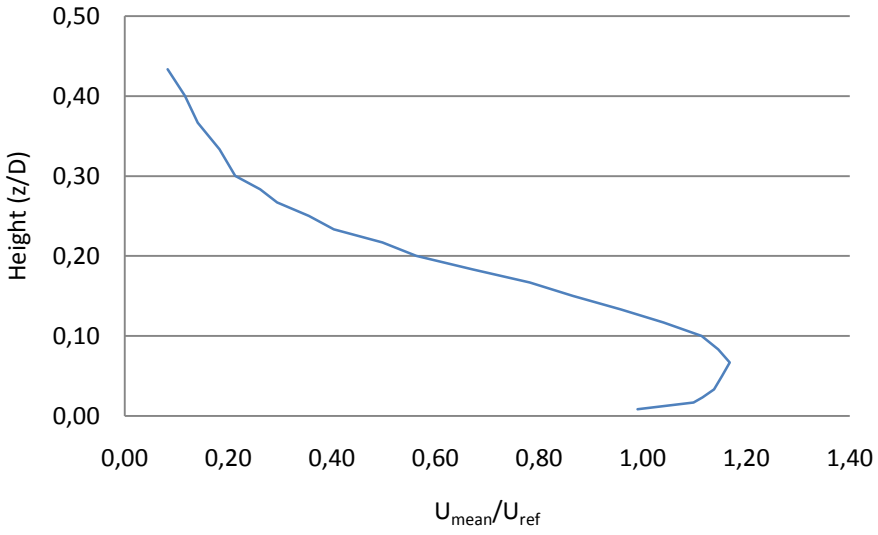

Figure 2.5 Mean horizontal wind speed profile of a simulated thunderstorm

2.1.4 Topographical effects

Wind features in mountainous terrain can be separated into two principal categories (Whiteman, 2000).

(a) Where the wind is produced by meso-scale weather systems and the mountains modify the velocity, direction and turbulence of the wind. The topographical features behave like bluff bodies which act as obstacles to the oncoming wind, creating zones of highly turbulent wake regions and creating intense winds in mountain channels.

(b) Local wind conditions can be created due to thermal differences in the atmosphere. In complex topography, thermal gradients will be developed in the atmosphere, driving localized wind conditions (i.e. anabatic/katabatic or bora/foehn conditions).

2.1.4.1 Flow induced by topographical obstacles

The terrain effects on the atmospheric flow conditions are dependent on the geometry of the terrain. Figure 2.6 presents the wind flow patterns for two simplified mountain geometries (Holmes, 2001). In the case of smooth hills (Figure 2.6(a)), or small crests, the wind speed increases when the flow travels up the face of the hill, reaching a maximum wind speed at the top of the hill before decreasing in magnitude as it travels down the downstream face of the hill. In this case no flow separation occurs.

For hills with a slope, z/L, greater than 0.3 (Figure 2.6(b)), flow separation occurs along the upstream and downstream slopes of the hill. The region within the separation bubbles are highly turbulent and will contain significant eddies and gusts. The wake region may also exhibit harmonic flow patterns, such as regular vortex streets.

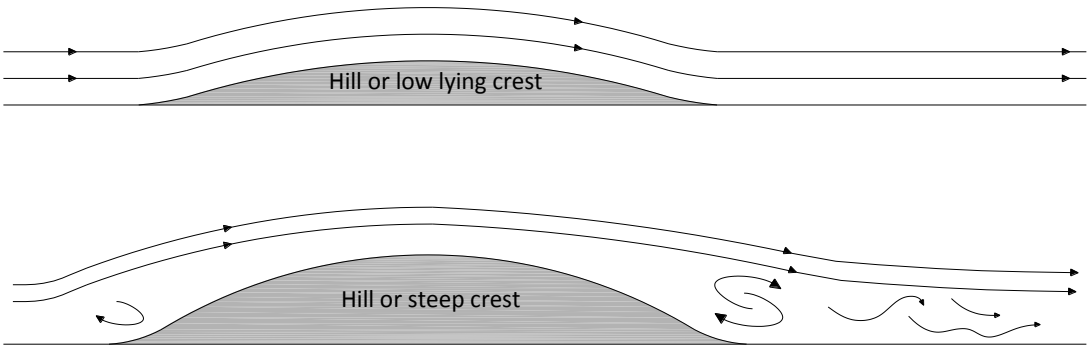

Figure 2.6 Illustration of wind flow patterns of different isolated topography profiles

Valleys and basins within the mountainous terrain are usually protected from the driving winds and exhibit low velocity flows. However, if the winds are strong at the mountain summit, eddies can be generated which can produce strong, localized, gusty winds within the valley.

The flow over mountains can also produce mountain waves, or gravity waves, in the atmosphere (Figure 2.7). This occurs when the warm air is forced above a mountain. As the warm air rises, it cools and becomes denser than the surrounding air and begins to fall due to gravity. Due to its momentum, the air drops too low so that it is warmer than the surrounding air and begins to rise again. It continues to oscillate until it reaches equilibrium with the surrounding air. The mountain waves tend to create a regular pattern which can form harmonic loading pulsations on the leeside of mountains. The wavelength of the wave is a function of the wind speed and the stability of the approaching flow.

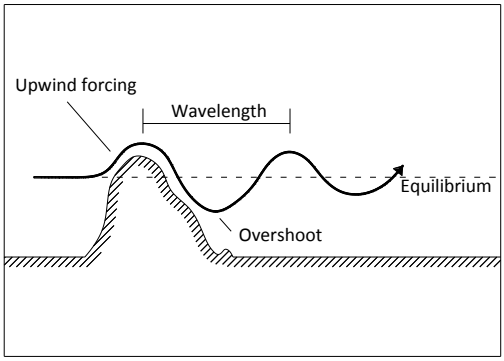

Figure 2.7 Mountain wave formation (Adapted from (Whiteman, 2000))

Strong winds are almost always present within channels between mountain ranges, as illustrated in Figure 2.8. The winds are primarily driven by pressure differences at either end of the channel and are particularly evident in coastal mountain ranges, due to the enhanced temperature differences between the air masses above the sea and above the mountains. During the winter months (Figure 2.8(a)), the air is cooler in the mountains. If the air cools enough, it will spill over the lowest crest of the mountain and accelerate through the mountain valleys in the direction of the sea. In contrast, during the summer the air is warmer over the land, causing the wind to flow in the direction of the mountain (Figure 2.8(b)). It is common to experience strong seasonal winds within valleys which have characteristic directions during summer and winter months.

Figure 2.8(b) also presents another feature of mountainous terrain, termed barrier jets. This occurs when the mountain range is too large for the wind to pass over its peak, so it must travel around the side of the mountain. In the northern hemisphere, the wind will always turn to the left, creating intense winds travelling along the side of the mountain range.

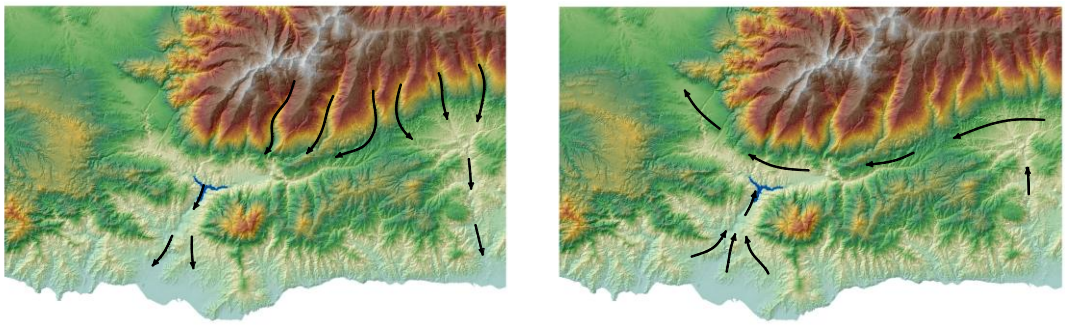

Figure 2.8 Flow channeling through mountain valleys (a) Winter months; and (b) Summer months

2.1.4.2 Local thermally induced flow

The local topography can also intensify the local diurnal wind patterns, in particular in coastal regions. As the diurnal wind patterns are created by temperature gradients in the atmosphere they may develop complex flow patterns within mountainous terrain. Typically, the circulation cells will be concentrated in valleys due to the temperature differences along the valley axis, as illustrated in Figure 2.9.

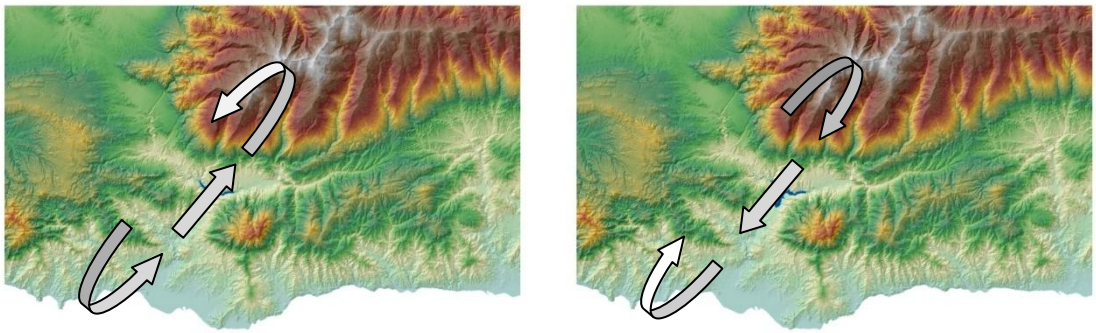

Figure 2.9 Diurnal mountain winds (a) Daylight hours featuring up-slope valley winds; and (b) Nighttime hours featuring down-slope valley winds

As the slope winds of the diurnal cycle are dominated by local temperature differences, they do not form a logarithmic boundary layer profile, but resemble more of a jet profile, as illustrated in Figure 2.10. The slope winds generally contain a maximum velocity of 1-5m/s, but will have higher magnitudes in coastal regions due to the increased temperature gradients. The peak wind speed occurs a few meters above the ground for down-slope winds and between 10-20m for upslope winds.

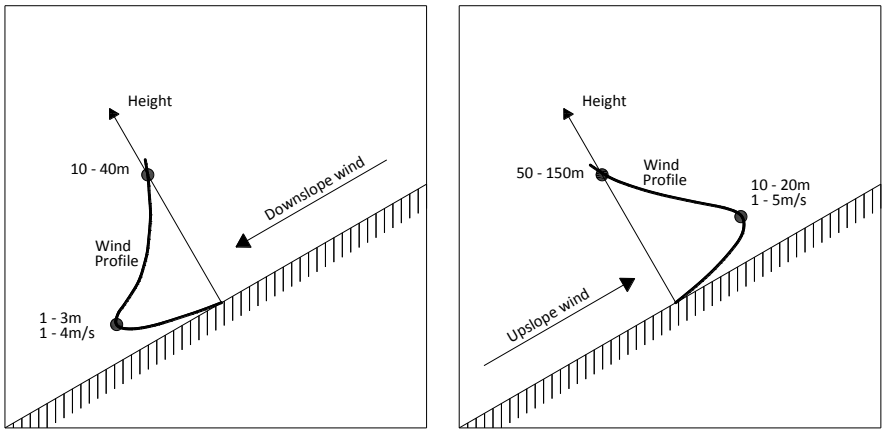

Figure 2.10 Mean velocity profiles for (a) Nighttime downslope winds and (b) Daytime upslope winds (Adapted from (Whiteman, 2000))

As the winds are developed from local temperature variations, their strength is determined by the local surface energy budget, which is a function of the climatic, regional and seasonal temperature variations, along with vegetation ground cover, cloud cover, snowcover and rainfall.

At this present time, successful analytical or numerical simulations of flow over mountains are limited to isolated hills. Simulations in complex flows are complicated by the difficulties in modeling the flow patterns around mountains that are situated within the wake of upstream topography. The lack of reliable mathematical models has led to the development of sophisticated experimental techniques, based on field measurements and wind tunnel simulations. Within the boundary layer wind tunnel, the simulation is performed within a carefully controlled environment to reproduce the atmospheric boundary layer due to synoptic winds, but at a much smaller scale. The simulations do not attempt to model thermally induced winds. Other types of wind events, such as thunderstorms or tornadoes have also been reproduced in scaled laboratory experiments.

2.2 Wind induced water circulation

In the management of man-made lakes and reservoirs, it is becoming increasingly important to be able to predict and control the mixing characteristics of the water circulation, caused by either atmospheric forcing on the water surface or due to lake inflow/outflow conditions. Predominantly, these studies are interested in determining the water quality by studying the resident time of fluid particles, bed sediment transport and the biological and chemical processes of the reservoir.

In closed basins, the surface boundary layer is the most complex zone of the water body. The processes in the upper region are the strongest due to the physical interaction of the water with the atmospheric forcing above (heat, kinetic energy, momentum, mass), enhancing the mixing of chemicals and nutrients. Sunlight and nutrients allow photosynthesis of phytoplankton, which is the most basic food source of the reservoir, setting the framework of the food chain (Wetzel, 2001). In addition, the water currents created by the atmospheric forcing are important for determining the thickness of the diffusive boundary layer on the bed, which controls the mixing and re-suspension of sediments within the water column. Directionally varying winds have been found to have a greater influence on the sediment concentration distribution than the lake advection and diffusion (Bailey & Hamilton, 1997). Hence, to understand the complex interactions that take place within close water bodies, the interaction between the water and the atmosphere is very important and is the focus of many hydrodynamic studies (Olsen, Hedger, & George, 2000; Wuest & Lorke, Small scale hydrodynamics in lakes, 2003).

Lakes react like mechanical oscillators to external forcing. The forcing may appear in a variety of forms, including atmospheric pressure variations, surface wind shear, temperature variations, the location and volume of inflow and outflow points, flood discharge, seismic activity and submarine mudslides. The response of the water body is through oscillations at the water surface and within the internal layer of the water body, which are determined by the shape and depth of the lake (Wetzel, 2001). For example, surface seiches are the rhythmic oscillation of the water in a closed or semi-closed water body which has a characteristic wavelength in the same order as the basin dimension. As illustrated in Figure 2.11, surface seiches are formed when the water is initially displaced by some external forcing. Once formed, the oscillations may continue for many cycles, slowly decaying to equilibrium through friction and gravitational forces. The node point represents the point of zero vertical velocity and maximum horizontal velocity and the inverse for the anti-node point.

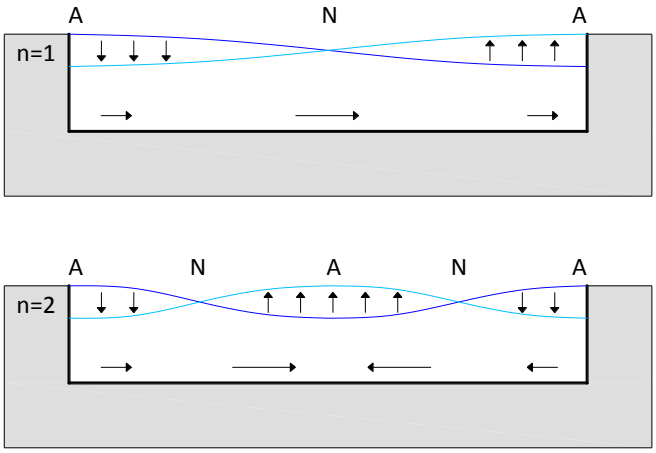

Figure 2.11 Idealization of surface seiches formed by atmospheric loading on a closed rectangular basin (Adapted from (Wuest & Farmer, 2003)). N – node point, A – antinode point.

The period of the oscillation is determined by the geometry of the basin and is independent on the loading. Therefore, theoretically, if an isolated load were applied at any location on the water surface, other than at the node point, the free surface will eventually oscillate in the form of a seiche. For closed basins, such as lakes and reservoirs, the generalized seiche period, T_b, can be estimated through Merian's formula:

$$T_b = \frac{2L_b}{n\sqrt{gh_b}} \qquad (2.2)$$

where L_b and h_b is the characteristic basin length and depth respectively, n is the n^{th} mode of oscillation. The formula is simplistic and does not consider the bathymetry of the basin, but it has been shown to estimate well the free surface period of lakes and reservoirs.

The amplitude of the free surface oscillation is a function of the forcing and its intensity. However, if the forcing is periodic with a frequency equal to the characteristic modal frequency of the basin, the amplitude of the seiche will increase through resonant excitation. As detailed in the previous section, the atmospheric forcing inherently contains harmonic components, such as four days for the passing of atmospheric pressure systems, 24 and 12 hours for diurnal and semi-diurnal variations and higher frequency components due to local topographical effects. Obviously, if the characteristic period of the lake seiche is similar to the periodicity of the surrounding atmospheric conditions, the seiche oscillations may go into resonance, increasing the intensity and amplitude of the oscillation with each successive load pulsation. For example, the Gulf of Mexico, Adriatic and Baltic Seas have a characteristic seiche period of around 24 hours which matches the diurnal period of the atmospheric forcing. Similarly, the Japan and Aegean Seas and Lake Erie, have seiche periods of around 12 hours, which match the semi-diurnal period of the atmospheric forcing. Consequently, these large water basins contain a regular, near-resonant, seiche, oscillating over the entire water basin.

Around the perimeter of the lake or sea, seiches also exist in the smaller bays, gulfs, lagoons and harbours, in particular in areas that do not exhibit large tidal variations (i.e. Mediterranean Sea). Two primary forcing mechanisms are responsible for the formation of the seiches in semi-closed basins, high frequency atmospheric loading and low frequency loading from the sea. The low frequency component is due to low frequency infra-gravity waves entering into the sub-basin that are generated by meteorological forces further out in the sea. There effects are commonly observed behind frontal systems, where there exists a region of instability with small, regularly occurring, convection cells behind the leading front. If the resonant motion matches the frequency of the harbour mode, resonant excitation may occur within the harbour with amplitudes of up to 2m; a phenomena which is known to occur regularly in Nagasaki Bay, Japan (Yu & Togashi, 1996), and the Sicily Strait (Candela, y otros, 1999), along with many harbours of the Mediterranean Sea, the Baltic Sea and the Port of Rotterdam (Vilibic & Mihanovic, 2003; Jordi, Basterretxea, Casas, Anglés, & Garcés, 2008; Wilding, Collins, & Ferentinos, 1980; Alpar & Yuce, 1996; Vilibic, Domijan, & Cupic, Wind versus air pressure seiche triggering in the Middle Atlantic coastal waters, 2005; Otsmann, Suursaar, &

Kullas, 2001; Suursaar, Kullas, & Otsmann, A model study of the sea level variations in the Gulf of Riga and the Vainameri Sea, 2002; Suursaar, Kullas, Otsmann, & Kouts, Extreme sea level events in the coastal waters of western Estonia, 2003; de Jong & Battjes, 2004).

Seiche oscillations within coastal lagoons have also been shown to be driven more from atmospheric forcing than by tidal variations, even if the period of the oscillations is in the order of 12 hours, which matches both the astronomical tidal frequency and the semi-diurnal atmospheric forcing frequency (Niedda & Greppi, 2007; Ferrarin & Umgiesser, 2005; Luettich, Carr, Reynolds-Fleming, Fulcher, & McNinch, 2002).

For smaller enclosed basins, such as lakes and reservoirs, the time scale of the lake oscillation is much lower, in the order of minutes, meaning that the macro-scale diurnal or semi-diurnal components of the atmospheric forcing will not create resonance of the free surface oscillation. Typically, the most significant seiches in small lakes and reservoirs are formed due to the passing of intense storms, where the large wind speeds instigate the set-up of the water at one end of the lake which is then released as the wind intensity decreases. The resulting surface seiche produces a large initial oscillation which then decays rapidly after instigation. For example, surface seiches of between 0.1-0.3m and periods of around 9.4 hours are observed a few times a year on Lake Kariba, a 280km long reservoir, which then quickly decay following a lognormal factor of 0.35 (Ward, 1979). Field studies of Lake Zurich showed the free surface oscillations are the combination of its first three modes due to its abnormal bathymetry, with periods between 14-45 min. (Hutter, Raggio, Bucher, & Salvade, 1982). Similarly, surface seiches of 0.04m were recorded on Lake Trichonis, a 21km long lake, which occurred after a storm with a mean wind speed of 10m/s. The bean shape of the lake did not tend to form clear oscillation patterns, but the primary seiche modes were observed to be between 6- 35 min (Zacharias & Ferentinos, 1997).

Resonant excitation of small lakes and reservoirs may also occur if the atmospheric forcing contains a harmonic component within the micro-scale range (Figure 2.1). As illustrated in the previous section, high frequency harmonics in the atmospheric forcing occurs from the formation of eddies behind local topographical features. Recent studies at Carchuna Beach has showed local topographical features may contribute to the formation of beach embayments due to wind vortex shedding off coastal headlands coupling with the downstream coastal hydrodynamics (Ortega-Sánchez, Bramato, Quevedo, Mans, & Losada, 2008).

The spatial variation of the atmospheric forcing also becomes important for accurately determining the free surface response, in particular for small lakes and reservoirs. In typical studies, the information for the atmospheric forcing is taken from a single anemometer located close to the lake or a nearby airport weather station. However, studies by (Podsetchine & Schernewski, 1999) have shown that simulations of a small lake with spatially homogenous loading produced a two-cell circulation, whereas, the simulation with a more accurate spatially variable loading produces a single cell circulation. Similar conclusions were presented by (Falconer, George, & Hall, 1991), who

concluded that the spatial resolution of the atmospheric forcing can modify the accuracy of numerical model predictions, in particular for lakes surrounded by topographical features and forests.

Below the surface boundary layer of the water body, the interior zone is characterized by stratification, reduced mixing and internal waves. The periodic oscillation of internal waves due to wind forcing is commonly observed and can be significantly greater than the free surface oscillations, but at a much lower frequency. Wind forcing on large lakes may create a surface seiche of around 0.02m, but can generate an internal seiche of up to 10m. Understandably, the internal seiches produce considerable vertical motion which dominates the mixing processes.

Internal waves within the Spanish reservoirs Sau and Baznar (Catalonia and Andalucia, Spain) were found to oscillate due to wind forcing (Hurtado, 2006). During the summer months, the thermally stratified layers of the reservoirs oscillated with clear and distinct frequencies which matched the diurnal and semi-diurnal atmospheric forcing (12 and 24hrs), directly effecting the circulation of the phytoplankton in the reservoir. Significant internal seiches were also observed in Lake Zurich, formed due to wind pulsations during the passage of storm events (Horn, Mortimer, & Schwab, 1986). The response of the internal seiches is dependent on the timing, strength and duration of the wind pulse and how it correlated with the existing motion of the internal seiche.

3 Numerical Modeling of Surface Seiches in a closed basin

3.1 Development of numerical model

Similar to the current study, the majority of previous researchers simulate water circulation in a small closed basin using a two-dimensional, depth-averaged, hydrodynamic model. Typical variations between models include the form of the bed friction term and the treatment of the coriolis forcing, along with the modeling method.

The water circulation in a reservoir is induced by a variety of forcing terms and damped by the frictional effects of the viscous forces. The behavior of a fluid element can be described by the spatial and temporal variation of its velocity, pressure, temperature and density. Assuming a small fluid volume, conservation of the physical laws of continuity, momentum and energy provide a complete description of the fluid flow.

The analytical or numerical modeling of lake circulation can be tackled in a variety of forms, from 1D linear models, two-dimensional depth or breadth averaged models, two dimensional multi-layered models (Falconer, George, & Hall, 1991; Wang, Hutter, & Bauerle, 2001; Hedger, Olsen, Malthus, & Atkinson, 2002; Olsen, Hedger, & George, 3D numerical modeling of Microcystis distribution in a water reservoir, 2000) to complex three dimensional computations using CFD codes. The CFD models have the added advantage of including complex turbulence models, dispersion and sediment re-suspension modeling options (Luketa-Hanlin, Koopman, & Ermak, 2007; Gavelli, Bullister, & Kytomaa, 2008; Olsen, Hedger, & George, 3D numerical modeling of Microcystis distribution in a water reservoir, 2000; Ta & Brignal, 1998; Kennedy, 2003).

For modeling of the surface seiche on a closed or semi-closed basin, a complex three dimensional model is not required. Assuming the water is homogenous, which is valid for lakes without stratification, the water circulation can be estimated using a depth integrated two-dimensional model. Although simplified, the model still successfully simulates the interaction between the total mass transport, free-surface displacement, atmospheric pressure gradient, wind stresses on the free surface and the bed bottom stresses and is known to provide a good approximation of the hydrodynamic processes of closed or semi-closed basins (Cheng & Dillon, 1976).

For the present study, the response of a closed water body to atmospheric forcing is solved using the shallow water equations, which are derived by depth integrating the Navier Stokes equations (See Appendix A for a complete derivation of the shallow water equations). The model assumes that the vertical velocity of the fluid is null and the fluid velocity is constant through its depth. Following (Dean & Dalrymple, 1991), the linearized form of the shallow water equations is derived for the equations of continuity and momentum, with the following assumptions (Sobey R. J., 2002):

1. Advective accelerations are negligible.
2. Coriolis accelerations are negligible.
3. The water free surface elevation is much less than the water depth ($\eta \ll h$).
4. The bed shear stress can be linearized to: $\tau_{b\alpha}/\rho_w = \lambda q_\alpha$, where λ is a linear friction factor.

The simplifications result in the linear form of the shallow water equations:

$$\frac{\partial \eta}{\partial t} + \frac{\partial q_x}{\partial x} + \frac{\partial q_y}{\partial y} = 0 \tag{3.1}$$

$$\frac{\partial q_x}{\partial t} = -gh\frac{\partial \eta}{\partial x} - \lambda q_x + F_x \tag{3.2}$$

$$\frac{\partial q_y}{\partial t} = -gh\frac{\partial \eta}{\partial y} - \lambda q_y + F_y \tag{3.3}$$

where η(x,y,t) is the local water surface elevation at time, t, and q(x,y,t) is the local depth-averaged flow velocity, h is the water depth, η is the water surface elevation, λ is the linear bed friction factor and $\mathcal{F}$(x,y) is the local meteorological forcing, defined as:

$$F_\alpha = -gh\frac{\partial}{\partial x_\alpha}\left(\frac{P_s}{\rho_w g}\right) + \frac{\tau_{sy}}{\rho_w} \tag{3.4}$$

where P_s(x,y,t) is the surface pressure and τ_s(x,y,t) is the surface wind shear. Therefore, the meteorological forcing is defined as the summation of the horizontal surface wind shear and the horizontal spatial gradient of the surface atmospheric pressure.

The numerical solution of the water free surface response is solved by performing the partial derivative of [3.1] with respect to t, and [3.2] and [3.3] with respect to x and y respectively:

$$\frac{\partial [1]}{\partial t} = \frac{\partial^2 \eta}{\partial t^2} + \frac{\partial^2 (uh)}{\partial x \partial t} + \frac{\partial^2 (vh)}{\partial y \partial t} = 0 \tag{3.5}$$

$$\frac{\partial ([2]h)}{\partial x} = \frac{\partial^2 (uh)}{\partial x \partial t} = -\frac{\partial}{\partial x}\left(gh\frac{\partial \eta}{\partial x}\right) + \frac{\partial \mathcal{F}_x}{\partial x} - \lambda\frac{\partial}{\partial x}(uh) \tag{3.6}$$

$$\frac{\partial ([3]h)}{\partial y} = \frac{\partial^2 (vh)}{\partial y \partial t} = -\frac{\partial}{\partial y}\left(gh\frac{\partial \eta}{\partial y}\right) + \frac{\partial \mathcal{F}_y}{\partial y} - \lambda\frac{\partial}{\partial y}(vh) \tag{3.7}$$

Substituting [3.6] and [3.7] into [3.5] gives:

$$\frac{\partial^2\eta}{\partial t^2} - \frac{\partial}{\partial x}\left(gh\frac{\partial\eta}{\partial x}\right) - \frac{\partial}{\partial y}\left(gh\frac{\partial\eta}{\partial y}\right) + \frac{\partial\mathcal{F}_x}{\partial x} + \frac{\partial\mathcal{F}_y}{\partial y} - \lambda\left(\frac{\partial}{\partial x}(uh) - \frac{\partial}{\partial y}(vh)\right) = 0 \tag{3.8}$$

where:

$$\frac{\partial\eta}{\partial t} = -\left(\frac{\partial}{\partial x}(uh) - \frac{\partial}{\partial y}(vh)\right) \tag{3.9}$$

Substituting $\xi = \eta$:

$$\frac{\partial^2\xi}{\partial t^2} + \lambda\frac{\partial\xi}{\partial t} - \frac{\partial}{\partial x}\left(gh\frac{\partial\xi}{\partial x}\right) - \frac{\partial}{\partial y}\left(gh\frac{\partial\xi}{\partial y}\right) + \frac{\partial\mathcal{F}_x}{\partial x} + \frac{\partial\mathcal{F}_y}{\partial y} = 0 \tag{3.10}$$

To eliminate the term $\frac{\partial\xi}{\partial t}$, consider the solution in the form:

$$\xi = \eta e^{-\gamma t} \qquad \text{for } \eta = \eta(x, y, t) \tag{3.11}$$

leading to:

$$\begin{aligned}\frac{\partial\xi}{\partial t} &= \eta_t e^{-\gamma t} - \gamma\eta e^{-\gamma t} \\ &= (\eta_t - \gamma\eta)e^{-\gamma t} \quad where\ \eta_t \approx \gamma\eta + \xi_t e^{\gamma t}\end{aligned} \tag{3.12}$$

$$\begin{aligned}\frac{\partial^2\xi}{\partial t^2} &= (\eta_{tt} - \gamma\eta_t)e^{-\gamma t} - \gamma(\eta_t - \gamma\eta)e^{-\gamma t} \\ &= (\eta_{tt} - 2\gamma\eta_t + \gamma^2\eta)e^{-\gamma t}\end{aligned} \tag{3.13}$$

$$\begin{aligned}\frac{\partial^2\xi}{\partial t^2} + \lambda\frac{\partial\xi}{\partial t} &= \left(\eta_{tt} - 2\gamma\eta_t + \gamma^2\eta + \lambda(\eta_t - \gamma\eta)\right)e^{-\gamma t} \\ &= (\eta_{tt} + (\lambda - 2\gamma)\eta_t + (\gamma^2 - \lambda\gamma)\eta)e^{-\gamma t} \\ &= \left(\eta_{tt} + \frac{\lambda^2}{2}\eta\right)e^{-\gamma t}\end{aligned} \tag{3.14}$$

$$\eta_{tt} - \frac{\partial}{\partial x}\left(gh\frac{\partial\eta}{\partial x}\right) - \frac{\partial}{\partial y}\left(gh\frac{\partial\eta}{\partial y}\right) + \frac{\lambda^2}{2}\eta = -\left(\frac{\partial\mathcal{F}_x}{\partial x} + \frac{\partial\mathcal{F}_y}{\partial y}\right)e^{\gamma t} \tag{3.15}$$

where the subscript 't' represents the partial derivative with respect to time, t. With boundary condition, $\vec{u}.\vec{n} = 0$ for $\partial\Omega$:

$$\frac{\partial u}{\partial t} = -g\frac{\partial\eta}{\partial x}e^{-\gamma t} + \frac{\mathcal{F}_x}{h} - \lambda u \tag{3.16}$$

$$\frac{\partial v}{\partial t} = -g\frac{\partial\eta}{\partial y}e^{-\gamma t} + \frac{\mathcal{F}_y}{h} - \lambda v \tag{3.17}$$

$[3.16]n_x + [3.17]n_y \rightarrow$

$$\frac{\partial}{\partial t}\left(u \cdot n_x + v \cdot n_y\right) = -ge^{-\gamma t}\left(\frac{\partial \eta}{\partial x}n_x + \frac{\partial \eta}{\partial y}n_y\right) + \frac{\mathcal{F}_x}{h}n_x + \frac{\mathcal{F}_y}{h}n_y \qquad (3.18)$$

$$\frac{\partial \eta}{\partial x}n_x + \frac{\partial \eta}{\partial y}n_y = \frac{1}{gh}\left(\frac{\mathcal{F}_x}{h}n_x + \frac{\mathcal{F}_y}{h}n_y\right)e^{\gamma t}$$

In summary, the governing equation of the water free surface elevation is:

$$\frac{\partial^2 \eta}{\partial t^2} - \nabla \cdot (gh\nabla\eta) + \frac{\lambda^2}{2}\eta = f(x,y,t) \qquad (x,y) \in \Omega, \quad t \in (0,+\infty) \qquad (3.19)$$

with boundary condition:

$$\nabla\eta \cdot \vec{n} = e(x,y,t) \qquad (x,y) \in \partial\Omega \qquad (3.20)$$

and initial condition:

$$\eta(x,y,t=0) = 0 \qquad (x,y) \in \Omega$$
$$\eta_t(x,y,t=0) = 0 \qquad (x,y) \in \Omega$$

where:

$$f(x,y,t) = -\left(\frac{\partial \mathcal{F}_x}{\partial x} + \frac{\partial \mathcal{F}_y}{\partial y}\right)e^{\gamma t} \qquad (3.21)$$

$$e(x,y,t) = \frac{1}{gh}\left(\mathcal{F}_x n_x + \mathcal{F}_y n_y\right)e^{\gamma t} \qquad (3.22)$$

The problem is solved using the partial differential equation (PDE) toolbox in Matlab, where the equations are discretized using the finite element method (FEM).

3.2 Validation of 2D model

Before application, the model is first validated by comparing its solution with the exact analytical solutions to different types of generalized atmospheric forcing events. The simulations are performed on a closed rectangular basin due to two forcing conditions, as presented by (Sobey R. J., 2002):

a. A sudden and uniform wind shear loading across the entire basin.
b. A travelling wind pulsation similar to the passing of a storm front.

3.2.1 ST1: Sudden uniform wind on a closed basin

The most basic atmospheric loading is due to a sudden and constant forcing applied across the length of the basin. The response is calculated for a one dimensional basin of length and uniform depth (L=2500m, h=5m), with forcing conditions: $q_y = \mathcal{F}_y = 0$, $q_x = q$ and $\mathcal{F}_x = \mathcal{F} = 1.5 \times 10^{-3}\ m^2/s^2$. The friction coefficient, λ, is assumed to be constant and equal to $1x10^{-4}$.

The analytical solution is presented in (Sobey R. J., 2002) and summarized below. The governing linearized equations are:

$$\frac{\partial \eta}{\partial t} + \frac{\partial q}{\partial x} = 0 \tag{3.23}$$

$$\frac{\partial q}{\partial t} = -gh\frac{\partial \eta}{\partial x} - \lambda q + \mathcal{F} \tag{3.24}$$

Assuming a constant and sudden application of atmospheric forcing across the surface of the basin, the initial boundary conditions of the analytical solution are:

$$\eta(x,0) = 0 \qquad \left.\frac{\partial \eta}{\partial t}\right|_{(x,0)} = 0 \tag{3.25}$$

$$\left.\frac{\partial \eta}{\partial x}\right|_{(x=0,t)} = \frac{\mathcal{F}}{gh} \qquad \left.\frac{\partial \eta}{\partial x}\right|_{(x=L,t)} = \frac{\mathcal{F}}{gh} \tag{3.26}$$

and the forcing, F, is applied only through the boundary conditions.

The eigenvalues and eigenfunctions of the solution are:

$$\beta_n = \frac{n\pi}{L}, \quad X_n(x) = \left(\frac{2}{L}\right)^{1/2} \cos(\beta_n x), \quad n = 1, 2, 3, \ldots \tag{3.27}$$

The model coefficients are:

$$\widehat{f_n} = \int_0^L -\left[\frac{F}{gh}\left(x - \frac{L}{2}\right)\right] X_n(x)\,dx \tag{3.28}$$

The analytical solution of the free surface elevation is:

$$\eta(x,t) = \frac{F}{gh}\left(x - \frac{L}{2}\right) + e^{-\lambda t/2} \sum_{n=1}^{\infty} \left[\widehat{f_n} \cos \omega_n t + \frac{\lambda \widehat{f_n}}{2\omega_n} \sin \omega_n t\right] X_n(x) \tag{3.29}$$

The analytical and numerical solutions to the atmospheric forcing are presented in Figure 3.1. The x-axis of the figures represent the distance along the length of the basin (m), the y-axis represents time (sec) and the z-axis the free surface elevation, η (m).

The figures illustrate the formation of a surface seiche in a closed basin due to constant forcing. After the loading is applied to the basin, the water is displaced from the downward end of the basin towards its far end, reaching a maximum height of approximately 0.025m at t=200 sec. Due to gravitational forcing, the displaced water beings to return to its equilibrium state, but overshoots. The free surface will continue to oscillate in this manner until it reaches equilibrium where the gravitational forcing on the displaced water volume is balanced by the atmospheric forcing.

Comparison between the two solutions show the numerical model matches the analytical solution in both the amplitude of the free surface oscillation (A=0.05m) and the period of the first mode, T_1= 415 sec.

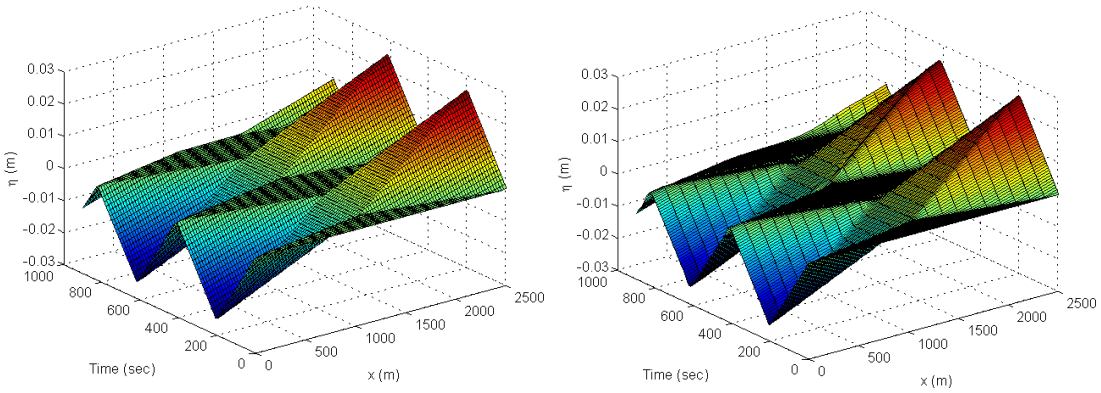

Figure 3.1 Free surface oscillation due to a sudden and uniform atmospheric loading on a 1D closed basin. (a) Analytical solution, (b) Numerical solution

3.2.2 ST2: Moving pulse on a closed basin

In this case, the solution for a storm moving across the length of a basin is solved for a basin with dimensions, L=5000m and h=5m. In this case, the atmospheric forcing is described as a rectangular loading pulse moving with a constant speed across the length of the basin:

$$\mathcal{F}(x,t) = F[H(x+a-Vt) - H(x-Vt)] \qquad (3.30)$$

where H is a Heaviside function, F is the maximum magnitude of the rectangular loading with width a, that is moving across the basin with a speed V_p. As with the previous example, the magnitude of the loading is equal to $\mathcal{F} = 1.5 \times 10^{-3}\ m^2/s^2$.

In this test case, the loading is not only applied on the boundaries, as with case ST1, but also over the water surface. From (Sobey R. J., 2002), the boundary conditions of the analytical solution are:

$$\eta(x,0) = 0 \qquad \left.\frac{\partial \eta}{\partial t}\right|_{(x,0)} = 0 \tag{3.31}$$

$$\left.\frac{\partial \eta}{\partial x}\right|_{(x=0,t)} = \frac{\mathcal{F}}{gh}\left[H(t) - H\left(t - \frac{a}{V}\right)\right] \tag{3.32}$$

$$\left.\frac{\partial \eta}{\partial x}\right|_{(x=L,t)} = \frac{\mathcal{F}}{gh}\left[H\left(t - \frac{L}{V}\right) - H\left(t - \frac{L+a}{V}\right)\right] \tag{3.33}$$

For the free modes, the eigenvalues and eigenfunctions of the solution are:

$$\beta_0 = 0, \quad X_0(x) = \left(\frac{1}{L}\right)^{1/2} \tag{3.34}$$

$$\beta_n = \frac{n\pi}{L}, \quad X_n(x) = \left(\frac{2}{L}\right)^{1/2} \cos(\beta_n x), \quad n = 1, 2, 3, \ldots \tag{3.35}$$

In this case f_n is null, however:

$$\begin{aligned}\hat{\phi}_n(t) &= \left(\frac{2}{L}\right)^{1/2} \int_0^L F[H(x - Vt) \\ &\qquad - H(x + a - Vt)] \cos(\beta_n x)\, dx \\ &= \left(\frac{2}{L}\right)^{1/2} F\left[\cos(\beta_n Vt)\left[H(t) - H\left(t - \frac{L}{V}\right)\right]\right] \\ &\qquad - \cos\left(\beta_n (Vt - a)\right) \\ &\qquad \times \left[H\left(t - \frac{a}{V}\right) - H\left(t - \frac{L+a}{V}\right)\right]\end{aligned} \tag{3.36}$$

$$\begin{aligned}\psi_n(t) = \left(\frac{2}{L}\right)^{1/2} F\Bigg[&(-1)^{\mathrm{n}}\left[H\left(t - \frac{L}{V}\right) - H\left(t - \frac{L+a}{V}\right)\right] \\ &- \left[H(t) - \left(t - \frac{a}{V}\right)\right]\Bigg]\end{aligned} \tag{3.37}$$

The analytical solution for the free surface elevation is:

$$\begin{aligned}\eta(x,t) = \sum_{n=0}^{\infty} \Bigg[&\int_0^t \frac{1}{\omega_n} e^{(-\lambda(t-\tau)/2)} \\ &\times \sin \omega_n (t - \tau) \left\{\hat{\phi}_n(\tau) + \psi_n(\tau)\right\} d\tau \Bigg] X_n(x)\end{aligned} \tag{3.38}$$

The analytical and numerical solutions of the free surface elevation are described in Figure 3.2. The figures show the initial setup of the free surface after the passing of the storm (x=5000), with a maximum free surface elevation in the order of of 0.1m. After the storm has crossed the basin (T=5000 sec), the free surface is forced only be gravity and the basin is free to oscillate until it reaches equilibrium. This is reflected in the

solutions, which shows the free surface quickly dampens after the initial displacement by the storm, with a free surface oscillation in the first mode, T_1 = 415 sec, but with an amplitude in the order of 0.01m.

Comparison between the two simulations show the numerical model successfully simulates the free surface response due to the moving pulse loading.

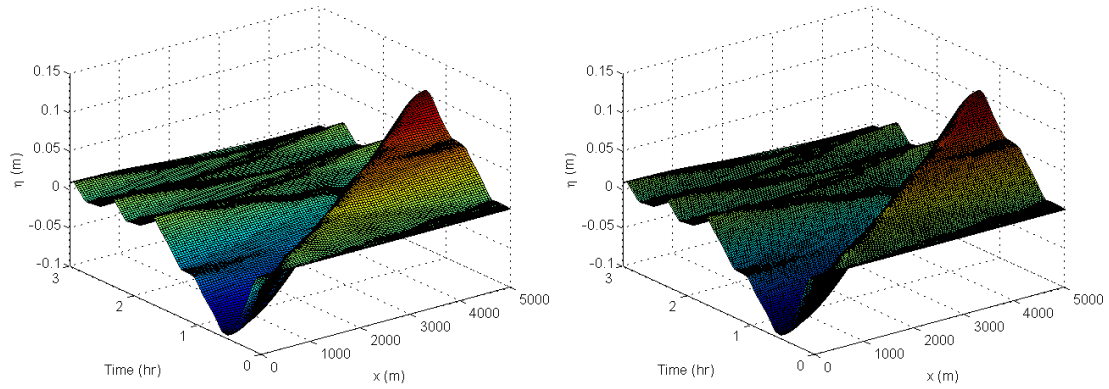

Figure 3.2 Free surface oscillation due to a moving atmospheric loading on a closed basin (a) Analytical solution, (b) Numerical solution

4 Rules Reservoir

4.1 General description

The Rules Reservoir is located along the Mediterranean coast of southern Spain, roughly 20km inland from the coastal town of Motril. Construction of the reservoir was completed in 2003 after blocking the valley of the Guadalfeo River shortly downstream from its intersection with the River Ízbor. Its purpose is to supply drinking water to the residents along the Granada coastline and to irrigate the subtropical and greenhouse crops that exist along the coastal region (Pérez, 2004). Table 4.1 details the usage of the reservoir.

Table 4.1 Water usage proportions of Rules Reservoir (Pérez, 2004)

Usage	Percent of Usage
Water supply	19
Irrigation	40
Flood control	30
Production of hydroelectric power	9
Recreational and other uses	2

The reservoir is an ideal test case for the study, as it located in a region of extremely complex topography which can create a wide variety of atmospheric flow patterns. Figure 4.1 describes the topography of the reservoir catchment area and the surrounding region. As illustrated, the reservoir lies at the end of a mountain valley that links the Sierra Nevada to the Mediterranean Sea, orientated in the south-west/north-east direction. At its northern end, the reservoir divides into the two valleys of the Ízbor and Guadalfeo rivers. The topography is dominated by the mountains of the Sierra Nevada to the north, which includes the highest mountain peak in the Iberian Peninsula (3480m). The topography to the east and west of the reservoir are also significant, with peaks of around 1800m and 1200m, respectively.

The catchment area of the reservoir covers a total surface area of 1070 km^2, which yields an annual water runoff of 210 Hm^3/yr (Pérez, 2004). At full capacity, the water level of the reservoir is 243m above sea level, as illustrated in Figure 4.1, with a maximum water volume of 117Hm^3.

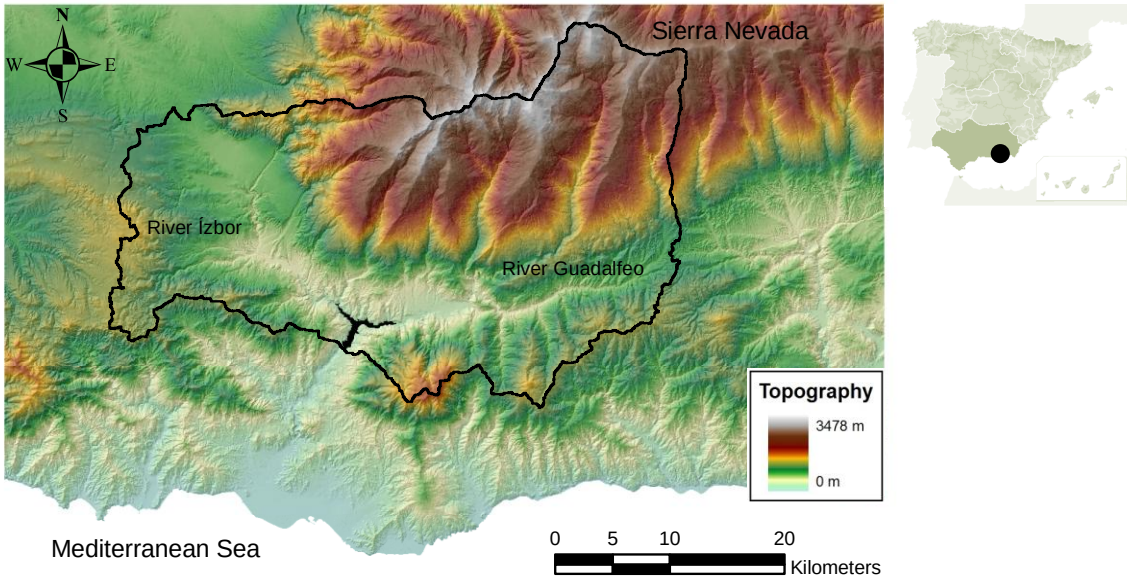

Figure 4.1 Topography of the reservoir catchment area and surrounding region

4.2 Local wind climate

An analysis of the local wind climate for the region is presented using historical data obtained from the Motril Nautical Club (Latitude 36327, Longitude 331492, Height 3m), situated approximately 20km to the south of the reservoir on the Mediterranean Coast. The historical data was provided by the Instituto Nacional de Meteorología in excel format, consisting of 20 years of valid data, between 1986 and 2008 (excluding the years 1994 and 1999). It is assumed that the meteorology station at Motril is sufficiently outside of the mountainous terrain and is free from any local topographical effects.

4.2.1 Wind directionality

The wind directionality for the region is presented in Figure 4.2. The x axis represents the proceeding wind direction, where North is 0º and East is 90º. The y axis represents the frequency of observations. The figure shows winds from the west are the most common and also produce winds with the largest magnitude (>12m/s). High velocity

winds also originate from the east-southeast. This suggests the local climate is dominated by synoptic winds from the easterly and westerly directions.

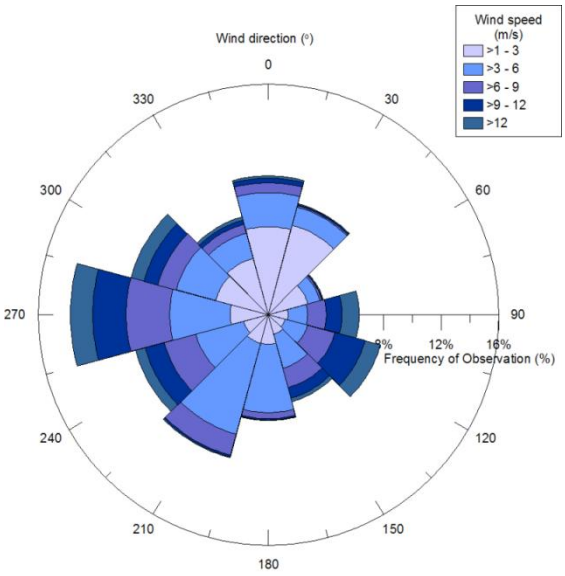

Figure 4.2 General wind directionality of the region

Figure 4.3 presents the seasonal wind directionality, highlighting the diurnal processes that occur within the region. During the summer months, the heating of the air mass over the Sierra Nevada produces a sea breeze with winds ranging between 3-6 m/s, with a dominant south-southwest wind direction (210º). During the autumn and winter months the wind changes direction, with winds originating more frequently from the north, with almost no winds originating from the sea. As described in Section 2.1.4, this is typical for coastal mountain ranges, where the large temperature differences in the mountains create seasonal variations in wind directionality. During all months, the larger magnitude winds consistently originate from the south-easterly and westerly directions.

4.2.2 Extreme Wind speed

The extreme wind speed variation, in function with wind direction and return period are illustrated in Figure 4.4. The analysis is performed assuming a Gumbel Type I extreme value distribution, where the winds are presented as mean hourly wind speeds at a height of 10m. It is assumed that the anemometer at the Motril Nautical Club is surrounded by open terrain in all directions and no roughness length corrections were used in the analysis. The figure shows the easterly and westerly winds provide the highest wind speeds, as they dominated the directions of the synoptic winds.

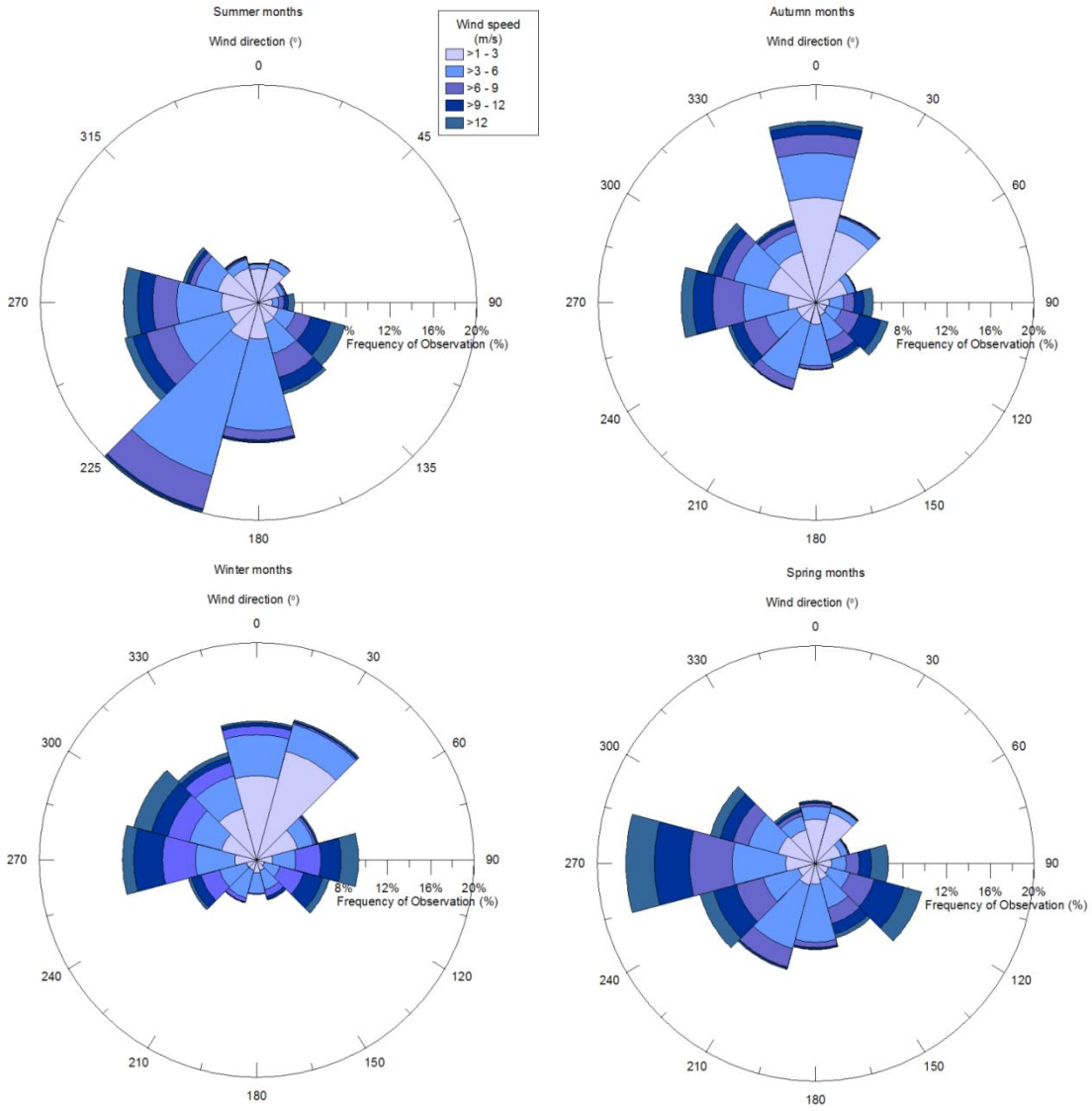

Figure 4.3 Seasonal wind directionality of the region

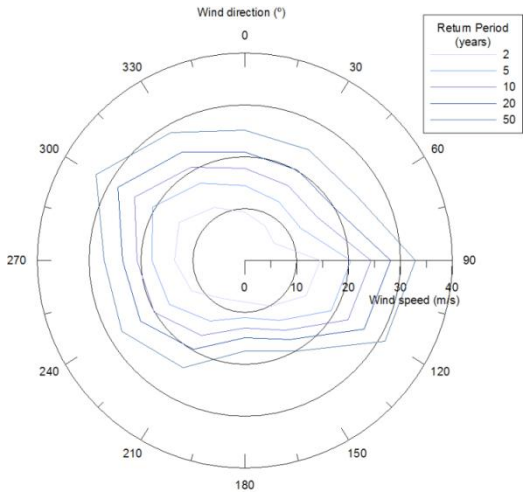

Figure 4.4 Extreme wind speed variation for the region according to wind direction and return period

4.3 Reservoir bathymetry

Figure 4.5 illustrates the bathymetry of the reservoir at its maximum capacity. As indicated, construction of the reservoir was completed in 2003 and and such it has not filled to capacity. The figure indicates the water level at the time of the present study (183m ASL). The bathymetry of the reservoir was taken from a detailed survey performed in 2005 through a series of sondar measurements (Ruiz & Nanía Escobar, 2006). The survey was limited to the depth of the water at the time, which was approximately 173m ASL. For water depths greater than this, the digital topography from (Molero Melgarejo, 2004) is merged with the surveyed data to create a hybrid bathymetry dataset. As illustrated in the figure, the topography from (Molero Melgarejo, 2004) does not contain the same resolution as the surveyed data, but is adequate for the current study.

In the years since the bathymetry survey in 2005, considerable earthworks have been performed in the construction of a bridge crossing the reservoir at the junction of the Ízbor and Guadalfeo Rivers. Additionally, construction works have been ongoing along the northern shoreline of the River Ízbor, which may have also modified the local topography in the Ízbor valley. Although the earthworks will have modified the local bathymetry surrounding the junction and may also have created an increase in sedimentation within the reservoir, the surveyed bathymetry data has not been modified to compensate for any changes that may have occurred.

At its current level, the reservoir is almost two-dimensional in nature and can be estimated to be roughly rectangular in shape with an average water depth, h_{mean}, of 15m (h_{max}=35m beneath the dam wall), with characteristic dimensions of length 2500m and width of 200m. At its maximum capacity, the reservoir stretches into the two valleys of the Rivers Ízbor and Guadalfeo, which are orientated in the easterly and westerly directions. At maximum capacity, the average water depth becomes h_{mean}=35m, with a maximum depth of h_{max}=95m. The water depth within the Ìzbor and Guadalfeo valleys remains relatively shallow (<10m), but extend for a considerable distance into the two valleys. At an intermediate depth of 213m a.s.l., the average water depth is h_{mean}=28.7m.

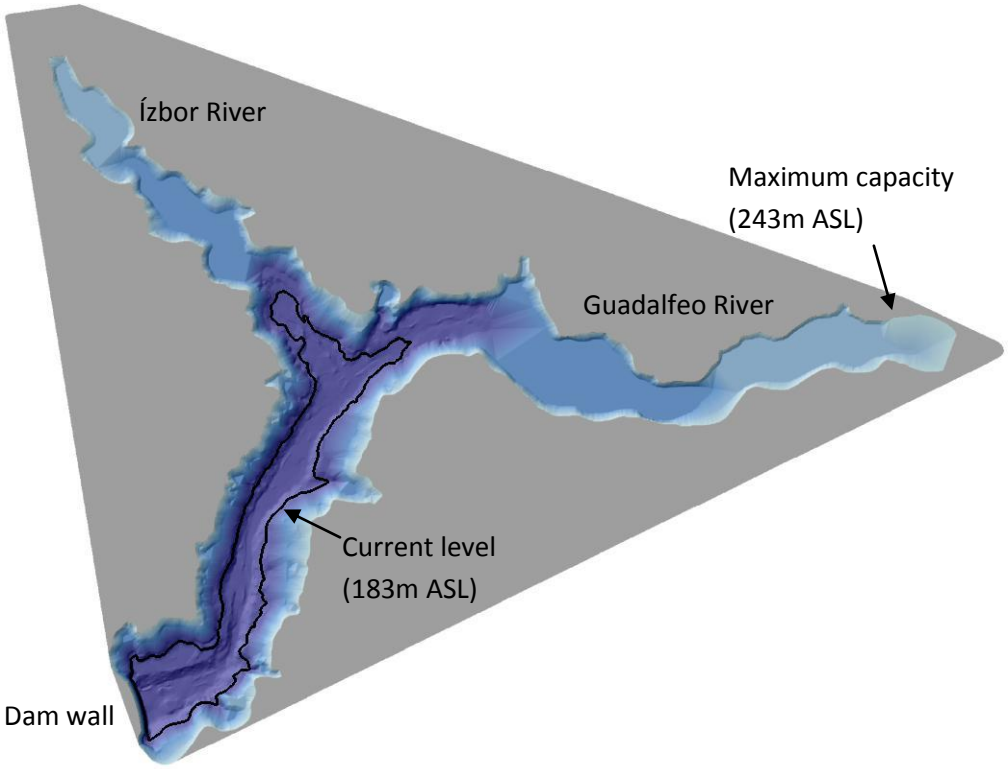

Figure 4.5 Reservoir bathymetry at full capacity (243m ASL) with the current water level (183m ASL) indicated

4.4 Normal mode decomposition

Identification of the free surface eigenmodes of the reservoir are obtained through an eigenvalue analysis. The shape and period of the seiche modes are a function of the basin shape and independent of the atmospheric forcing. This allows the natural modes of the reservoir to be readily determined for various water levels with no prior knowledge of the forcing conditions. The response of the reservoir to random atmospheric forcing is then the summation of the response for each of the eigenmodes, where most of the energy content is typically dominated by the first few modes.

The first four surface seiche modes are derived assuming the water density is constant throughout the basin. The eigenvectors, X, and the eigenvalues, β, of the reservoir are determined by solving:

$$AX = \beta X \tag{4.1}$$

where A is constructed based on the reservoir bathymetry (represented as a triangular mesh with 967 elements) and the boundary conditions. The matrix A and the equation are both constructed and solved using the Matlab Partial Differential Equation toolbox. The eigenfrequencies, ω, are:

$$\omega_n = \sqrt{\beta_n} \tag{4.2}$$

The period of each seiche mode, n, can then be calculated from the eigenfrequencies:

$$T_n = \frac{2\pi}{\omega_n} \tag{4.3}$$

Figure 4.6 presents the first four seiche modes of the reservoir at the current free surface elevation of 183m. The first three modes present a shape similar to that of a rectangular basin, with the first mode having a single point of inflexion at the centre of the reservoir. The second and third modes, respectively, present two and three node points (N) along the length of the reservoir. The fourth mode is dominated by oscillations at the northern end of the reservoir between the inlets to the Ízbor and Guadalfeo rivers. The periods of the first four modes are also represented in the figure, with the first mode calculated as being less than 10 minutes (503 seconds). This does not match well with the estimate of the first mode according to Merian's formula:

$$T_b = \frac{2L_b}{n\sqrt{gh_b}} \tag{4.4}$$

where L_b and h_b is the basin length and depth respectively, n is the n^{th} mode (n=1). Assuming, the length of the reservoir is 2500m with a constant water depth of 15m, the period of the first mode is estimated as 412 seconds, an underestimation of 18%. The estimated values also differ from the eigenvalue periods for the higher modes, with underestimations of 9% for the period of the second and third modes. The fourth mode does not oscillate along the length of the reservoir, but between the two small northern branches of the Ízbor and Guadalfeo Rivers and is not estimated by Merian's formula. The mode shapes of the free surface for the reservoir at full capacity (243m ASL) and at an intermediate depth (213m ASL) are also provided in Appendix B.

Table 4.2 summarises the periods of the first four fundamental modes of the reservoir free surface, calculated according to the eigenvalue analysis. The table indicates the periods of the first four modes remain relatively similar between the current water level and the intermediate water level of 213m ASL, however the mode shapes are quite varied as illustrated in Appendix B, due to the change in the reservoir geometry. As indicated, the water begins to enter further into the Ízbor and Guadalfeo river valleys, complicating the mode shape response. At full capacity, the water stretches for approximately 2km into the northern valleys, but the water within the valleys remains shallow (<10m), increasing the period of the first four modes. The first two modes responds with oscillations concentrated in the Guadalfeo and Ízbor valleys respectively. The remaining two mode shapes are primarily due to oscillations between the Ízbor and Guadalfeo valley water bodies with less contribution from the water body in the southern valley.

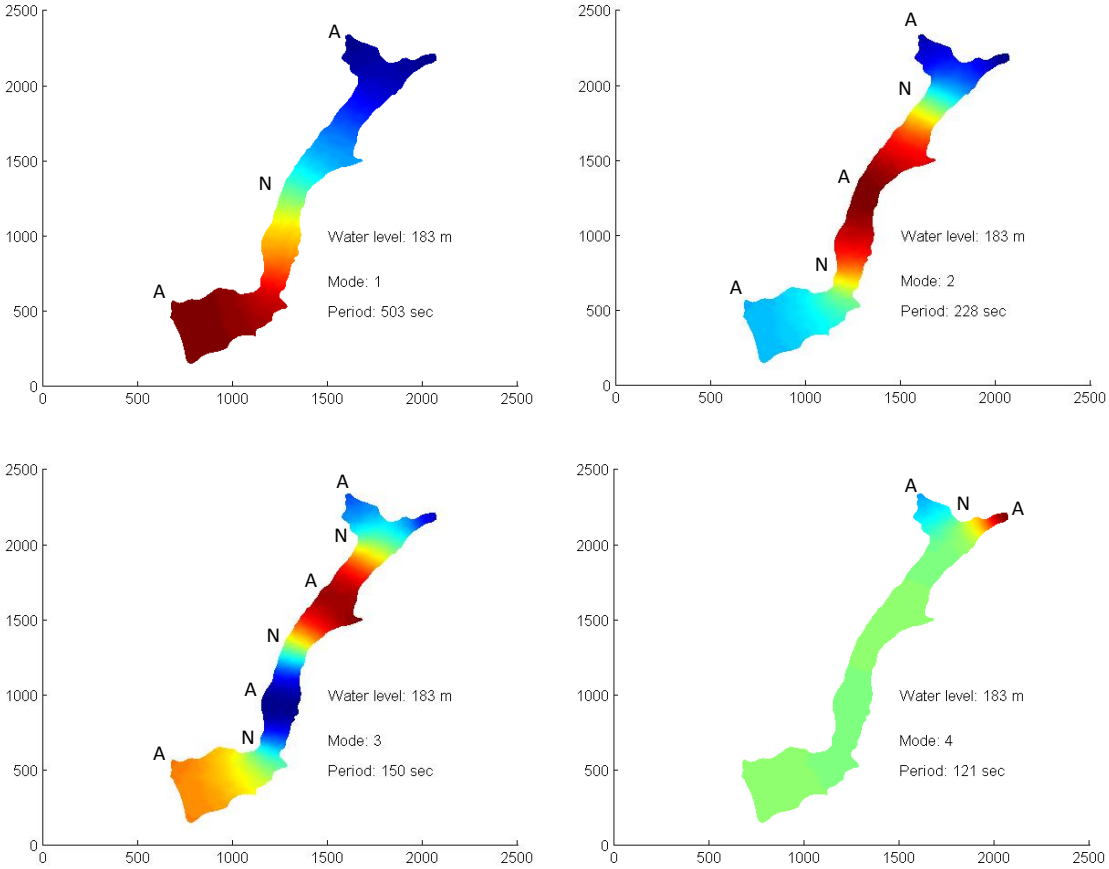

Figure 4.6 First four eigenmode shapes of Rules Reservoir (Water elevation 183m ASL)

Table 4.2 Fundamental periods of oscillation according to the eigenvalue analysis

Water depth (ASL)	Period according to eigenmode (sec)			
	1	2	3	4
183 (current level)	503	228	150	121
213	402	223	167	120
243 (full capacity)	703	456	357	248

4.5 Field measurements

Field measurements of the reservoir response to atmospheric forcing were recorded over a 13 day period in February, 2008. Simultaneous measurements of the atmospheric forcing (barometric pressure and wind speed and direction) and the hydrodynamic response (free surface elevation and current profiles) were captured at various locations along the principal axis of the reservoir.

4.5.1 Instrumentation

The atmospheric conditions were obtained with three weather stations, each consisting of a Setra atmospheric pressure sensor and a Gill 2D sonic wind anemometer. The data were recorded by a Campbell Scientific CR800 datalogger and manually downloaded during the field survey. The sensors captured the atmospheric pressure and wind speed and direction at a continuous sample rate of 5 seconds during the 13 day period. The anemometers were located as close to the water´s edge as possible while still preserving their safety, at a height of 10m above the water level.

The reservoir hydrodynamics were measured with a series of wave and current sensors, placed along the central axis of the reservoir and adjacent to the meteorological sensors. Two NORTEK acoustic wave and current meters (AWAC) and an acoustic doppler current profiler (ADCP) were used in the field study, where each system comprises of temperature, compass, tilt and pressure sensors. The three hydrodynamic sensors were programmed to measure both the water surface elevation and the water current profiles at regular intervals.

Each system was fixed to a metal tripod and lowered down to the reservoir bed, facing in the upward direction. Figure 4.7 presents a photograph of the anemometer at Station A and the ADCP current profiler mounted on its tripod, prior to deployment in the field.

The night before deployment, the hydrodynamic profilers were calibrated and the measurement programs were downloaded to the onboard controller. The onboard clocks of the profilers and the anemometer dataloggers were all set to the computer time of each sensor to ensure correlation between the various instruments utilized during the field campaign.

Figure 4.7 Photographys of the instruments used in the field study (a) Meteorological station at Location A (b) ADCP sensor fixed to tripod prior to deployment at Location C

4.5.2 Instrument locations

Figure 4.8 presents the deployed locations of the meteorological anemometers and current profilers. The current profilers have a separation distance of approximately 550 - 900m, in water depths ranging between 10 – 25m. The central probe was positioned with a small offset from the nodal point of the first mode oscillation.

The water depths at the test locations were verified with a handheld sondar at the time of deployment. The soundings were found to coincide well with the bathymetry data measured during the original survey.

4.5.3 Data acquisition

The meteorological and hydrodynamic sensors were programmed to continuously monitor the atmospheric conditions, water surface elevation and water current profiles during the 13 day period. The atmospheric conditions (wind speed, direction and barometric pressure) were continuously sampled with a sample frequency of 5 seconds. Due to battery limitations, the ADCP sensor at Station C lasted for six days, which was replaced on day 7. Therefore, the current profile measurements at Station C are continuous for the first six days (February 14-19), with a single day with no data, followed by another six days of continuous data (February 21-26). The measurement parameters of the current meters differed at each station, in most cases to set the sensor to its maximum allowable resolution (within battery and computer memory limitations), as summarized in Table 4.2.

The AWAC and ADCP sensors are not capable of simultaneously measuring the water current profiles and the water free surface elevation. Instead, the sensors alternate between the two measurements, with the first 1024 seconds of every hour designated for measuring the water surface elevation. For the remaining 42 minutes of the hour, the sensor records the water velocity profile at 60 sec averages. The process is then repeated every hour.

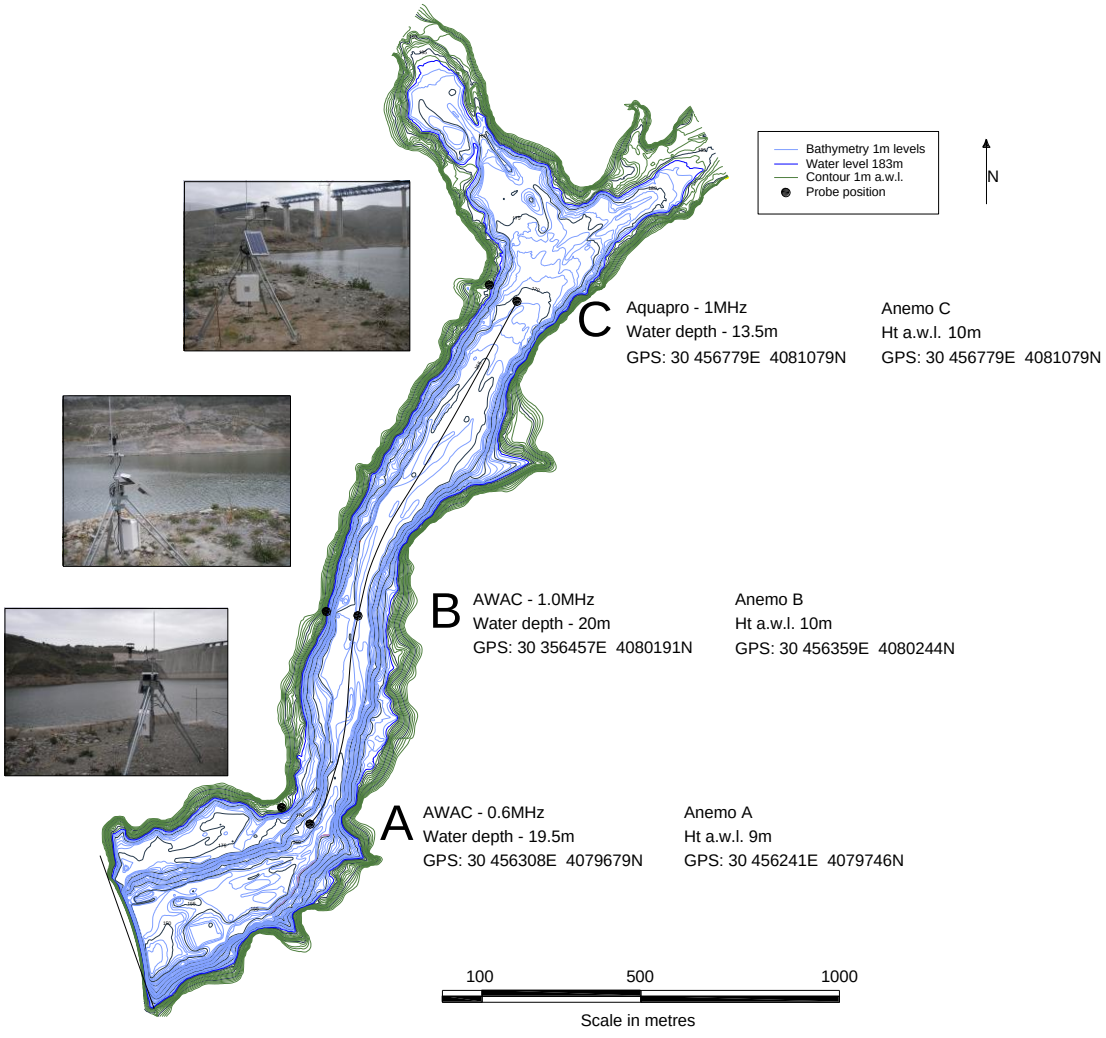

Figure 4.8 Bathymetry of Rules Reservoir at its current water depth with study locations. Adapted from (Ruiz & Nanía Escobar, 2006)

Table 4.2 Probe settings of current profile and water surface elevation measurements

Stat.	Probe	Water Depth (m)	Current profile			Water surface elevation		
			Aver. Int.	Aver. time	Cell size	Num. sample	Sample rate	Sample Int.
			(sec)	(sec)	(m)		(Hz)	(sec)
A	AWAC 0.6MHZ	19.5	60	55	1	1024	1	3600
B	AWAC 1MHZ	20	60	55	0.5	2048	2	3600
C	ADCP 1MHz	13	60	55	1	1024	1	3600

4.5.3.1 Atmospheric conditions

The atmospheric conditions, measured at each of the three stations around the reservoir, are presented in Figure 4.9. Figure 4.9(a) shows the barometric pressure variation, presenting two clear periodicities in the mesoscale, corresponding to 6 days and 12 hours. These periodicities are clearly defined in the frequency distribution of the barometric pressure, as shown in Figure 4.10(a), where periods of 6.3 days, 24 hours and 12 hours are evident. As described in Chapter 2, the large scale periods of six days are due to the passing of the atmospheric pressure systems across Spain, while the diurnal and semi-diurnal undulations are due to the diurnal circulation cells. Peak pressures occurred almost daily at 11:00 in the morning, prior to the onset of the afternoon breeze blowing from the Mediterranean Sea. The second peak in the atmospheric pressure occurred daily at around midnight before the winds began to return to the sea from the Sierra Nevada.

Figure 4.9(b) presents the variation of the wind speed during the two weeks. The wind speed presents a clear diurnal cycle, where the winds increase in the afternoon hours, as commonly observed in coastal mountainous areas. Daily peaks were consistently recorded with a magnitude in the order of 10m/s, with one instance of a peak gust wind speed of 22m/s on February 19th. Larger wind speeds are noted to occur consistently at Station A, which is the station located closest to the dam and in an area where the valley contracts slightly. The winds tend to reduce in magnitude with increasing distance from the dam wall as the valley widens. The diurnal variation in the wind speed is apparent in the frequency distribution of the wind speed, as illustrated in Figure 4.10(b), with a clear peak at 24 hours. The semi-diurnal peak at 12 hours is present, but it is lost amongst other peaks of similar frequency (10, 12 and 15 hours). Figure 4.9(c) presents the variation of the wind directionality in time.

Figure 4.11 presents the wind directionality recorded at the three locations in the form of windroses. Two wind directions dominate the local wind conditions above the reservoir, following the alignment of the reservoir valley. The wind directionality recorded at Motril (Mediterranean Sea) is also presented, which displays greater variation but similar trends. During the afternoon hours, when the wind speed is at its greatest, the winds originate from the Mediterranean Sea moving in the direction towards the Sierra Nevada, following the alignment of the valley. During the evening hours, the winds from the Sierra Nevada return to the sea, but flow through the valley at a much lower speed. The wind direction varies slightly between stations, matching closely with the alignment of the local topography at each location.

For reference, Appendix C presents daily charts of the atmospheric forcing captured during the field study.

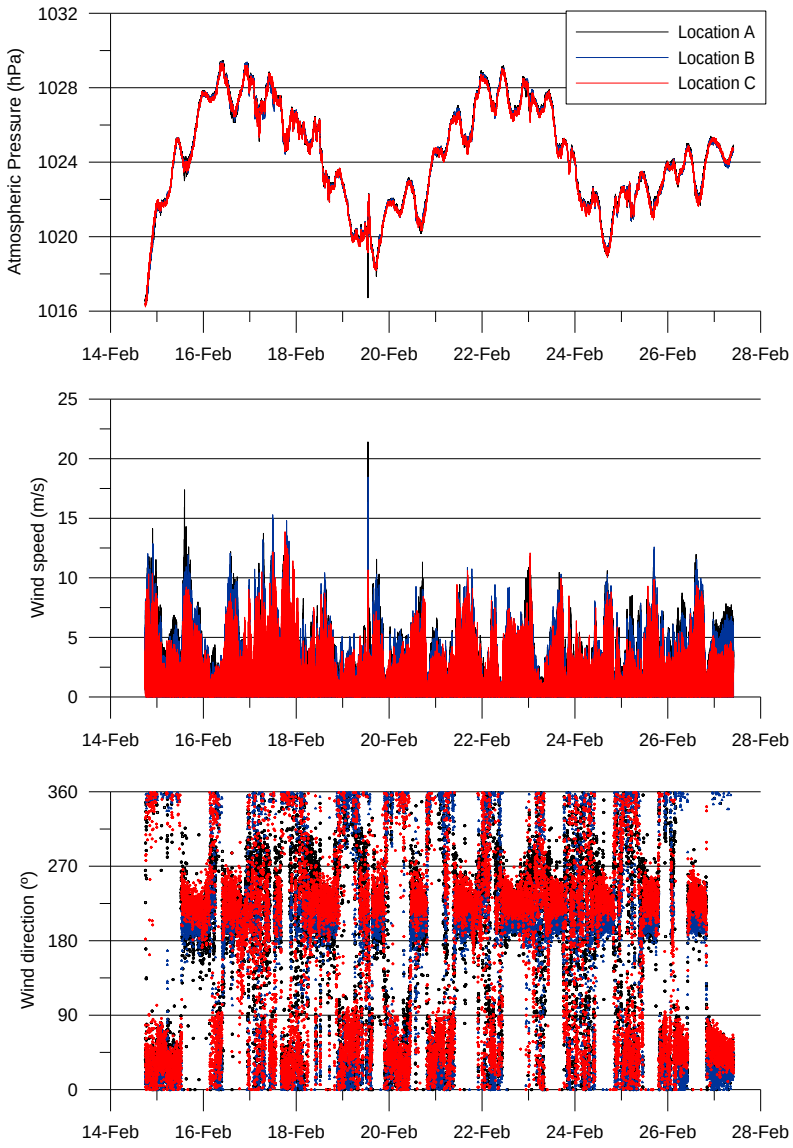

Figure 4.9 Atmospheric conditions recorded during the 13 day field campaign. (a) Atmospheric pressure (hPa), (b) Wind speed (m/s), (c) Wind direction (º)

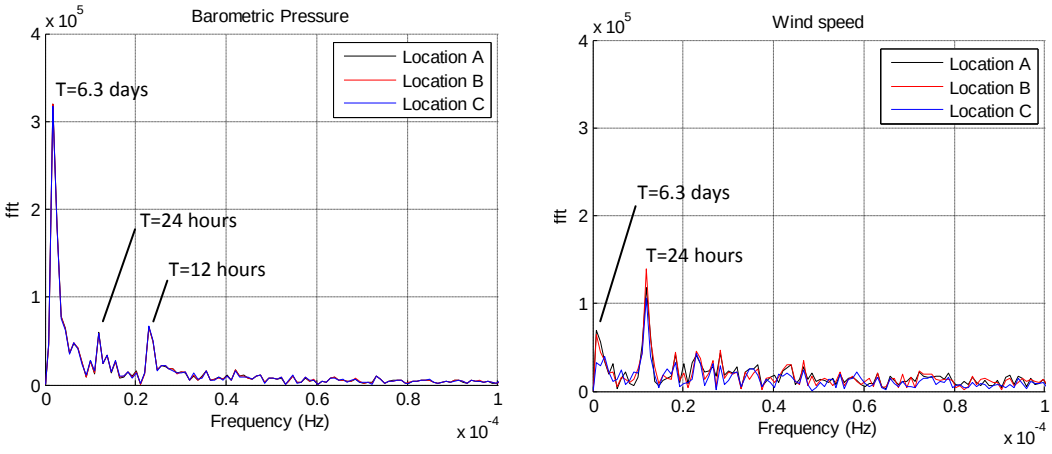

Figure 4.10 Frequency distribution of atmospheric forcing (a) Barometric pressure; (b) Wind speed

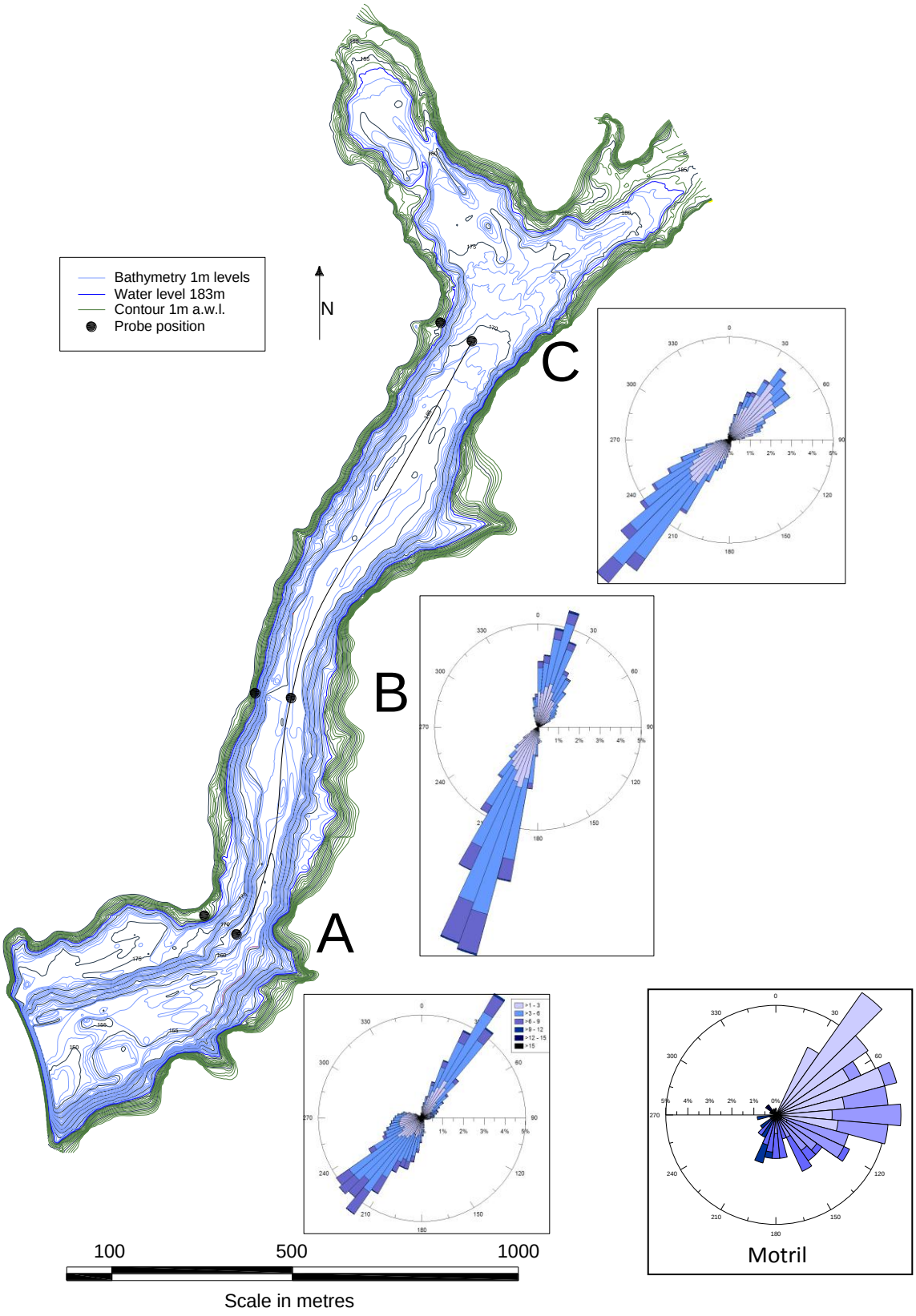

Figure 4.11 Local wind directionality windroses at the three reservoir meteorological stations and Motril

4.5.3.2 Water level variation

Based on reports from the Agencia del Agua Andaluz (Hidrosur), the water level at the beginning of the field campaign, 14th of February, was roughly 183.1m (a.s.l.). Assuming 183.1m as the base value, the mean hourly water free surface elevation registered at Location A is presented in Figure 4.12. During the period of the field study, in particular after the 24th of February, the water level inside the reservoir rose to a height of 184.1m. From personal communication with the reservoir control staff, the outflow from the reservoir was maintained constant at 1000m^3/s during the 13 day period. Flow measurements along the Gualdalfeo River, upstream of the reservoir, show the inflow from the Guadalfeo River remained constant at 1000m^3/s until the 24th of February, after which the inflow increased to around 3000m^3/s, before returning to a value of 1600m^3/s by the 27th of February (Ruiz, Personal communication, 2008). No information regarding the inflow from the Ízbor River was available.

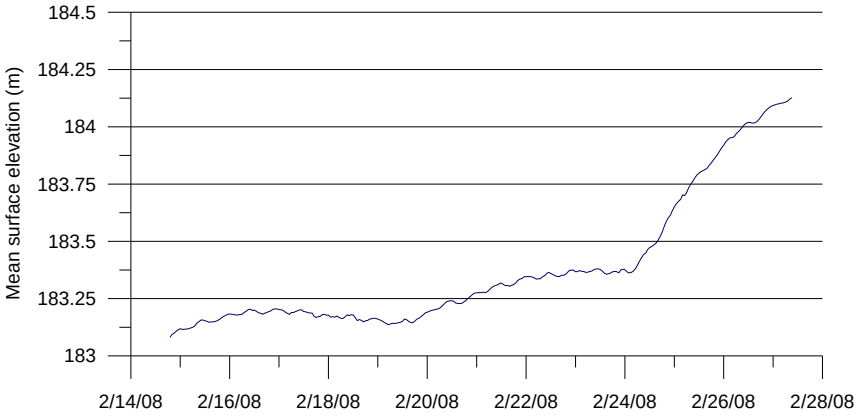

Figure 4.12 Variation of mean water elevation (m) during the period of the field campaign

4.5.3.3 Water current

Although not discussed in this thesis, the water velocity profiles at the three locations were also captured. As an example, a single hourly mean profile is presented in Figure 4.13, taken from Location A on the 19th of February. The upper surface layer was consistently found to have a depth of 2m, with the surface velocity correlating well with the magnitude of the wind velocity. At intermediate depths and at the lake bed, the current is uniform and at a low velocity. Although measured, no further analysis of the water current profiles will be discussed. It is anticipated that the three dimensional water circulation patterns will be studied in greater detail in the future with simultaneous measurements of the atmospheric forcing, water current and temperature profiles, along with the inflow and outflow characteristics of the reservoir.

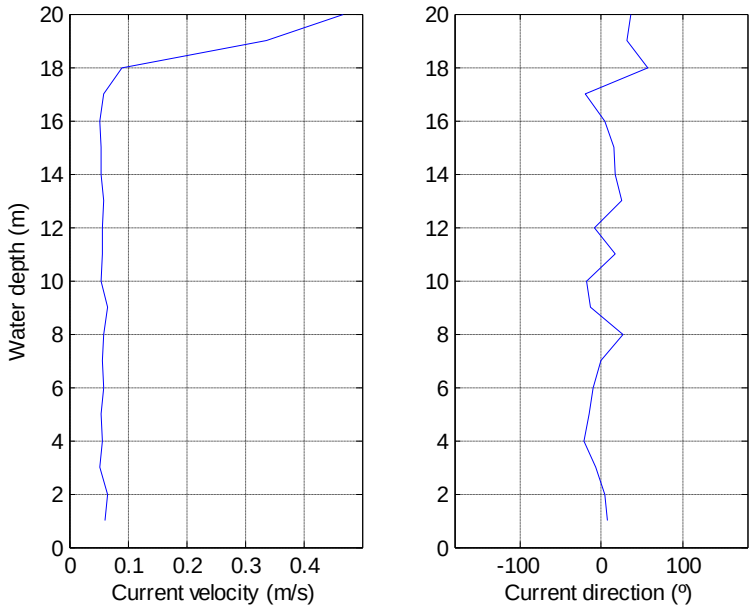

Figure 4.13 Example of water current velocity (m/s) and current direction (º) recorded during the survey (Station A, 16:00 19th Feb)

4.5.4 Reservoir free surface response to atmospheric events

Surface seiches of up to 1cm were regularly observed during the period of the field study, however, the occurance of two significant short term atmospheric events triggered the reservoir into larger oscillations that are worthy of discussion. Both forcing events are of short duration (5min and 40min respectively), but each with different forcing characteristics. The first event occurred on the 19th of February, due to the passingof a short but intense storm with a peak wind speed of 22m/s. The second event consisted of much lower wind speeds, in the order of 9m/s, but contained a harmonic component which matched the first mode of the reservoir, promoting resonant excitation of the free surface.

4.5.4.1 Event 1. February 19, 2008

At 13:00 February 19th, a storm frontal system passed over the reservoir, producing a short burst of high intense winds coinciding with a large drop in the atmospheric pressure.

Figure 4.14 presents the atmospheric conditions recorded during the 45min period of the storm, between 12:55 and 13:40. At 13:02, a storm front passes through the valley, moving in the northerly direction from the Mediterranean Sea. The storm causes a sharp drop of 3.5hPa in the barometric pressure at Station A, lowering from 1020hPa to

1016.4hPa in the space of a few seconds, before rising to 1021.5hPa within two minutes. Similarly, the wind speeds increased rapidly, in particular at Station A, with a maximum wind speed of 22m/s. The magnitude of the maximum wind speeds reduced with increasing distance from the dam, with peak wind speeds of 18m/s and 10m/s recorded at Stations B and C respectively.

The atmospheric conditions do not rise and fall smoothly during the storm front, but consist of sharp peaks with a harmonic frequency in the range of 25-30 sec. The observed harmonic component may be due to flow separation occurring from the upstream reservoir dam wall. The period of the vortices created by the dam wall, T_v, can be estimated according to the Strouhal number:

$$T_v = \frac{H}{0.21\ U} \tag{4.5}$$

where H is the characteristic height of the dam (130m) and U is the mean wind speed above the dam structure, estimated as 20m/s, and 0.21 is the Strouhal number. According to the relationship, the vortex shedding frequency from the wall structure is in the order of 30 seconds, matching well with the observed value.

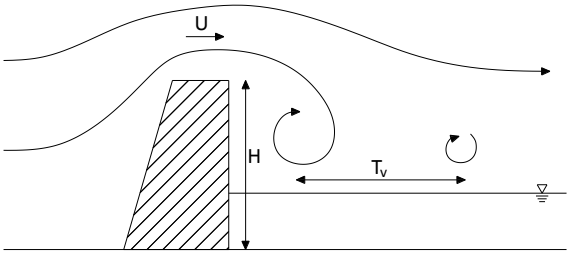

The free surface response to the passage of the storm front is illustrated in Figure 4.15, presenting the water free surface elevation recorded at the three stations between the hours 13:00 to 13:17. Although the water depth varies at the three locations, the scale of the vertical axis for the three subplots remains fixed at 0.06m.

The figure shows the water level responds dramatically to the passing of the storm front, with vertical displacements in the water level of up to 4cm. By calculating the time lag between the occurrences of the peak wind speeds at each station, the storm front is estimated to be travelling at a speed of approximately 12m/s through the valley. This is shown to closely match the long-shore phase speed of the water volume ($\sqrt{gh} = 12m/s$), helping to push the water volume downstream and increasing the magnitude of the initial setup. The high frequency content observed in the atmospheric forcing (30 sec) creates agitation in the free surface as the storm passes Station A. By 13:06, the storm has passed across the entire length of the reservoir and the wind speeds return to negligible values. The water surface is now free to oscillate and forms a surface seiche, predominantly in the first mode, with the agitation observed at Station A dissappearing quickly. The surface seiche is clearly evident in the free surface measurement captured in the following hour, between 14:00 and 14:18, as shown in Figure 4.16.

Figure 4.17 presents the frequency distribution of the surface elevation data calculated by applying the FFT algorithm to the free surface elevation data measured at each hour of the day during February 19th. The figure clearly illustrates the excitation of the water free surface at 13:00, where the low frequency energy content of the water surface increases dramatically. The peak in the frequency distribution corresponds to a frequency of 1.95×10^{-3} Hz, or approximately 512 seconds, which matches well with the predicted value of 503 seconds according to the eigenvalue analysis. The differences in the measured and derived seiche periods are probably due to non-linear effects not considered in the eigenvalue analysis and also could be due to changes in the reservoir bathymetry that may have occurred in the time between the survey and the measurement campaign, caused by the bridge excavation works at the northern end of the reservoir. The higher frequency oscillations observed at Station C, can be attributed to the interaction of the free surface oscillations from the entrances to the valleys Ízbor and Guadalfeo, predicted as the fourth mode of the eigenvalue analysis (See Figure 4.6).

The decay of the seiche is presented in Figure 4.18. The amplitude at Location B returns to zero almost immediately as it is located close to the nodal point of the first mode. The reservoir is shown to continue oscillating at Stations A and B for the remaining hours of the day, decaying exponentially over a period of eleven hours, similar to previous observations at Lake Kariba (Ward, 1979).

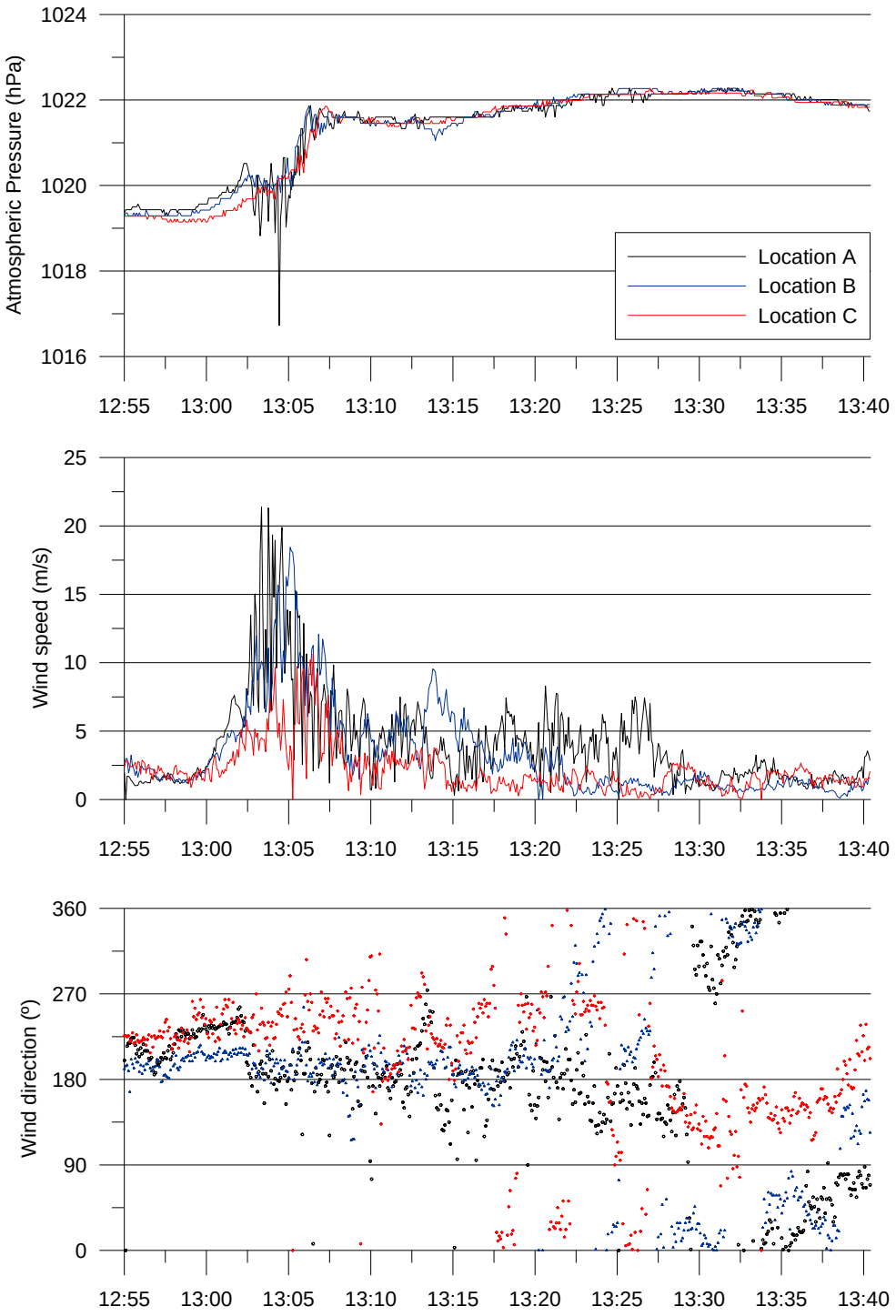

Figure 4.14 Atmospheric conditions recorded at the three stations between 12:55 and 13:40, 19th of February, 2008. (a) Atmospheric pressure (hPa), (b) Wind speed (m/s), (c) Wind direction (º)

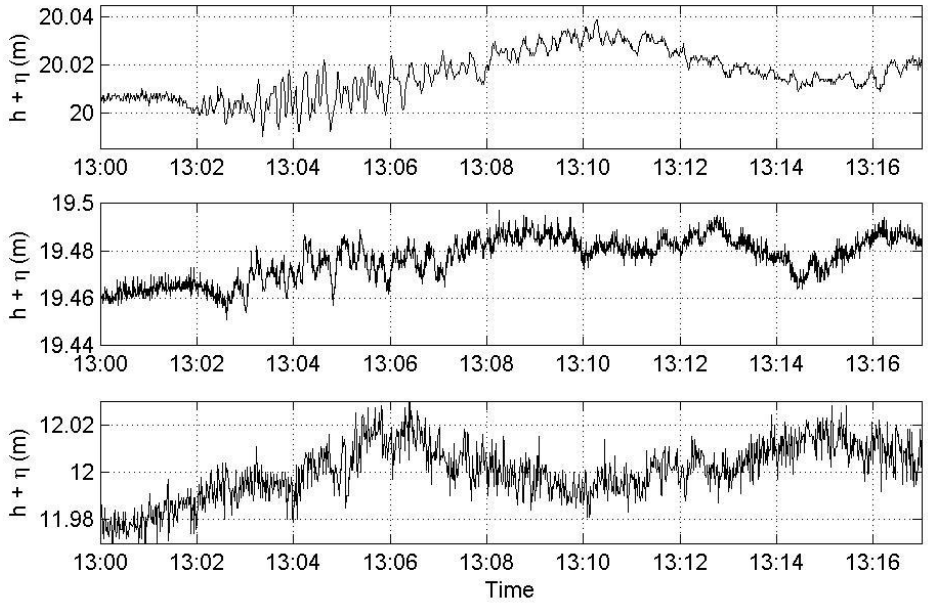

Figure 4.15 Reservoir water free surface elevation during the passage of the storm event, 13:00 Feb 19th at (a) Station A; (b) Station B; (c) Station C; (d) Filtered overlap

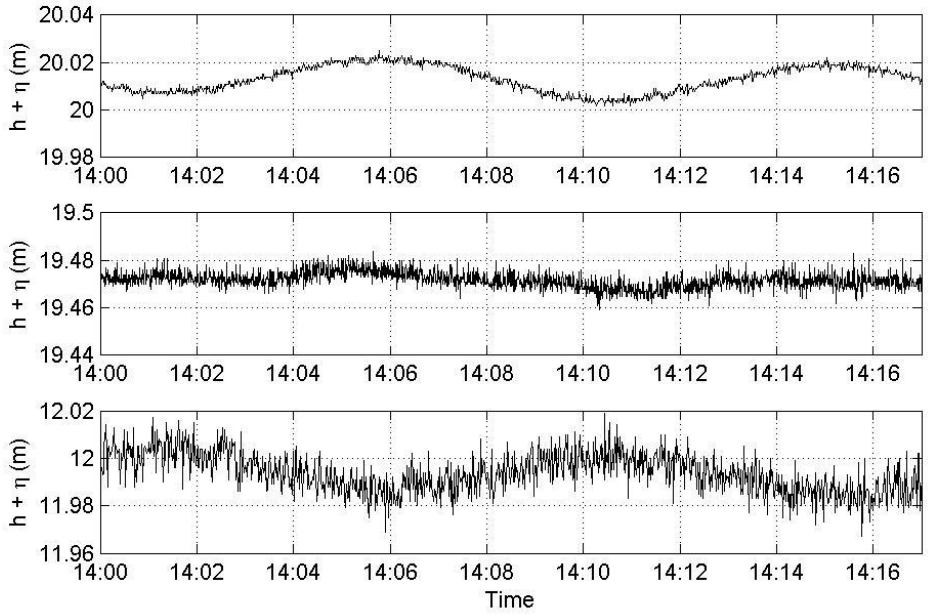

Figure 4.16 Reservoir water free surface elevation during the passage of the storm event, 14:00 Feb 19th at (a) Location A; (b) Location B; (c) Location C; (d) Filtered overlap

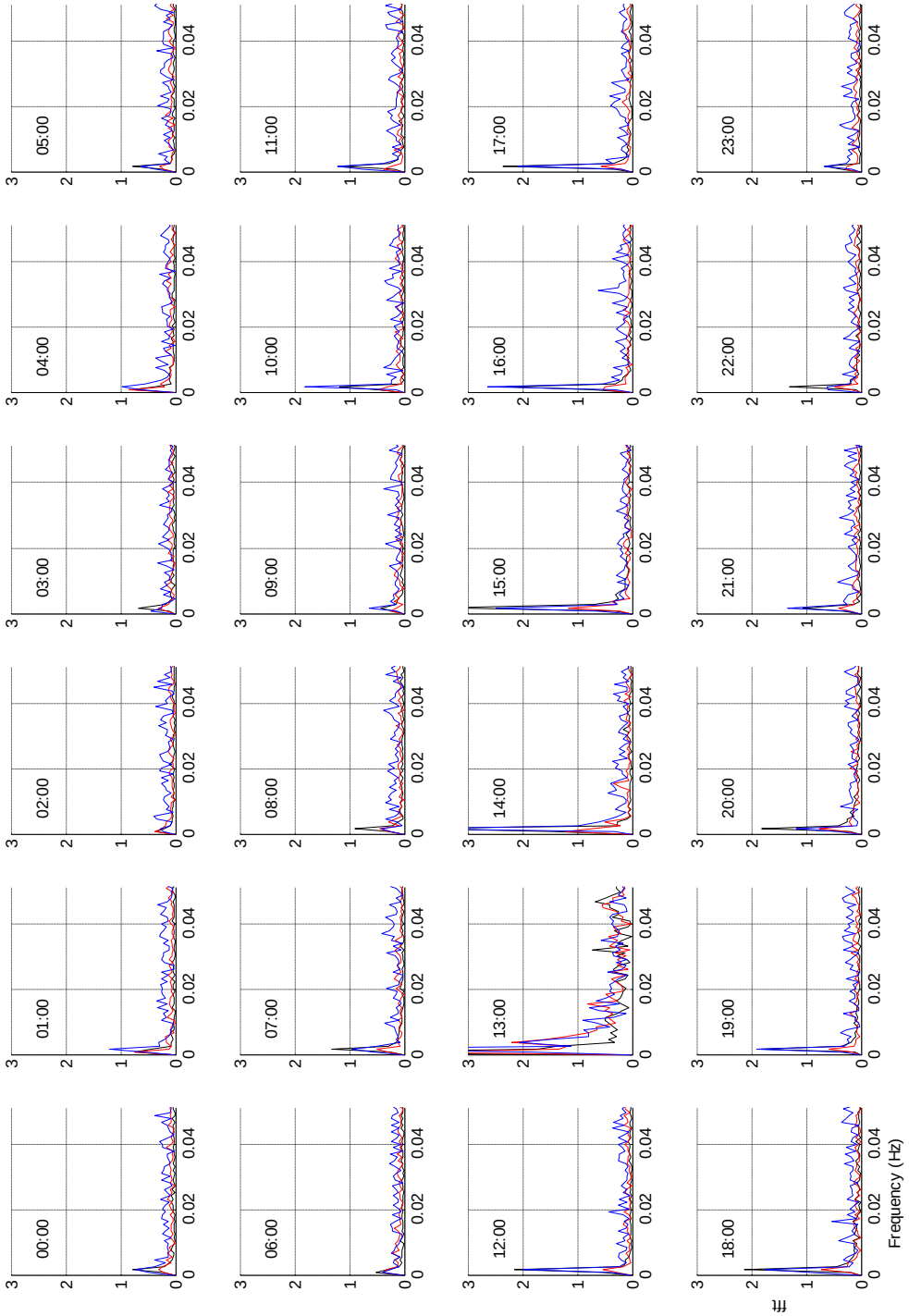

Figure 4.17 Hourly FFT of water free surface elevation recorded at the three study locations during the 19th of February, 2008

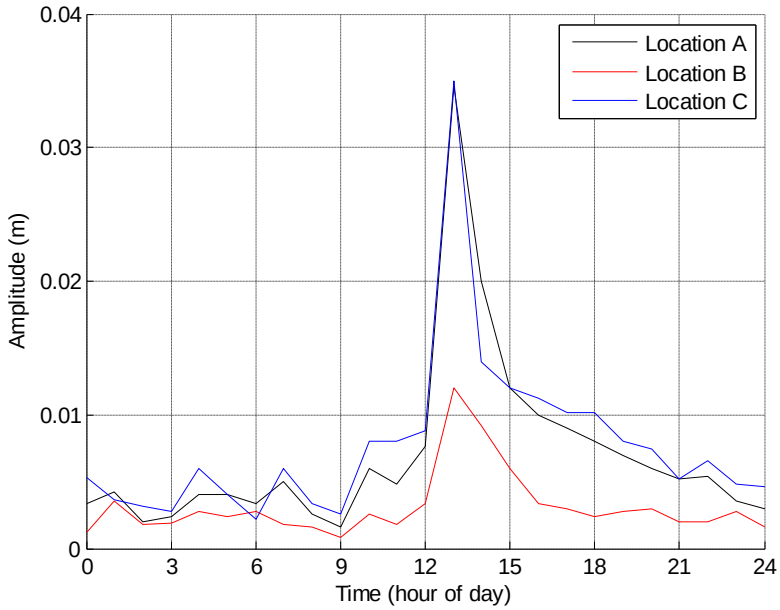

Figure 4.18 Time variation of surface seiche measured on the 19th of February, 2008

4.5.4.2 Event 2. February 23, 2008

The second event to trigger the oscillation of the reservoir occurred at 1:00am on the morning of the 23rd of February. Figure 4.19 presents the atmospheric conditions recorded during a 6 hour period on the evening of the 22nd of February. No large peaks in the atmospheric pressure or wind speeds are shown to occur; however, the reservoir clearly begins to oscillate as a surface seiche, as shown in Figure 4.20. Figure 4.21 presents the temporal variation of the maximum amplitude of the surface seiche, which presents a peak of 1.6cm at Locations A and C, which are in the same order of magnitude as the previous event recorded on the 19th of February.

The cause of the oscillation is apparent by examining the correlation between the frequency distribution of the wind velocity and the free surface, as illustrated in Figure 4.22. Figure 4.22(a) presents the frequency distribution of the wind speed in the hour leading up to the onset of the surface seiche, where distinct peaks in the energy component at Stations A and B are observed, corresponding to periods of 514 and 225 seconds. These periods match closely to the first and second reservoir eigenmodes, with the reservoir free surface responding in the first mode, as indicated in Figure 4.22(b).

Thus, although the resonant wind speed was less than 9m/s in the hour leading up to the free surface oscillations and the harmonic component of the wind speed lasted for less than four cycles, it was capable of creating resonant excitation of the surface seiche.

Additionally, in the hour during the development of the surface seiche, the atmospheric pressure at the northern end of the reservoir (Location C) presented a significant drop in pressure in comparison with the other two stations. This will create an uneven loading

over the water surface at the northern end of the reservoir. It is not clear from the field data if the atmospheric pressure gradients or the harmonic component in the wind speed were responsible for the creation of the surface seiches. However, as will be shown in Chapter 6, numerical model simulations show the surface seiches are created before the pressure gradient occurred and its formation is due to the resonant excitation with the wind speed, but the pressure gradient may have aided in amplifying the resonance of the surface seiche.

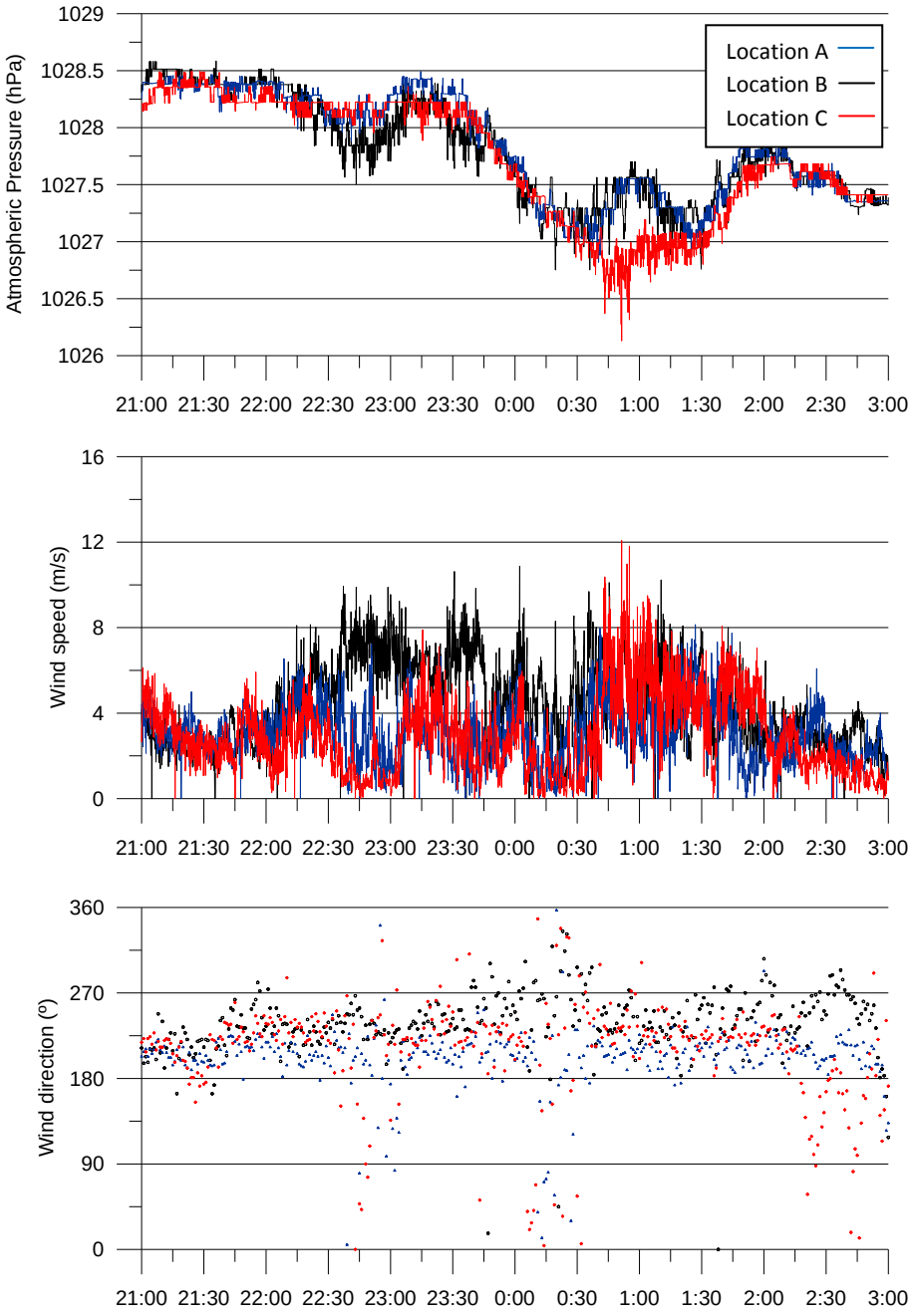

Figure 4.19 Atmospheric conditions recorded at the three stations between 21:00 and 3:00, 23rd of February, 2008. (a) Atmospheric pressure (hPa), (b) Wind speed (m/s), (c) Wind direction (º)

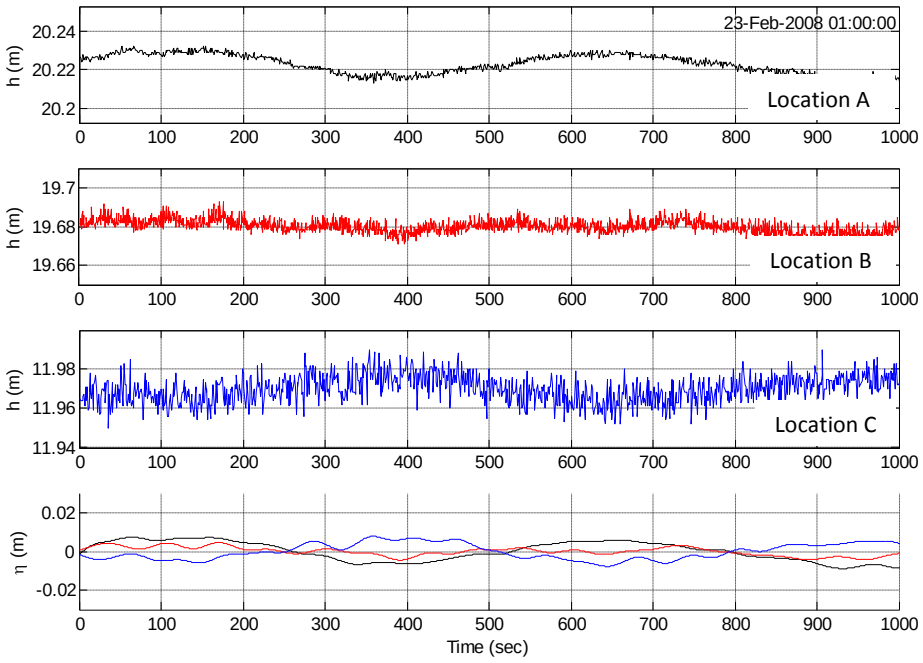

Figure 4.20 Reservoir water free surface elevation during the passage of the storm event, 1:00am Feb 23th at (a) Location A; (b) Location B; (c) Location C; (d) Filtered overlap

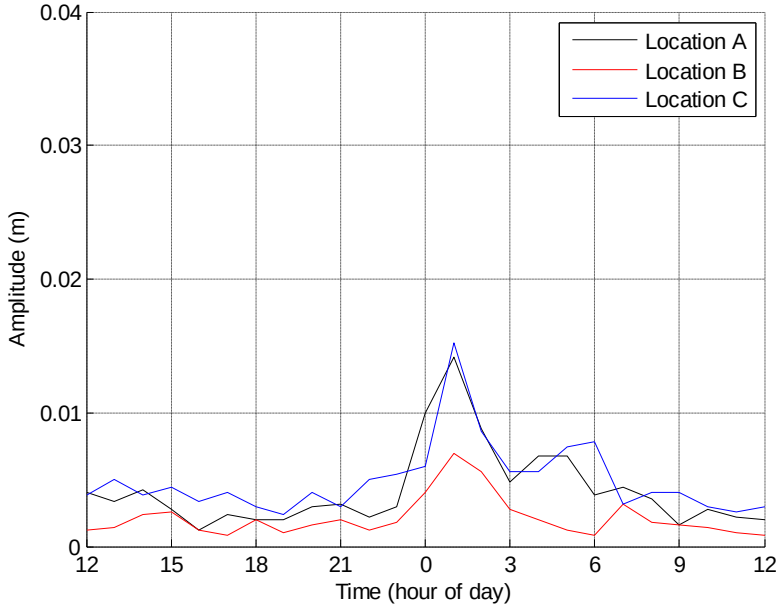

Figure 4.21 Time variation of surface seiche measured between 12:00 on the 22nd of February to 12:00 on the 23rd of February, 2008

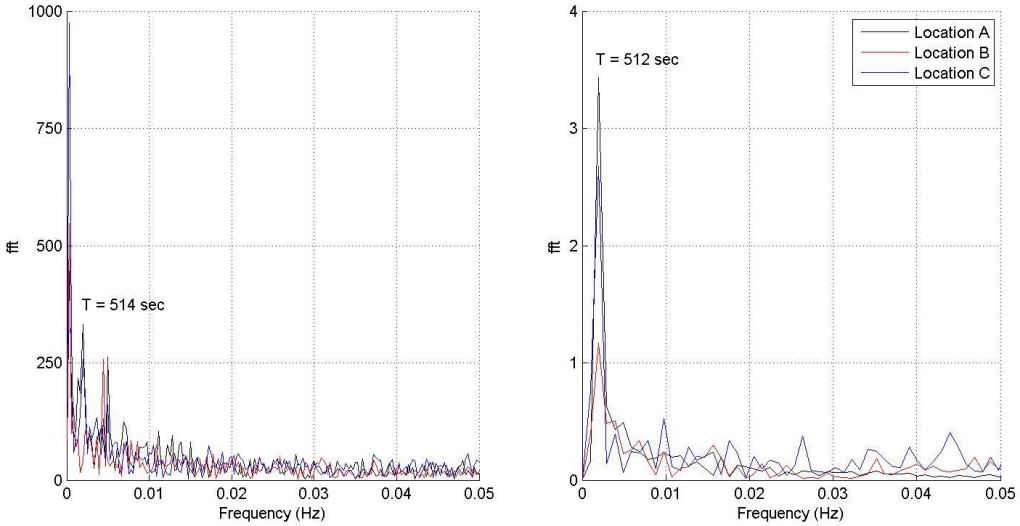

Figure 4.22 Frequency distribution of the wind speed and free surface recorded at the three locations during the second event: (a) wind speed between 00:00-01:00, Feb 23; and (b) free surface response, between 1:00-01:17, Feb 23.

The harmonic components in the atmospheric forcing can be attributed to either flow separation from local topographical features or local thermal differences in the mountains. High frequency harmonics in the atmospheric forcing, with the same or similar frequencies, were also observed at other times during the field campaign. In response, small oscillations in the water free surface occurred sporadically during the two week period, predominantly in the first mode.

At other times during the study period, the wind speed contained harmonic components with alternative frequencies, ranging between 200-700 seconds. Appendix D presents the frequency distribution of the hourly water surface oscillations recorded during the field campaign. The reservoir free surface did not respond at these times because the forcing frequencies did not match any of the lower eigenmodes. However, the observed harmonic events may become significant as the water level within the reservoir rises and the eigenmode frequencies of the reservoir free surface match the harmonic loading.

The free surface response forced by the passing of storm fronts has previously been reported for larger lakes, typically due to the passing of synoptic scale winds (Ward, 1979; Hutter, Raggio, Bucher, & Salvade, 1982; Zacharias & Ferentinos, 1997). The correlation between the high frequency forcing (<10min) and the free surface response shows how small reservoirs are easily excited by localized small-scale variations in the atmospheric forcing. The observations also illustrate how small reservoirs require high spatial and temporal resolution measurements to properly identify the forcing mechanisms, at the very least in the order of magnitude of the basin resonant frequency.

It is worth noting that the atmospheric forcing of both events were captured only thanks to the high temporal resolution of the measurement, and in all likelihood would not have been captured if the traditional 10min averaging period were utilized during the field campaign.

5 Wind tunnel simulation of Rules Reservoir

A complete mapping of the wind field above the reservoir cannot be sufficiently captured through field measurements alone, in particular in regions of complex topography like Rules Reservoir. Instead, laboratory measurements in a boundary layer wind tunnel provide a useful method for enhancing the spatial resolution of the atmospheric forcing on the reservoir through a series of measurements on a scaled model of the reservoir.

The simulation models the atmospheric conditions during neutral conditions, that is, during synoptic events. During synoptic winds, which generally have constant and steady winds for a number of days, all local temperature differences in the atmosphere are transported out of the zone and the local topography become bluff body features which interact with the flow; an effect which can be satisfactorily simulated in a wind tunnel. The diurnal wind variations due to local temperature differences in complex terrain cannot be simulated in a wind tunnel and are not attempted.

Despite this, the simulation provides a description of the effects of the surrounding topography on the wind speed and directional variation above the reservoir, along with the variation of the atmospheric pressure on the water surface. This gives an idea of the variation of the complete boundary layer above the reservoir and not at isolated points through field measurements alone.

In particular, when used in combination, the field and wind tunnel measurements provide an enhanced description of the atmospheric loading over the reservoir water surface. As an example, in typical studies the atmospheric forcing is taken from records of a single anemometer located in the region of the lake or reservoir. It is generally accepted that the single point record will not be representative of the spatial distribution of the wind speed above the water surface. Wind tunnel modeling provides a method for determining a relationship between the information captured by a single anemometer and the spatial distribution of the wind speed and pressure across the entire surface area of the water basin.

The wind tunnel simulations in this study were performed in the boundary layer wind tunnel I, at the Centro Andaluz de Medio Ambiente (CEAMA), University of Granada. The wind tunnel is an open circuit wind tunnel, with a test section width and height of 2.14m by 1.8m. The overall length of the test section is 15m.

5.1 Topography model

Due to the complexity of the topography surrounding Rules Reservoir, a complete simulation of the wind field above the water surface requires a precise representation of the topography, extending for a considerable distance for the complete 360º spectrum of wind direction.

However, as shown in Figure 4.11, the local wind directionality above the reservoir is limited to two predominant wind directions, fixed by the geometry of the valley, with the highest velocity winds originating from the Mediterranean Sea. Thus, for simplicity the wind tunnel simulation was restricted to a single geostrophic wind direction of 208º, which follows the principal direction of the valley leading up to the reservoir from the Mediterranean Sea, as shown in Figure 5.1.

The simulation in the boundary layer wind tunnel models the wind conditions for a synoptic scale wind approaching the reservoir from the Mediterranean Sea. As shown in the figure, the model includes all significant topographical features between the Mediterranean Sea and the reservoir.

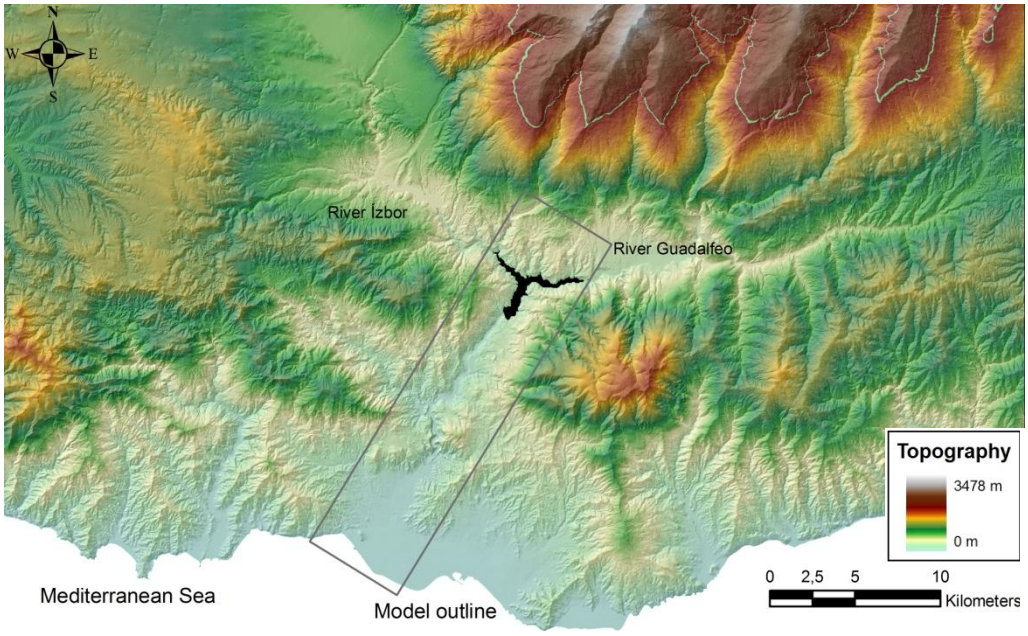

Figure 5.1 Outline of 1:3000 scale topography model

Figure 5.2 illustrates in greater detail the extents of the topography model and the simulated wind direction. The model begins at the Mediterranean Sea and extends until beyond the reservoir for a constant wind direction, including the townships of Salobreña and Velez de Benaudalla. The topography model is scaled at 1:3000, which is an acceptable scale for this type of study (Holmes, 2001) and is constructed from layers of polystyrene sheets, each with a thickness of 4.5mm (13.5m in full scale). The overall dimensions of the model are 8000mm by 2140mm, corresponding with full scale dimensions of 6.4km by 24km.

Construction of the model is made with a two-dimensional cutting machine, designed and built specifically for this study, which is capable of cutting a polystyrene sheet with dimensions of 1000mm by 2500mm. A photograph of the foam cutting machine is presented in Figure 5.3. The machine consists of a frame that supports the polystyrene sheet, with a heated wire to cut the foam. The movement of the heated wire is controlled by two motors: one to control the motion in the horizontal direction and the other for the vertical direction. By combining the motion of the two motors, it is possible to cut the polystyrene sheet into any two dimensional shape.

The topographical data of the reservoir and the surrounding region are adapted from the digital topography from (Molero Melgarejo, 2004), which was first transferred into Autocad .dxf format. A Matlab program was completed to separate the topography contour information into the x-y coordinates required to cut each level of the model. The matrix containing the coordinates of motion is then transferred to the motor controller using the software program DMC Smart Terminal (Galil, 2005). After all the layers of the model are cut they are glued together to form the final topography model.

The water level of the reservoir is modeled with a 5mm acrylic sheet, assuming the reservoir is at full capacity (243m ASL). Figure 5.4 present photographs of the topography model in the wind tunnel.

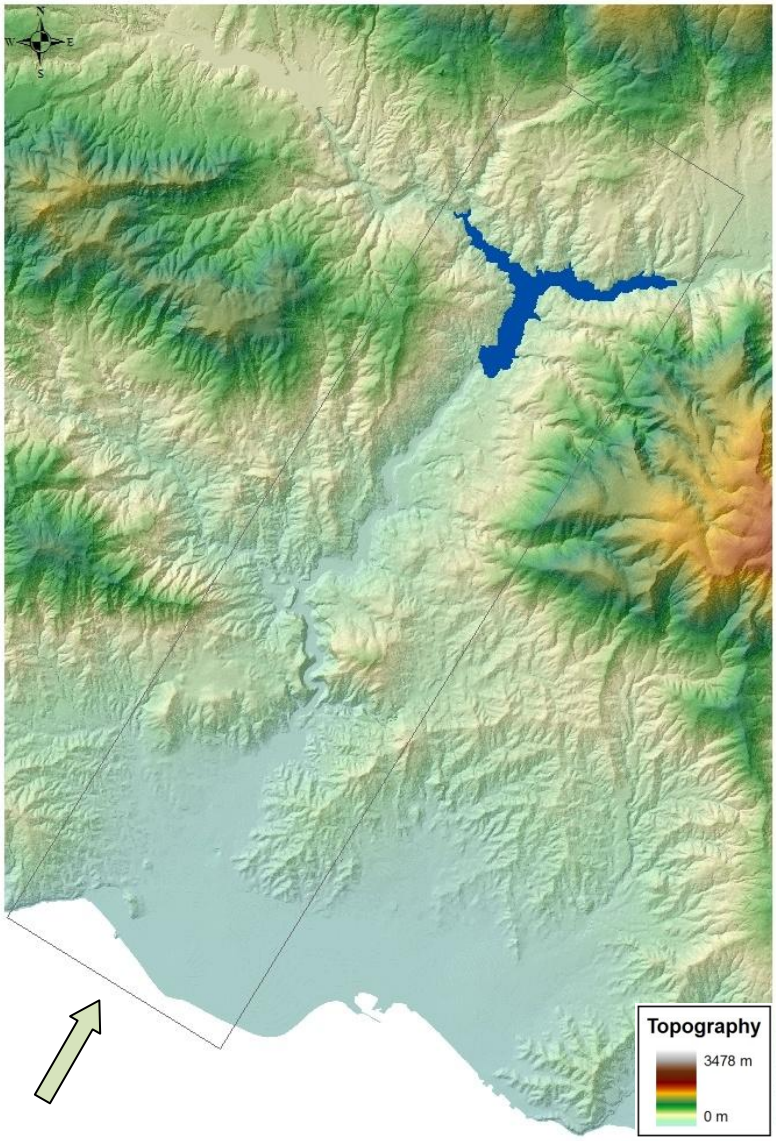

Figure 5.2 Extents of topography model simulated in the wind tunnel and simulated wind direction (208º)

Figure 5.3 Photographs of the foam cutting machine

Figure 5.4 Photographs of the topography model inside the wind tunnel, (a) view from the Mediterranean Sea; (b) detail of the modelled water surface

5.2 Scaling parameters

To correctly reproduce the wind characteristics in the boundary layer wind tunnel, it is important to satisfy a number of similarity requirements. The correct simulation of the atmospheric boundary layer depends on a number of factors, including the mean wind speed at 10m, U_{10m}, the surface roughness length, z_o, the standard deviation of the longitudinal

turbulence, σ_u, the length scale of the longitudinal turbulence, l_u, the air density, ρ_a coriolis force, f_c, air viscosity, ν, and the acceleration of gravity, g. The factors can be grouped together into a series of non-dimensional relationships:

L/z_o – Jenson number (5.1)
σ_u/U – Longitudinal turbulence intensity (5.2)
$U/L\nu$ – Reynolds number (5.3)
U/Lf_c – Rossby number (5.4)

To perfectly reproduce the structure of the wind in the wind tunnel, the non-dimensional relationships of the four relationships should be scaled exactly. However, the final two similarity relationships cannot be satisfied in the wind tunnel.

The similarity of the Reynolds number is related to the viscous and inertial forces of the fluid. But, in the wind tunnel the cinematic viscosity, ν, is equal to the model scale, or $\nu_m/\nu_{fs}=1$, as the same fluid is used in the simulation, air. In this investigation, the geometrical scale of the simulation in the wind tunnel is 1:3000, or $L_m/L_{fs}=1/3000$, thus to correctly satisfy the similarity of the Reynolds number, the wind speed in the wind tunnel should be 3000 times the wind speed in the real scale, which cannot be satisfied and is not attempted. This mis-match signifies that there is a difference between the viscous forces in the real scale and in the model scale and the development of the turbulence decay is not perfectly simulated in the wind tunnel.

Assuming the wind speed reproduced in the wind tunnel is around 10m/s and the depth of the boundary layer is 0.3m, the Reynolds number can be calculated according to:

$$\left(\frac{\overline{U}}{Lv}\right)_{model-scale} = \frac{10 \times 0.3}{1.5 \times 10^{-5}} = 2.0 \times 10^5 \qquad (5.5)$$

For a Reynolds number in this order, the flow in the wind tunnel is turbulent and is within the inertial subrange, thus the flow turbulence does not significantly change with Reynolds number. Therefore an exact match of the Reynolds number is not important as the turbulence characteristics are not significantly altered with increasing wind speed. Therefore, a wind tunnel simulation is typically considered adequate if the wind tunnel Reynolds number is greater than 10^5, or $Re_{model\text{-}scale} > 1x10^5$.

One method of reducing the mis-match of the Reynolds number is to increase the surface roughness of the model, thereby increasing the turbulence level in the flow. Unfortunately, for simulations at a scale in the order of 1:1000, the differences between the exaggerated surface roughness and the model characteristics would be difficult to distinguish, potentially leading to errors if the exaggerated surface roughness interferes with measurements close to the surface. An alternative method for reducing the mis-match is to construct the topography model in levels, so that the edges of each level provide additional roughness, similar to the procedure incorporated in the current study. However, care must be taken during the flow measurement, as the edges will lead to an increase in the turbulence close to the model surface, generating significant errors in the flow measurement close to the model steps. In the case of the current study, this is not important as all measurements are performed on the flat water surface of the reservoir at a distance sufficiently far away from the modeled contour steps.

The fourth similarity requirement, the Rossby number, refers to the simulation of the coriolis forces. A conventional wind tunnel cannot simulate the coriolis acceleration and the Rossby number is not satisfied in a wind tunnel simulation. To safely ignore the Rossby number similarity, the limiting factor is the length scale, $L_{full\text{-}scale}/L_{model\ scale}$. According to (AWES, 2001) the limiting length scale is 5000. Values less than this, the local terrain effects dominate the flow conditions and the similarity of the Rossby number can be safely ignored.

5.3 Instrumentation

The wind tunnel study utilized three principal measurement devices: a calibrated x-wire hotwire; a Laser Doppler Velocimetry (LDV) system; and a PSI pressure system. Further details of the equipment used in the study can be found in (Mans, 2006).

- Hotwire Anemometer

  The hotwire system is a TSI IFA300 constant temperature anemometer (CTA). The sensor consists of a very fine wire film, within the order of microns, which changes temperature in function with the change of the speed of the surrounding fluid. The system is capable of measuring fluid speeds with a very high temporal resolution, ideal for highly turbulent flow measurements and spectral analysis. The x-wire hotwire consists of two wire films, which combine together to simultaneously measure the x-y components of the fluid velocity.

  Prior to measurement in the wind tunnel, the probe is calibrated by submerging the sensor within a jet of air with uniform wind speed and no turbulence. A polynomial transfer function is obtained to the fourth order to describe the relationship between the current maintained by the system and the fluid velocity.

- Laser Doppler Velocimetry (LDV) System

  The LDV system is based on the principals of optics that measures the fluid velocity through the measurement of small particles immersed in the fluid. The system is ideal as the optical system is situated outside of the wind tunnel, thus does not interfere with the flow conditions of the measured fluid. Unlike the hotwire, the LDV system can measure flow reversal, which is important for situations where the fluid velocity is expected to be very small and with high directional variability as is expected with the current study. As the system is based on optics it does not require calibration prior to measuring.

The system utilized in the study incorporates an Argon Ion laser, with a wavelength of 488 nm. The longitude of the focal lens is 1533mm, with a beam separation of 50 mm. With this configuration, the diameter of the measurement control volume is 0.1mm.

- Pressure System

  Pressure measurements on the reservoir water surface are captured with a PSI 8400 System. The system is built from modules and is capable of measuring up to 5000 pressure channels per second. Similar to the hotwire, it contains a scanner module to transfer the measured pressure into a voltage signal. The relationship between the pressure and voltage is determined through a calibration process, where a transfer function is determined with a polynomial equation to the fourth order.

5.4 Boundary layer simulation

The mean wind velocity and turbulence intensity profiles are determined upstream of the topography model to correctly simulate the wind characteristics of the oncoming wind above the Mediterranean Sea. For the wind direction of study, the Mediterranean Sea is located upstream from the model, as such it is necessary to correctly simulate a boundary layer profile that corresponds with open sea, z_o=0.005m.

The modeling of the wind characteristics upstream of the topographic model are achieved by placing a 10mm barrier across the entrance to the test section in the wind tunnel. The barrier aids in generating the mean wind speed and turbulence profiles to correctly simulate the wind profiles for open sea conditions (Cuesta, 2005).

The wind profiles are recorded 0.5m upstream from the model, at five locations across the width of the tunnel, W (y/W of 0.2, 0.35, 0.5, 0.65 and 0.8). For each profile, the measurements are repeated using a calibrated X-wire hotwire at 20 heights, from 30m to 675m in real scale. The measurement time is 15 seconds, with a measurement frequency of 4000Hz. This corresponds with a full-scale time series of 2.5 hours, with a sample frequency of 30Hz. The profiles where performed with a mean wind speed of 7.7m/s, measured upstream of the topography model at a height such that the boundary layer effects from the tunnel floor and ceiling can be neglected.

Figure 5.5 presents the mean wind speed and turbulence intensity profiles measured at y/W = 0.5. The mean velocity profile is normalized with respect to the mean velocity measured at a height of 350m, which corresponds with the theoretical gradient height of the boundary layer. The open sea profile, according to Engineering Science Data Unit (ESDU), z_o=0.005m, is presented in the figure for comparison (ESDU 1, 1982; ESDU 2, 1982). The figure shows that the mean velocity profile in the wind tunnel is slightly quicker than the open sea profile according to ESDU, and the turbulence intensity profile is a little lower than the open sea profile. However, these differences are small and will be further reduced from the constriction

of the flow due to the topography upstream from the reservoir. Thus, the simulated boundary layer profile is satisfactory for the study.

Figure 5.6 and Figure 5.7, respectively, compare the mean velocity and turbulence intensity profiles measured across the width of the wind tunnel for y/W 0.2, 0.35, 0.5, 0.65 and 0.8. The open sea profile according to ESDU is also included for comparison. The figures clearly show that the flow is uniform across the width of the wind tunnel.

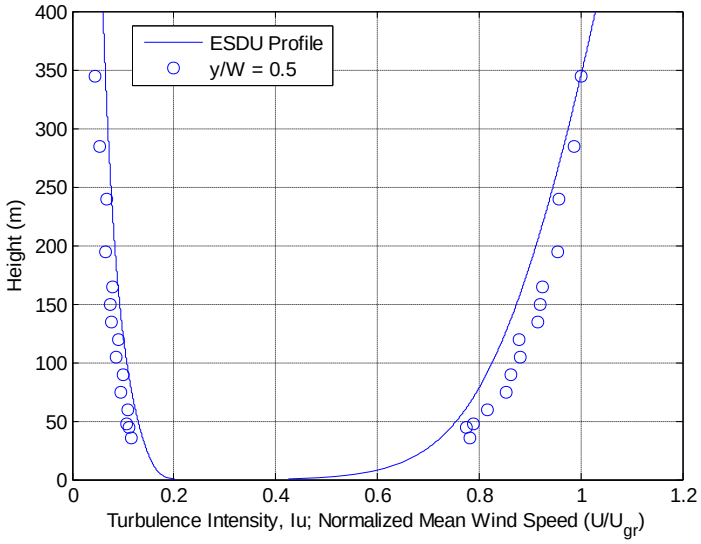

Figure 5.5 Comparison of an open sea boundary layer profile according to ESDU (zo=0.005m) and the mean velocity and turbulence intensity profiles measured in the wind tunnel (y/W=0.5)

Figure 5.8 presents the spectral energy distribution of the wind, measured at the centre of the wind tunnel, y/W = 0.5, at a height of 243m in full scale. This is the height of the modelled reservoir water surface, at full capacity. The open sea spectral energy distribution according to ESDU, for z_o=0.005, is also included for comparison (ESDU 2, 1982). As expected, the figure shows that the longitudinal turbulence length scale in the wind tunnel is lower than the target ESDU length scale by a factor of 10. This signifies that the turbulence length scale in the wind tunnel is greater than in reality. This is expected due to the large scale adopted for the study. However, the structure of the turbulence close to the reservoir water surface will be dominated by the effects of the topography upstream from the reservoir and not by the structure of the turbulence above the sea. Thus, the differences in the wind energy distribution are acceptable.

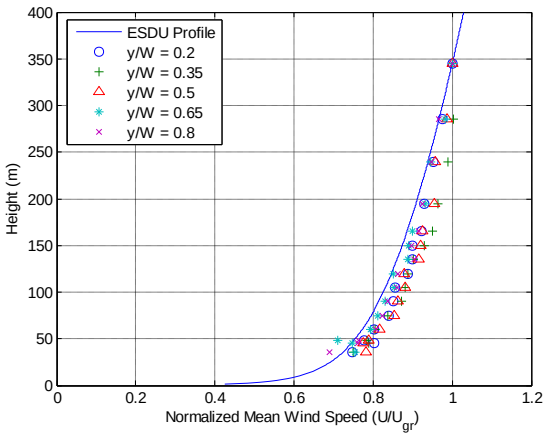

Figure 5.6 Mean wind velocity profiles measured across the width of the wind tunnel (y/W=0.2, 0.35, 0.5, 0.65, 0.8)

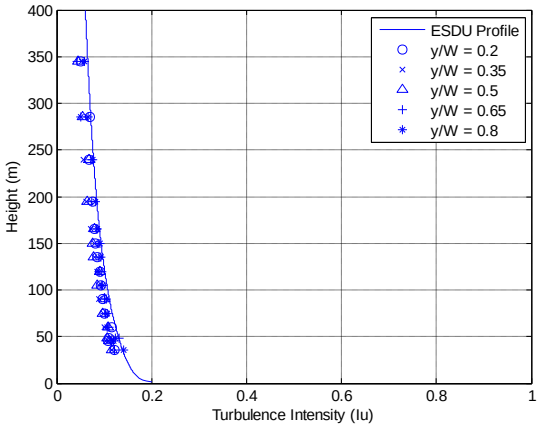

Figure 5.7 Turbulence intensity profiles measured across the width of the wind tunnel (y/W=0.2, 0.35, 0.5, 0.65, 0.8)

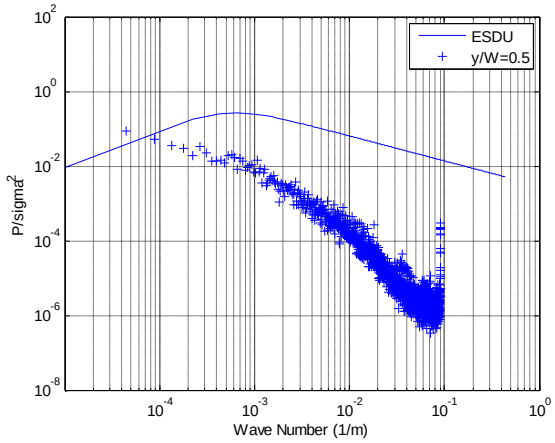

Figure 5.8 Power spectra of open sea boundary layer at H=243m according to ESDu (z0=0.005m) and measured in the wind tunnel (y/W=0.5)

5.5 Wind directionality above the reservoir

Although the wind tunnel study was performed for a single geostrophic wind direction of 208 degrees, the topography will affect the local wind directionality above the water surface of the reservoir. To determine the spatial variability of the wind directionality, measurements of the wind velocity above the water surface were performed with a calibrated hotwire anemometer. The measurements were repeated at 32 locations, as presented in Figure 5.9, for a single height of 90m (full scale) above the water surface. The sample period of each measurement is 120 seconds with a sample frequency of 4000Hz.

Figure 5.10 presents the measured local wind directionality above the water surface of the reservoir. The figure illustrates the wind directly follows the orientation of the valley, following the northerly orientation of the reservoir. At the junction of the rivers Ízbor and Guadalfeo, the wind directionality separates, following the direction of the two valleys to the east and to the west.

It is assumed that the wind directionality will vary with height, in particular at heights above which the surrounding topography will no longer influence the wind field. However, the presented wind directionality is representative of the wind direction close to the water surface, which is the objective of the study.

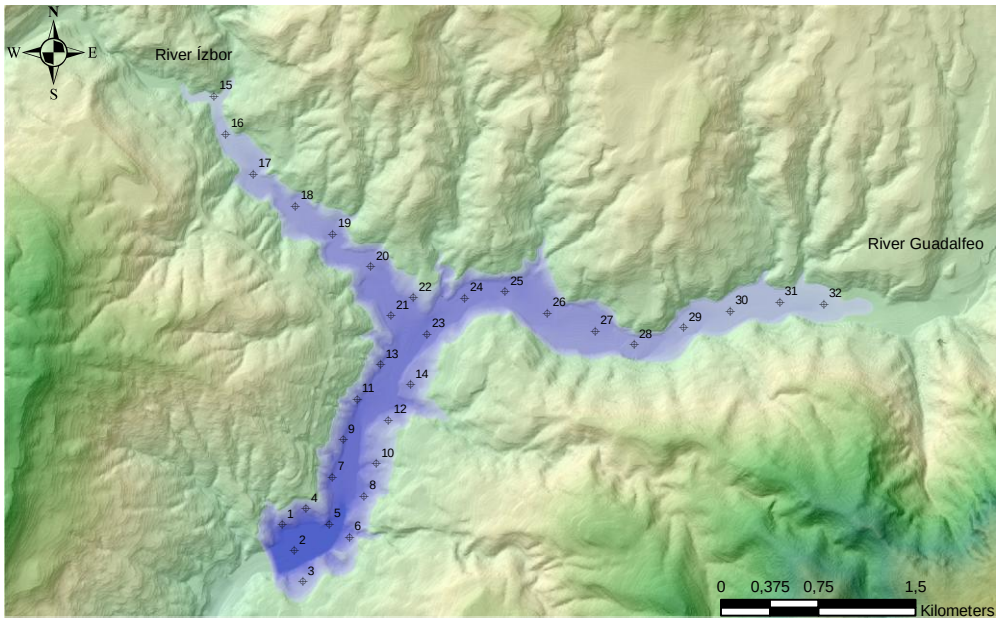

Figure 5.9 Positions of wind tunnel study points

It is important to note that the applied wind loading assumes a geostrophic wind direction of 208º, leading in the northerly direction along the valley. As the wind exits the valley, the wind tunnel simulation assumes that it is free to turn into either the Ízbor valley or the Guadalfeo valley. In reality, it may be likely that the winds will be forced to turn into the Ízbor valley due to the effects of the Sierra Nevada acting as a mountain barrier. As briefly discussed in Chapter

2, the Sierra Nevada may force the coastal winds in the region to turn to the left as it meets the mountain barrier, generating a barrier jet along the southern edge of the Sierra travelling to the west. This may force the wind exiting the valley to turn to the left and travel predominantly along the Ízbor valley, with little flow entering the Guadalfeo valley. Further field measurements would be required to determine the wind variation within the Ízbor and Guadalfeo valleys due to the effects of the Sierra Nevada, which is outside of the limits of the wind tunnel simulation.

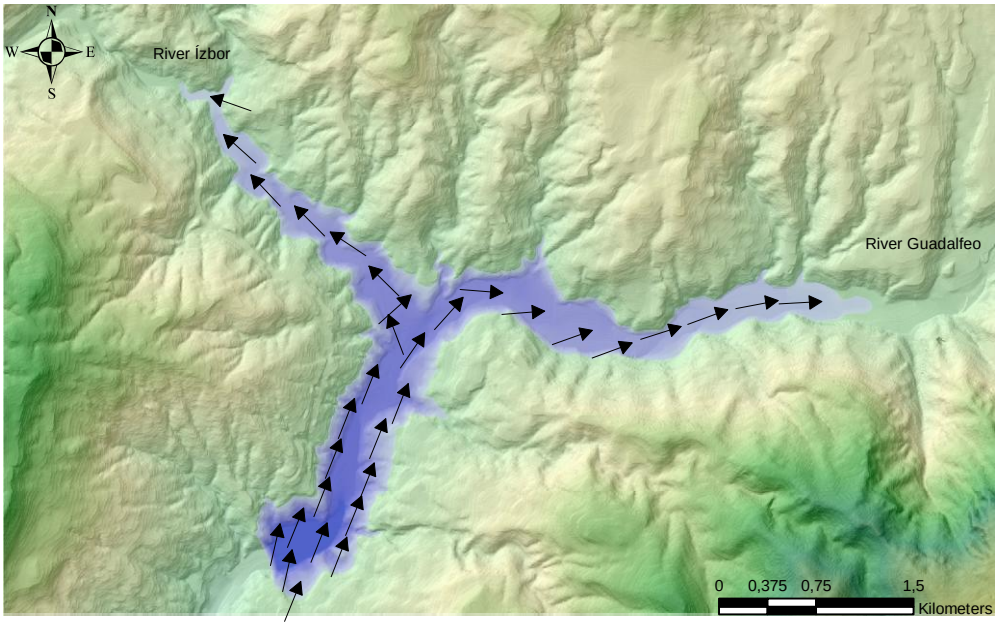

Figure 5.10 Local wind directionality above the reservoir water surface from wind tunnel simulation

5.6 Wind speed variation above the reservoir

Measurements of the wind speed profiles above the reservoir water surface were captured with the Laser Doppler Velocimeter (LDV) system. The measurements were repeated for both the horizontal and vertical components of the flow at the 32 locations presented in Figure 5.9. At each position, the wind velocity profile is captured at 23 heights, ranging between 3m to 645m in full scale.

The sample time of each height is 120 seconds. The sample frequency varies in function with the number of particles that pass through the control volume of the LDV system, which varies with each test point. For a full description of the LDV technique, see (Mans, 2006).

Using the results of the wind directionality study, it is possible to align the LDV optics in such a way that the x component of the LDV system corresponds with the horizontal direction of the flow. Thus, where physically possible, the LDV optics is positioned normal to the flow direction. In some instances it was not possible due to interference from the wind tunnel walls or from the topography of the model. In these cases, the LDV system is aligned with the x component

of the local flow conditions and the difference in the alignment is compensated by multiplying the measured wind speeds by a horizontal alignment factor, F_h, which considers the mis-alignment of the LDV optics in relation with the local wind directionality.

To measure the vertical flow component at heights close to the water surface, it is necessary to incline the LDV optics on a vertical angle. This permits measurements of the flow properties at heights within 1mm above the water surface (3m in full scale). The vertical alignment factor, F_v, is applied to all measured vertical velocities to correct for the inclination of the LDV optics. The horizontal and vertical alignments factors, F_h and F_v, applied in the study are presented in Table 5.1.

The measured velocity profiles are also adjusted with an acceleration factor, F_s. This factor is related to the artificial acceleration of the flow inside the wind tunnel due to the obstruction of the topography model that, due to its presence inside the wind tunnel, reduces the cross sectional area of the tunnel test section. Comparisons are made between the wind velocity measured at gradient height above the reservoir (2400m in full scale), with and without the presence of the topography model. The mean wind speed measured at gradient height with the topography model in place was found to be 14.5% greater than the mean wind speed without the model inside the wind tunnel. Consequently, a reduction factor, F_s, of 0.87 is applied to all measured wind speeds above the water surface. In this way, the measured wind speeds consider the artificial acceleration of the flow due to the contraction of the wind tunnel test section due to the presence of the model. The acceleration factor is important if the wind speeds measured in the wind tunnel are to be scaled to real full-scale values, but should not modify the local variation of the wind speed and directionality along the reservoir water surface as is the intention of the study.

The presented wind velocity profiles are normalized with respect to the hourly mean wind velocity, measured at gradient height, upstream of the topography model, $U_{grad\ upstrm}$. This position corresponds with the gradient height wind speed of Motril, 500m above the Mediterranean Sea.

Table 5.1 Horizontal and Vertical LDV alignment factors, F_h and F_v

Point	Horizontal alignment factor F_h	Vertical alignment factor F_v
1	1,01	0,894
2	1,01	0,894
3	1,03	0,894
4	1,01	0,894
5	1,02	0,894
6	1,02	0,894
7	1,01	0,894
8	1,01	0,894
9	1,01	0,894
10	1,0	0,894
11	1,0	0,894
12	1,0	0,894
13	1,0	0,894
14	1,0	0,894
15	2,27	0,894
16	1,37	0,894
17	1,26	0,894
18	1,3	0,894
19	2,08	0,894
20	1,39	0,894
21	1,11	0,894
22	1,02	0,894
23	1,0	0,894
24	1,0	0,894
25	1,39	0,894
26	1,18	0,825
27	1,0	0,894
28	1,0	0,825
29	1,0	0,825
30	1,0	0,825
31	1,01	0,825
32	1,03	0,825

Thus, the presented horizontal velocity profiles are in the form of coefficients, C_u:

$$C_U = \frac{U_i \times F_h \times F_s}{U_{grad\ upstrm}} \tag{5.6}$$

where U_i is the horizontal velocity measured at point 'i' by the LDV system above the water surface, F_h is the horizontal alignment factor of the LDV optics, F_s is the factor for the artificial acceleration of the flow due to the model and $U_{grad\ upstrm}$ is the mean hourly wind speed, measured at gradient height, upstream of the model.

Similarly, the vertical velocity profiles are in the form of coefficients, C_v:

$$C_V = \frac{V_i \times F_v \times F_s}{U_{grad\ upstrm}} \tag{5.7}$$

where V_{meas} is the vertical velocity measured at point 'i' by the LDV system above the water surface and F_v is the vertical alignment factor of the LDV optics.

Figure 5.12 presents examples of the mean horizontal (C_u) and vertical (C_v) velocity profiles captured at various measurement points above the reservoir (See Figure 5.9), where the y-axis represents the full scale height, in meters, measured above the water surface. Appendix E presents the horizontal and vertical mean wind speed profiles recorded at each of the 32 test locations.

The figures demonstrate the influence of the surrounding topography in the wind field, in particular within the northern valleys of the reservoir. Points 1, 10 and 13 represent the wind field through the principal valley of the reservoir, which present a rapid increase in horizontal wind speed within the lower 20m, followed by an almost linear increase in the mean speed up until a height of 600m. Point 1 presents a lower mean wind speed within the lower 50m, as it is believed to be within the wake zone of flow separation off the reservoir dam wall. Note, for the three profiles the mean velocity coefficient is close to a value of unity at the height of 500m above the water surface, signifying that there is conservation of mass through the wind tunnel, giving confidence in the the quality of the presented profiles. The mean vertical velocity profiles present very little variation with height across the principal valley of the reservoir.

The wind profiles within the Ízbor and Guadalfeo Valleys show greater variation. The sheltering afforded by the surrounding topography reduces considerably the mean horizontal velocities within the two valleys (z<200m), as illustrated by Points 17 and 19 (Ízbor valley) and Points 28 and 30 (Guadalfeo valley). Much larger variations in the vertical velocity component are also observed at low heights within the Guadalfeo Valley.

The variation over the entire reservoir is better represented in Figures 5.13-5.15, which represent the mean horizontal and vertical wind speed profiles as contour diagrams, separated according to the three principal branches of the reservoir, the principal southern branch (5.13), the River Guadalfeo (5.14) and the River Ízbor (5.15). The x-axis of the figures represents the normalized horizontal distance, as indicated in Figure 5.11. The y-axis represents the height

above the reservoir water surface, in meters full scale, and the contour curves represent the horizontal and vertical mean velocity coefficients (C_u and C_v).

Figure 5.13 shows that the mean velocity field does not change significantly above the southern branch of the reservoir. It appears that the local flow separation created by the reservoir structure (x=0.0) is reattached to the water surface at approximately x=0.2. Close to the water surface, there is a further reduction in the mean horizontal wind speed at x=0.6, which coincides with a small outcrop in the topography along the western shoreline of the reservoir.

In contrast, the wind speeds vary greatly within the northern valleys. Figure 5.14 shows how the mean wind speeds decrease rapidly at x=0.2 at low heights, which marks the entrance to the Guadalfeo valley. At a distance of x=0.5, the valley deepens and the winds are reduced throughout the complete depth of the measured profile. At the entrance to the valley (x=0.4-0.6), the vertical velocities are shown to change in direction from negative (downward) to positive (upwards), indicating a localized zone of flow separation occurring along the upstream edge of the valley.

The heights of the mountains surrounding the Ízbor valley are not as large in comparison with the Guadalfeo valley. This is reflected in the wind velocities within the Ízbor valley, which do not show the rapid reduction in horizontal wind speeds throughout the complete depth of the measured profile (Figure 5.15). The wind speeds are still reduced within the valley, but the reduction is limited to heights of up to 200m. The figure shows a large increase in the mean horizontal velocities at x=0.5 throughout the upper portion of the profile, which corresponds with the entrance to the valley and an outcrop in the topography along the upstream edge of the shoreline. The increase in the wind speed may be localized flow separation, or accelerated flow due to the contraction of the valley.

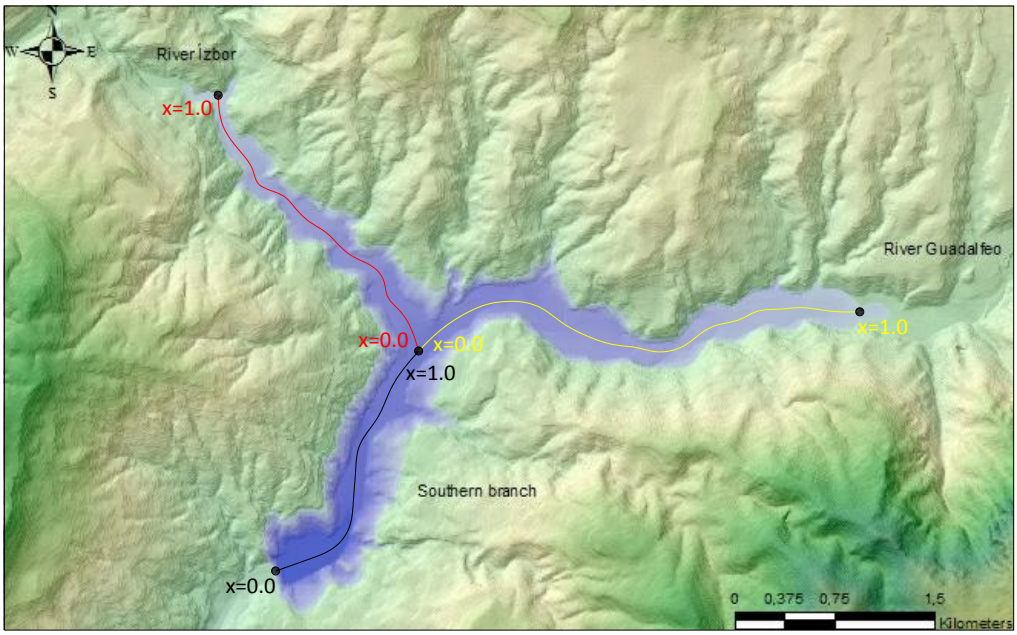

Figure 5.11 Definition of the orientation of the normalized distances used for the contour diagrams

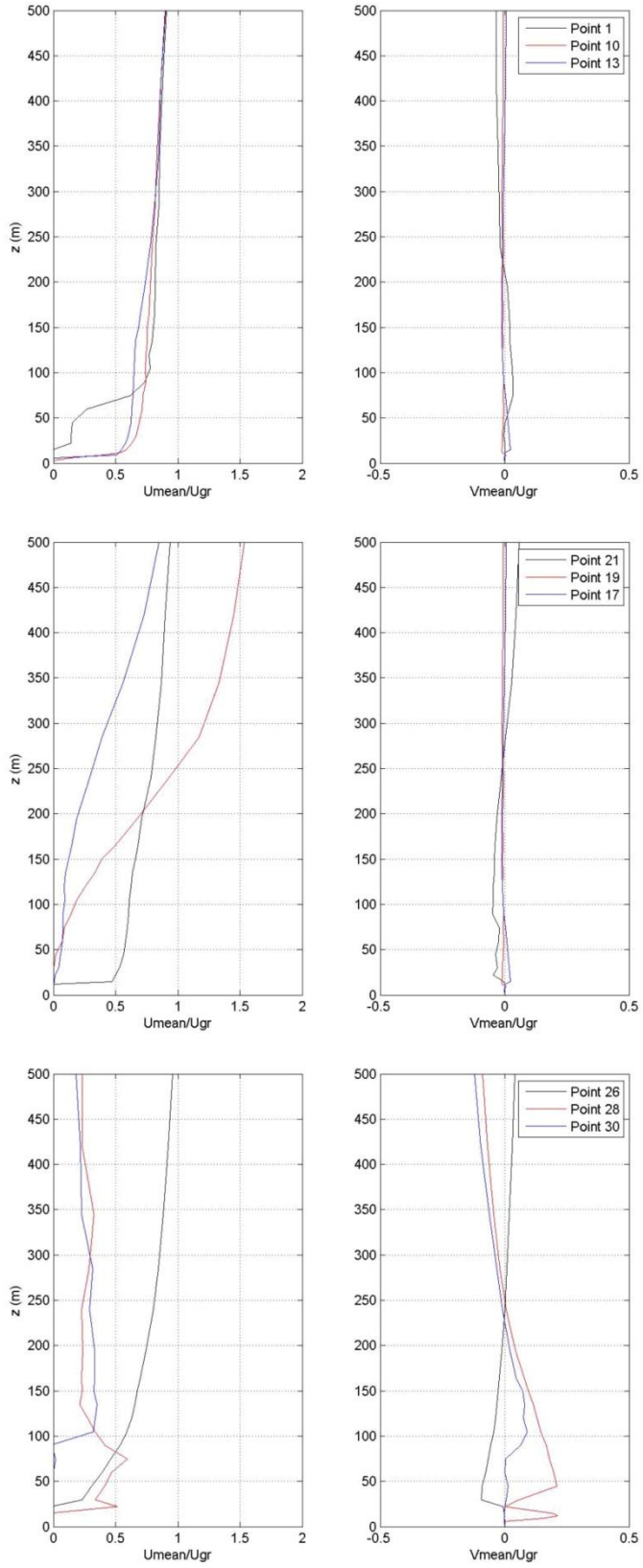

Figure 5.12 Examples of mean horizontal (C_u) and vertical (C_v) velocity profiles recorded in the wind tunnel in the southern branch (Points 1, 10 and 13), Ízbor Branch (Points 17, 19 and 21) and Guadalfeo branch (Points 26, 28 and 30)

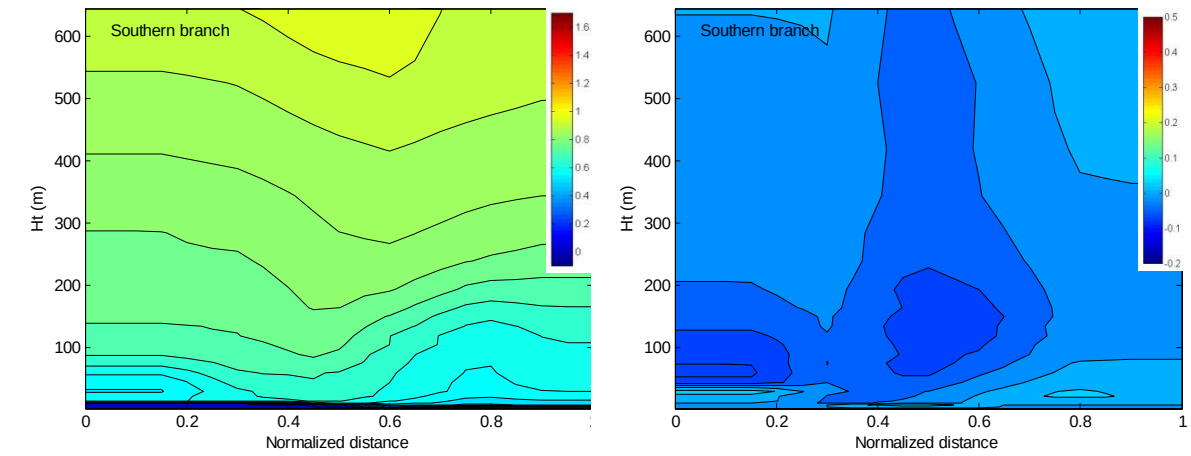

Figure 5.13 Variation of the (a) Horizontal and (b) Vertical mean wind velocity coefficients above the southern branch of the reservoir.

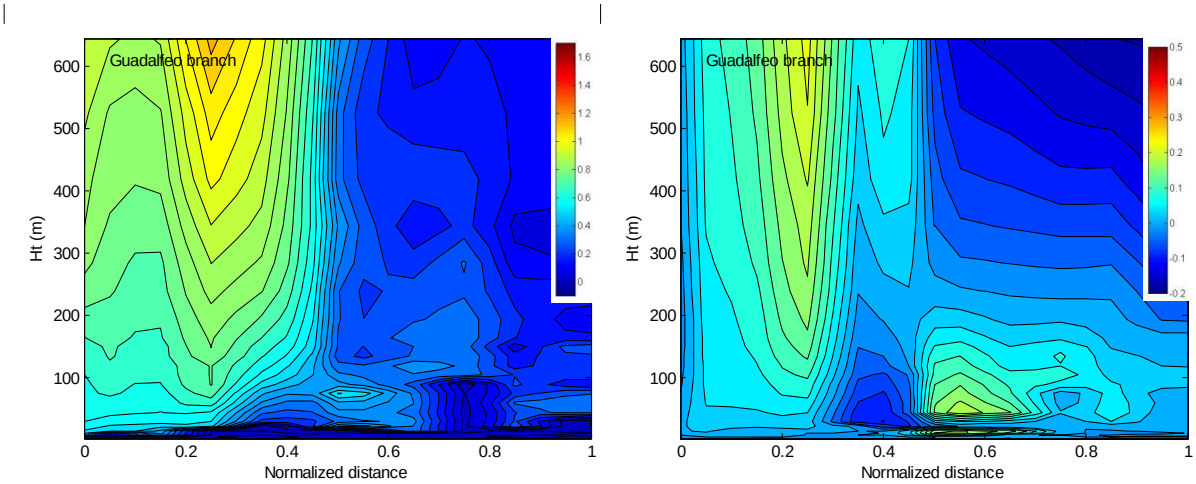

Figure 5.14 Variation of the (a) Horizontal and (b) Vertical mean wind velocity coefficients above the Guadalfeo branch of the reservoir.

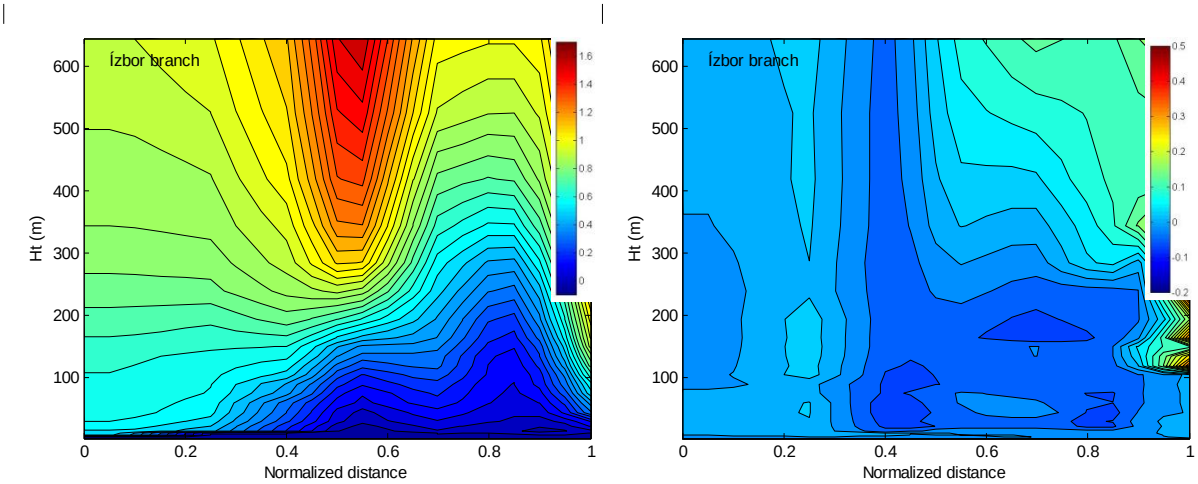

Figure 5.15 Variation of the (a) Horizontal and (b) Vertical mean wind velocity coefficients above the Ízbor branch of the reservoir.

Figure 5.16 presents the spatial variability of the horizontal and vertical wind speed coefficients, C_U and C_V, at a constant height of 15m above the water surface. The figure shows that the horizontal wind speeds vary considerably across the water surface. The C_U coefficients at the base of the reservoir wall are reduced to close to null values due to the sheltering afforded by the structure. Further downstream, the largest horizontal wind speeds occur where the valley converges slightly. This is close to the zone where anemometers A and B were positioned during the field study. At the junction where the reservoir splits into the Ízbor and Guadalfeo valleys, the surface wind speeds are reduced to close to null values. This is expected due to the considerable sheltering effects afforded by the surrounding valley walls.

The vertical wind speed coefficients, C_V, are small in comparison and relatively constant throughout the reservoir, only showing an increase within the Guadalfeo Valley, suggesting the local topography in this zone is creating a region of high local turbulence. This turbulence may create localized agitation of the reservoir water surface and aid in the formation and excitation of free surface undulations within the valley.

The observed spatial variation in the mean wind speeds demonstrates that wind tunnel studies are an adequate method for determining the spatial varation of the wind speeds on the reservoir surface. The wind tunnel simulation can provide a detailed map of the spatial variation of the atmospheric forcing which may be included in numerical simulations of the reservoir hydrodynamics, as will be illustrated in Chapter 6.

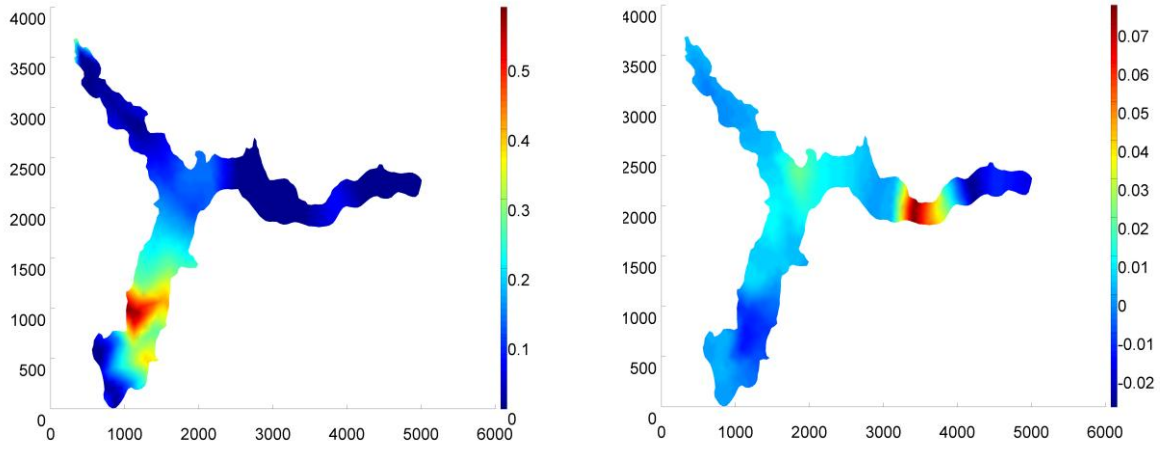

Figure 5.16 Spatial variability of (a) horizontal, C_U, and (b) vertical, C_V, mean wind speeds coefficients, 15m above the water surface

5.7 Atmospheric pressure above the water surface

The surface pressures on the reservoir water surface were recorded using a PSI 8400 pressure system. The pressures are presented at the 32 locations presented in Figure 5.9. The sample time of the measurements is 60 seconds, with a sample frequency of 100 Hz. This corresponds with a full scale sample time of 15 hours and a sample frequency of 6 Hz.

The system 8400 provides the measured surface pressures in PSI units. To convert the measured pressures into Pascals, it is necessary to apply a conversion factor, where 1 PSI is equivalent to 4984.75 Pa. In addition, the pressure coefficients are corrected for the blockage effects of the topography model in the wind tunnel, using the reduction factor, F_r=0.87, as described in the previous section. Therefore, the resulting pressures are converted to Pascals according to:

$$P_{i,corr} = (P_i - P_{st}) \times 4984.75 \times F_r^2 \text{ (Pa)} \quad (5.8)$$

The measured surface pressures are presented in the form of coefficients:

$$C_{pi} = \frac{P_{i,corr}}{\frac{1}{2}\rho_a U_{grad}^2} \quad (5.9)$$

where C_{pi} represents the surface pressure coefficient measured at point 'i' , P_i represents the measured surface pressure at point 'i', P_{st} represents the static reference pressure and U_{grad} is the mean hourly wind speed, at gradient height, above Motril. The static reference pressure, P_{st}, is measured with a Pitot tube, located in the low turbulent region, well outside of the simulated boundary layer flow in the wind tunnel.

5.7.1 Mean surface pressure variation

Figure 5.17 presents the variation of the mean pressure coefficient measured on the water surface. Note that the presented pressure coefficients have negative values, signifying that the pressures are suctions, acting in the upward direction away from the water surface. As expected, the worst suction pressures occur along the main branch of the reservoir, where the horizontal surface wind speeds are the largest. The mean surface pressures within the Ízbor and Guadalfeo valleys are lower, reflecting the lower wind speeds that occur within the valleys.

The largest negative pressure coefficients are found to occur at the base of the reservoir structure, believed to be due to local flow separation from the reservoir structure. Along the length of main body of the reservoir, the atmospheric pressure is shown to remain relatively constant, with pressure coefficients ranging between -1.20 to -1.25. Within the valley Ízbor the pressure coefficients remain relatively constant, however, noticeable variations in the pressure coefficients are observed in the Valley Guadalfeo, where the highest coefficients of -1.0 are observed.

The pressure gradient across the water surface of interest in hydrodynamic studies and not the magnitude of the atmospheric pressure. The figure shows the largest pressure differences occur at the junction between the Ízbor and Guadalfeo rivers, where the pressure coefficients are reduced from coefficients of -1.2 along the southern branch to coefficients of -1.1 inside the two northern branches.

The pressure gradients that exist at the junction of the three branches, and also within the Guadalfeo Valley, can produce inequalities in the spatial distribution of the atmospheric forcing and aid in the formation of surface seiches.

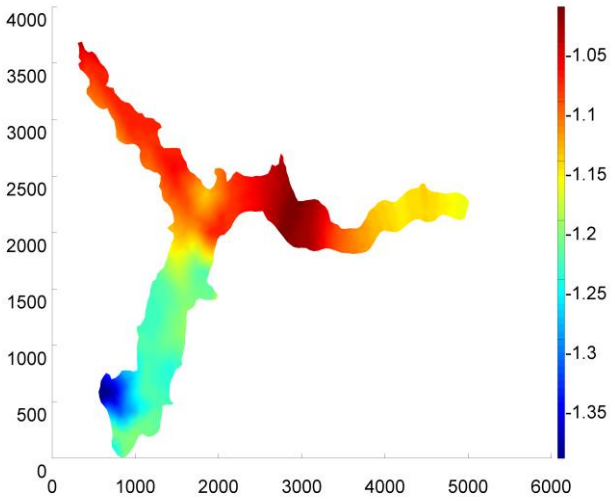

Figure 5.17 Mean pressure coefficient, C_p, measured above the reservoir water surface

5.7.2 Frequency distribution of surface pressures

As described in the introduction, the local topography may also create disturbances in the atmospheric conditions with a distinct harmonic component, for example, eddies and vortex streets in the wake region behind large topographical features or from mountain waves. Figure 5.18 presents the frequency distribution of the measured pressure coefficients at selected locations to determine if the local topography surrounding the reservoir is creating resonance in the atmospheric pressure. The frequencies are represented as full-scale values, assuming a mean gradient wind speed, U_{grad}, of 40m/s, which is equivalent to a mean wind speed of 22m/s at 10m above ground level (open country terrain). For clarity, the frequency distributions of the pressures of the three branches of the reservoir are presented separately, defined as the southern, Ízbor and Guadalfeo Valleys respectively.

Figure 5.18(a) shows that the frequency component of the water surface pressures remains relatively constant along the principal branch of the reservoir, with the exception of location 2, which is located immediately upstream of the reservoir structure. This is due to the local separation of the flow created by the reservoir structure, creating an increase in the turbulence in the wake region. The figure illustrates an increase in the energy around a full scale frequency of 0.0175 Hz at most locations along the southern branch of the reservoir. This signifies the possibility of pulsations in the surface pressures with a full scale period of 57 seconds.

Similarly, Figure 5.18(b) shows how the energy content of the pressure increases with distance into the valley, with the exception of Points 27 and 28, which are located midway along the valley. This corresponds with the location where there appears a large increase in the vertical velocity coefficients, as shown in Figure 5.16.

Figure 5.18(c) illustrates how the energy content of the surface pressures increases with distance within the Ízbor Valley, where the lowest energy content is observed at Point 13, which is located upstream of the valley entrance. The energy content grows relatively uniformly along the valley, reaching a maximum at Point 15.

The three figures present a small increase in the energy content around a frequency of 0.015Hz along the principal branch of the reservoir, including the zone within the junction to the northern valleys. This signifies that there is the possibility of pressure pulsations on the water surface with a period of approximately 57 seconds, during synoptic events with a gradient height wind speed of 40m/s.

The period varies in function with the magnitude of the gradient height wind speed. Therefore, for a gradient height wind speed of 10m/s, the period of the pulsation is in the order of 230 seconds.

An exact match of the harmonic frequencies measured in the wind tunnel were not observed in the 13 day field study. However, this may be because no synoptic scale events occurred during the short time period of the field study. Further field studies of longer duration will be required to perform a proper comparison with the pulsations observed in the wind tunnel.

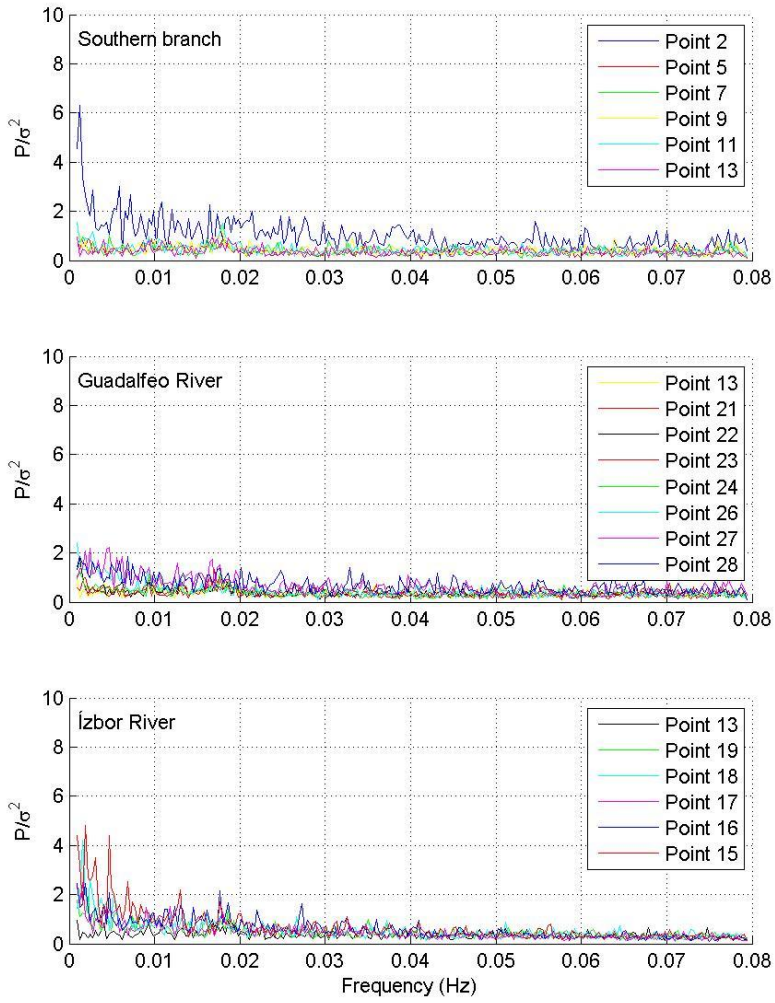

Figure 5.18 Frequency distribution of surface pressure coefficients (a) Southern branch, (b) Guadalfeo River, (c) Ízbor River

6 Numerical model simulation of Rules Reservoir

In this chapter, the numerical model developed in Chapter 3 is applied to the Rules Reservoir. The atmospheric forcing is constructed by merging together the high temporal resolution of the field data with the enhanced spatial resolution of the wind tunnel surface velocity and surface pressure data. As a benchmark comparison, an additional load case is studied assuming a sudden and uniform atmospheric loading across the reservoir water surface. The simulations with the numerical model provide an insight into the response of the water free surface to the atmospheric forcing and can also be used to predict the reservoir behavior when the water level will be at full capacity or at intermediate levels.

6.1 Bathymetry

As described in Chapter 4, the bathymetry of the reservoir is constructed from two sources. The general topography information for the Guadalfeo catchment area, provided in 5m contour intervals, was used as the primary source of the topography of the zone (Molero Melgarejo, 2004). This was merged together with the high resolution measurements obtained by a field survey of the reservoir, which is valid up to an elevation of 173m (Ruiz & Nanía Escobar, 2006). The merged bathymetry is then imported into ArcGis and meshed with a uniform grid of 2m, creating the final bathymetry file in text format.

The bathymetry information is then imported into the meshing software, Gambit, for cleaning. Gambit is a companion program of Fluent used to construct the three dimensional mesh of the domain. In zones close to the shoreline of the reservoir, large errors in the calculated surface oscillations can be induced due to the shallow water depths in these zones. To eliminate these errors, the bathymetry is cut at 2.5m below the water surface. The perimeter edges of the cut surface are then copied up 2.5m to create the final water surface. Vertical faces were then created around the perimeter, such that the upper 2.5m of the water body contains a vertical wall around the entire perimeter of the reservoir. The removal of the shallow water regions around the perimeter of the reservoir resulted in a small loss of water surface area, predominantly in the northern corners of the reservoir at the entrances of the rivers Ízbor and Guadalfeo. Figure 6.1 presents the final three-dimensional bathymetry (183m ASL) incorporated into the numerical model.

The numerical model adjusts the bathymetry to create a triangular mesh, with greater resolution placed around the perimeter of the reservoir, as illustrated in Figure 6.2. The number of node points varied with water depth, with 967 nodes for the 183m simulation, and 649 and 1403 for the 213m and 243m simulations. The resolution of the final mesh used by the numerical model is sufficient to accurately capture the bathymetry of the reservoir.

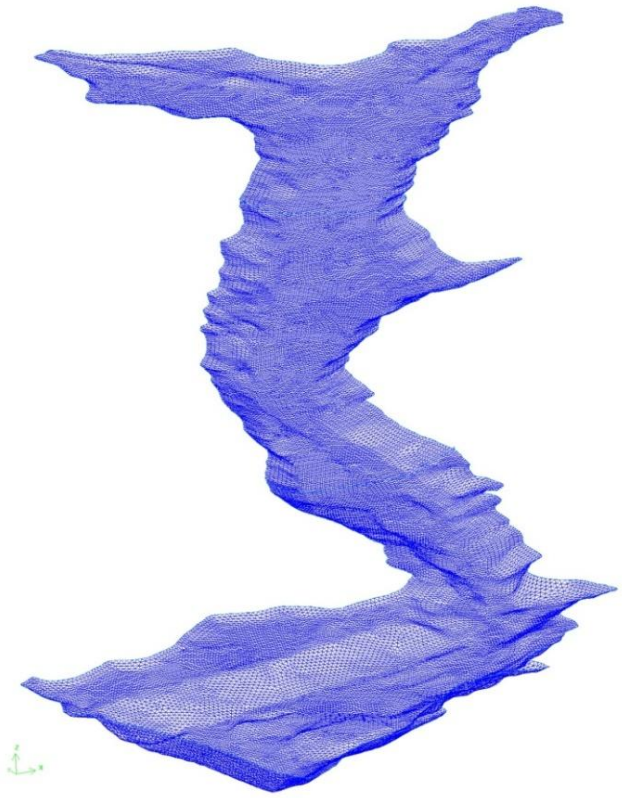

Figure 6.1 Bathymetry of Rules Reservoir inputted into the numerical model (183m a.s.l.)

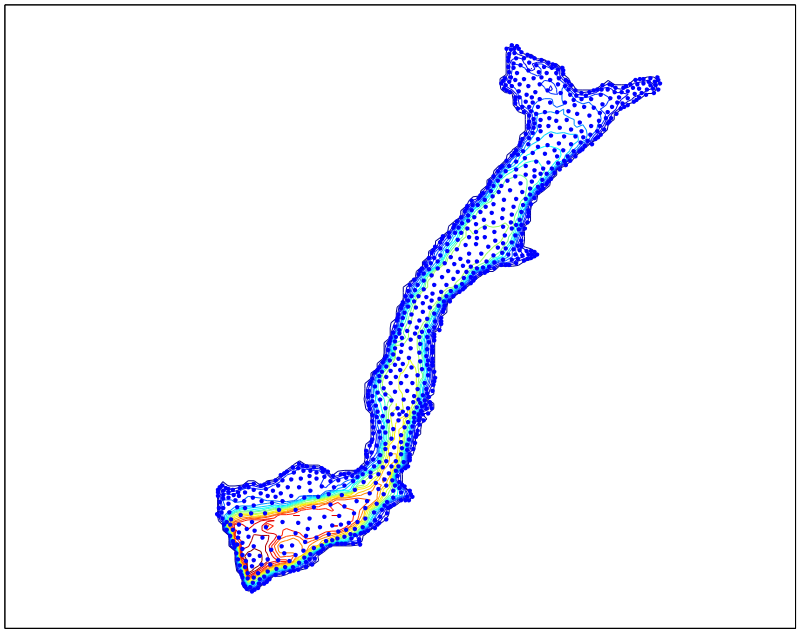

Figure 6.2 Nodal points of triangular mesh created by the numerical model (183m a.s.l.)

6.2 Atmospheric forcing

The spatial and temporal variation of the atmospheric forcing term, F, is obtained from the measured field data. As described in Appendix A, the forcing term is expressed as:

$$\mathcal{F}_\alpha = -g(h+\eta)\frac{\partial}{\partial x_\alpha}\left(\frac{P_s}{\rho g}\right) + \frac{\sum \tau_\alpha}{\rho} \tag{6.1}$$

The atmospheric pressure term, P_s, is obtained directly from the observed field data. The surface wind shear forcing, τ, is calculated from:

$$\begin{aligned} \tau_{xz} &= C_d\, \rho_{air}\, u\|\boldsymbol{u}\| \\ &= C_d\, \rho_{air}\, \|\boldsymbol{u}\|\|\boldsymbol{u}\|\, \sin\theta \end{aligned} \tag{6.2}$$

$$\begin{aligned} \tau_{yz} &= C_d\, \rho_{air}\, v\|\boldsymbol{u}\| \\ &= C_d\, \rho_{air}\, \|\boldsymbol{u}\|\|\boldsymbol{u}\|\, \cos\theta \end{aligned} \tag{6.3}$$

where $\|\boldsymbol{u}\|$ is the wind velocity magnitude, θ is the wind direction, ρ_{air} is the air density and C_d is the drag coefficient.

6.2.1 Drag coefficient, C_d

The drag coefficient is a non-dimensional numerical function relating the exchange of energy between the atmospheric forcing and the water volume. Typically, values in the order of $1x10^{-3}$ are used, but this is based on measurements in a neutral boundary layer, in open sea terrain conditions and for long averaging periods. For applications in complex terrain, the turbulence in the atmosphere will be higher leading to a larger vertical component of the wind and an increase in the energy exchange between the two fluids.

The drag coefficient originates from field studies, where the presented coefficients inherently contain a large degree of scatter. Figure 6.3 presents the variation of the surface drag coefficient with wind speed, although it is also dependent on wave height. For wind speeds greater than 5m/s, the drag coefficient follows Charnock´s law with values between $1.0x10^{-3}$ and $2.0x10^{-3}$, where the coefficient is represented as:

$$C_d = \left\{k^{-1}\, ln\left(\frac{g}{C_d U_{10}^2}\right) + K\right\}^{-2} \tag{6.4}$$

A simplified version is also available, which presents the drag coefficient as a function of the surface roughness, z_o:

$$C_d = \left(\frac{k}{ln\left(\frac{10}{z_o}\right)} \right)^2 \tag{6.5}$$

For open sea conditions, the drag coefficient can also be expressed as:

$$C_d = \left(0.63 + 0.066 \left|\vec{U}_{10}\right|\right) 10^{-3} \tag{6.6}$$

where U_{10} is the wind speed at 10m height.

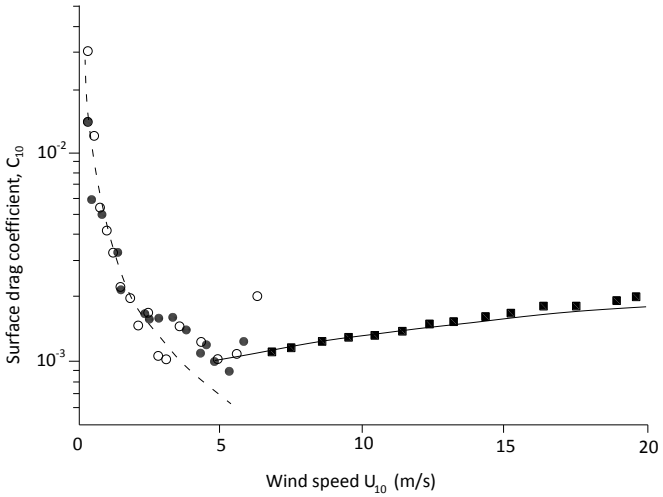

Figure 6.3 Wind drag coefficient, C_d, for developed waves (Adapted from (Wuest & Lorke, 2003))

For wind speeds less than 5m/s, the coefficient roughly follows a least square fit, increasing to values of $1x10^{-2}$ for low wind speeds. However, the data indicated in Figure 6.3 is relevant for neutral boundary layer conditions over the open ocean, or at least for lakes with fully developed waves. As noted by (Wuest & Lorke, 2003), the interaction between the atmospherical forcing and the lake does not reach equilibrium in small lakes with a limited fetch distance. Instead, the momentum uptake of the lake remains in a state of transition and is highly dependent on local effects, such as topography. Therefore, the surface stress in lakes is typically larger in lakes than in oceans and will be further enhanced due to the increased vertical turbulence generated by surrounding topography features.

This modification may be expressed with higher values of drag coefficient than those represented in the figure. Through a series of model calibration runs, a drag coefficient value of $2x10^{-2}$ was selected as adequate for simulating the free surface response of Rules Reservoir.

6.2.2 Coriolis acceleration

The assumption that the Coriolis acceleration is negligible for the Rules Reservoir is verified by comparing the Rossby radius of deformation with the characteristic width of the reservoir. Assuming a characteristic depth, h=15m, and a coriolis force of $f_c \approx 4x10^{-5}$, the Rossby radius, a_r, is calculated according to:

$$a_r = \frac{\sqrt{gh}}{|f_c|} = 3 \times 10^5 \tag{6.7}$$

This is much greater than the characteristic width of the reservoir, estimated as 100m. Therefore, the geostrophic influence will be weak in the reservoir and the coriolis acceleration can be ignored, satisfying assumption (b) in the derivation of the numerical model (Chapter 3.1).

6.2.3 Spatial and temporal variation of atmospheric loading from field data

The spatial and temporal variation of the atmospheric forcing is incorporated in the model by using the wind velocity and atmospheric pressure measurements from the three anemometers deployed during the field campaign. The model assumes a linear weighting function between the three anemometers along the length of the reservoir centerline, as illustrated in Figure 6.4 (183m ASL).

The weighting coefficients comprise of values between 0.0 and 1.0, varying linearly with distance along the centerline of the reservoir. Therefore, the final atmospheric loading applied to each nodal point is the summation of the atmospheric forcing recorded by the three anemometer stations according to:

$$F_{Total} = C_A F_A + C_B F_B + C_C F_C \tag{6.8}$$

where $C_{A\text{-}C}$ is the linear weighting coefficient for each of the three anemometers and $F_{A\text{-}C}$ is the atmospheric forcing recorded by each of the anemometer stations (wind shear or barometric pressure). At each nodal point, i, the summation of the weighting coefficients must equal unity:

$$C_{A,i} + C_{B,i} + C_{C,i} = 1.0 \tag{6.9}$$

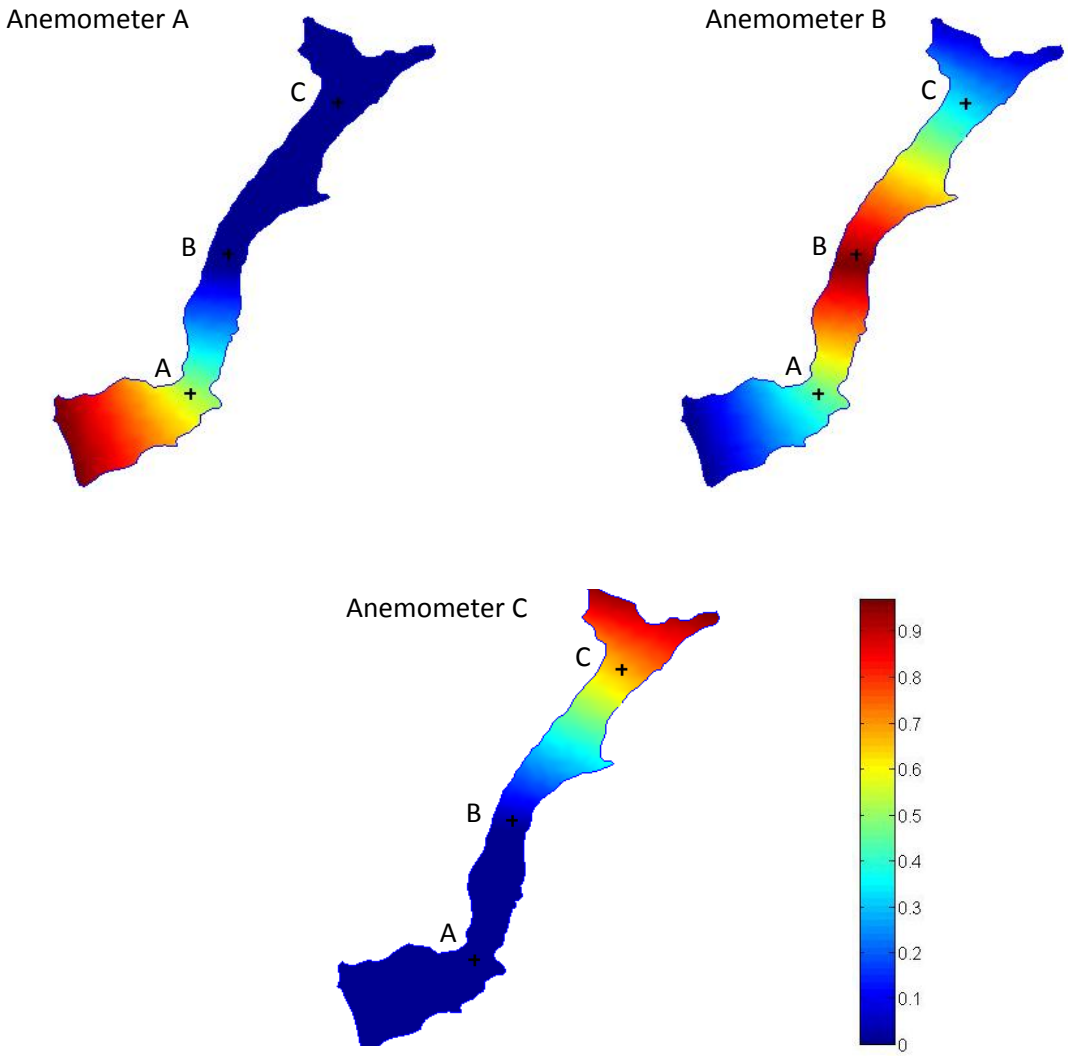

Figure 6.4 Linear weighting coefficients of atmospheric forcing measured by the three anemometers during the field campaign; (a) Anemometer A; (b) Anemometer B; (c) Anemometer C

6.2.4 Spatial variation of atmospheric loading from wind tunnel data (Íźbor and Guadalfeo branches)

The spatial resolution of the atmospheric forcing is enhanced by utilizing the measurements from the wind tunnel simulation. The wind tunnel simulations illustrated the large spatial variations that occur over the length of the reservoir, in particular within the Íźbor and Guadalfeo Valleys, where the atmospheric forcing is greatly reduced (See Chapter 5).

The wind tunnel information is integrated into the numerical model by deriving a series of weighting coefficients, which are referenced to the measurement points located as close

possible to the positions of the Anemometers during the field study. Therefore, the zone towards the southern end of the reservoir is governed by field measurements by Anemometer A. Therefore, the wind tunnel coefficients are normalized by the measurements at Point 4 in the wind tunnel study, which matches well with the position of Anemometer A. Similarly for Anemometers B and C, the wind tunnel coefficients are normalized with respect to Points 9 and 13 respectively.

From the wind tunnel and field study information, the local wind directionality did not vary greatly across the length of the southern branch of the reservoir, but is shown to follow the general direction of the topography. Therefore, the local variability in the wind directionality is not applied to the information from Anemometer A and B. However, large changes in the wind directionality are observed inside the Ízbor and Guadalfeo valleys. Therefore, the variability of the wind directionality is included in the weighting coefficients added to the Anemometer C information.

The weighting coefficients for the wind shear, C_τ, and barometric pressure, C_P, forcing terms are calculated according to the following:

$$C_{\tau A} = \frac{C_{ui}^2}{C_{u\ i=4}^2} \tag{6.1}$$

$$C_{\tau B} = \frac{C_{ui}^2}{C_{u\ i=9}^2} \tag{6.2}$$

$$C_{\tau Cx} = \frac{C_{ui}^2\ \cos(\theta_i)}{C_{u\ i=13}^2\ \cos(\theta_{i=13})} \tag{6.3}$$

$$C_{\tau Cy} = \frac{C_{ui}^2\ \sin(\theta_i)}{C_{u\ i=13}^2\ \sin(\theta_{i=13})} \tag{6.4}$$

$$C_{PA} = \frac{C_{P\ i}}{C_{P\ i=4}} \tag{6.5}$$

$$C_{PB} = \frac{C_{P\ i}}{C_{P\ i=9}} \tag{6.6}$$

$$C_{PC} = \frac{C_{P\ i}}{C_{P\ i=13}} \tag{6.7}$$

where C_{ui} is the horizontal wind velocity coefficient and θ_i its wind direction measured at Point 'i' during the wind tunnel simulation. $C_{u\ i=4}$, $C_{u\ i=9}$ and $C_{u\ i=13}$ is the lateral wind velocity coefficient measured at Points 4, 9 and 13 respectively, with $\theta_{i=13}$ the corresponding wind direction at Point 19. Thus, the wind shear coefficients from Anemometer C consider the variation in the magnitude of the wind speed and the change in wind direction observed during the wind tunnel simulations. Likewise, C_{pi} and $C_{p\ i=13}$ are the surface pressure coefficients measured at Point 'i' and at Point 13 respectively.

The weighting coefficients from the wind tunnel data are then combined with the weighting coefficients from the field data, to derive a complete spatial and temporal map of the atmospheric forcing across the complete surface area of the reservoir.

Figure 6.5 presents the resulting weighting coefficients applied to the atmospheric forcing components based on the wind tunnel measurements. The wind shear coefficients for Anemometer C are now separated into the two components, x (East) and y (North), to incorporate the modification of the magnitude and directional changes of the wind shear.

The weighting coefficients reflect the observed spatial variation in the atmospheric forcing recorded in the wind tunnel study, including the reduction in wind speeds experienced within the valleys, in particular at the entrance to the Ízbor branch. Values of the wind shear coefficient for Anemometer B, $C_{\tau B}$, are greater than 1.0, due to the increase in wind shear indicated by the wind tunnel simulation around this zone. The negative value of the x-component wind shear coefficient, $C_{\tau Cx}$, reflects the change in wind direction from eastward to westward as the flow enters into the valley.

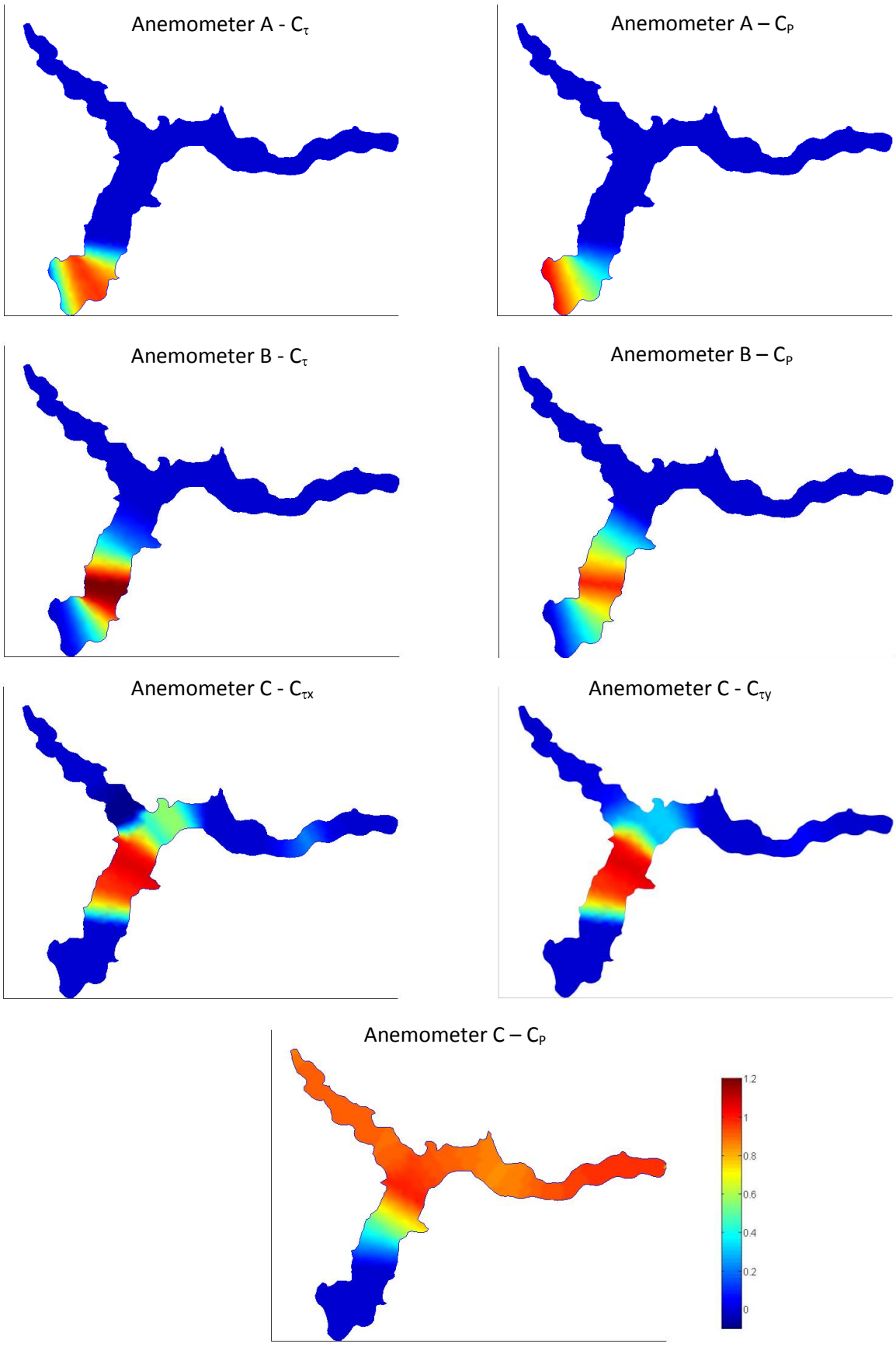

Figure 6.5 Linear weighting coefficients of atmospheric forcing measured by the three anemometers during the field campaign after application of the wind tunnel weighting functions

6.3 Simulation Case Studies

The reservoir response is simulated with the numerical model for a number of water depths and atmospheric forcing conditions. Table 6.1 presents a summary of the load cases investigated with the numerical model.

Table 6.1 Summary of load cases simulated with the numerical model

Load Case Identifier	Water elevation ASL (m)	Atmospheric Loading
183_uniform	183	Uniform loading, F=1.5 x 10^{-3}
183_Feb19	183	Event 1, February 19th, 2008
183_Feb23	183	Event 2, February 23rd, 2008
213_uniform	213	Uniform loading, F =1.5 x 10^{-3}
213_Feb19	213	Event 1, February 19th, 2008
213_Feb23	213	Event 2, February 23rd, 2008
243_uniform	243	Uniform loading, F =1.5 x 10^{-3}
243_Feb19	243	Event 1, February 19th, 2008
243_Feb23	243	Event 2, February 23rd, 2008

6.3.1 Simulation of uniform wind loading

The simplest and most common method of analyzing the free surface response of a small lake or reservoir is to apply a constant atmospheric loading across the water surface. While this may be an appropriate loading condition for lakes with uniform exposure, it can produce misleading responses in situations where spatial and temporal variation in the loading are expected. This is particularly significant for small lakes which are sensitive to small changes in the atmospheric forcing, particularly in the case of lakes surrounded by topographical features, significant vegetation or man-made features.

The simulation applied a sudden and uniform forcing with a magnitude, F, of 1.5 x 10^{-3} m^2/s^2. The directionality of the forcing followed the direction of the reservoir centerline, as shown in Figure 6.6. As shown in the figure, the geometry of the reservoir changes dramatically with increasing water depth. Therefore, the reservoir centerline was adapted for the 213m and 243m water elevation simulations to conform to the changing geometry such that the loading also follows the directionality of the two valleys, Ízbor and Guadalfeo.

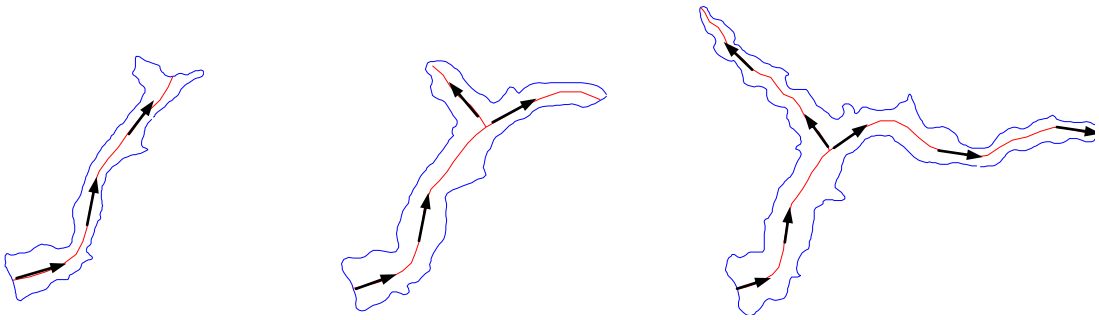

Figure 6.6 Reservoir centerline indicating the directionality of the uniform atmospheric forcing applied over the reservoir, for water elevations (a) 183m; (b) 213m; and (c) 243m.

6.3.1.1 Water elevation 183m ASL

Figure 6.7 presents the response of the reservoir at its current water elevation (183m ASL), after the application of the uniform atmospheric loading. The x-axis represents the normalized length of the reservoir along its centerline, with x=0 corresponding to the southern end of the reservoir (the dam wall) and x=1.0 corresponding to the northern end of the reservoir. The orientation of the reservoir centerline is indicated in the sub-figure. The figure shows the reservoir responds to the atmospheric forcing in a similar manner to a rectangular basin. After the forcing is initialized, the water is displaced from the southern end of the reservoir towards the direction of the loading, with a maximum vertical displacement of approximately 0.025 m (x=1.0). The displaced water then travels back to the dam wall due to gravitational forcing. This oscillation continues until the free surface displacement reaches equilibrium between the gravitational and atmospheric forcing.

The frequency distribution of the free surface response obtained by the numerical model is illustrated in Figure 6.8. As indicated, three nodal points are investigated. These points match the locations (A, B and C) where the instruments were deployed during the field study, as indicated in the subfigure o Figure 6.7. The frequency distribution shows the reservoir response is primarily in the first eigenvalue mode, T_1=503 sec, with additional energy contributions from the higher order modes (T_2=228 sec, T_3= 150sec, T_6=83 sec). Appendix B provides a description of the eigenvalue modal distribution for the first eight modes. The energy component of the first mode at location B is much less that the other two locations, as it is positioned close to the nodal point of the first reservoir eigenmode.

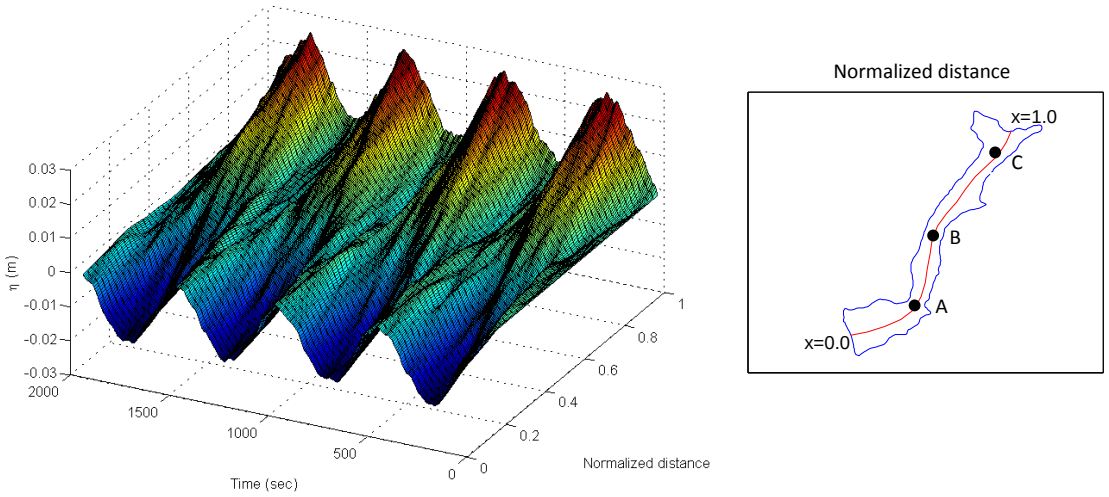

Figure 6.7 Simulated free surface response to constant and uniform atmospheric forcing, F=0.0015 m^2/s^2. Water elevation 183m ASL

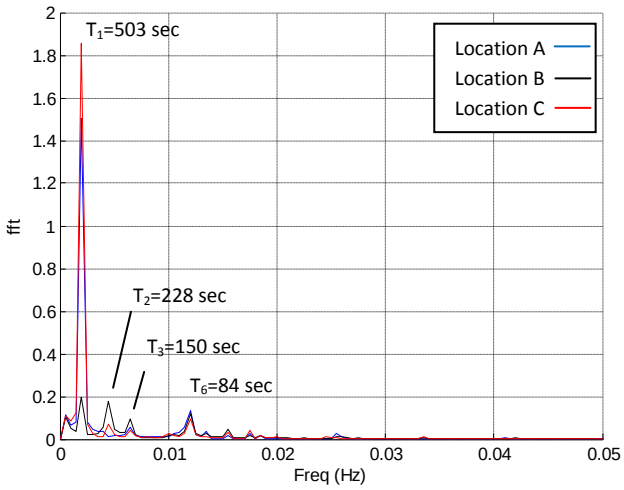

Figure 6.8 Frequency distribution of simulated free surface response to a constant and uniform atmospheric forcing, F=0.0015 m^2/s^2. Water elevation 183m ASL

6.3.1.2 Water elevation 213m ASL

A similar response is observed for the intermediate water elevation of 213m ASL. The free surface oscillation is illustrated in Figure 6.9, with the centreline beginning at the base of the dam extending until the end of the Guadalfeo valley, as illustrated in the sub-figure. The figure shows the period of the first mode is reduced due to the increased length of the reservoir, with a first mode period T_1=402 sec. The magnitude of the oscillation is also reduced, with a maximum displacement within the Guadalfeo Valley of approximately 0.012m. Although not shown, the oscillation also enters into the Ízbor Valley but with less energy content. Appendix B describes the reservoir eigenmodes for the water elevation of 213m ASL.

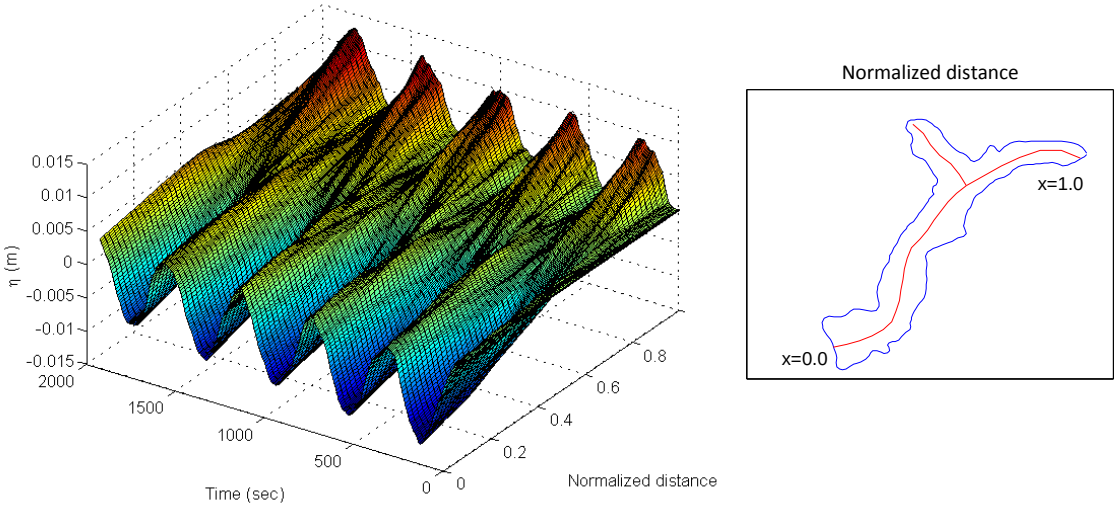

Figure 6.9 Simulated free surface response to constant and uniform atmospheric forcing, F=0.0015 m^2/s^2. Water elevation 213m ASL

6.3.1.3 Water elevation 243m ASL

The response of the reservoir at full capacity (243m ASL) is presented in Figure 6.10. In this case, the water extends further into the Ízbor and Guadalfeo Valleys, greatly extending the length of the reservoir. Figure 6.10(a) represents the time varying free surface displacement between the dam structure (x=0.0) and the end of the Guadalfeo Valley (x=1.0), while Figure 6.10(b) represents is the free surface displacement between the end of the Ízbor Valley (x=0.0) and the end of the Guadalfeo Valley (x=1.0).

As illustrated in the figures, the reservoir can no longer be considered as single rectangular basin. Instead, the reservoir responds more like three partially open basins joined together at a common junction, with the first two eigenmodes dominated by oscillations between the valleys Ízbor and Guadalfeo. After the onset of the atmospheric loading, the water is initially displaced from the southern branch of the reservoir and is moved, first into the Ízbor Valley,

and afterwards into the Guadalfeo Valley. The displacement of the free surface is much greater in the Guadalfeo Valley, with an initial increase in the water level of 0.04m, compared with the Ízbor Valley of 0.02m.

Figure 6.11 provides two snapshots of the water free surface elevation, at T=360 sec and T=700 seconds, which coincide with instances when of maximum vertical displacement in the Guadalfeo and Ízbor Valleys respectively. The figures demonstrate that, after the initial forcing and displacement of the water in the southern branch, the movement of the water is restricted to the two northern branches.

The frequency distribution of the free surface response is presented in Figure 6.12 for four locations, coinciding with node points at the far ends of the Ízbor, Guadalfeo and southern valleys (Location A), along with a fourth point at the junction between the three branches (Location C). The figure shows the oscillations in the two northern branches are dominated by different modes, with the Guadalfeo valley mode of 703 seconds (which corresponds with the first reservoir eigenmode), and the Ízbor valley mode of 456 seconds (the second reservoir eigenmode). The frequency distribution at the southern end of the reservoir is a combination of the first two modes, but with much less energy content. Appendix B describes the reservoir eigenmodes for the water elevation of 243m ASL.

The figure also shows the Guadalfeo Valley presents a much broader energy distribution over frequencies of up to 100 seconds, unlike the other two sections of the reservoir. This suggests the oscillations within the Guadalfeo Valley are a combination of many modes, although dominated by the first mode. The water within this section of the valley will likely be more turbulent as a result.

While the amplitude of the oscillation within the Guadalfeo Valley is relatively constant, the oscillation within the Ízbor Valley is variable. This is because the two oscillating waves that are formed within the two valleys have different periods and the peaks in the Ízbor Valley occur when the two waves meet together at the junction. At the same time, the wave exits the northern valleys and produces a larger oscillation along the southern branch of the reservoir.

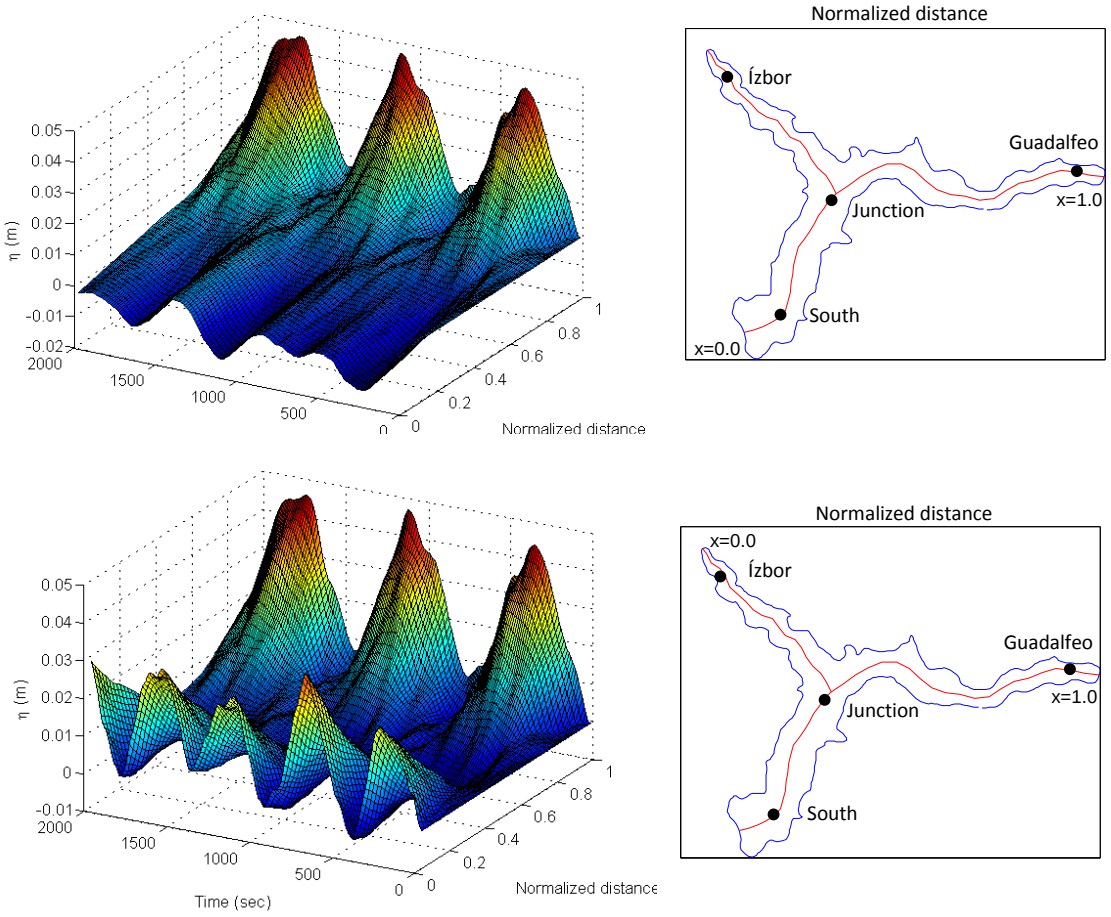

Figure 6.10 Simulated free surface response to constant atmospheric forcing, F, of 0.0015 m^2/s^2, for (a) Southern and Guadalfeo valley; and (b) Ízbor and Guadalfeo valley. Water elevation 243m ASL

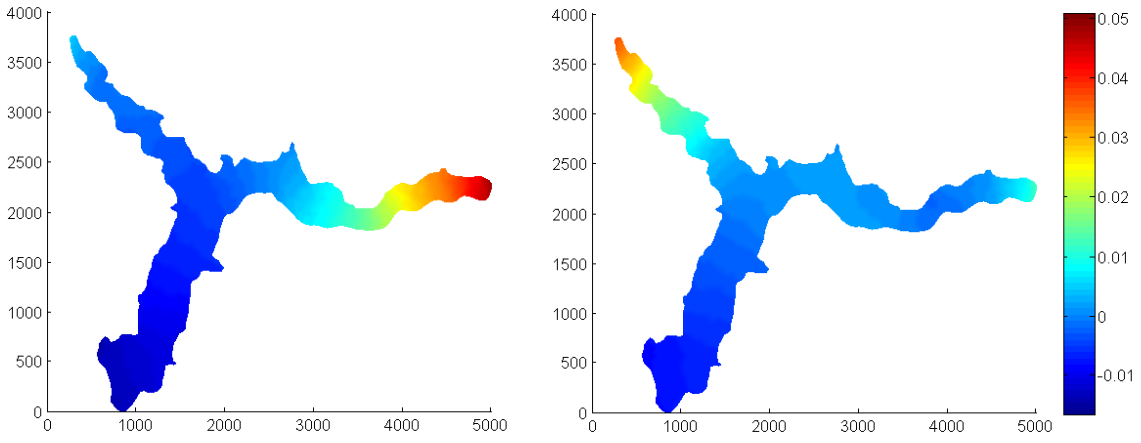

Figure 6.11 Snapshots of simulated reservoir oscillation at two instances in time for a uniform wind loading, (a) t=360 sec and (b) t=700 sec. Water elevation 243m ASL

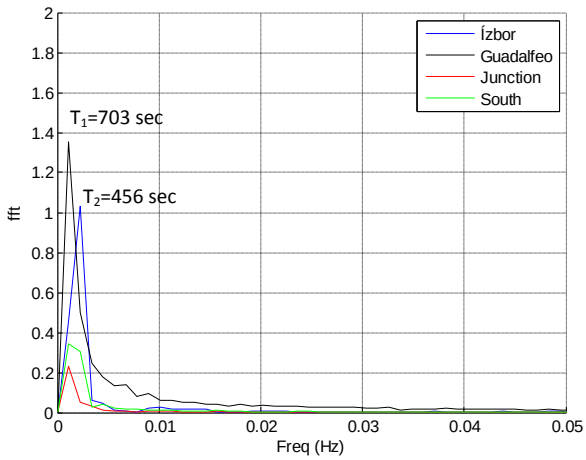

Figure 6.12 Frequency distribution of simulated free surface response to a uniform atmospheric forcing, F=0.0015 m^2/s^2. Locations of analysed points are indicated in the previous figure. Water elevation 243m ASL

6.3.2 Simulation of measured Storm 1, 19th Feb

The free surface response to the atmospheric forcing measured during the field study is presented. As discussed in Chapter 4.5, field measurements of the free surface response to the storm event measured on the 19th of February showed the reservoir began to oscillate in its first mode, with an amplitude 0.045m at Station C. The storm had duration of less than five minutes, presenting a peak wind speed of 22m/s and an instantaneous reduction in the barometric pressure of 3.5hPa.

The simulation begins approximately 500 seconds before the onset of the storm and continues for a total duration of 2000 seconds, adequately capturing the response of the reservoir to the storm passage and its subsequent free oscillation.

6.3.2.1 Water elevation 183m ASL

Figure 6.13 presents the simulated response of the reservoir to the storm event, for the current water elevation of 183m ASL. The figure presents the x-y components of the wind shear forcing, along with the atmospheric pressure, measured by the three anemometers at locations A, B and C. The simulated free surface response at three nodal points is also represented, which coincide with the locations of the measurement instruments deployed in the field study: Stations A, B and C. In this way, direct comparison between the measured response in the field study and the simulated response of the model can be made.

The figure shows the numerical model successfully simulates the resonance of the water surface, with the reservoir oscillating in its first mode after the passage of the storm event. The amplitude of the oscillation is similar to the amplitude measured at the same locations in the field study, with a simulated amplitude of 0.05m at Location ‘C’ compared to 0.045m recorded at the same location during the field study.

Figure 6.14 presents two snapshots of the water free surface elevation at two instances in time, at T=1000 sec and T=1250 sec. Similar to observations in the field, the displacement at the centre of the reservoir (Location B) is much smaller than at the extremes, indicating that the reservoir is oscillating in its first mode.

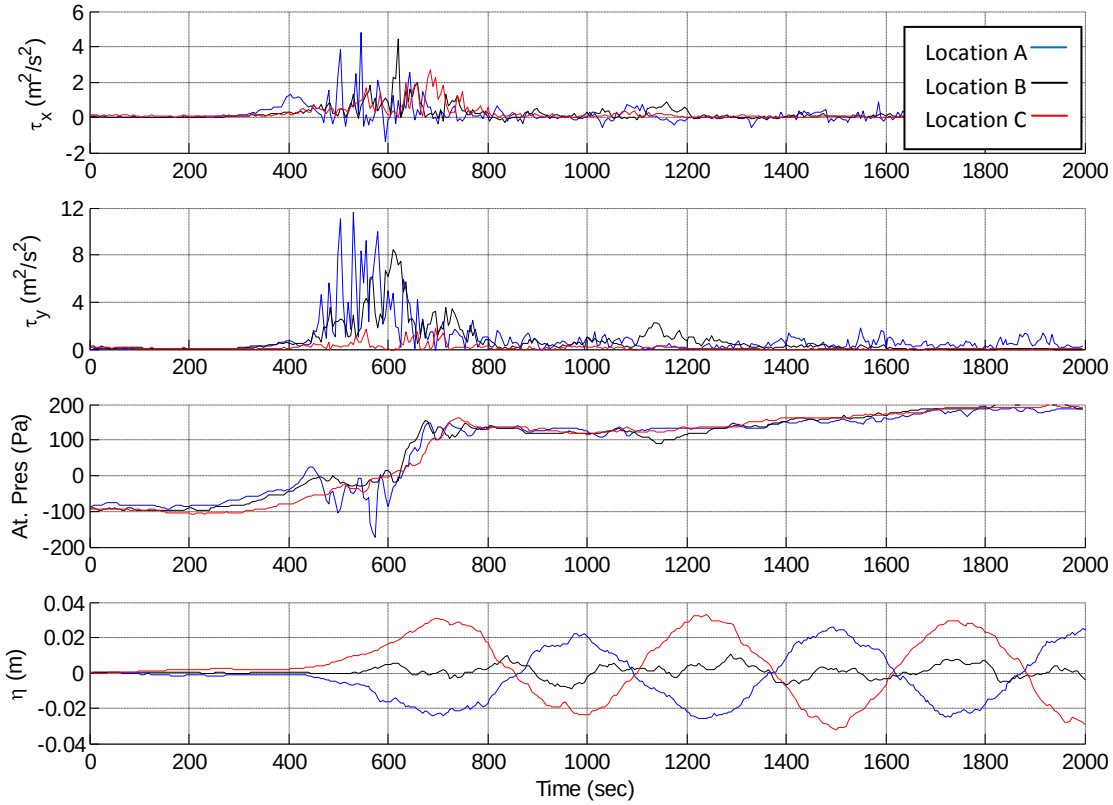

Figure 6.13 Numerical model simulation of free surface response after the passing of Storm 1, Feb 19th. (a) x-component wind shear loading; (b) y-component wind shear loading; (c) Atmospheric Pressure loading; (d) Free surface response simulated by the numerical model. Water elevation 183m ASL

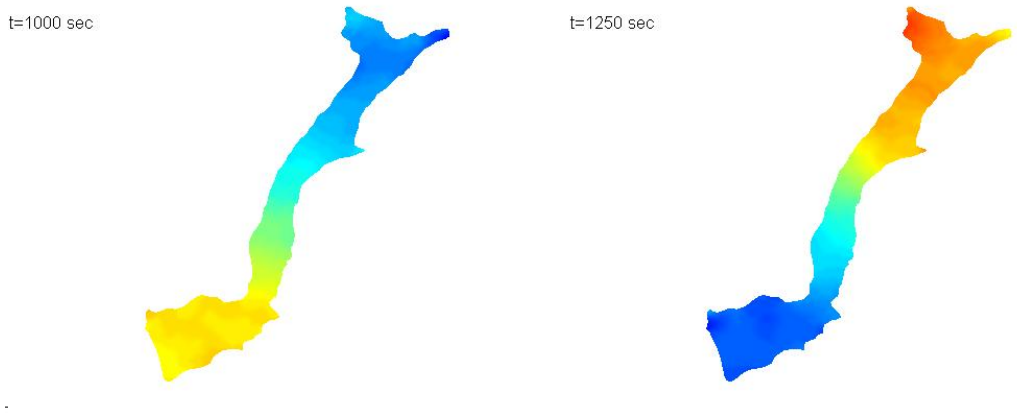

Figure 6.14 Snapshots of simulated reservoir oscillation at two instances in time for Storm event 1, 19th Feb, (a) t=1000 sec and (b) t=1250 sec. Water elevation 183m ASL

The time variation of the free surface elevation along the reservoir centreline is illustrated in Figure 6.15. The figure shows the storm front moving along the length of the reservoir after time T=500 seconds, producing a water displacement at the northern end of the reservoir. After the storm passes, the displaced water is released and the surface seiche is created, oscillating predominately in the first mode.

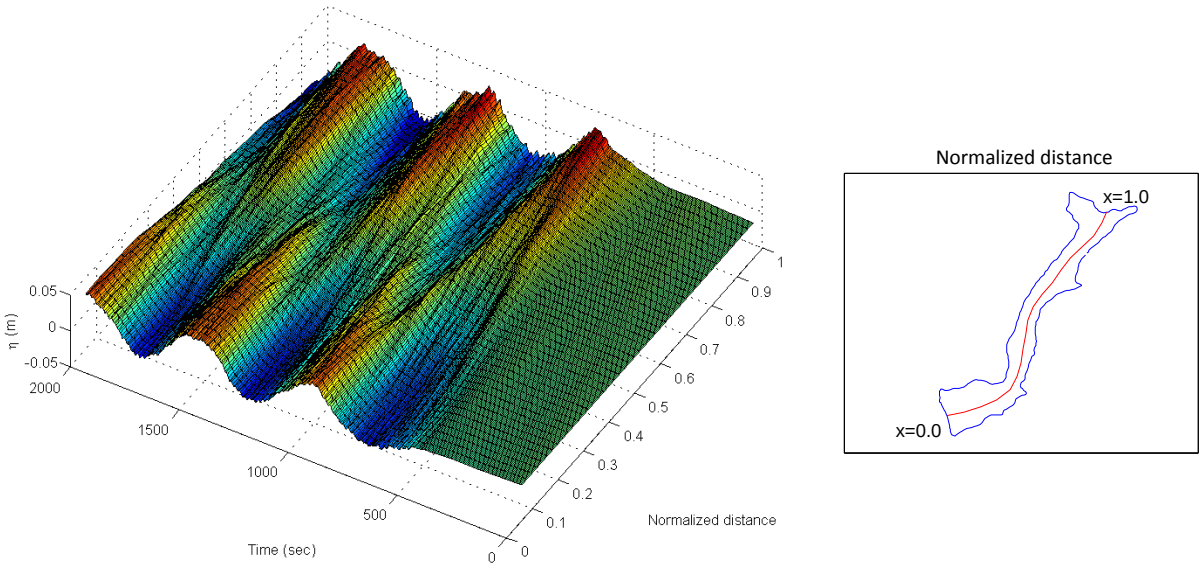

Figure 6.15 Simulated reservoir oscillation along reservoir centreline for Storm 1, 19th Feb. Water elevation 183m ASL

Comparisons of the frequency distribution of the free surface oscillation estimated by the numerical model and the distribution measured during the field campaign are presented in Figure 6.16. The frequency distribution of the field data was recorded over a 17 minute period at 14:00-14:17 on the 19th of February, one hour after the storm had travelled across the reservoir. The figure shows that the model predicts well the frequency distribution of the reservoir response. The peaks in the field data and the numerical model both coincide with the first mode, with higher energy content at locations A and C, with location C being slightly higher. The lack of a significant peak at location B suggests the position is very close to the nodal point of the first mode. The numerical model also predicts well the presence of the second mode at location B and a slight contribution of the second mode at position C, although the field data presents a broadening of the frequency distribution around the second node and not a peak as the numerical simulation suggests. The field data also presents a response of the fourth mode at position C (T_4=121 sec), which is not predicted in the numerical solution. Higher frequency peaks are also present in the field data that are not predicted in the model.

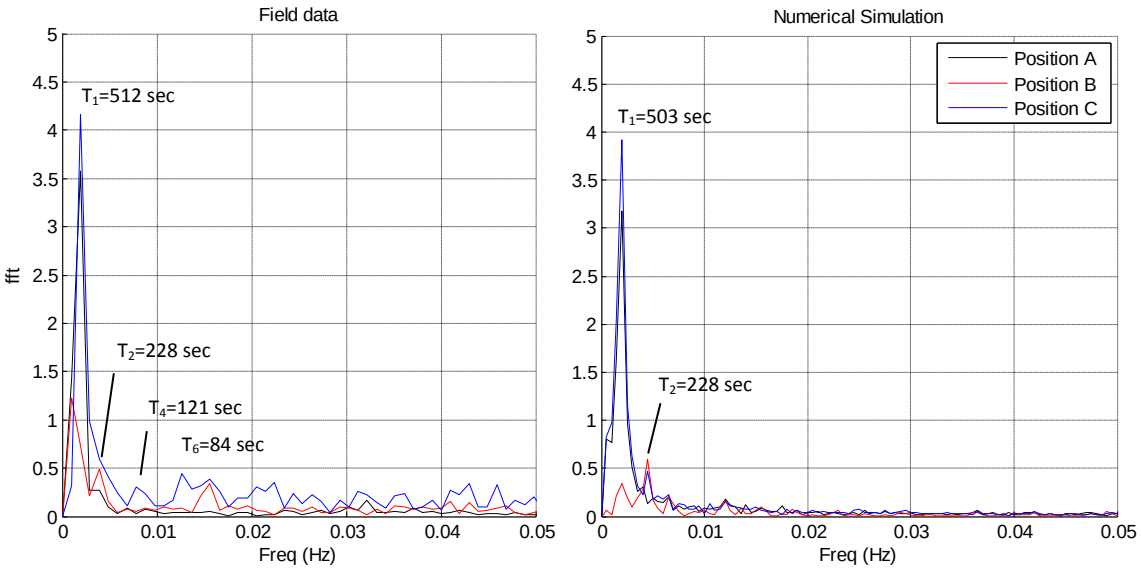

Figure 6.16 Comparison of frequency distribution of field data (14:00, 19th Feb) with numerical simulation of Storm 1, 19th Feb.

The differences between the field data and the numerical solution at position C may be due to changes in the local bathymetry at the northern end of the reservoir due to the earthworks works in the area and also due to non-linear effects not considered in the numerical solution. Further analysis of the frequency distribution estimated by the numerical model, within the northern zone of the reservoir, is presented in Figure 6.17 which examines the frequency content of additional nodal points within the Ízbor and Guadalfeo valleys, as indicated in the sub-plot. For comparison, the simulated frequency distribution at location C (red) is also included. The figure indicates three clear peaks in the frequency distribution which match the first, second and fourth modes of the predicted eigenvalue modal frequencies. Therefore, although the numerical solution does not predict that the fourth mode occurs at location C, it does successfully predict the excitation of the fourth mode within the two valleys. The nodal point within Guadalfeo Valley (black) also demonstrates a higher order frequency of 55 sec.

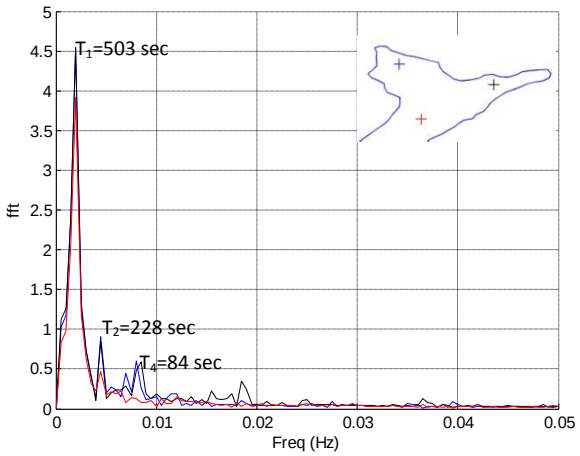

Figure 6.17 FFT analysis of the simulated water free surface at three nodal points at the northern end of the reservoir. Storm 1, 19th Feb. Water elevation 183m a.s.l.

In order to determine the separate contributions of the wind shear and the atmospheric pressure, simulations of the reservoir response are performed with each forcing term analysed separately. Figure 6.18 presents the water free surface elevation estimated at the three locations (A, B and C) due to (a) the wind shear stress; and (b) the atmospheric pressure components. The figure illustrates that the wind shear component is clearly the dominating the forcing component. The large deviations recorded in the barometric pressure are not sufficient to force the water surface into oscillating, but do create high frequency agitations in the form of surface waves. Large gradients are observed during the two minutes of the passage of the storm, in particular at Station A, but only for instantaneous pulses. It is believed that these instantaneous pressure pulsations were significant enough to create travelling waves across the reservoir, but do not contribute in the formation of the reservoir oscillation.

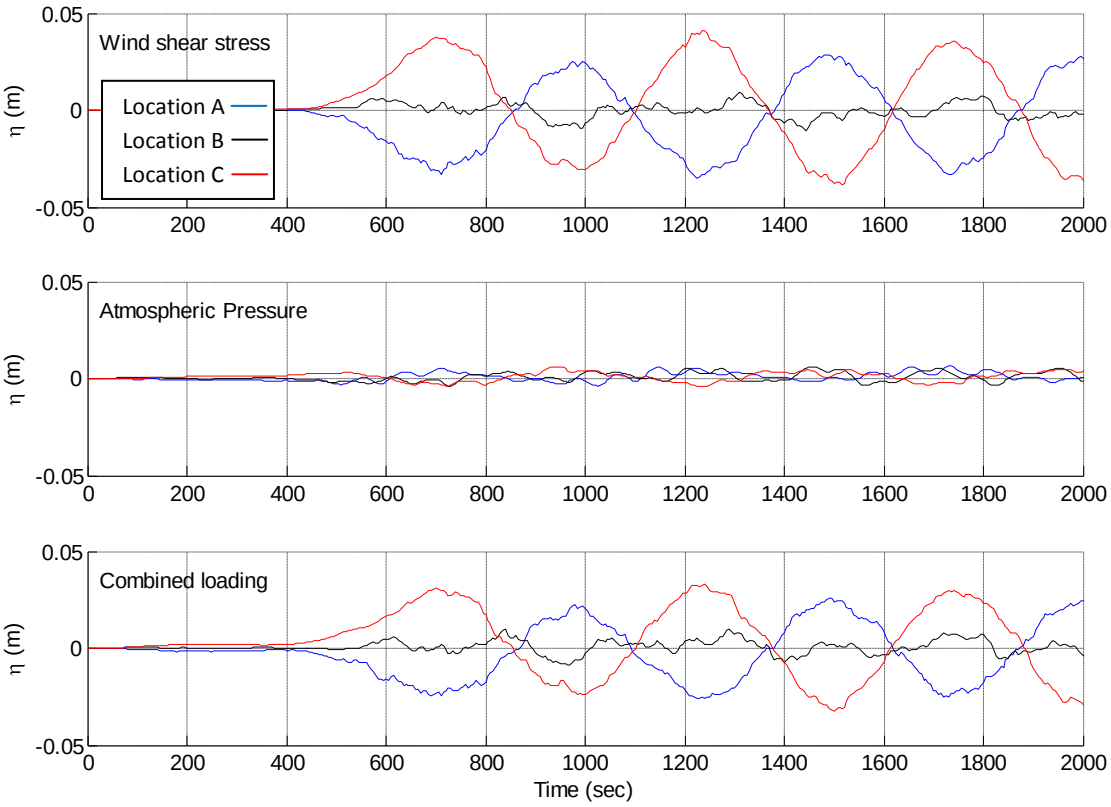

Figure 6.18 Numerical model simulation of free surface elevation after the passing of Storm 1, Feb 19th for water depth of 183m (a) Wind shear contribution; (b) Atmospheric Pressure contribution; and (c) Combined loading. Water elevation 183m ASL

6.3.2.2 Water elevation 213m ASL

The response of the reservoir with an increased water elevation of 213m ASL is presented for the same storm event. Figure 6.19 presents the simulated atmospheric forcing, with the free surface response calculated at locations A, B, and C. For this water elevation, the free surface response contains greater high frequency oscillations in comparison with the simulation of the current water level of 183m. Of the three points, the amplitude of the oscillation is largest at Location A, with an oscillation of roughly 0.02m. As shown in Appendix B, the first mode of the reservoir with a water elevation of 213m ASL responds with a single node point located roughly midway between Locations B and C. This is represented in the response pattern, with the oscillation at Locations B and C having a dis-phase of 180 degrees, but with similar amplitudes of 0.005m.

Snapshots of the water surface response at two instances in time (T=900 sec and T=1150sec) are presented in Figure 6.20, which represent the instances of greatest free surface displacement at the southern and northern ends of the reservoir respectively. Likewise, Figure 6.21 presents the time varying free surface oscillation along the centreline of the reservoir (The main southern branch and the Guadalfeo Valley). The figures illustrate that the response is not as smooth as the free surface oscillations for a water elevation of 183m, because in this case the higher modes are contributing much more energy to the response. This is due to the increased complexity of the reservoir bathymetry, with much greater interaction occurring between the oscillations entering and exiting the valleys Ízbor and Guadalfeo.

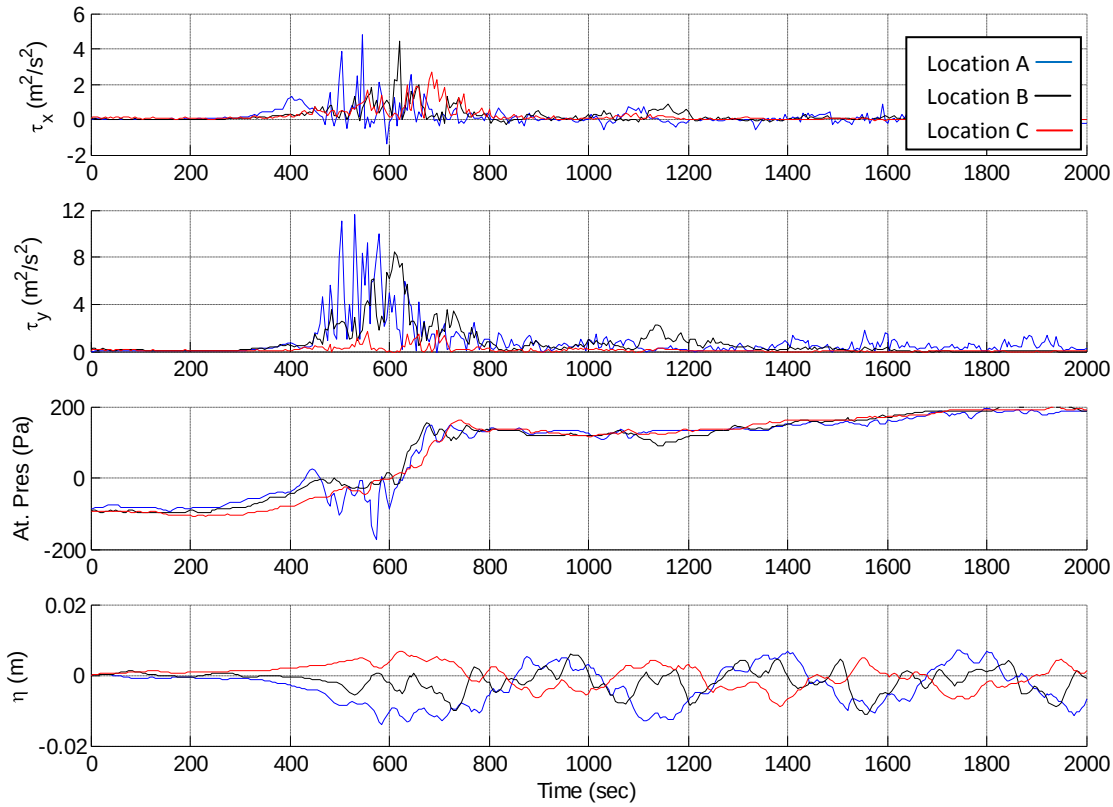

Figure 6.19 Numerical model simulation of free surface elevation after the passing of Storm 1, Feb 19th for water depth 213m. Free surface elevation is presented at Locations A, B and C.

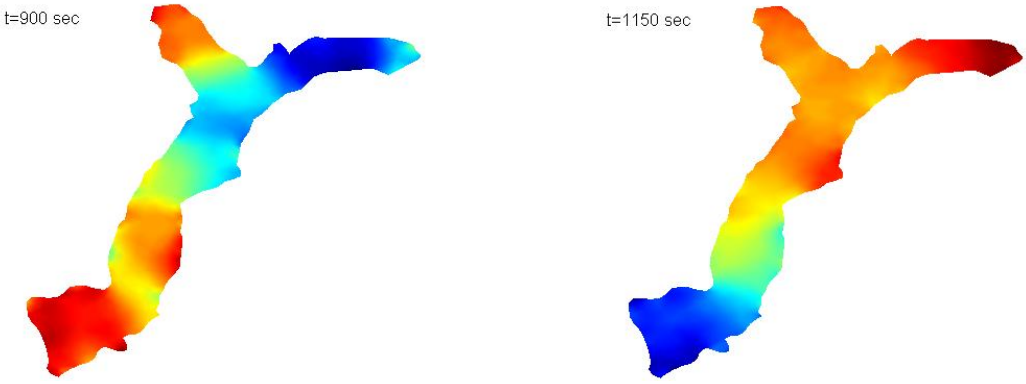

Figure 6.20 Snapshots of simulated reservoir oscillation at two instances in time for Storm event 1, 19th Feb, (a) t=900 sec and (b) t=1150 sec. Water elevation 213m ASL

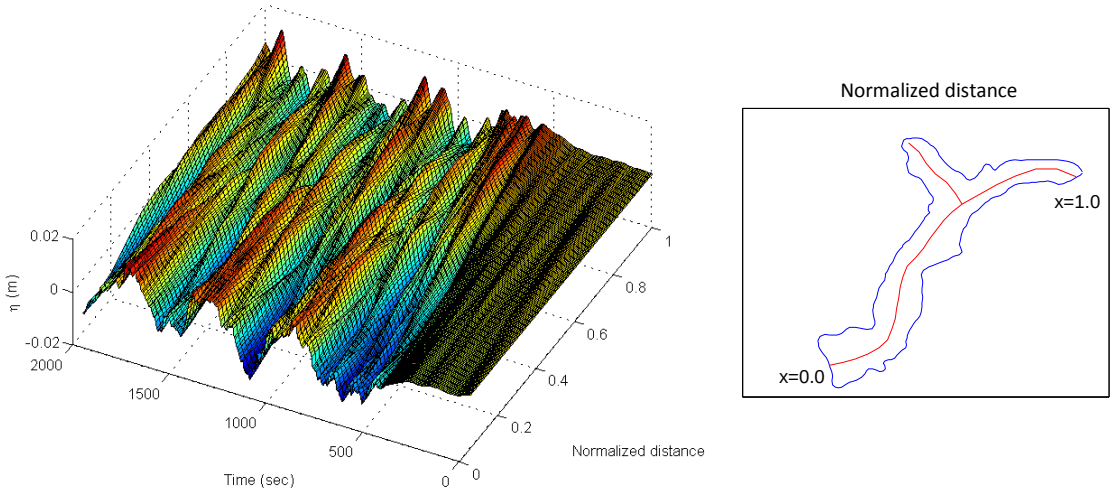

Figure 6.21 Simulated reservoir free surface oscillation along the main branch of the reservoir for Storm 1, 19th Feb. Water elevation 213m ASL

Further analysis of the free surface elevations within the two northern valleys (and their frequency distributions) help to clarify the free surface response to the passing of the storm. Figure 6.22 presents the free surface elevation and the frequency distribution of the water free surface at a number of locations within the three branches of the reservoir (a) the southern branch; (b) Ízbor valley; and (c) Guadalfeo valley. The locations of the nodal points are indicated in the sub-plot.

The figure shows the free surface oscillation in the Guadalfeo and Ízbor valleys are dominated by the first mode and have a dis-phase of 180 degrees with respect to the oscillation at Location A, at the southern end of the reservoir. This shows the oscillation of the reservoir is still dominated by the first mode (See Appendix B). The amplitude of the seiche in the Guadalfeo valley (0.02m) is slightly larger than in the Ízbor valley (0.015m) as the Guadalfeo valley has a shallower bathymetry. Overall, the oscillation of the reservoir free surface for the water elevation of 213m (0.02m) is less than the observed oscillation for the current water elevation of 183m (0.05m).

The frequency distributions of the free surface, at the same locations, are also presented in the figure (bottom right). The spectral analysis shows all points are dominated by the contribution of the first mode, with a period of 402 sec. The second mode of 228 seconds is also present, but represented by a broad peak, while the third mode (168 sec) contributes very little energy input into the response. The fourth and fifth modes, however, are shown to contribute significantly to the response, with periods of 118 and 105 seconds, respectively. Further peaks are also present in the main branch of the reservoir, corresponding with the tenth and eleventh modes, with periods of 52 seconds and 47 seconds.

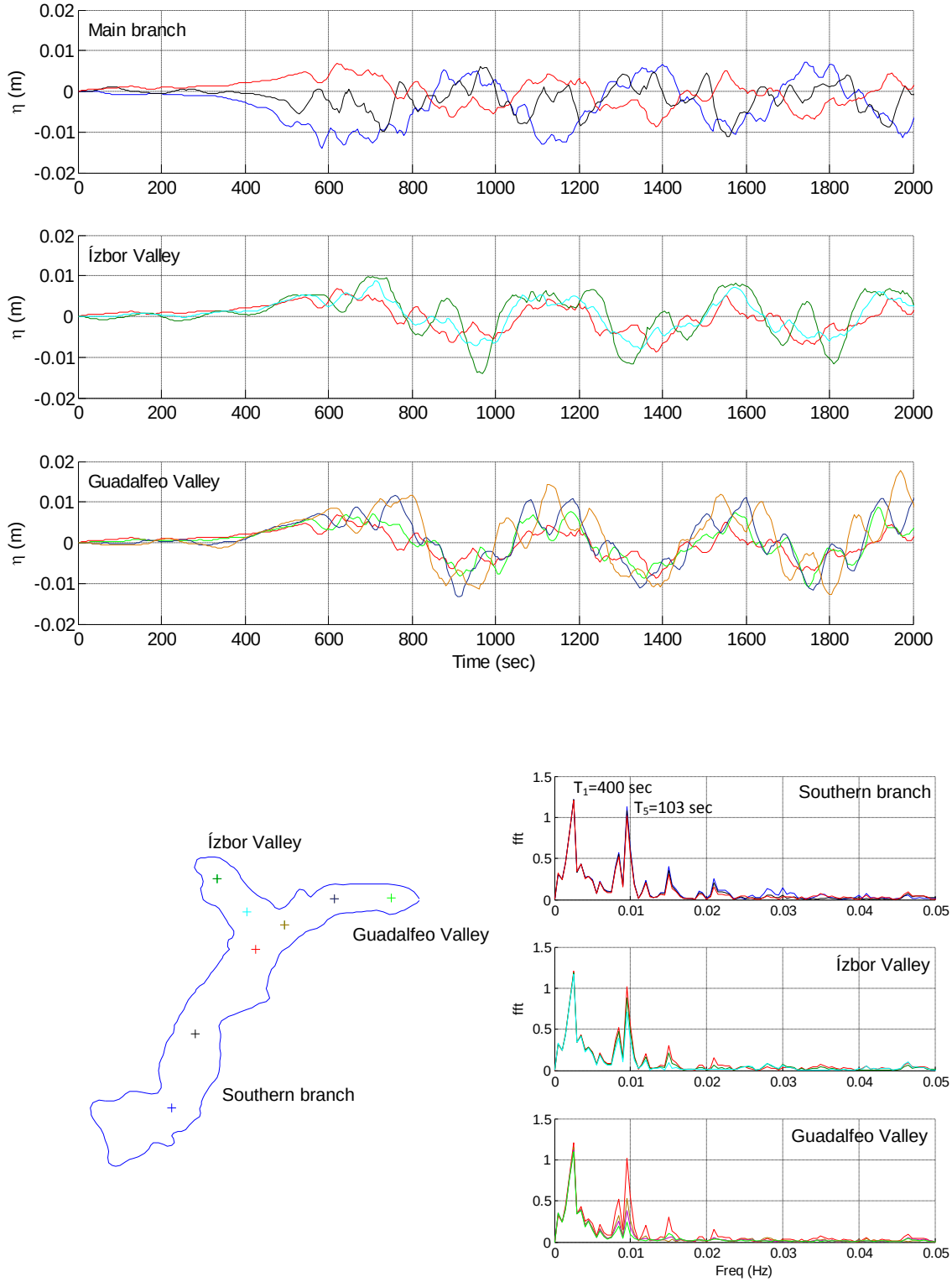

Figure 6.22 Numerical model simulation of free surface elevation after the passing of Storm 1, Feb 19th for water elevation 213m (a) Main reservoir branch (Locations A, B and C); (b) Ízbor Valley; and (c) Guadalfeo Valley. (Bottom left) Location of analyzed nodal points. (Bottom Right) Frequency distribution of free surface oscillation

6.3.2.3 Water elevation 243m ASL

The predicted free surface response for the reservoir at full capacity is also presented. The observed response for the atmospheric loading is very different from the response predicted for a uniform wind loading, presented in Chapter 6.3.1. Figure 6.23 presents the temporal variation of the atmospheric forcing and the free surface response along the southern branch of the reservoir (Locations A, B and C). The figure shows the reservoir does not oscillate in any of its lower eigenmodes as the storm passes across the reservoir with no clear oscillation within the southern branch.

Snapshots of the water surface response at two instances in time (T=1250 sec and T=1500sec) are presented in Figure 6.24. The figures demonstrate that the water is displaced in localized oscillations within the branches of the reservoir, with higher order modes dominating the response in the Guadalfeo Valley.

Figure 6.25 illustrates the time varying free surface response along the centreline of the reservoir. Due to the complexity of the bathymetry at this water depth, two figures are presented where Figure 6.25(a) represents the free surface displacement between the dam structure (x=0.0) and the end of the Guadalfeo Valley (x=1.0), while Figure 6.25(b) represents is the free surface displacement between the end of the Ízbor Valley (x=0.0) and the end of the Guadalfeo Valley (x=1.0). The figures illustrate that the response is not as smooth as the free surface oscillations for the lower water elevations, because in this case the higher modes are contributing much more energy to the response.

The free surface elevations within the two northern valleys and their frequency distributions help to clarify the free surface response to the passing of the storm. Figure 6.26 presents the free surface elevation and the frequency distribution of the water free surface at a number of locations within the three branches of the reservoir (a) the southern branch; (b) Ízbor valley; and (c) Guadalfeo valley. The locations of the nodal points are indicated in the sub-plot.

The figure shows the free surface oscillations in all branches of the reservoir are very choppy, with no clear eigenmodes dominating the response. The frequency distributions of the free surface, at the same locations, are presented in the figure (bottom right). The fft analysis shows the response is due to energy contributions from a number of modes, with similar contributions up until the eleventh mode. The peaks coincide with the 1^{st}, 3^{rd}, 7^{th}, 10^{th} and 11^{th} eigenmodes. A further peak at 0.03Hz (35 seconds) is also present, which matches the high frequency component observed in the atmospheric forcing. This high frequency component is believed to be due to flow separation off the dam structure, which is shown to promote higher order oscillations throughout the entire length of the reservoir.

The simulation for the measured storm event, for all three water depths, presents a clear divergence in the free surface response in comparison to the simulation due to a uniform loading. The response of the reservoir to uniform loading is dominated by the low eigenmode frequencies, while, the response due to a realistic atmospheric forcing is a combination of many modes, with contributions up to the 11^{th} mode.

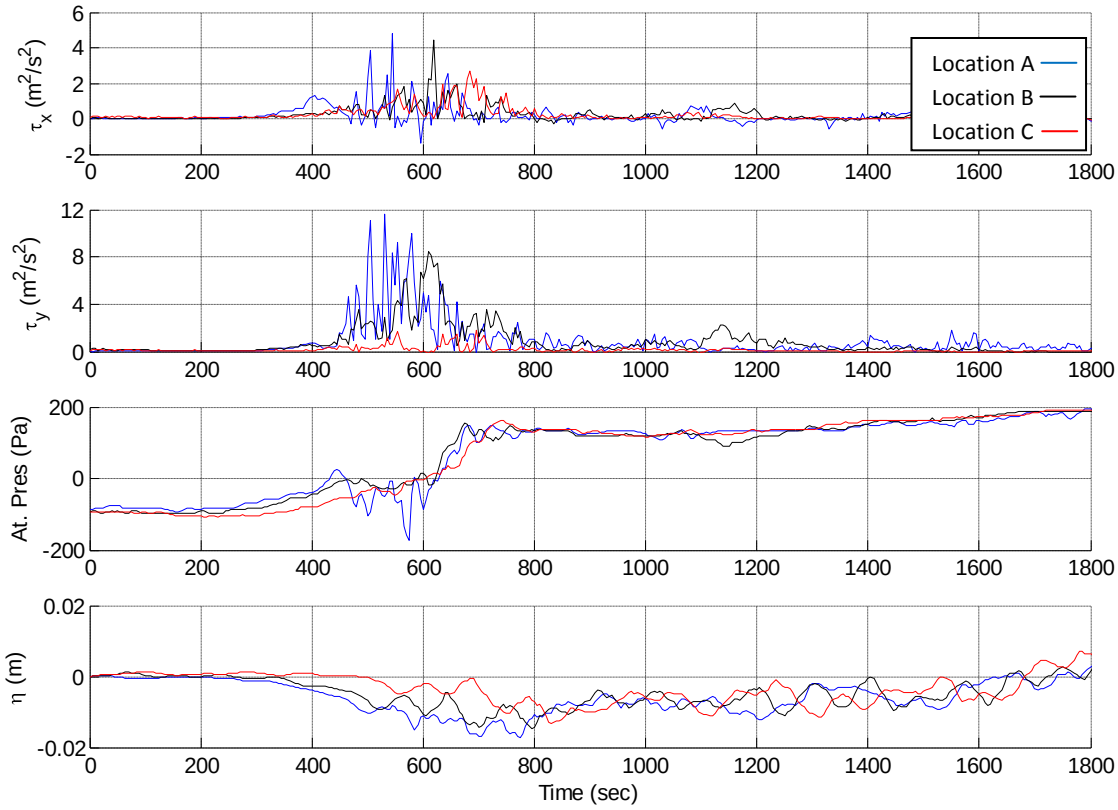

Figure 6.23 Numerical model simulation of free surface elevation after the passing of Storm 1, Feb 19th for water depth 243m. Free surface elevation is presented at Locations A, B and C.

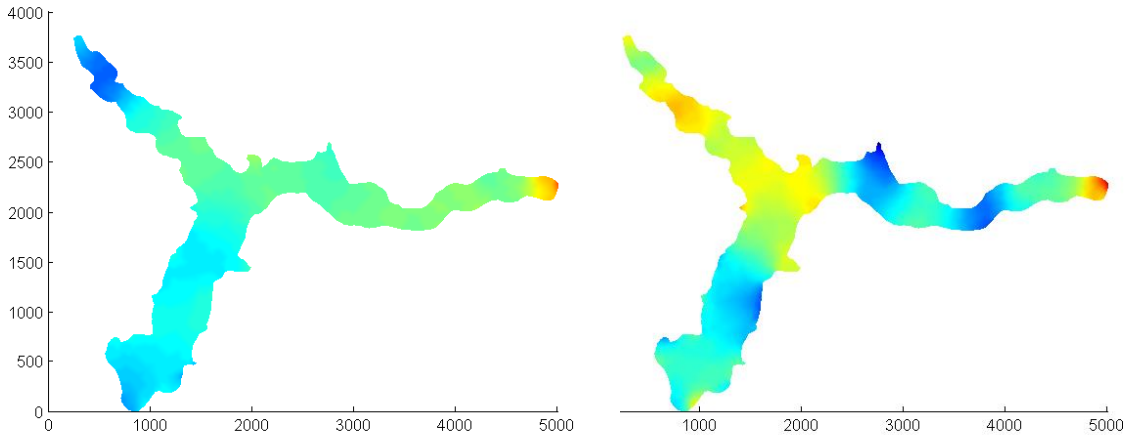

Figure 6.24 Snapshots of simulated reservoir oscillation at two instances in time for Storm event 1, 19th Feb, (a) t=1250 sec and (b) t=1500 sec. Water elevation 243m ASL

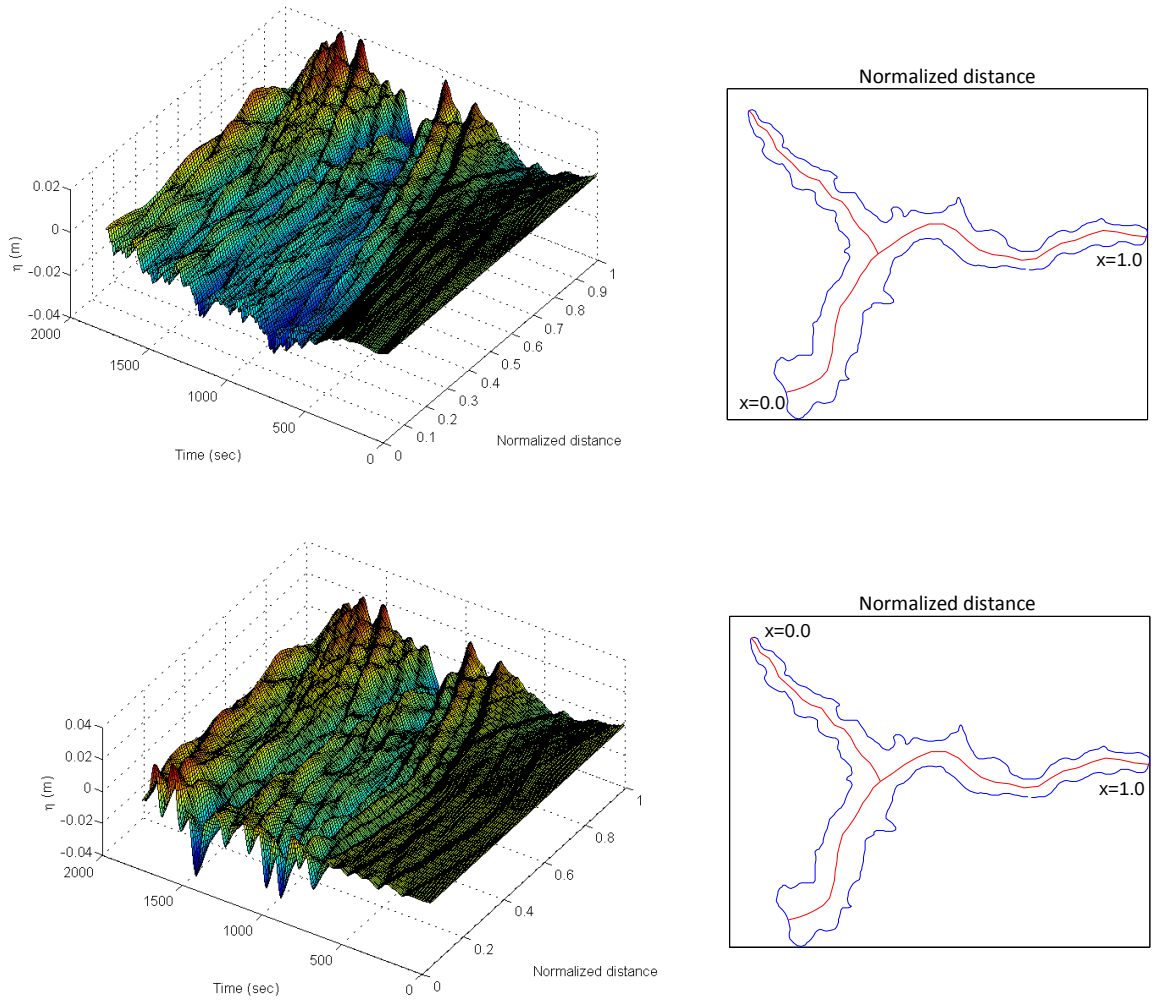

Figure 6.25 Simulated reservoir free surface oscillation along the main branch of the reservoir for Storm 1, 19th Feb. Water elevation 243m ASL

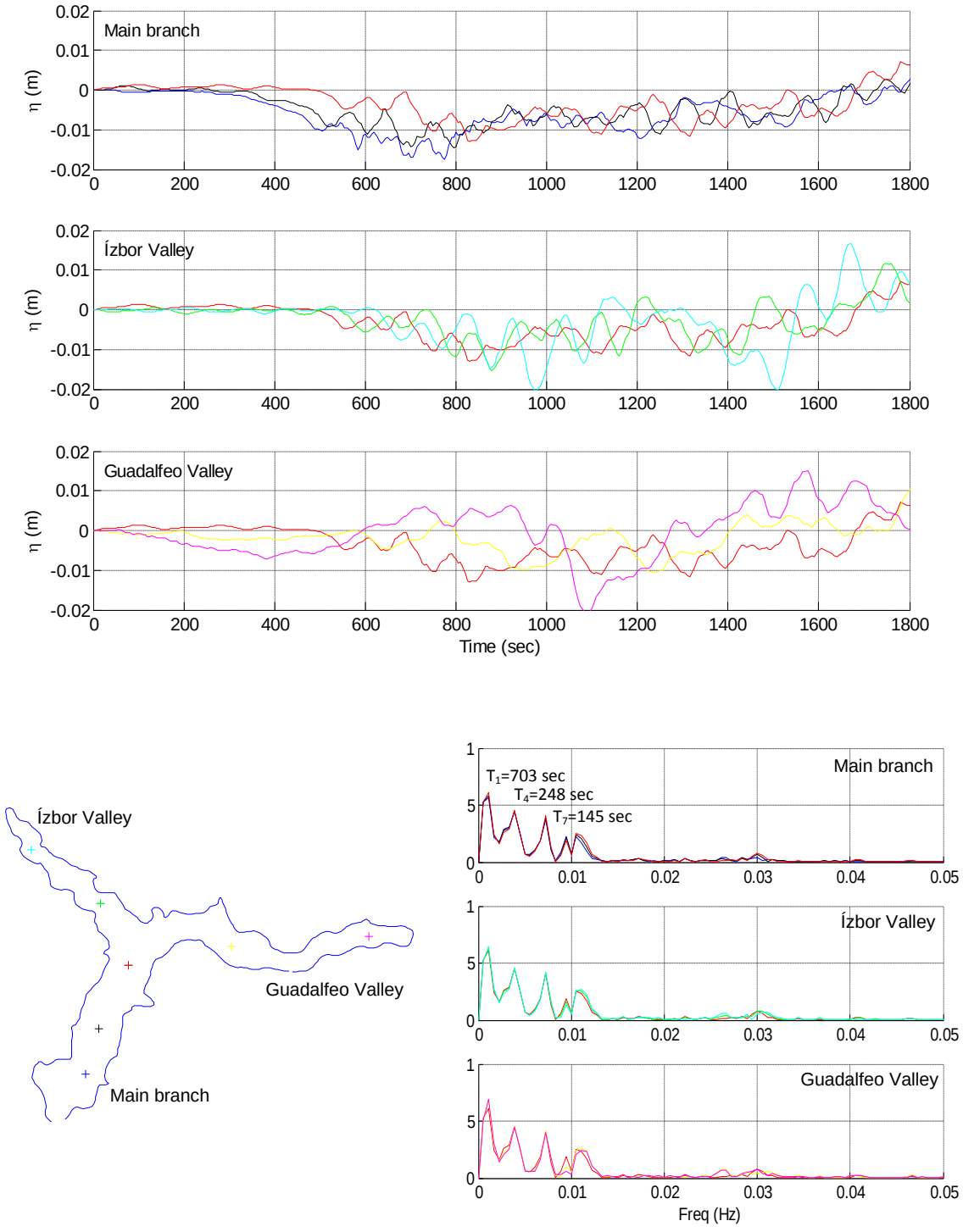

Figure 6.26 Numerical model simulation of free surface elevation after the passing of Storm 1, Feb 19th for water elevation 243m (a) Main reservoir branch (Locations A, B and C); (b) Ízbor Valley; and (c) Guadalfeo Valley. (Bottom left) Location of analyzed nodal points. (Bottom Right) Frequency distribution of free surface oscillation.

6.3.3 Simulation of measured Storm 2, 23rd Feb

The second storm event simulated by the numerical model occurred at 01:00 on the 23rd of February. As discussed in Chapter 4.5, field measurements at the reservoir showed the free surface began to oscillate in its first mode, with amplitude 0.02m. Although the magnitude of the wind velocity was not significant (<9 m/s), it contained a harmonic component with a frequency of around 500 seconds, which matches the first eigenmode frequency.

The simulated atmospheric forcing is extracted from the recorded field data and applied over the entire water surface, based on the temporal and spatial loading coefficients described in Chapter 6.2. The simulation begins approximately 500 seconds before the first atmospheric pulsation and continues for a total duration of 2000 seconds, adequately capturing the free surface response of the reservoir.

6.3.3.1 Water elevation 183m ASL

The storm event is characterized, not be a significant burst of loading, but a small harmonic component of the wind shear, as illustrated in Figure 6.27. The figure shows the horizontal shear at the first anemometer location contains a small recurring component with a magnitude of approximately 1.0 – 2.0 m^2/s^2 and a frequency in the order of 500 seconds. Although the magnitude of the loading is not significant, the period of the loading matches the period of the reservoir first mode and is enough to generate a surface seiche of 0.015m over the entire water body. As illustrated in the figure, the numerical model is able to successfully simulate the oscillation of the reservoir free surface, with the final amplitude equal to the seiche measured in the field (See Chapter 4.3.3). The simulation shows the growth of the free surface oscillations with each successive load pulsation, demonstating that the frequency component of the atmospheric forcing is equally as important as the magnitude of the forcing.

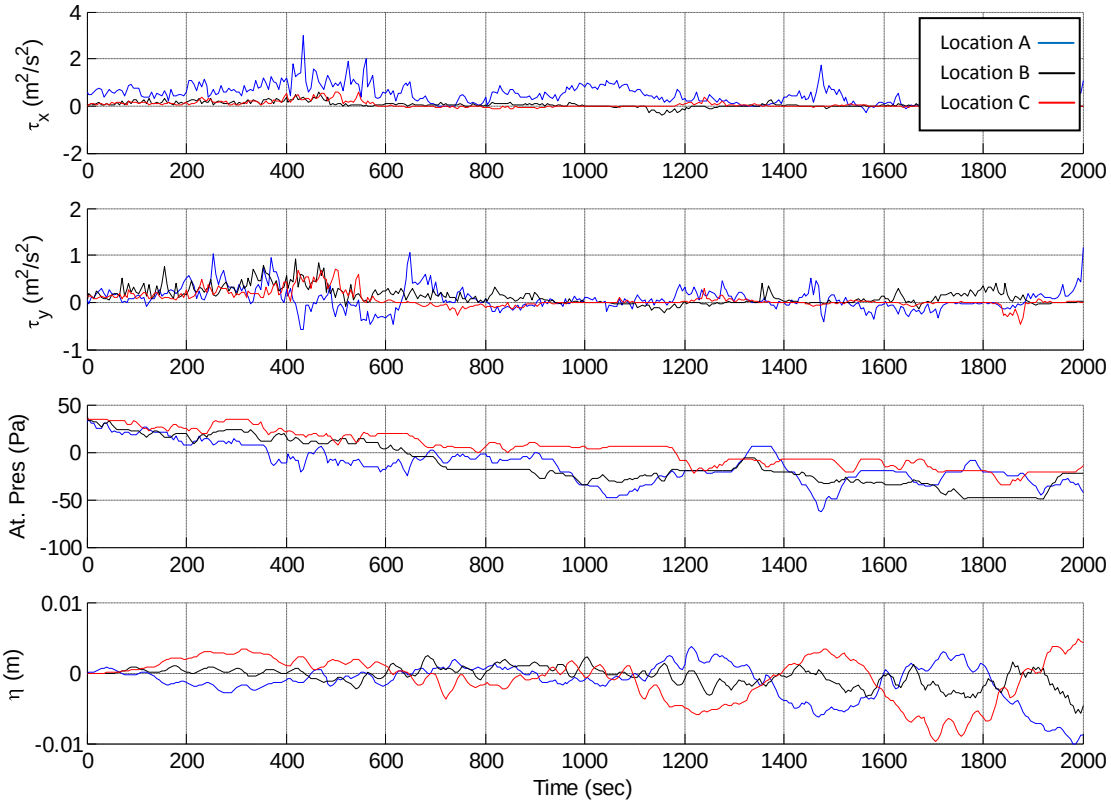

Figure 6.27 Numerical model simulation of free surface response after the passing of Storm 2, Feb 23rd. (a) x-component wind shear loading; (b) y-component wind shear loading; (c) Atmospheric Pressure loading; (d) Free surface response simulated by the model. All information is presented for Locations A, B and C. Water elevation 183m a.s.l.

Figure 6.28 presents the free surface response along the centreline of the reservoir. The figure illustrates the surface seiche beginning to form after 750 seconds when the pulsation in loading occurs. The figure also shows a large quantity of high-frequency undulations in the response. This is from the loading pattern during the first 500 seconds of the simulation, where the atmospheric forcing is gusty and random. The gusts produce a series of waves that begin travelling to the far end of the reservoir which are then reflected back, creating a choppy water surface. This is reflected in the frequency distribution of the free surface (Figure 6.29), where there is a small peak in the frequency component of 50 seconds (0.02 Hz).

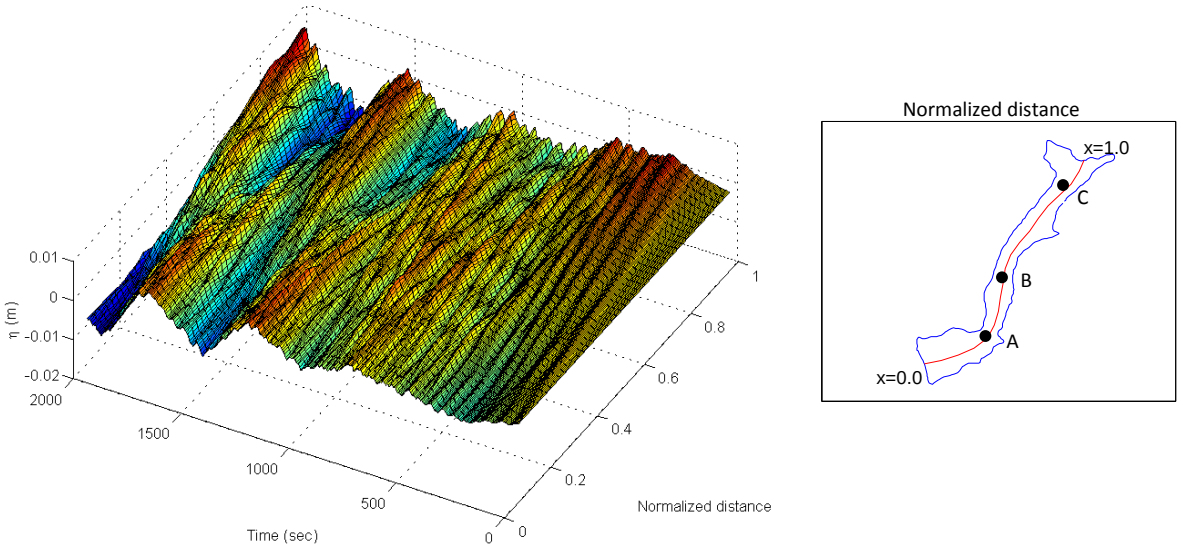

Figure 6.28 Simulated reservoir oscillation along reservoir centreline for Storm 2, 23rd Feb. Water depth 183m ASL

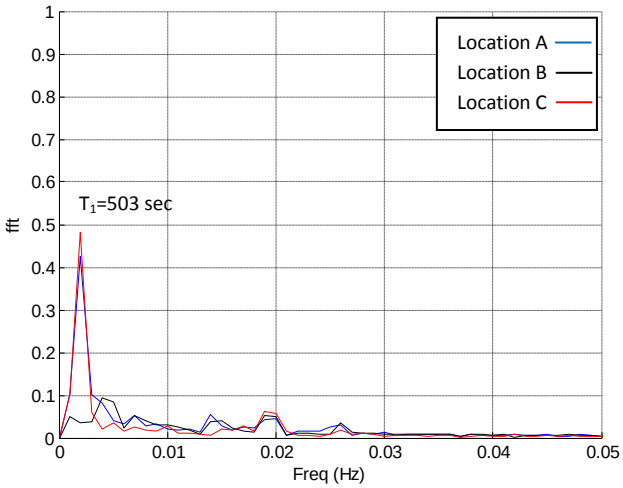

Figure 6.29 Frequency distribution of simulated free surface response to Storm event 2, 23rd of Feb. Locations of analysed points are indicated in the previous figure. Water elevation 183m ASL

6.3.3.2 Water elevation 213m ASL

For the same atmospheric forcing, the simulated response of the reservoir for the intermediate water elevation of 213m ASL is presented in Figure 6.30. As with the response at the current water elevation, the reservoir begins to oscillate after 750 seconds, which coincides with the end of the first loading pulsation. The amplitude of the seiche clearly increases with each successive load pulsation. Unlike the response to the first storm, the reservoir oscillates predominantly in the first mode, as illustrated in Figure 6.31, which presents the free surface oscillation along the centreline of the reservoir. The figure clearly illustrates that the growth of the surface seiche is due to the harmonic pulsations of the

atmospheric forcing. The magnitude of the final oscillation (0.015m) is also greater than the oscillations with the reservoir at its current water depth (0.01m).

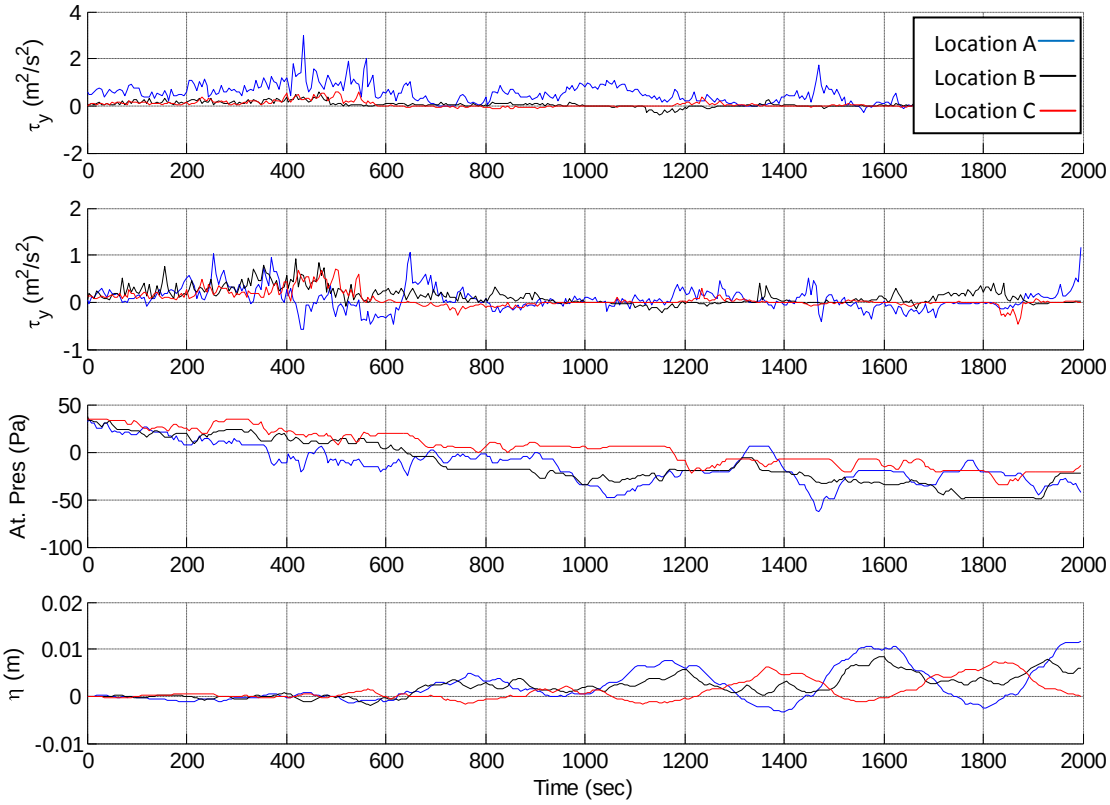

Figure 6.30 Numerical model simulation of free surface elevation after the passing of Storm 2, Feb 23rd for water elevation 213m. Free surface elevation is presented at Locations A, B and C.

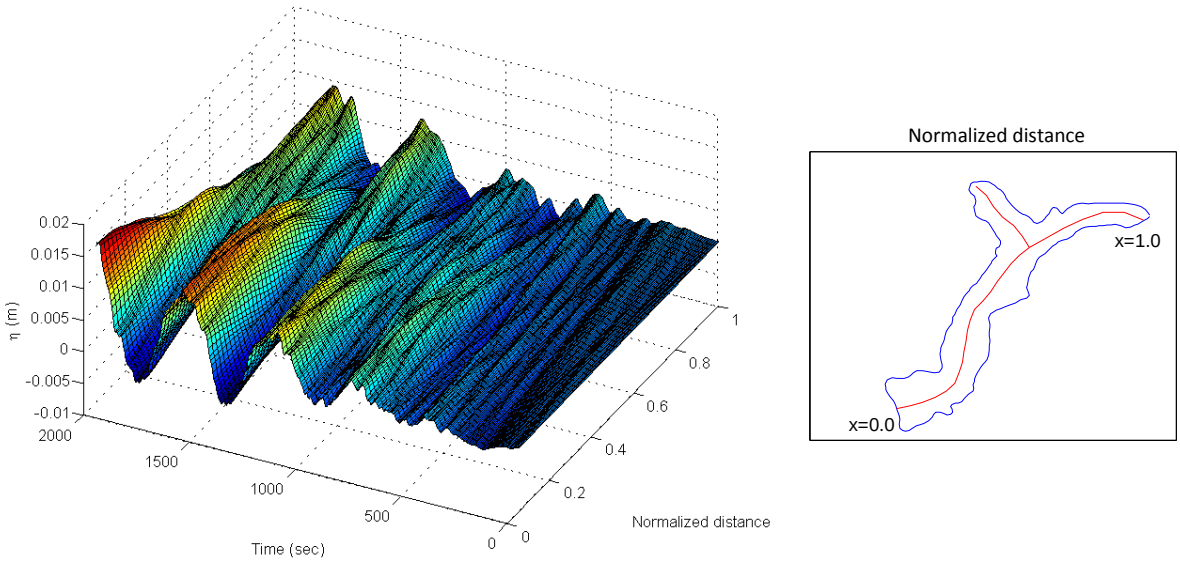

Figure 6.31 Simulated reservoir free surface oscillation along the main branch of the reservoir for Storm 2, 23rd Feb. Water elevation 213m ASL

Figure 6.32 presents the simulated oscillations at additional node points within the Ízbor and Guadalfeo valleys, along with their associated frequency distributions. The figure shows the response is dominated by the first mode, with additional energy contributions from the fourth and fifth modes. Within the Gaudalfeo Valley the energy contributions from the fourth and fifth modes disappears, producing a much smoother oscillating pattern.

Although the response of the reservoir at this water level cannot be verified through field measurements, it appears that the numerical model can be successfully extended to different reservoir water depths. That said, the results from the two storm simulations for the water elevation of 213m show that, even though the magnitude of the atmospheric forcing for the second storm event is much less than the first storm, the amplitude of the resulting seiche is similar, albiet with a very different distribution of modal energy contributions. The harmonic atmospheric forcing recorded during the second storm event did not extend beyond the time simulated with the numerical model and the oscillations slowly decayed, however, Figure 6.31 illustrates that the magnitude of the surface seiche will clearly continue to increase if atmospheric loading were to continue pulsating.

It also appears that the greater water depth aids in dampening out the higher frequency oscillations. In comparison with the results from the water elevation of 183m, the response of the reservoir for a water elevation of 213m does not contain the high frequency (50 sec) component.

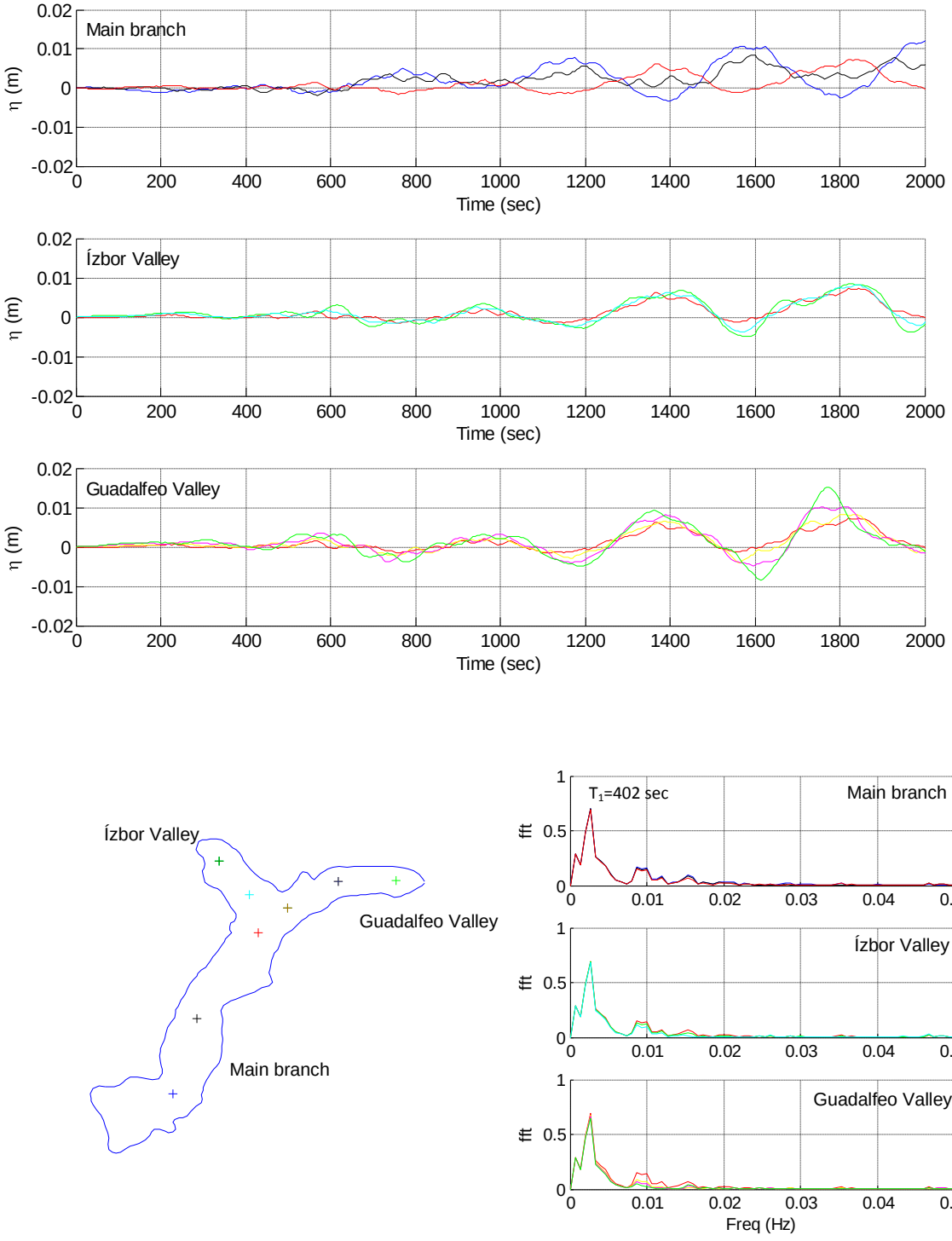

Figure 6.32 Numerical model simulation of free surface elevation after the passing of Storm 2, Feb 23rd for water depth 213m (a) Main reservoir branch (Locations A, B and C); (b) Ízbor Valley; and (c) Guadalfeo Valley. (Bottom left) Location of analyzed nodal points. (Bottom Right) Frequency distribution of free surface oscillation

6.3.3.3 Water elevation 243m ASL

As shown in Figure 6.33, for the reservoir at full capacity, the harmonic frequency in the atmospheric forcing no longer matches the first eigenmode frequency of the reservoir, equal to 703 seconds (See Appendix B). Therefore, the forcing does not induce a surface seiche over the entire reservoir. However, the harmonics of the atmospheric forcing is closer to the third eigenmode frequency, creating a surface seiche confined within the Ízbor valley, with little energy transferred through to the southern valley. The magnitude of the oscillation within the Ízbor valley is approximately 0.015m and appears to be increasing with each successive pulsation of the atmospheric forcing.

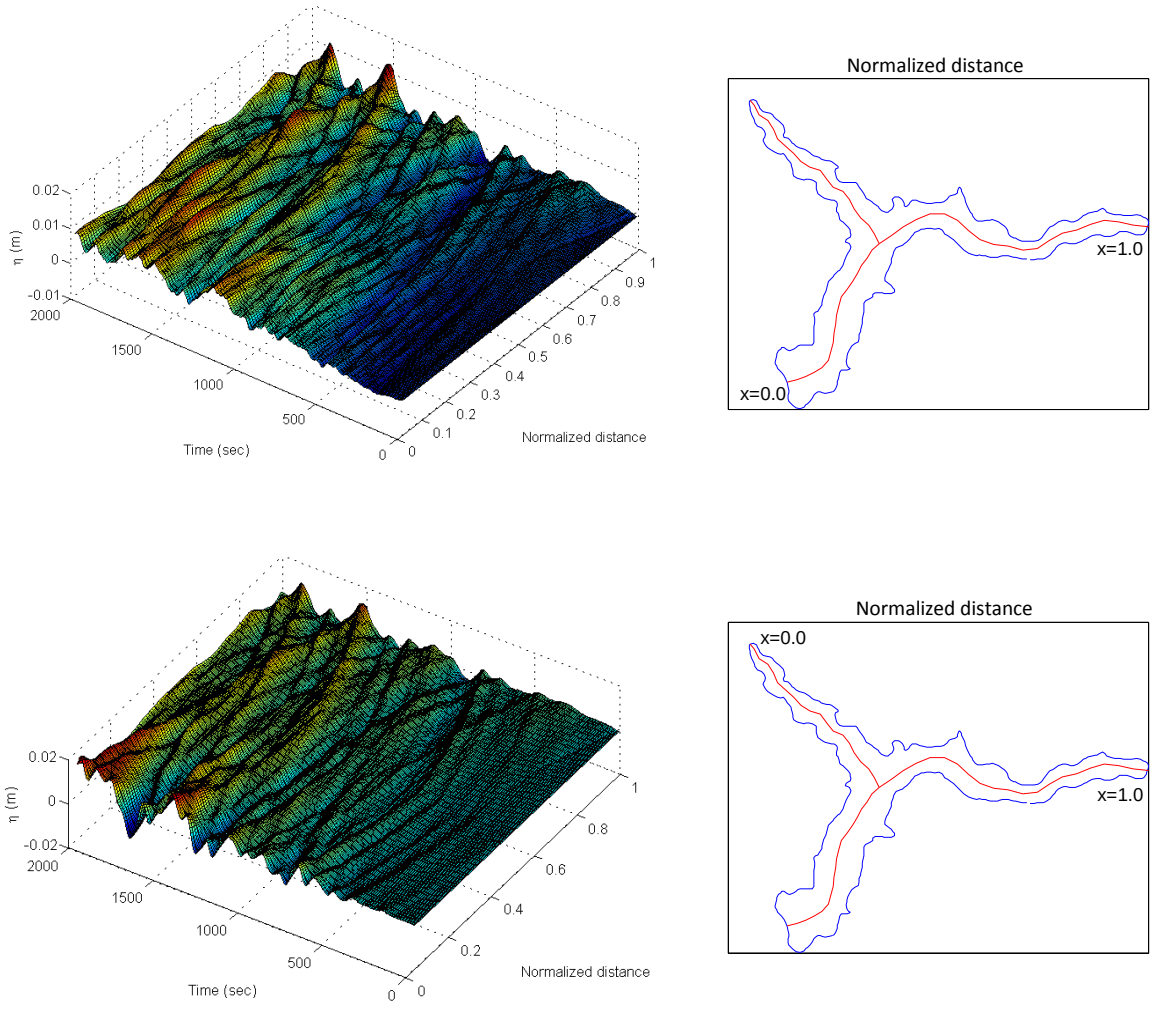

Figure 6.33 Simulated reservoir free surface oscillation along the main branch of the reservoir for Storm 2, 23rd Feb. Water elevation 243m ASL

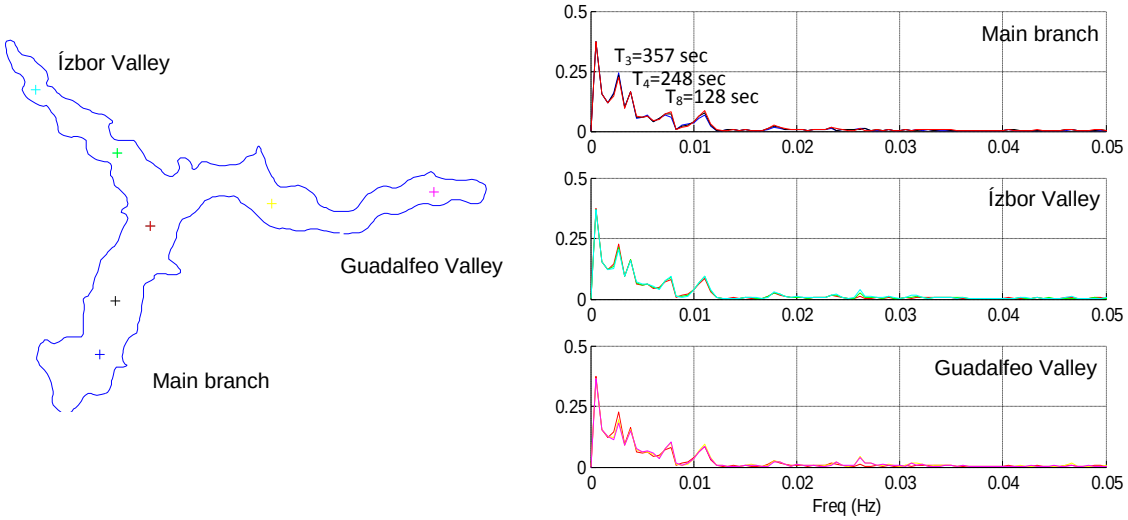

Figure 6.34 Frequency distribution of simulated free surface elevation after the passing of Storm 2, Feb 23rd for water depth 243m (a) Main reservoir branch (Locations A, B and C); (b) Ízbor Valley; and (c) Guadalfeo Valley.

Figure 6.34 shows the frequency distribution of the simulated free surface response to the storm event. In this case, the energy distribution is concentrated in the third mode, along with contributions from the 4th and 8th modes, with some additional contribution from the higher modes. The frequency distribution of this storm event is markedly different from the first simulated storm event with the reservoir at full capacity. In this case, the 3rd mode is excited as it is in the range of the atmospheric forcing frequency, as with the 4th and 8th modes, which are the super-harmonics of the forcing.

Therefore, the frequency of the atmospheric forcing can not only generate the free surface oscillations in modes with the same period as the atmosopheric forcing, but also promotes the response due to higher order modes, which also contribute significantly to the response of the free surface.

Table 6.2 summarises the maximum free surface displacements predicted by the simulations and the general locations of the maximum displacement. The table indicates that the maximum displacements are in the order of centimetres, with a maximum of 0.065m recorded after the storm which occurred on the 19th of February for the current water level. The displacement was four times greater than the maximum displacement predicted by the storm on the 23rd of February (0.013m). The maximum oscillations occurred consistently at the end of the Guadalfeo valley. The results are similar for the intermediate water level of 213m, however at full capacity the location of the maximum displacement varies with the loading type.

Table 6.2 Maximum free surface displacement for the simulated case studies

Storm event	Water depth (a.s.l.) (m)	Max. free surface displacement, η (m)	Location of max. displacement
Uniform load	183	0.037	Guadalfeo Valley
	213	0.027	Guadalfeo Valley
	243	0.053	Guadalfeo Valley
13:00, 19th Feb	183	0.065	Guadalfeo Valley
	213	0.027	Guadalfeo Valley
	243	0.047	Guadalfeo Valley
1:00, 23rd Feb	183	0.013	Guadalfeo Valley
	213	0.018	Guadalfeo Valley
	243	0.019	Ìzbor Valley

7 Conclusiones y futuras líneas de investigación

7.1 Conclusiones

Empleando medidas de campo, simulaciones en un túnel de viento de capa limite y resultados proporcionados por un modelo numérico, el presente estudio ha demostrado que fluctuaciones de alta frecuencia (< 10 min) de los agentes forzadores atmosféricos pueden inducir una excitación resonante de las oscilaciones en la superficie libre de un pequeño lago o de un embalse. Este fenómeno es particularmente relevante en el caso de lagos y embalses situados en terrenos complejos, donde los patrones de circulación del flujo se generan por efecto de diferencias térmicas locales en la atmosfera y por la separación del flujo inducida por las características topográficas. Se ha mostrado que si el periodo del forzamiento atmosférico coincide con una de las bajas frecuencias modales del embalse, se verifica una excitación resonante en la superficie libre.

Las observaciones no se limitan solo a las situaciones de terreno complejo, sino que pueden ser relevantes en pequeños lagos, embalses y dársenas de puertos ubicados en zonas urbanas, donde fenómenos de separación de flujo y armónicos de alta frecuencia se pueden generar por efecto de los edificios circundantes o de estructuras construidas por el hombre. Estudios recientes en la playa de Carchuna han demostrado como obstáculos geográficos de elevadas dimensiones pueden contribuir a reforzar las formaciones morfológicas de gran escala en la línea de costa, gracias a fenómenos de separación de flujo y generación de vórtices turbulentos en la superficie libre que se acoplan con los parámetros hidrodinámicos (Ortega-Sánchez, Bramato, Quevedo, Mans, & Losada, 2008).

Se han presentado las oscilaciones de alta frecuencia en los agentes forzadores atmosféricos (presión barométricas y esfuerzo de corte del viento) y la respuesta hidrodinámica (sobrelevación y perfiles de corriente) a partir de las medidas de campo efectuadas en un pequeño embalse situado en terreno complejo (Embalse de Rules, Granada). Las medidas de las frecuencias armónicas de los agentes atmosféricos forzadores, con periodo de 500 segundos, coinciden con el primer modo del embalse, creando una excitación resonante de las oscilaciones de la superficie libre, aunque la velocidad de viento no es elevada. Se pueden además excitar modos armónicos de más

alto orden que pueden contener contribuciones de energía más elevadas que los modos de orden inferior.

Los armónicos presentes en los agentes atmosféricos han sido además observados en correspondencia de otras frecuencias durante el periodo de estudio, en un rango entre 200-700 segundos. La superficie libre del embalse no ha mostrado respuesta en este caso, porque las frecuencias de los agentes forzadores no coinciden con ninguno de los modos de orden inferior. Sin embargo, los eventos armónicos observados pueden ser significativos cuando el nivel de agua en el embalse crece y las frecuencias modales se modifican.

La variación espacial de los agentes forzadores en la superficie libre del embalse se ha estudiado a partir de las simulaciones en un túnel de viento de capa limite. Las formaciones topográficas alrededor del embalse han sido modeladas en escala 1:3000 para una sola dirección de viento que coincide con la orientación del eje principal del embalse y la direccionalidad local del viento sobre el mismo. Las simulaciones en el túnel de viento han demostrados ser una útil herramienta para la comprensión de los patrones complejos de flujo que se verifican en la capa limite atmosférica sobre el embalse y para obtener un mapa detallado de las variaciones espaciales de los forzamientos atmosféricos en la superficie de agua en condiciones de vientos sinópticos. Siempre más frecuentemente se emplean simulaciones computacionales en tres dimensiones para definir completamente la circulación de los patrones de agua dentro de embalses y en pequeños lagos. Sin embargo, su resolución es limitada a causa de la resolución espacial de los términos de forzamientos, entre otros parámetros. Las simulaciones en el túnel de viento podrían ser en este sentido, una herramienta fundamental para desarrollar, con elevada resolución espacial, las condiciones atmosféricas forzadoras (velocidad de viento y presión barométrica) sobre la superficie de agua del embalse y emplearlas como condiciones de entrada en los modelos computacionales.

La respuesta de la superficie libre de agua a los agentes forzadores se ha estudiado empleando un modelo numérico hidrodinámico en dos dimensiones desarrollado a partir de las ecuaciones lineales de agua somera integradas en profundidad. Las medidas de campo y las simulaciones en el túnel de viento se han combinado para proporcionar un mapa detallado de alta resolución espacial y temporal de la variabilidad de los parámetros atmosféricos, que se ha empleado como condiciones de entrada en el modelo numérico. El modelo predice bien las oscilaciones de la superficie medidas durante la campaña de campo. El modelo muestra como modos armónicos de alto orden pueden ser excitados por las componentes de alta frecuencia en los agentes forzadores, generando oscilaciones de la superficie libre que son diferentes con respectos a las condiciones de carga uniforme. El modelo es capaz de predecir no solo cuál es el modo dominante en el embalse sino también dónde se verifica el máximo desplazamiento vertical. Además se ha simulado numéricamente la respuesta del embalse con profundidades más elevadas bajo el mismo forzamiento atmosférico, para predecir su comportamiento en condiciones de llenado total e intermedio. El modelo puede predecir la respuesta futura de la superficie libre del embalse en condiciones

atmosféricas forzadoras reales y cuáles son los modos dominantes en la respuesta de la superficie libre.

Las conclusiones del estudio pueden ayudar en la futura gestión de embalses y pequeños lagos. En particular en el caso de embalses, donde la calidad de agua es el factor más importante, considerando que el agua se emplea generalmente para uso público y para la irrigación de los cultivos. Durante el verano, el calentamiento solar de la capa superficial de agua crea una elevada termoclina, y una fuerte estratificación en la vertical. Este proceso separa las capas más superficiales desde el volumen de agua en profundidad, reduciendo los procesos de mezcla en profundidades más elevadas y deteriorando la calidad de agua en los niveles inferiores. La reducción de la concentración del oxigeno disuelto puede asimismo generar condiciones de hipoxias y de proliferación de bacterias. Solo durante condiciones forzadoras atmosféricas significativas los procesos de mezcla que derivan pueden anular tal estratificación. Sin embargo, si el embalse es forzado por eventos de vientos menos intensos pero más frecuentes, tal estratificación no tiene tiempo de desarrollarse completamente. Entonces, la recurrencia regular de oscilaciones superficiales puede promover la mezcla a lo largo de toda la columna de agua, incrementando la concentración de oxigeno disuelto y la calidad de agua.

Para una buena operatividad del embalse, es importante la evaluación del volumen de sedimento atrapado dentro del embalse y su distribución y movilización para definir su periodo de funcionamiento. En particular, el sedimento que se deposita dentro del embalse usualmente contiene muchas partículas finas, con respecto a los ríos y a los estuarios, y por esto es más expuestos a condiciones forzadoras débiles. El estudio ha demostrado que condiciones de carga de breve duración pueden inducir circulación del cuerpo de agua, incrementando en consecuencia los fenómenos de re suspensión y de transporte.

7.2 Futuras líneas de investigación

El estudio ha evidenciado que armónicos de alta frecuencia de los forzadores atmosféricos pueden inducir una excitación resonante en un pequeño lago o embalse. El estudio ha abierto nuevas líneas de investigaciones que se describen a continuación:

- *Determinar la influencia de los forzadores atmosféricos de alta frecuencia en la generación de oscilaciones internas.* Campañas de campo futuras incluirán medidas simultáneas de la variación de temperatura a lo largo de la columna de agua, de la elevación de la superficie libre y de los perfiles de corriente. Estas medidas permitirán determinar si las capas internas estratificadas pueden estar influenciadas por los agentes atmosféricos forzadores de alta frecuencia y sus implicaciones en los procesos de mezcla en toda la columna de agua del embalse.

- *El estudio local de las condiciones atmosféricas a lo largo de los valles del rio Ízbor y Guadalfeo.* Futuras campañas de campo para la obtención de los agentes forzadores atmosféricos tendrían que incluir además medidas de alta frecuencia de las estaciones meteorológicas instaladas en los valles del rio Ízbor y Guadalfeo, junto con las medidas de una estación lejos del embalse para determinar las condiciones de gobierno fuera de los valles a sur del embalse. Esta información extra permitirá completar las informaciones proporcionadas por la simulación en el túnel de viento y además proporcionar una más elevada resolución de los términos de forzamientos atmosféricos de entrada en el modelo numérico.

- *Desarrollar un modelo numérico de circulación en el embalse en tres dimensiones.* Este modelo permitirá avanzar en el estudio de la influencia de los agentes forzadores atmosféricos en la circulación de agua a lo largo de toda la profundidad del embalse, en particular, en condiciones de estratificación. El modelo proporcionará además una descripción de los esfuerzos de corte en el fondo, modelando directamente los efectos del forzamiento meteorológico en el trasportes de sedimentos y de re suspensión.

7 Conclusions and Future work

7.1 Conclusions

Through field measurements, wind tunnel simulations and numerical model calculations, this study has shown that high frequency fluctuations (<10min) in the atmospheric forcing can induce resonant excitation of the free surface oscillations on a small lake or reservoir. This is particularly relevant for lakes and reservoirs situated in mountainous terrain, where complex flow patterns are generated by local thermal differences in the atmosphere and flow separation from the topographical features. If the period of the atmospheric forcing matches one of the lower reservoir eigenmode frequencies, resonant excitation of the free surface is shown to occur.

The observations are not limited to situations of complex terrain, but may also be relevant for small lakes, reservoirs or harbours in urban locations, where flow separation and high frequency harmonics may be developed in the atmospheric forcing due to the eddies created by the surrounding buildings or other man-made structures. Recent studies at Carchuna Beach have showed local topographical features may contribute to the formation of beach embayments due to wind vortex shedding off coastal headlands coupling with the downstream coastal hydrodynamics (Ortega-Sánchez, Bramato, Quevedo, Mans, & Losada, 2008).

High frequency variations in the atmospheric forcing (barometric pressure and wind shear stress) and the free surface response are presented from field measurements of a small reservoir located in complex terrain (Rules Reservoir, Granada). Measurements of harmonic frequencies in the atmospheric forcing, with period 500 seconds, matched the first eigenmode of the reservoir, creating resonant excitation of the free surface oscillations despite the low wind speed. Higher order super-harmonic modes may also be excited and may have higher energy contributions than the lower modes.

Harmonics in the atmospheric properties were also observed at other frequencies during the period of the field, ranging between 200 - 700 seconds. The reservoir free surface did not respond at these times because the forcing frequencies did not match

any of the lower eigenmodes. However, the observed harmonic events may become significant as the water level within the reservoir rises, consequently modifying the geometry of the reservoir and the eigenmode shapes and frequencies.

The spatial variation of the atmospheric forcing on the reservoir water surface is studied from simulations in a boundary layer wind tunnel. The topographical features surrounding the reservoir are modeled at a scale of 1:3000 for a single wind direction which coincided with the orientation of the principal axis of the reservoir and the local wind directionality above the reservoir. The wind tunnel is shown to be a useful tool for defining the complex flow patterns that occur in the boundary layer above the reservoir and for providing a detailed map of the spatial variation of the atmospheric forcing on the water surface during synoptic conditions. Increasingly, three-dimensional CFD simulations are being performed to capture the complete water circulation patterns within reservoirs and small lakes. However, among other factors, their accuracy is limited by the resolution of the forcing terms. Wind tunnel simulations may be a useful tool for developing, with high spatial resolution, the atmospheric forcing conditions (wind speed and barometric pressure) over the reservoir water surface and used, in conjunction with field data, as a method for better defining the loading conditions in the computational model.

The water free surface response to the atmospheric forcing is studied with a two-dimensional, depth-averaged, hydrodynamic numerical model developed from the linearized shallow water equations. The measurements from the field study and the wind tunnel simulation are merged together to provide a detailed map of the high spatial and temporal variability of the atmospheric forcing, which are included as loading conditions in the numerical model. The model adequately predicts the free surface oscillations measured during the field campaign with the reservoir at its current water level. The model shows how higher order eigenmodes may be excited due to the high frequency component of the forcing, providing free surface oscillations markedly different to uniform loading conditions. It is also capable of predicting which higher order eigenmodes will contribute to the response of the free surface and where the maximum oscillations will occur.

The atmospheric forcing is also applied to simulations of the reservoir with higher water levels, predicting the response of the reservoir when it is at full capacity and at intermediate levels. The model predicts the future response of the reservoir free surface due to realistic atmospheric forcing conditions and which eigenmodes will dominate in the free surface response.

The novel methodology employed in the present study can aid in the future management of reservoirs or small lakes. In particular for reservoirs, where knowledge of the the water quality is the most important characteristic as it is generally used for public drinking or irrigation purposes. During summer, the solar heating of the surface layer creates a strong thermocline, creating a stratified layer. This separates the upper water layer from the lower water volume, reducing the mixing of the deeper waters and deteriorating the water quality in the lower levels. The reduction in the dissolved oxygen

concentration can create hypoxic conditions and bacterial outbreaks. Only during significant atmospheric forcing can the internal layer be destroyed by instabilities. However, if the reservoir is excited due to less intense but more frequent wind loading episodes, the internal layer may not have time to fully develop. Thus, regularly occurring surface seiches may promote mixing throughout the depth of the water column, increasing the concentration of dissolved oxygen and the quality of the water for drinking.

In addition, the calculation of the volume of sediment trapped inside the reservoir and its distribution and movement is important in determining its useful life expectancy. In particular, sediment deposits in reservoirs usually contain much finer particles compared with rivers and estuaries, which mean that the distribution of the sediment within the reservoir is susceptible to weak forcing conditions. The study has shown that short term loading conditions can promote circulation of the water body, possibly increasing the probability of sediment re-suspension and transport.

7.2 Future work

The study has proved that the high frequency harmonics in the atmospheric forcing can induce resonant excitation in a small lake or reservoir. The study has also opened new lines of future investigation, as listed below:

- *Determine the influence of the high frequency atmospheric forcing on internal seiches.* Future field measurements will include simultaneous measurements of the temperature variations throughout the water column in addition to the free surface elevation and current profiles. This will aid in detecting if the stratified internal layers may also be influenced by the high frequency atmospheric forcing and their effects on mixing throughout the depth of the reservoir.

- *Study the local atmospheric conditions through the Ízbor and Guadalfeo valleys.* Future field measurements of the atmospheric forcing should also include high frequency measurement stations within the valleys Ízbor and Guadalfeo, along with a station outside of the valley to detect the governing atmospheric conditions outside of the southern reservoir valleys. This extra information will also aid in determining the accuracy of the wind tunnel simulations and provide greater resolution of the atmospheric forcing terms in the numerical model.

- *Develop a three dimensional numerical model of the reservoir circulation*. The current numerical model will be advanced to study the influence of the high-frequency atmospheric forcing on the water circulation throughout the depth of the reservoir, in particular, under stratified conditions. The model will provide a description of the bed shear stresses, directly modeling the effects of the atmospheric forcing on sediment transport and re-suspension.

8 Bibliography

Ali, K. H., & Othman, K. (1997). Investigation of jet-forced water circulation in reservoirs. *Proceedings Institute of Civil Engineering, Waterways, Maritime Energy , 124(1)*, 44-62.

Alpar, B., & Yuce, H. (1996). Sea-level variations in the Eastern Coastsof the Aegean Sea. *Estuarine, Coastal and Shelf Science , 42*, 509-521.

As-Salek, J. A., & Schwab, D. J. (2004). High-frequency water level fluctuations in Lake Michigan. *Journal of Waterway, Port, Coastal and Ocean Engineering , 130*, 45-53.

AWES, A. W. (2001). *Wind Engineering Studies of Buildings AWES-QAM-1-2001.*

Bailey, M. C., & Hamilton, D. P. (1997). Wind induced sediment resuspension: a lake-wide model. *Ecological Modelling , 99*, 217-228.

Bramato, S. (2008). *Capa límite de fondo y superficial asociada a oscilaciones de múltiple escala: influencia en el transporte de sedimentos y la morfología costera. Doctoral thesis.* University of Granada.

Candela, J., Mazzola, S., Sammari, C., Limeburner, R., Lozano, C. J., Patti, B., et al. (1999). The 'Mad Sea' phenomenon in the Strait of Sicily. *Journal of Physical Oceanography , 29*, 2210-2231.

Cheng, R. T., & Dillon, T. M. (1976). Numerical models of wind-driven circulation in lakes. *Applied Mathematical Modelling , 1*, 141-159.

Chock, G. Y., & Cochran, L. (2005). Modelling of topographic wind speed effects in Hawaii. *Journal of Wind Engineering and Industrial Aerodynamics , 93*, 623-638.

Cuesta, J. A. (2005). *Modelización de capa límite atmosférica i evolución sobre topografía compleja. Investigación Tutelada.* Universidad de Granada.

Cushman-Roisin, B., Willmott, A. J., & Biggs, N. R. (2005). Influence of stratification on decaying surface seiche modes. *Continental Shelf Research , 25*, 227-242.

de Jong, M. P., & Battjes, J. A. (2004). Seiche characteristics of Rotterdam Harbour. *Coastal Engineering , 51*, 373-386.

Dean, R. G., & Dalrymple, R. A. (1991). *Water wave mechanics for engineers and scientists. Advanced Series of Ocean Engineering - Volume 2.* Singapore: World Scientific.

ESDU 1, E. S. (1982). *Strong winds in the atmosphere boundary layer. Part 1. Mean-hourly wind speeds. Data Item 82026.*

ESDU 2, E. S. (1982). *Strong winds in the atmosphere boundary layer. Part 2. Discrete gust speeds. Data Item 83045.*

Falconer, R. A., George, D. G., & Hall, P. (1991). Three-dimensional numerical modeling of wind driven circulation in a shallow homogeneous lake. *Journal of Hydrology , 124*, 59-79.

Ferrarin, C., & Umgiesser, G. (2005). Hydrodynamic modeling of a coastal lagoon: The Cabras lagoon in Sardinia, Italy. *Ecological Modelling , 188*, 340-357.

Galil. (2005). *DMC-21x2/21x3 Manual Rev. 1.0d.* Galil Motion Control Incorporated.

Gavelli, F., Bullister, E., & Kytomaa, H. (2008). Application of CFD (Fluent) to LNG spills into geometrically complex environments. *Journal of Hazardous Materials* .

Hamblin, P. F. (1982). On the free surface oscillations of Lake Ontario. *Limnology and Oceanography , 27(6)*, 1039-1049.

Harris, R. I. (2008). The macrometeorological spectrum - a preliminary study. *Journal of Wind Engineering and Industrial Aerodynamics , 96*, 2294-2307.

Hedger, R. D., Olsen, N. R., Malthus, T. J., & Atkinson, P. M. (2002). Coupling remote sensing with computational fluid dynamics modelling to estimate lake chlorophyll-a concentration. *Remote Sensing of Environment , 79*, 116-122.

Hidrosur. (n.d.). *Andaluza del agua*. Retrieved from http://hidrosur.agenciaandaluzadelagua.es/

Holmes, J. D. (2001). *Wind loading of structures.* London: Spon Press.

Horn, W., Mortimer, C. H., & Schwab, D. J. (1986). Wind-induced internal seiches in Lake Zurich observed and modeled. *Limnology and Oceanography , 31(6)*, 1232-1254.

Hurtado, J. V. (2006). *Basin scale hydrodynamics in a Mediterranean reservoir. Implications for the phytoplankton dynamics.* Universitat de Girona: PhD Thesis.

Hutter, K., Raggio, G., Bucher, C., & Salvade, G. (1982). The surface seiches of Lake of Zurich. *Schweiz. Z. Hydrology , 44(2)*, 423-454.

Jordi, A., Basterretxea, G., Casas, B., Anglés, S., & Garcés, E. (2008). Seiche-forced resuspension events in a Mediterranean harbour. *Continental Shelf Research , 28*, 505-515.

Kennedy, M. G. (2003). *Three-dimensional numerical modeling of hydrodynamics and transport in a reservoir.* Amherst, MA, U.S.A.: MSc Thesis, University of Massachusetts.

Large, W. G., & Pond, S. (1981). Open ocean momentum flux measurements in moderate to strong winds. *Journal of Physical Oceanography , 11*, 324-336.

Letchford, C., & Mans, C. (2001). Thunderstorm - their importance in Wind Engineering (A case for the next generation wind tunnel). *Journal of Wind Engineering , 89*, 31-44.

Luettich, R. A., Carr, S. D., Reynolds-Fleming, J. V., Fulcher, C. W., & McNinch, J. E. (2002). Semi-diurnal seiching in a shallow, micro-tidal lagoonal estuary. *Continental Shelf Research , 22*, 1669-1681.

Luketa-Hanlin, A., Koopman, R. P., & Ermak, D. L. (2007). On the application of computational fluid dynamics codes for liquefied natural gas dispersion. *Journal of Hazardous Materials , 140*, 504-517.

M. d. (n.d.). Communication.

Mans, C. (2006). *Campo de viento sobre el Embalse Rules, Granada.* Granada.

Meroney, R. N. (1980). Wind tunnel simulation of the flow over hills and complex terrain. *Journal of Wind Engineering and Industrial Aerodynamics , 5*, 297-321.

Molero Melgarejo, E. (2004). *Modelo digital de elevaciones (MDE). Cartografía base y metodología de generación.* Universidad de Granada, Grupo de Ordenación del Territorio (GUOT). Projecto Guadalfeo IT. I.1.

Moñino, A. (2006). *Wavelets aplicadas al análisis de velocidad del flujo en el Embalse de Rules. Informe Técnico IT II.9.* Grupo de Rios y Embalses, CEAMA, Universidad de Granada.

Niedda, M., & Greppi, M. (2007). Tidal, seiche and wind dynamics in a small lagoon in the Mediterranean Sea. *Estuarine, Coastal and Shelf Science , In press*, 1-10.

Olsen, N. R. (1999). *Computational fluid dynamics in hydraulic and sedimentation engineering. Class notes.* Norway: Norwegian University of Science and Technology.

Olsen, N. R., Hedger, R. D., & George, D. G. (2000). 3D numerical modeling of Microcystis distribution in a water reservoir. *Journal of Environmental Engineering* , 949-953.

Ortega-Sánchez, M., Bramato, S., Quevedo, E., Mans, C., & Losada, M. A. (2008). Field evidence of atmospheric-hydrodynamic coupling in the nearshore. *Geophysical Research Letter* , In press.

Otsmann, M., Suursaar, U., & Kullas, T. (2001). The oscillatory nature of the flows in the system of straits and small semienclosed basins of the Baltic Sea. *Continental Shelf Research , 21*, 1577-1603.

Park, J.-H., & Watts, D. R. (2005). Response of the southwestern Japan/East Sea to atmospheric pressure. *Deep-Sea Research II , 52*, 1671-1683.

Pérez, A. N. (2004). La presa de Rules. *Revista de Obras Publicas , 3,441*, 131-152.

Podsetchine, V., & Schernewski, G. (1999). The influence of spatial wind inhomogeneity on flow patterns in a small lake. *Water Research , Vol. 33, No. 15*, 3348-3356.

Rueda, F. J., & Schladow, S. G. (2002). Surface seiches in lakes of complex geometry. *Limnology and Oceanography , 47(3)*, 906-910.

Ruiz, A. L. (2008). Personal communication.

Ruiz, A. L., & Nanía Escobar, L. S. (2006). *Mapa batimétrico de los embalses de la cuenca del río Guadalfeo.*

Sobey, R. J. (2002). Analytical solutions for storm tide codes. *Coastal Engineering , 46*, 213-231.

Sobey, R. J. (2006). Normal mode decomposition for identification of storm tide and tsunami hazard. *Coastal Engineering , 53*, 289-301.

Stull, R. B. (2000). *Meteorology for scientists and engineers.* CA, USA: Brooks/Cole.

Suursaar, U., Kullas, T., & Otsmann, M. (2002). A model study of the sea level variations in the Gulf of Riga and the Vainameri Sea. *Continental Shelf Research , 22*, 2001-2019.

Suursaar, U., Kullas, T., Otsmann, M., & Kouts, T. (2003). Extreme sea level events in the coastal waters of western Estonia. *Journal of Sea Research , 49*, 295-303.

Ta, C. T., & Brignal, W. J. (1998). Application of computational fluid dynamics technique to storage reservoir studies. *Water Science Technologies , Vol. 37, No. 2*, 219-226.

Van der Hoven, I. (1957). Power spectrum of horizontal wind speed in the frequency range from 0.0007 to 900 cycles/h. *Journal of Atmospheric Sciences , 14*, 160-164.

Vilibic, I., & Mihanovic, H. (2003). A study of resonant oscillations in the Split Harbour (Adriatic Sea). *Estuarine, Coastal and Shelf Science , 56*, 861-867.

Vilibic, I., Domijan, N., & Cupic, S. (2005). Wind versus air pressure seiche triggering in the Middle Atlantic coastal waters. *Journal of Marine Systems , 57*, 189-200.

Wang, Y., Hutter, K., & Bauerle, E. (2001). Three-dimensional wind-induced baroclinic circulation in rectangular basins. *Advances in Water Resources , 24*, 11-27.

Ward, P. R. (1979). Seiches, tides and wind set-up on Lake Kariba. *Limnology and Oceanography , 24(1)*, 151-157.

Wetzel, R. G. (2001). *Limnology. Lake and river ecosystems.* USA: Academic Press.

Whiteman, C. D. (2000). *Mountain Meteorology.* New York: Oxford University Press.

Wilding, A., Collins, M., & Ferentinos, G. (1980). Analyses of sea level fluctuations in Thermaicos Gulf and Salonica Bay, Northwestern Aegean Sea. *Estuarine and Coastal Marine Science , 10*, 325-334.

Wuest, A., & Farmer, D. M. (2003). *Encyclopedia of Science and Technology.* McGraw-Hill.

Wuest, A., & Lorke, A. (2003). Small scale hydrodynamics in lakes. *Annual Review of Fluid Mechanics , 35*, 373-412.

Yu, X., & Togashi, H. (1996). Oscillations in a coupled bay - river system. 2. Numerical method. *Coastal Engineering , 28*, 165-182.

Zacharias, I., & Ferentinos, G. (1997). A numerical model for the winter circulation in Lake Trichonis, Greece. *Environmental Modelling and Software , Vol. 12, No. 4*, 311-321.

Appendix A – Development of shallow water equations

Conservation of mass

The conservation of mass of a fluid element is the mass balance of the fluid element volume, where the rate of the increase of mass in a fluid element is equal to the net rate of flow of mass into the element. For an incompressible fluid, the mass conservation in the element is:

$$\nabla \cdot \boldsymbol{u} = 0$$

where ∇ is the gradient operator, or equally can be expressed as:

$$\underset{[i]}{\frac{\partial u}{\partial x}} + \underset{[ii]}{\frac{\partial v}{\partial y}} + \underset{[iii]}{\frac{\partial w}{\partial z}} = 0$$

Integrating through the water column according to the Leibnitz rule:

$$\frac{\partial}{\partial x}\int_{\alpha(x)}^{\beta(x)} Q(x,y)dy = \int_{\alpha(x)}^{\beta(x)} \frac{\partial}{\partial x} Q(x,y)dy + Q\big(x,\beta(x)\big)\frac{\partial \beta(x)}{\partial x} - Q\big(x,\alpha(x)\big)\frac{\partial \alpha(x)}{\partial x}$$

Term [i] in equation 3.2 becomes:

$$\int_{-h}^{\eta} \frac{\partial u}{\partial x} dz = \frac{\partial}{\partial x}\int_{-h}^{\eta} u\, dz - u(x,y,\eta)\frac{\partial \eta}{\partial x} - u(x,y,-h)\frac{\partial(-h)}{\partial x}$$

Assuming U is the mean velocity through the water column in the x direction and H is the total water depth in the water column:

$$U = \frac{1}{H}\int_{-h}^{\eta} u\, dz, \quad where\ H = h + \eta$$

$$\int_{-h}^{\eta} \frac{\partial u}{\partial x} dz = \frac{\partial}{\partial x} UH - u(x,y,\eta)\frac{\partial \eta}{\partial x} - u(x,y,-h)\frac{\partial(-h)}{\partial x}$$

Similarly term [ii] in equation 3.2 becomes:

$$\int_{-h}^{\eta} \frac{\partial v}{\partial y} dz = \frac{\partial}{\partial y}\int_{-h}^{\eta} v\, dz - v(x,y,\eta)\frac{\partial \eta}{\partial y} - v(x,y,-h)\frac{\partial(-h)}{\partial y}$$

Assuming that V is the mean velocity through the water column in the y direction:

$$V = \frac{1}{h+\eta}\int_{-h}^{\eta} v\, dz$$

$$\int_{-h}^{\eta} \frac{\partial v}{\partial y} dz = \frac{\partial}{\partial y} VH - v(x,y,\eta)\frac{\partial \eta}{\partial y} - v(x,y,-h)\frac{\partial(-h)}{\partial y}$$

Term [iii] in equation 3.2 becomes:

$$\int_{-h}^{\eta} \frac{\partial w}{\partial z} dz = \int_{-h}^{\eta} dw = w(x,y,\eta) - w(x,y,-h)$$

The problem is simplified by considering the boundary conditions at the free surface and at the bed:

(a) The kinematic equation at the free surface is:

$$w(x,y,\eta) = \frac{\partial \eta}{\partial t} + u(x,y,\eta)\frac{\partial \eta}{\partial x} + v(x,y,\eta)\frac{\partial \eta}{\partial y}$$

(b) The bed is fixed and does not vary in time ($\frac{\partial h}{\partial t} = 0$)

$$w(x,y,-h) = -u(x,y,-h)\frac{\partial h}{\partial x} - v(x,y,-h)\frac{\partial h}{\partial y}$$

Summing [i], [ii] and [iii]:

$$\frac{\partial}{\partial x} UH - \frac{\partial \eta}{\partial x} u(x,y,\eta) - \frac{\partial(-h)}{\partial x} u(x,y,-h) + \frac{\partial}{\partial y} VH - \frac{\partial \eta}{\partial y} v(x,y,\eta) - \frac{\partial(-h)}{\partial y} v(x,y,-h)$$
$$+ \frac{\partial \eta}{\partial t} + u(x,y,\eta)\frac{\partial \eta}{\partial x} + v(x,y,\eta)\frac{\partial \eta}{\partial y} + u(x,y,\eta)\frac{\partial h}{\partial x} + v(x,y,\eta)\frac{\partial h}{\partial y} = 0$$

$$\frac{\partial}{\partial x} UH + \frac{\partial}{\partial y} VH + \frac{\partial \eta}{\partial t} = 0$$

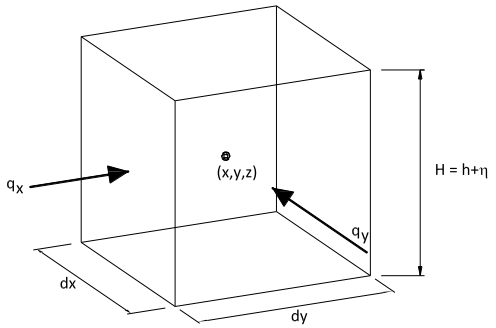

$$\frac{\partial \eta}{\partial t} + \frac{\partial q_x}{\partial x} + \frac{\partial q_y}{\partial y} = 0$$

with:

$$q_x = UH$$

$$q_y = VH$$

Conservation of momentum

The conservation of momentum is the momentum balance of the fluid element, where the rate of increase of momentum of a fluid element is equal to the sum of the forces on the fluid element. Two types of forces act on the element, body forces (gravity) and surface forces

(pressure, viscous), which are each handled differently in the formation of the momentum equations.

For a closed water body, gravity is the only body force acting on the fluid, which can be expressed as (per unit volume):

$$\boldsymbol{f}_{body} = \rho \boldsymbol{g}$$

where g is the acceleration of gravity.

The surface forces are expressed as the pressure (normal to the element surface) and the viscous stresses (parallel to the element surface) which act on the fluid element, leading to (per unit volume):

$$\boldsymbol{f}_{surface} = -\nabla p + \nabla . \tau_{ij}$$

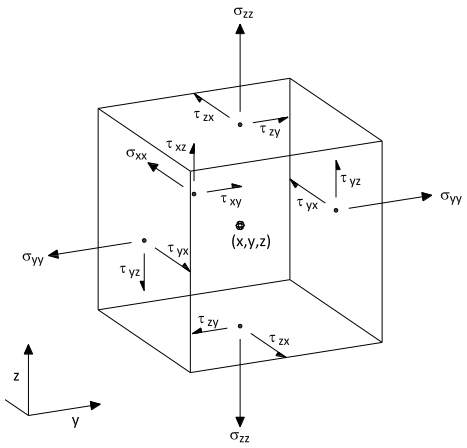

The surface shear forces are generated by forces that act tangentially to the surface. Assuming that the forces act per unit surface area, the convention adopted is that the first index refers to the axis that is perpendicular to the surface and the second index refers to the direction of the shear force, as shown in the figure.

The equation of the conservation of momentum with respect to the x axis is:

$$\frac{\partial u}{\partial t} + u\frac{\partial u}{\partial x} + v\frac{\partial u}{\partial y} + w\frac{\partial u}{\partial z} = -\frac{1}{\rho}\frac{\partial P}{\partial x} + \frac{1}{\rho}\left(\frac{\partial \tau_{xx}}{\partial x} + \frac{\partial \tau_{yx}}{\partial y}\frac{\partial \tau_{zx}}{\partial z}\right) + \frac{\rho}{\rho} f_c v$$

where $\rho f_c v$ is the contribution of the coriolis and the earths rotation, and $f_c = 2\Omega \sin\varphi$.

Considering the LHS of the equation:

$$\frac{\partial u}{\partial t} + u\frac{\partial u}{\partial x} + v\frac{\partial u}{\partial y} + w\frac{\partial u}{\partial z}$$

Summing and subtracting $u\frac{\partial u}{\partial x}, u\frac{\partial v}{\partial y}, u\frac{\partial w}{\partial z}$:

$$\frac{\partial u}{\partial t} + u\frac{\partial u}{\partial x} + \left(u\frac{\partial u}{\partial x} - u\frac{\partial u}{\partial x}\right) + v\frac{\partial u}{\partial y} + \left(u\frac{\partial v}{\partial y} - u\frac{\partial v}{\partial y}\right) + w\frac{\partial u}{\partial z} + \left(u\frac{\partial w}{\partial z} - u\frac{\partial w}{\partial z}\right)$$

$$\frac{\partial u}{\partial t} + \left(2u\frac{\partial u}{\partial x} - u\frac{\partial u}{\partial x}\right) + \left(u\frac{\partial v}{\partial y} + v\frac{\partial u}{\partial y} - u\frac{\partial v}{\partial y}\right) + \left(u\frac{\partial w}{\partial z} + w\frac{\partial u}{\partial z} - u\frac{\partial w}{\partial z}\right)$$

$$\frac{\partial u}{\partial t}+\left(\frac{\partial^2 u}{\partial x^2}-u\frac{\partial u}{\partial x}\right)+\left(\frac{\partial uv}{\partial y}-u\frac{\partial v}{\partial y}\right)+\left(\frac{\partial uw}{\partial z}-u\frac{\partial w}{\partial z}\right)$$

$$\frac{\partial u}{\partial t}+\frac{\partial^2 u}{\partial x^2}+\frac{\partial uv}{\partial y}+\frac{\partial uw}{\partial z}-u\left(\frac{\partial u}{\partial x}+\frac{\partial v}{\partial y}+\frac{\partial w}{\partial z}\right)$$

$$\frac{\partial u}{\partial t}+\frac{\partial^2 u}{\partial x^2}+\frac{\partial uv}{\partial y}+\frac{\partial uw}{\partial z}$$

Following the hypothesis of the shallow water equations $\left(\frac{h}{L}<\frac{1}{20}\right)$, if the slope of the bed is small (w<<u,v), the local accelerations and the convection in the vertical direction will be negligible with respect to the horizontal direction.

Considering the conservation of momentum in the z direction:

$$\rho\frac{Dw}{Dt}=-\rho g-\frac{\partial P}{\partial z}+\left(\frac{\partial \tau_{xz}}{\partial x}+\frac{\partial \tau_{yz}}{\partial y}+\frac{\partial \tau_{zz}}{\partial z}\right)$$
$$\rho\frac{Dw}{Dt}=-\rho g-\frac{\partial P}{\partial z}+\mu\nabla^2 \mathrm{w}$$
$$\frac{\partial P}{\partial z}=\rho g$$
$$P(x,y,z,t)=-\rho g z+f(x,y,t)$$

Assuming that the pressure at the water surface is equal to the atmospheric pressure:

$$P(z=\eta)=P_s$$
$$f(x,y,t)=\rho g\eta+P_s$$

Giving:

$$P(x,y,z,t)=\rho g(\eta-z)+P_s$$

The momentum equation in x then becomes:

[AA] [AB] [AC] [AD] [BA] [BB] [BC] [BD] [BE]

$$\rho\left(\frac{\partial u}{\partial t}+\frac{\partial^2 u}{\partial x^2}+\frac{\partial uv}{\partial y}+\frac{\partial uw}{\partial z}\right)==-\frac{\partial P}{\partial x}+\left(\frac{\partial \tau_{xx}}{\partial x}+\frac{\partial \tau_{yx}}{\partial y}+\frac{\partial \tau_{zx}}{\partial z}\right)+\rho f_c v$$

Integrating in z:

[AA]

$$\int_{-h}^{\eta}\frac{\partial u}{\partial t}dz=\frac{\partial}{\partial t}\int_{-h}^{\eta}u\,dz-u(x,y,\eta)\frac{\partial \eta}{\partial t}+\frac{\partial(-h)}{\partial t}u(x,y,-h)$$
$$=\frac{\partial}{\partial t}(UH)-\frac{\partial \eta}{\partial t}u(x,y,\eta)-\frac{\partial h}{\partial t}u(x,y,-h)$$

Assuming the bed is fixed and does not vary in time, $\frac{\partial h}{\partial t}=0$.

[AB]

$$\int_{-h}^{\eta} \frac{\partial u^2}{\partial t} dz = \frac{\partial}{\partial x}\int_{-h}^{\eta} u^2 \, dz - u^2(x,y,\eta)\frac{\partial \eta}{\partial x} - \frac{\partial h}{\partial x}u^2(x,y,-h)$$
$$= \frac{\partial}{\partial x}(U^2 H) - \frac{\partial \eta}{\partial x}u^2(x,y,\eta) - \frac{\partial h}{\partial x}u^2(x,y,-h)$$

[AC]

$$\int_{-h}^{\eta} \frac{\partial uv}{\partial y} dz = \frac{\partial}{\partial y}\int_{-h}^{\eta} uv \, dz - \frac{\partial \eta}{\partial y}u(x,y,\eta)\, v(x,y,\eta) - \frac{\partial h}{\partial x}u(x,y,-h)\, v(x,y,-h)$$
$$= \frac{\partial}{\partial y}(UVH) - \frac{\partial \eta}{\partial y}u(x,y,\eta)\, v(x,y,\eta) - \frac{\partial h}{\partial x}u(x,y,-h)\, v(x,y,-h)$$

[AD]

$$\int_{-h}^{\eta} \frac{\partial uw}{\partial z} dz = \frac{\partial}{\partial z}\int_{-h}^{\eta} d(uw) = u(x,y,\eta)\, w(x,y,\eta) - u(x,y,-h)\, w(x,y,-h)$$
$$= u(x,y,\eta)\frac{\partial \eta}{\partial t} - u(x,y,-h)\frac{\partial(-h)}{\partial t}$$
$$= u(x,y,\eta)\left[\frac{\partial \eta}{\partial t} + u(x,y,\eta)\frac{\partial \eta}{\partial x} + v(x,y,\eta)\frac{\partial \eta}{\partial y}\right]$$
$$+ u(x,y,-h)\left[\frac{\partial h}{\partial t} + u(x,y,-h)\frac{\partial h}{\partial x} + v(x,y,-h)\frac{\partial h}{\partial y}\right]$$

[BA]

$$\int_{-h}^{\eta} -\frac{\partial P}{\partial x} dz = -\int_{-h}^{\eta} \frac{\partial}{\partial x}\,(\rho g(\eta - z) + P_s) dz$$
$$= -\left[\frac{\partial}{\partial x}\left(\int_{-h}^{\eta} \rho g \eta \, dz + \int_{-h}^{\eta} \rho g z \, dz \, + \int_{-h}^{\eta} P_s \, dz\right)\right]$$
$$= -\left(\rho g \frac{\partial \eta}{\partial x} + \frac{\partial P_s}{\partial x}\right) H$$

[BB]

$$\int_{-h}^{\eta} \frac{\partial \tau_{xx}}{\partial x} dz = \frac{\partial \tau_{xx}}{\partial x}\int_{-h}^{\eta} dz = \frac{\partial \tau_{xx}}{\partial x} H$$

[BC]

$$\int_{-h}^{\eta} \frac{\partial \tau_{yx}}{\partial y} dz = \frac{\partial \tau_{yx}}{\partial y}\int_{-h}^{\eta} dz = \frac{\partial \tau_{yx}}{\partial y} H$$

[BD]

$$\int_{-h}^{\eta} \frac{\partial \tau_{zx}}{\partial z} dz = \tau_{zx}(\eta) - \tau_{zx}(-h) = \tau_{sx} - \tau_{bx}$$

[BE]

$$\int_{-h}^{\eta} \rho f_c v \, dz = \rho f_c \int_{-h}^{\eta} v \, dz = \rho f_c VH$$

Putting the integrations [AA] – [BE] together results in:

$$\begin{aligned}\rho \Big[&\frac{\partial}{\partial t}(UH) - \frac{\partial \eta}{\partial t} u(x,y,\eta) - \frac{\partial h}{\partial t} u(x,y,-h) + \frac{\partial}{\partial x}(U^2 H) - \frac{\partial \eta}{\partial x} u^2(x,y,\eta) - \frac{\partial h}{\partial x} u^2(x,y,-h) \\ &+ \frac{\partial}{\partial y}(UVH) - \frac{\partial \eta}{\partial y} u(x,y,\eta)\, v(x,y,\eta) - \frac{\partial h}{\partial x} u(x,y,-h)\, v(x,y,-h) \\ &+ u(x,y,\eta)\frac{\partial \eta}{\partial t} + u^2(x,y,\eta)\frac{\partial \eta}{\partial x} + u(x,y,\eta) v(x,y,\eta)\frac{\partial \eta}{\partial y} + u(x,y,-h)\frac{\partial h}{\partial t} \\ &+ u^2(x,y,-h)\frac{\partial h}{\partial x} + u(x,y,-h) v(x,y,-h)\frac{\partial h}{\partial y} \Big] \\ &= -\left(\rho g \frac{\partial \eta}{\partial x} + \frac{\partial P_s}{\partial x}\right) H + \frac{\partial \tau_{xx}}{\partial x} H + \frac{\partial \tau_{yx}}{\partial y} H + \tau_{sx} - \tau_{bx} + \rho f_c VH\end{aligned}$$

$$\begin{aligned}&\rho \left[\frac{\partial}{\partial t}(UH) + \frac{\partial}{\partial x}(U^2 H) + \frac{\partial}{\partial y}(UVH) \right] \\ &\qquad = -\rho g H \frac{\partial}{\partial x}\left(\eta + \frac{P_s}{\rho g}\right) + H\left(\frac{\partial \tau_{xx}}{\partial x} + \frac{\partial \tau_{yx}}{\partial y}\right) + \tau_{sx} - \tau_{bx} + \rho f_c VH\end{aligned}$$

where τ_{sx} and τ_{bx} are the shear stress components in the x direction at the free surface and the bed, respectively. Similarly, for the y direction:

$$\begin{aligned}&\rho \left[\frac{\partial}{\partial t}(VH) + \frac{\partial}{\partial y}(V^2 H) + \frac{\partial}{\partial x}(UVH) \right] \\ &\qquad = -\rho g H \frac{\partial}{\partial y}\left(\eta + \frac{P_s}{\rho g}\right) + H\left(\frac{\partial \tau_{xy}}{\partial x} + \frac{\partial \tau_{yy}}{\partial y}\right) + \tau_{sy} - \tau_{by} + \rho f_c UH\end{aligned}$$

As with the conservation of mass, it is convenient to express the equations with respect to a unit width, $q_x = UH$, and , $q_y = VH$.

$$\begin{aligned}&\frac{\partial q_x}{\partial t} + \frac{\partial}{\partial x}\left(\frac{q_x^2}{H}\right) + \frac{\partial}{\partial y}\left(\frac{q_x q_y}{H}\right) \\ &\qquad = -gH \frac{\partial}{\partial x}\left(\eta + \frac{P_s}{\rho g}\right) + \frac{H}{\rho}\left(\frac{\partial \tau_{xx}}{\partial x} + \frac{\partial \tau_{yx}}{\partial y}\right) + \frac{1}{\rho}(\tau_{sx} - \tau_{bx}) + f_c q_y\end{aligned}$$

$$\begin{aligned}&\frac{\partial q_y}{\partial t} + \frac{\partial}{\partial y}\left(\frac{q_y^2}{H}\right) + \frac{\partial}{\partial x}\left(\frac{q_x q_y}{H}\right) \\ &\qquad = -gH \frac{\partial}{\partial y}\left(\eta + \frac{P_s}{\rho g}\right) + \frac{H}{\rho}\left(\frac{\partial \tau_{xy}}{\partial x} + \frac{\partial \tau_{yy}}{\partial y}\right) + \frac{1}{\rho}(\tau_{sy} - \tau_{by}) + f_c q_x\end{aligned}$$

The above equations are commonly known as the shallow water equations of motion, which along with the equation of continuity are non-linear. The linearized form of the equations can be readily obtained by assuming that the values of U, V and h are small, and hence thier products will be negligible. The linearized form of the shallow water equations are derived with the following assumptions:

5. Advective accelerations are negligible
6. Coriolis accelerations are negligible
7. The free surface movement is much less than the water depth ($\eta \ll h$)
8. The bed shear can be linearized to: $\tau_{b\alpha}/\rho = \lambda q_\alpha$, where λ is a linear friction factor

The simplifications result in the linear form of the shallow water equations:

$$\frac{\partial \eta}{\partial t} + \frac{\partial q_x}{\partial x} + \frac{\partial q_y}{\partial y} = 0$$

$$\frac{\partial q_x}{\partial t} = -gh\frac{\partial \eta}{\partial x} - \lambda q_x + F_x$$

$$\frac{\partial q_y}{\partial t} = -gh\frac{\partial \eta}{\partial y} - \lambda q_y + F_y$$

with the meteorological forcing defined as:

$$F_\alpha = -gH\frac{\partial}{\partial x_\alpha}\left(\frac{P_s}{\rho g}\right) + \frac{\tau_{sy}}{\rho}$$

where Ps is the atmospheric pressure at the water surface, $\tau_{sx\alpha}$ is the surface shear stress, h is the water depth, η is the water surface elevation and λ is the linear bed friction factor.

Appendix B – Mode shapes of Rules Reservoir

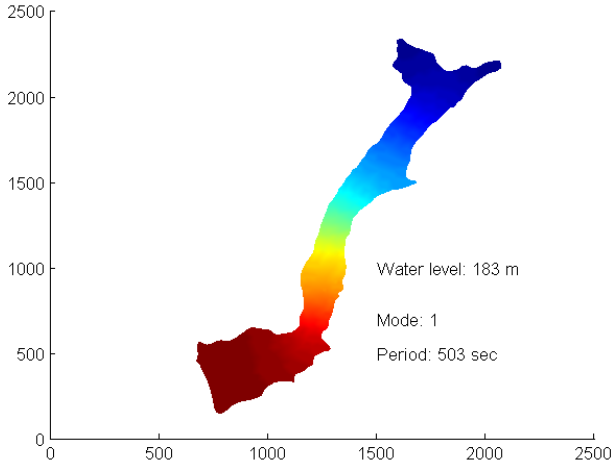

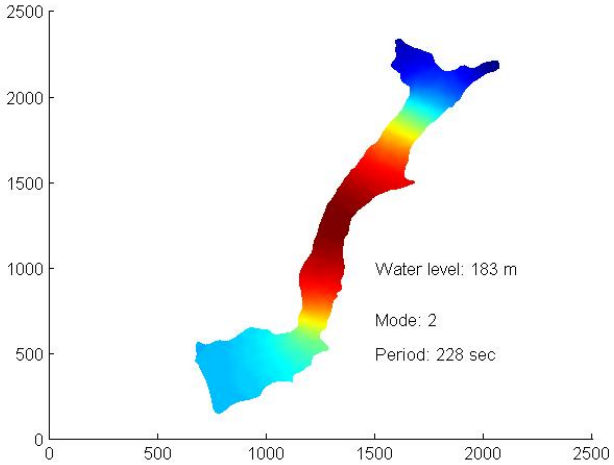

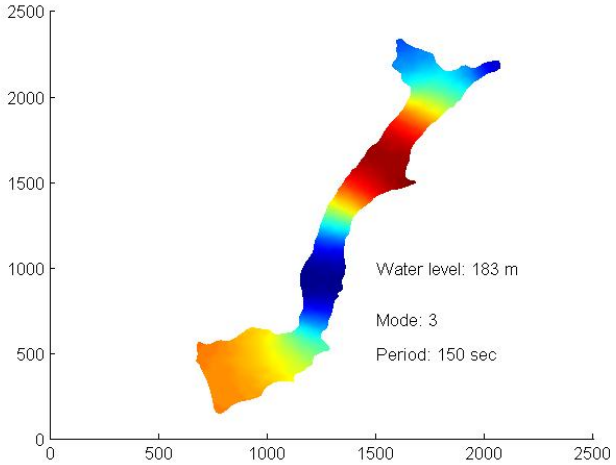

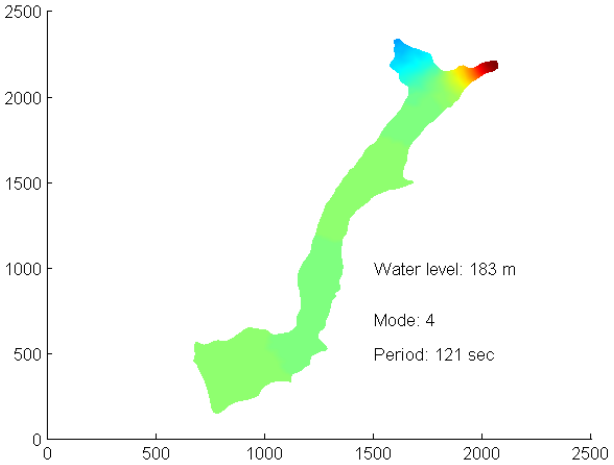

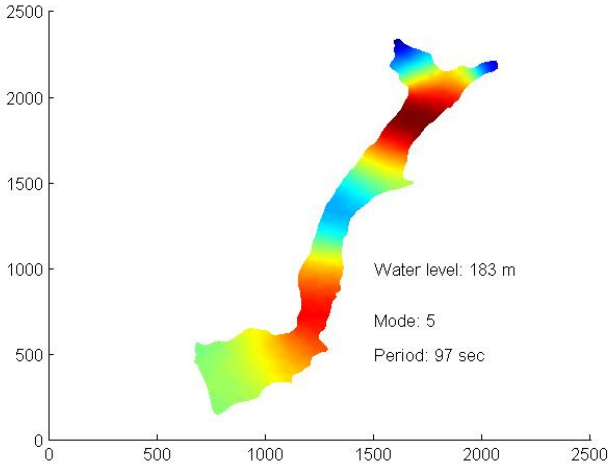

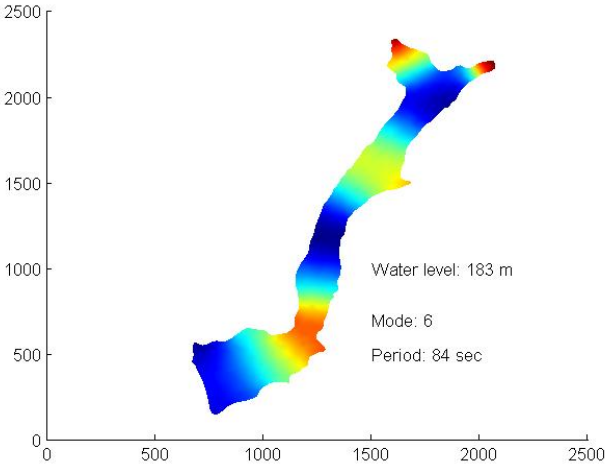

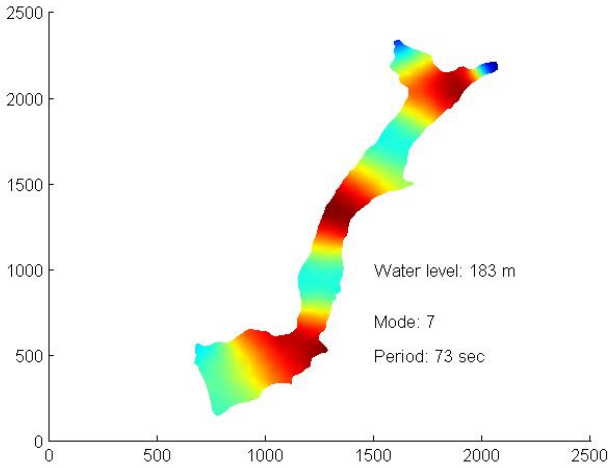
2500
2000
1500
1000
500
0
0
500
1000
1500
2000
2500
Water level: 183 m
Mode: 7
Period: 73 sec

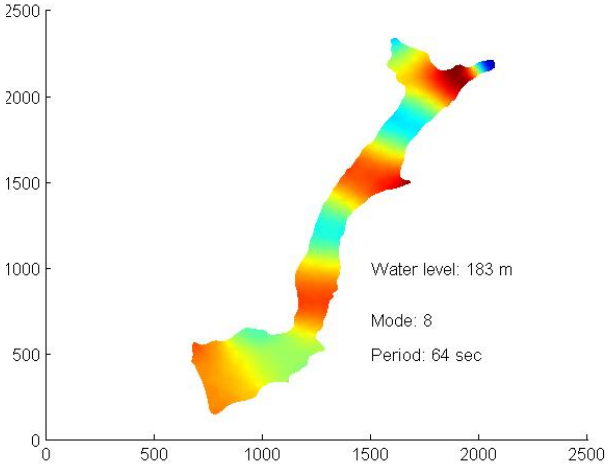
2500
2000
1500
1000
500
0
0
500
1000
1500
2000
2500
Water level: 183 m
Mode: 8
Period: 64 sec

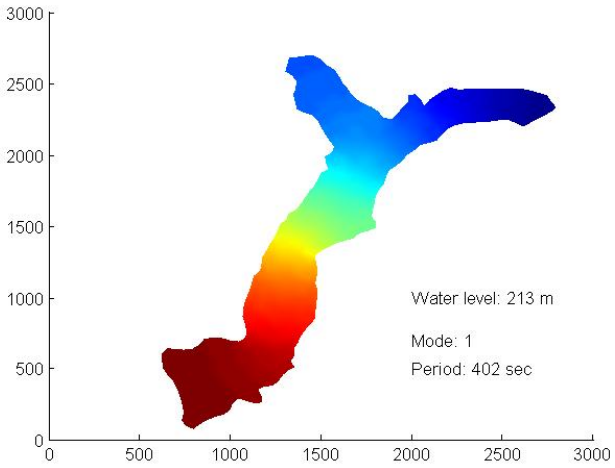
Water level: 213 m
Mode: 1
Period: 402 sec

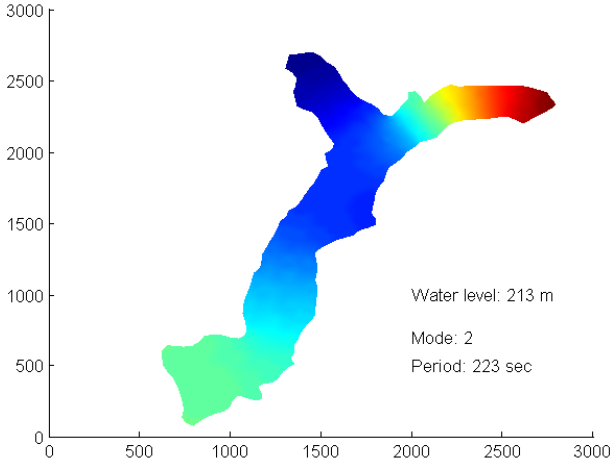
Water level: 213 m
Mode: 2
Period: 223 sec

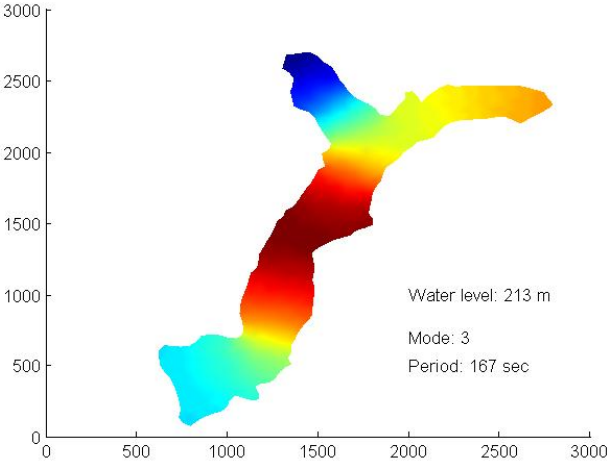
Water level: 213 m
Mode: 3
Period: 167 sec

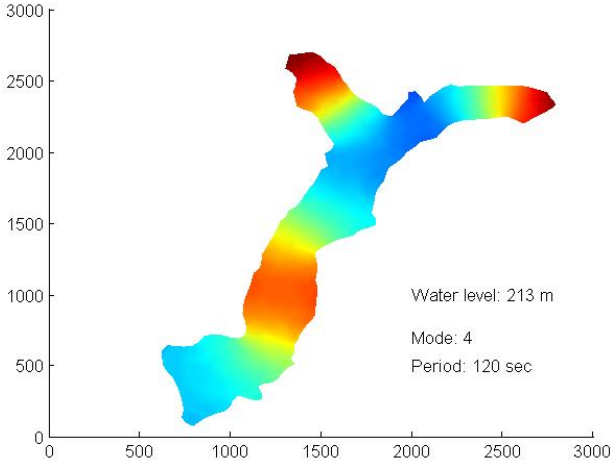
Water level: 213 m
Mode: 4
Period: 120 sec

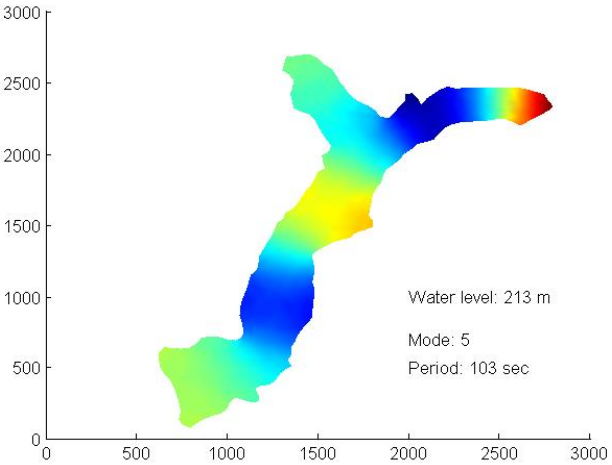
Water level: 213 m
Mode: 5
Period: 103 sec

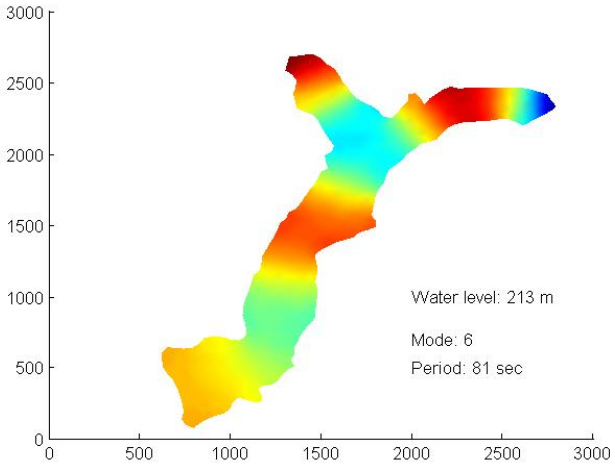
Water level: 213 m
Mode: 6
Period: 81 sec

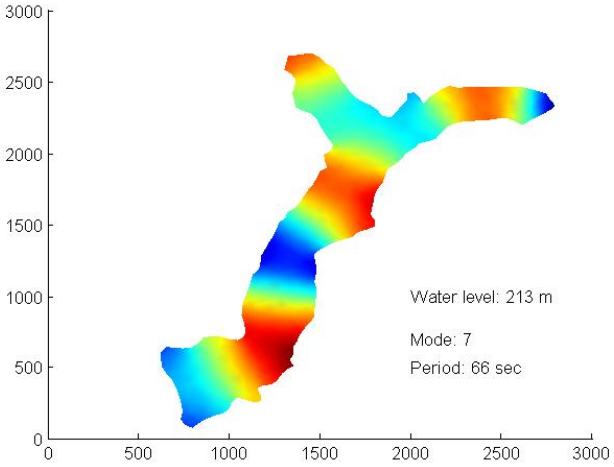
Water level: 213 m
Mode: 7
Period: 66 sec

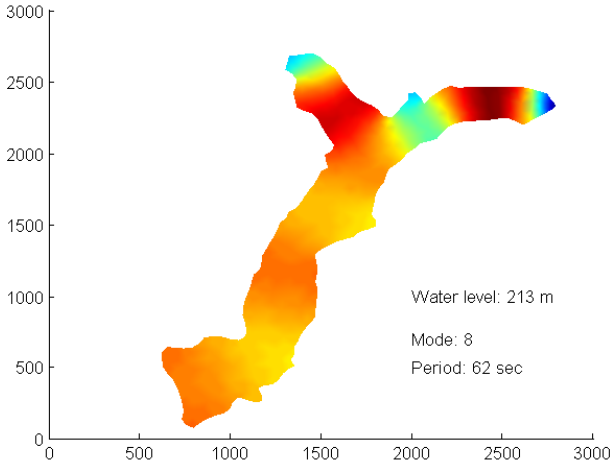
Water level: 213 m
Mode: 8
Period: 62 sec

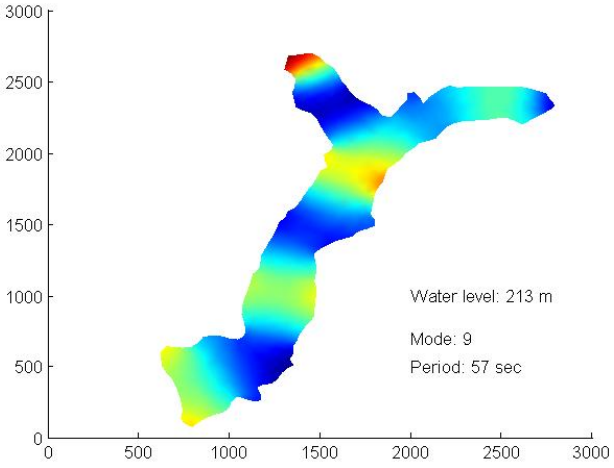
Water level: 213 m
Mode: 9
Period: 57 sec

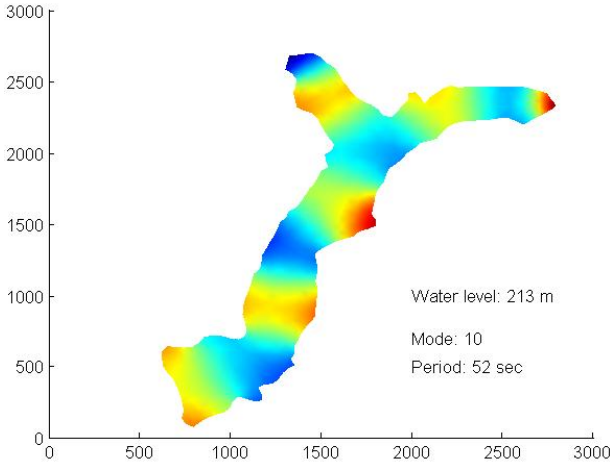
Water level: 213 m
Mode: 10
Period: 52 sec

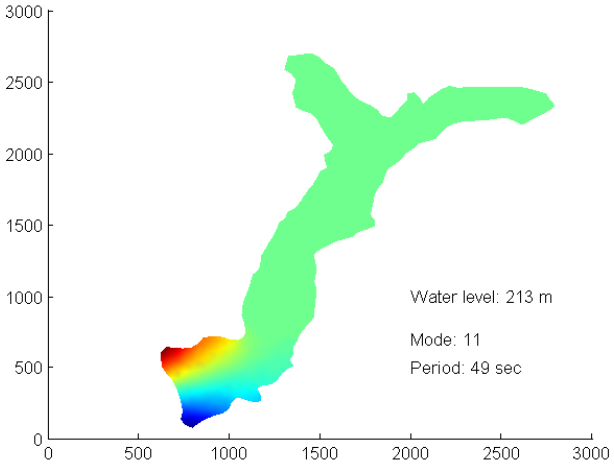
Water level: 213 m
Mode: 11
Period: 49 sec

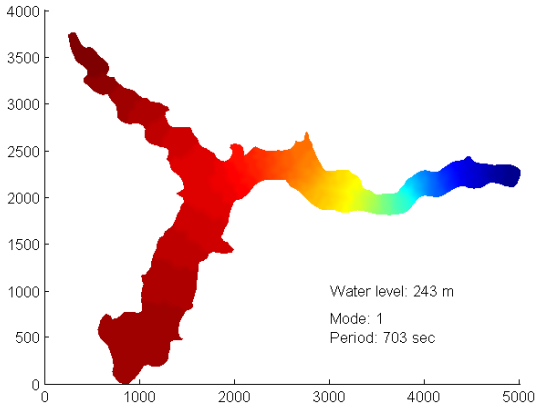
Water level: 243 m
Mode: 1
Period: 703 sec

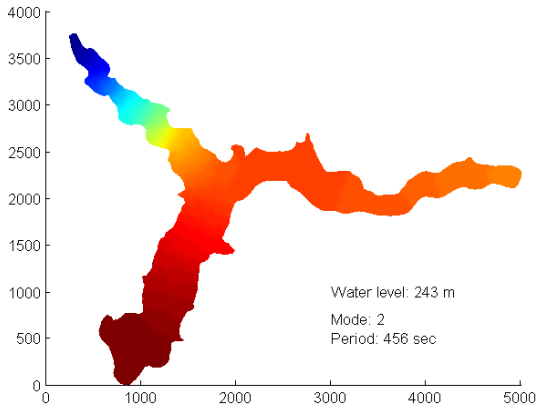
Water level: 243 m
Mode: 2
Period: 456 sec

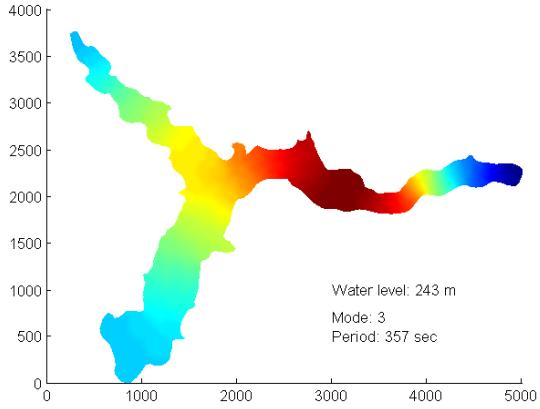
Water level: 243 m
Mode: 3
Period: 357 sec

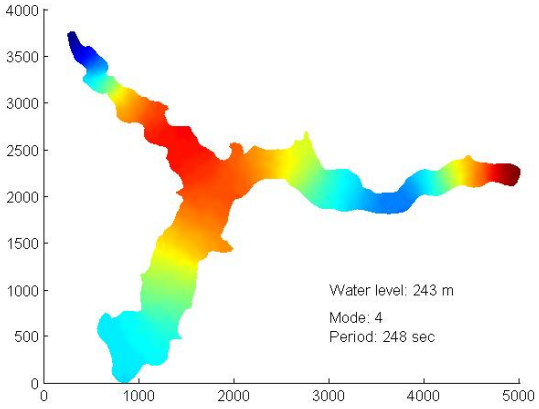
Water level: 243 m
Mode: 4
Period: 248 sec

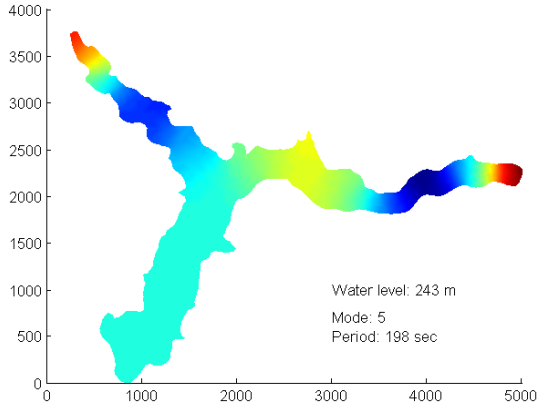
Water level: 243 m
Mode: 5
Period: 198 sec

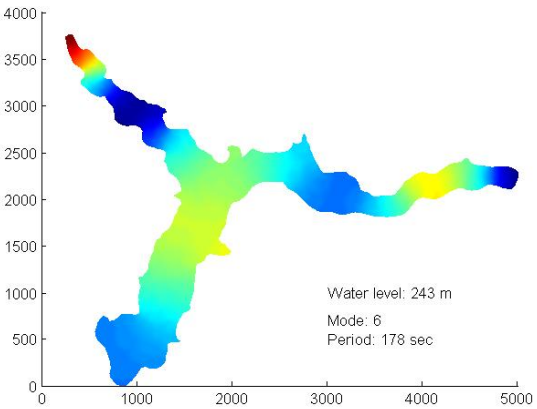
Water level: 243 m
Mode: 6
Period: 178 sec

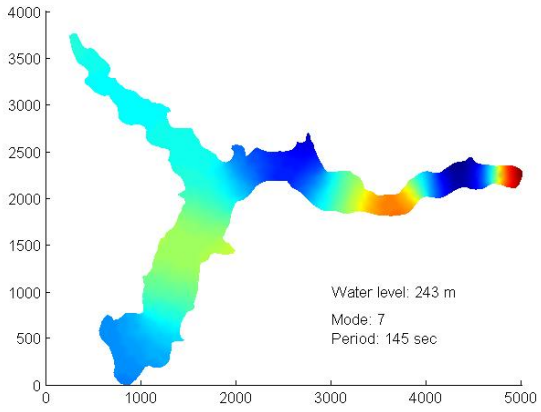
Water level: 243 m
Mode: 7
Period: 145 sec

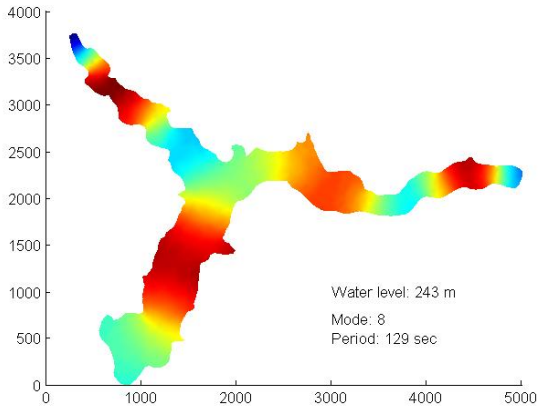
Water level: 243 m
Mode: 8
Period: 129 sec

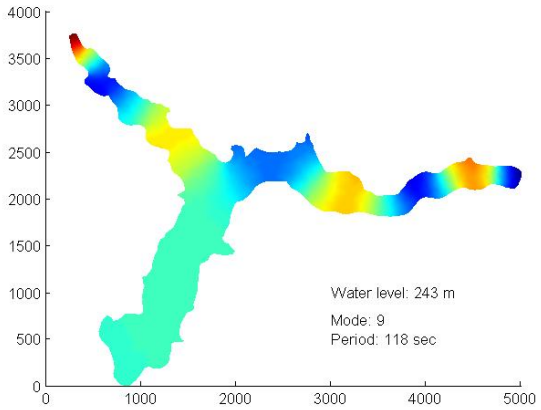
Water level: 243 m
Mode: 9
Period: 118 sec

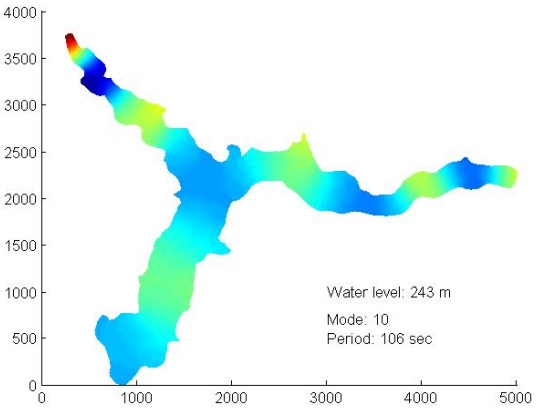
Water level: 243 m
Mode: 10
Period: 106 sec

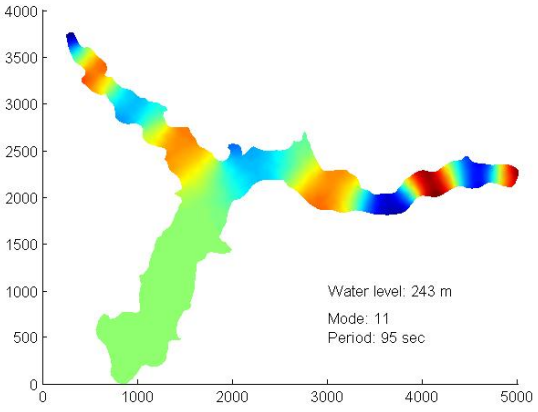
Water level: 243 m
Mode: 11
Period: 95 sec

Appendix C - Field data

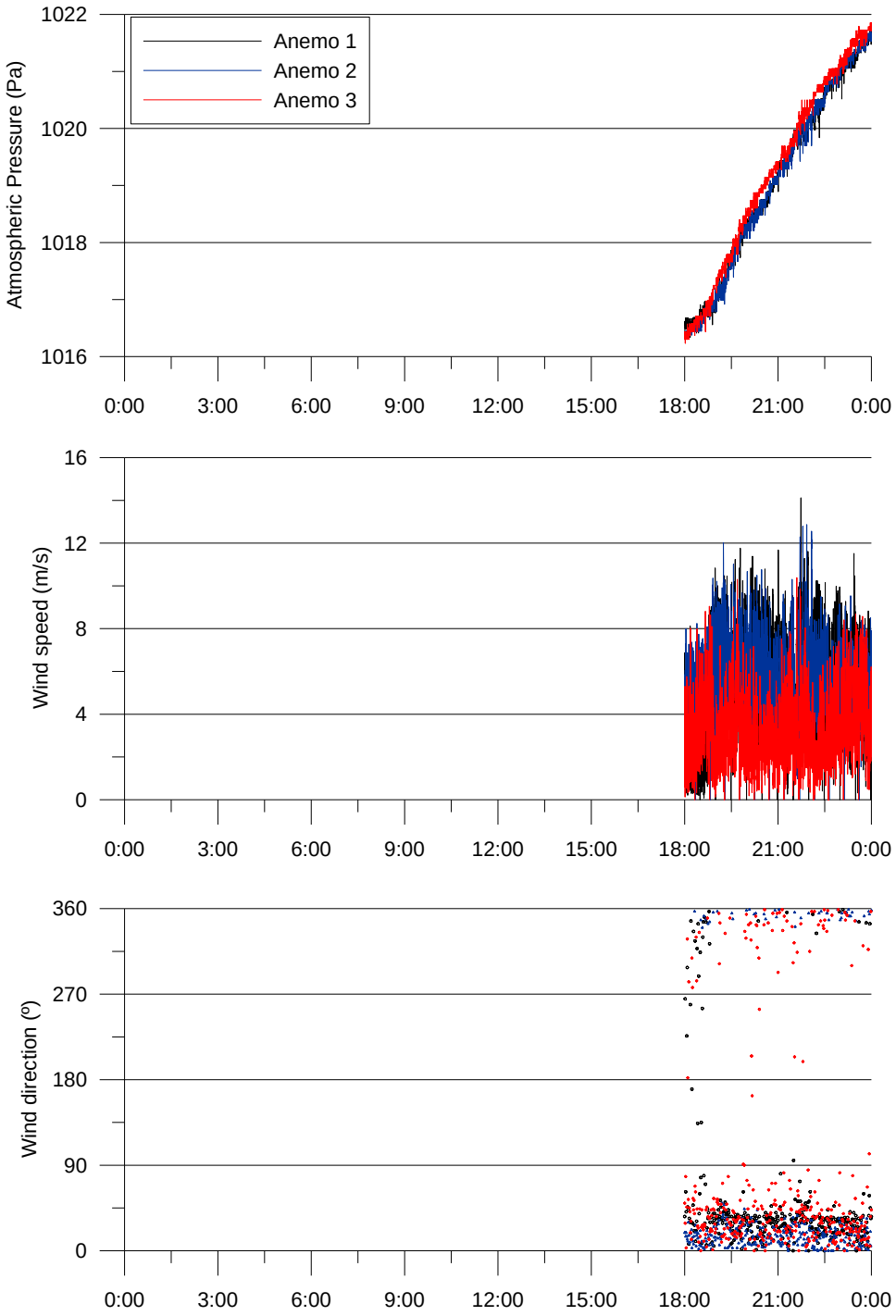

Daily atmospheric conditions. February 14th, 2008.

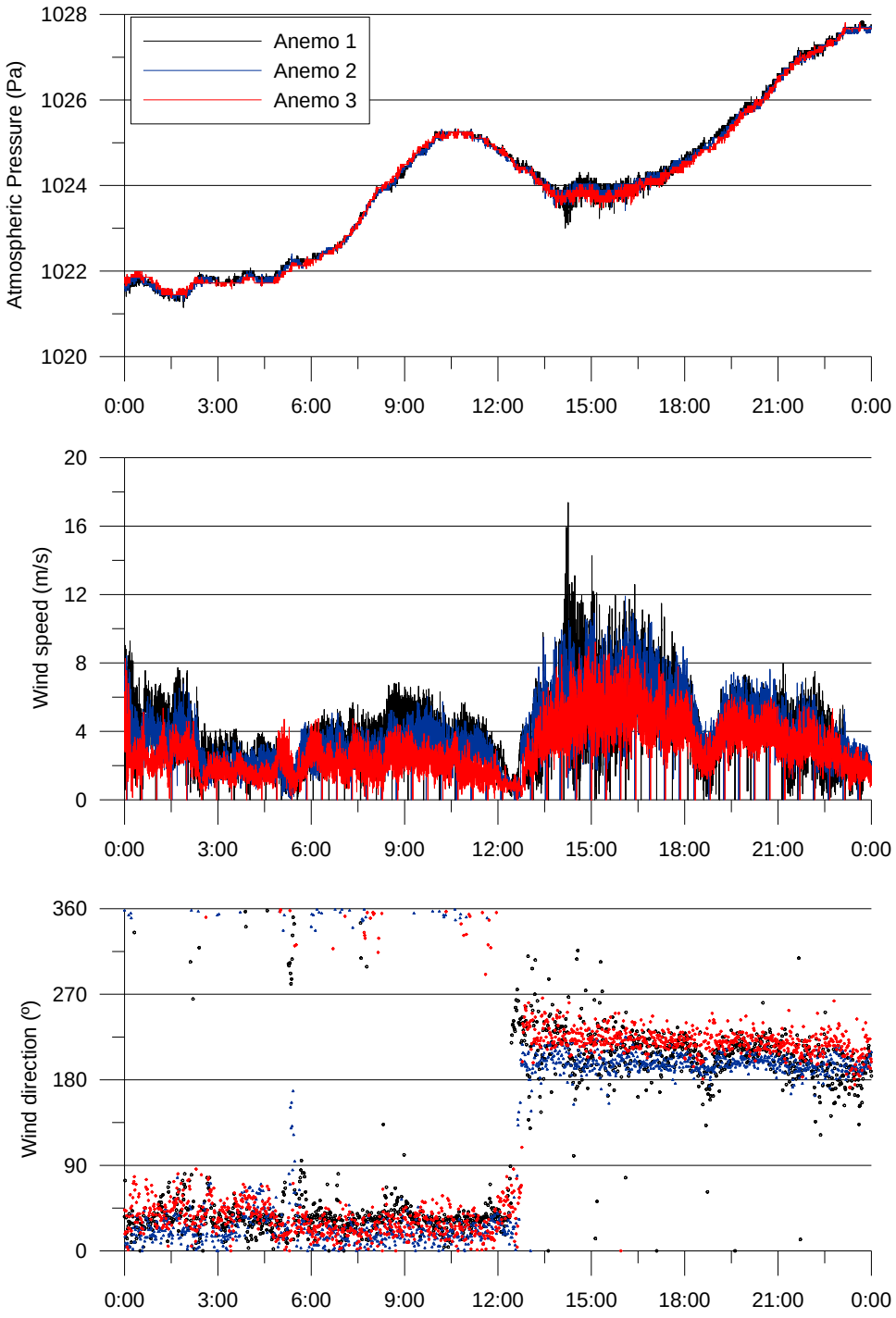

Daily atmospheric conditions. February 15th, 2008.

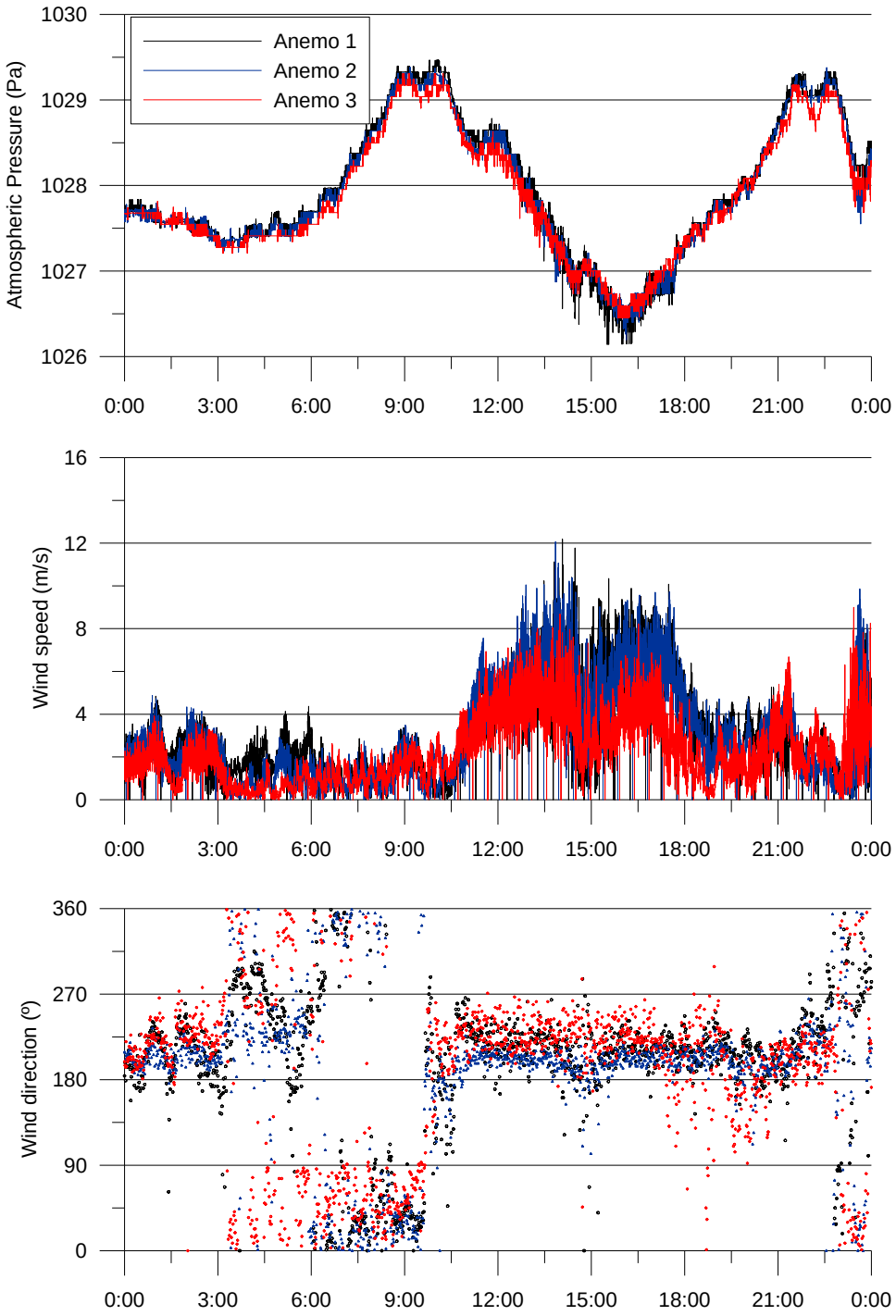

Daily atmospheric conditions. February 16th, 2008.

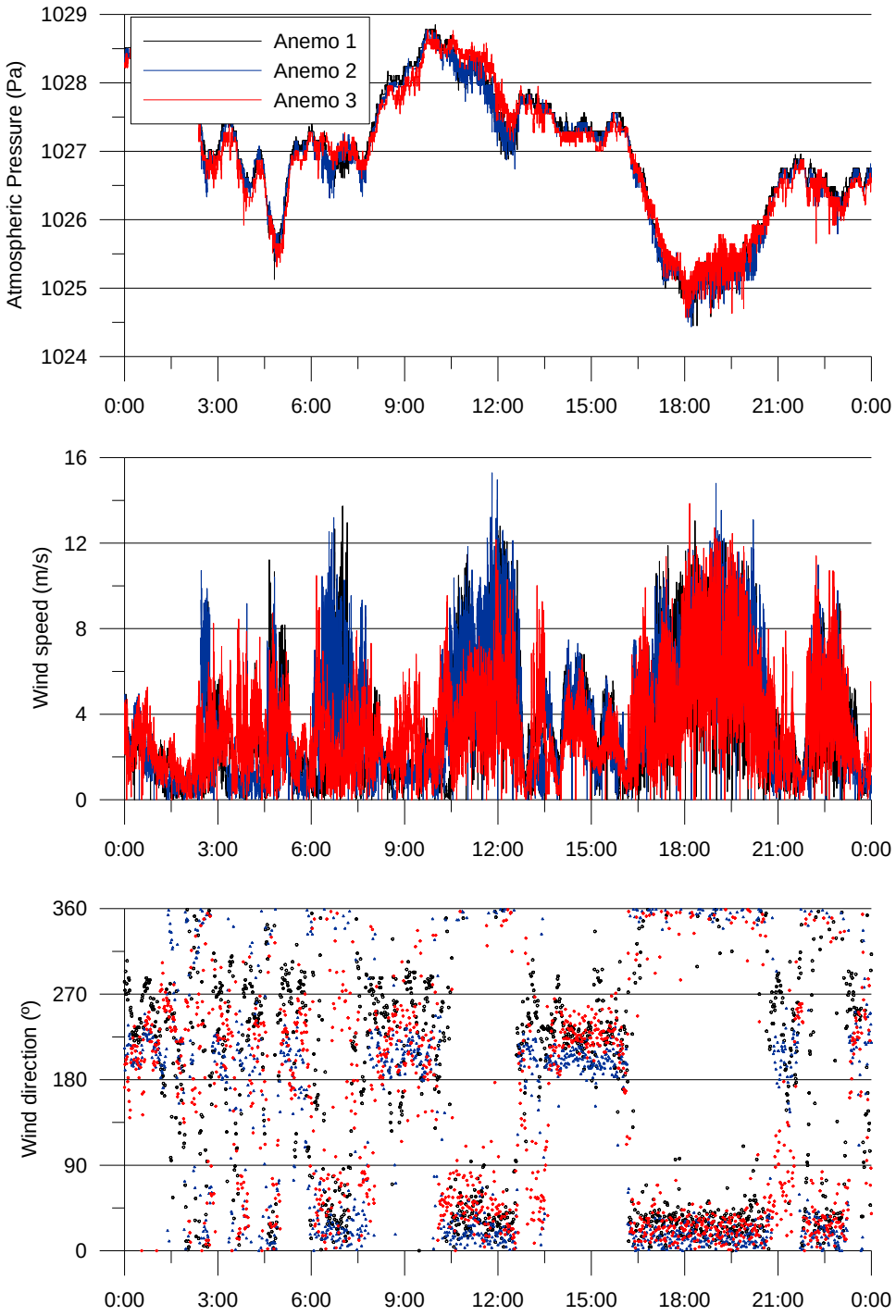

Daily atmospheric conditions. February 17th, 2008.

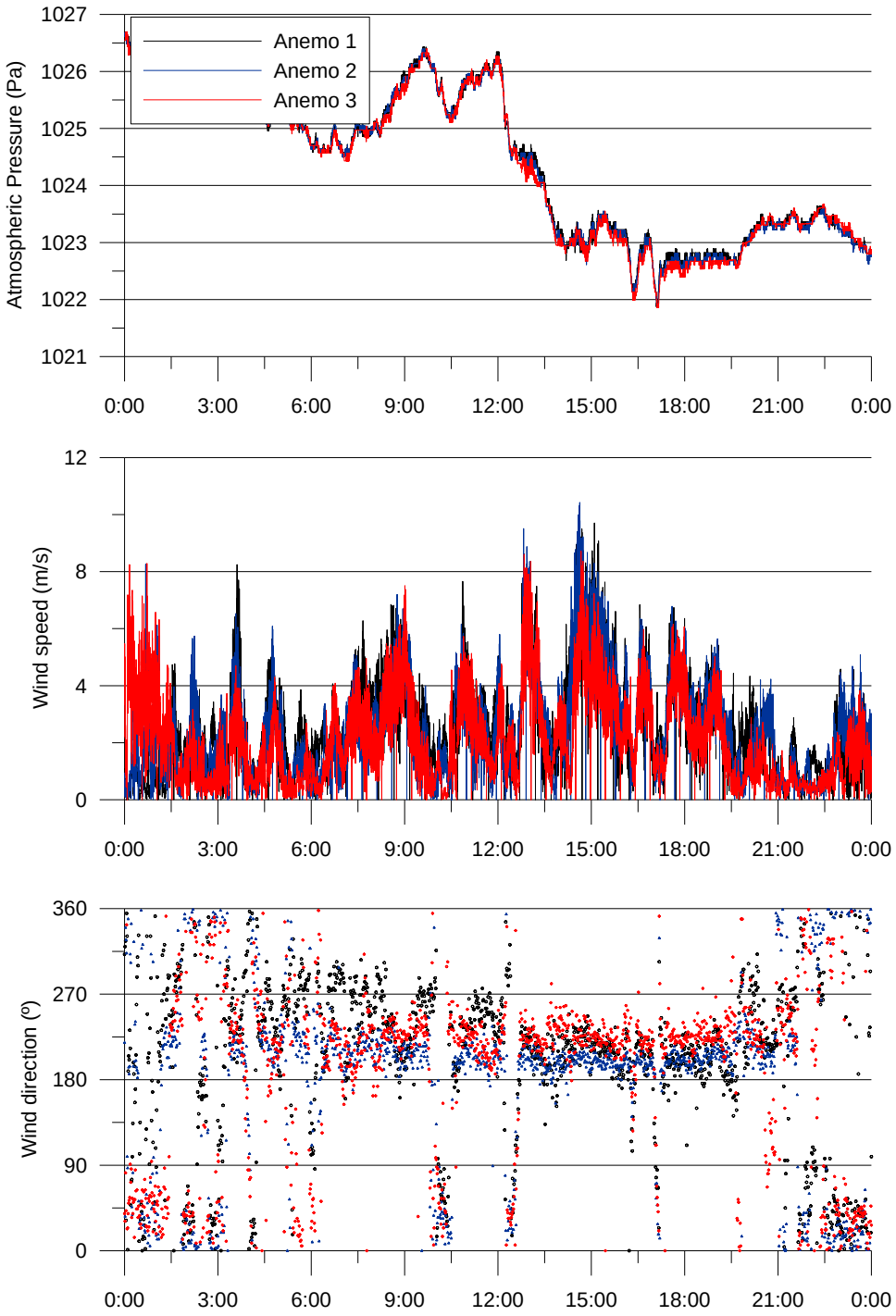

Daily atmospheric conditions. February 18th, 2008.

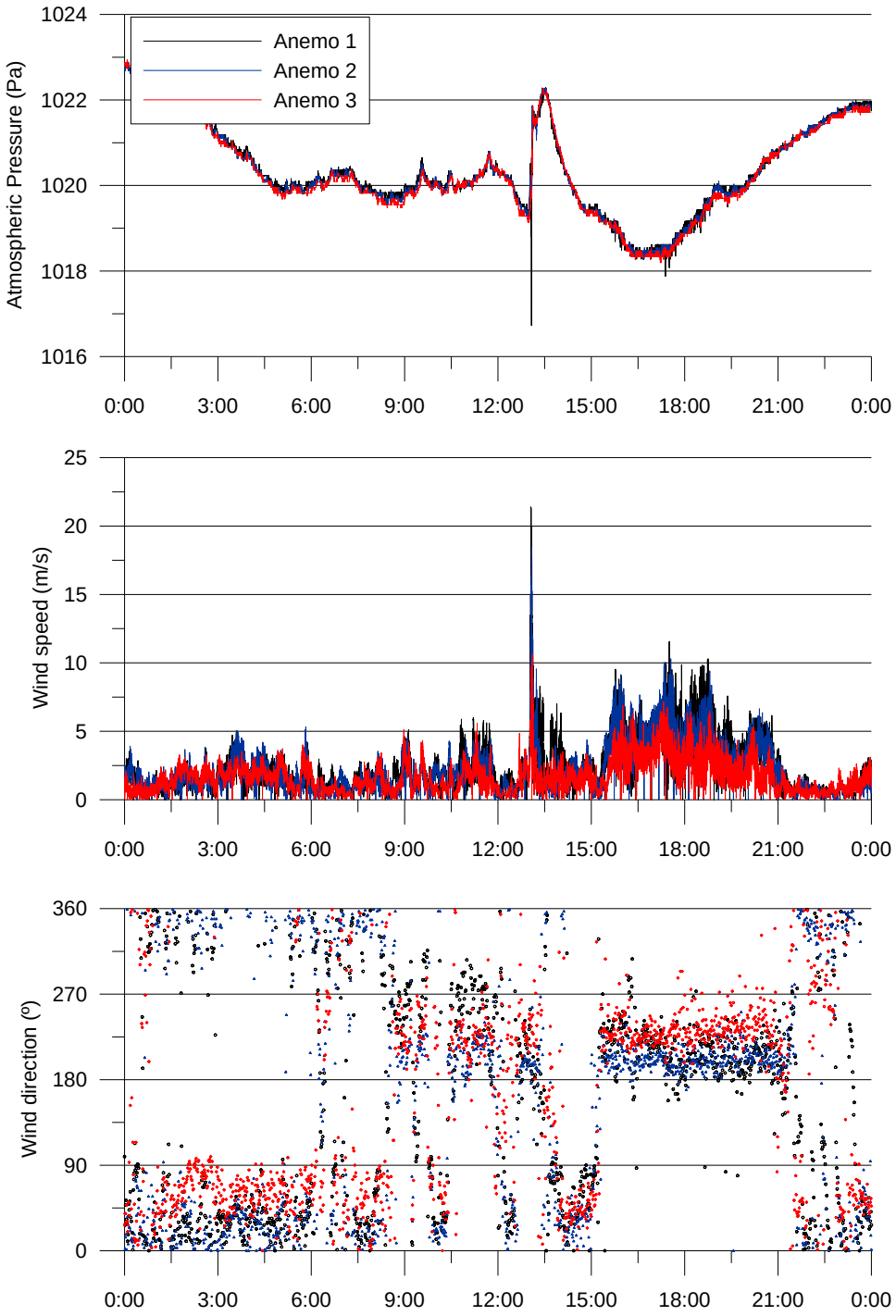

Daily atmospheric conditions. February 19th, 2008.

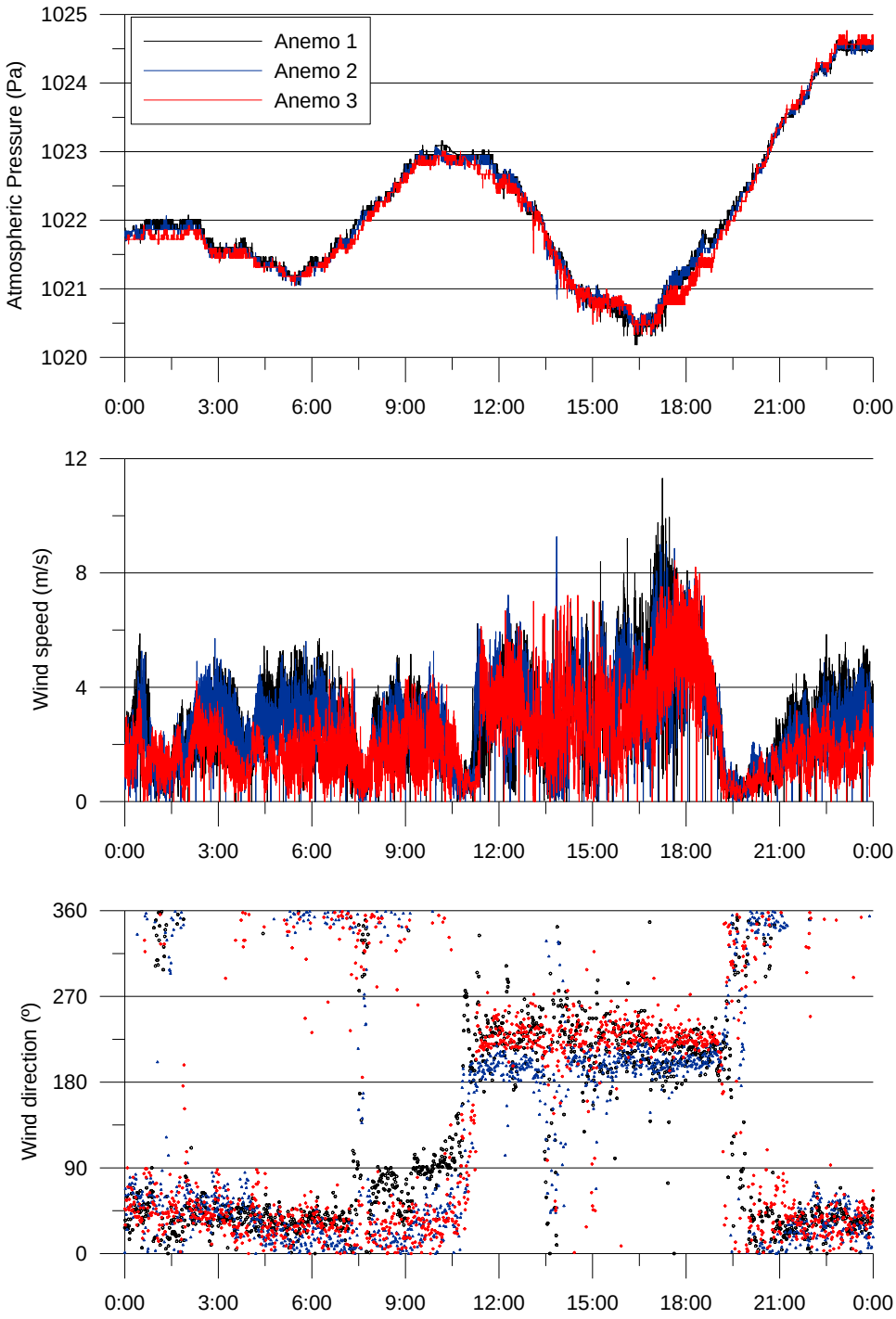

Daily atmospheric conditions. February 20th, 2008.

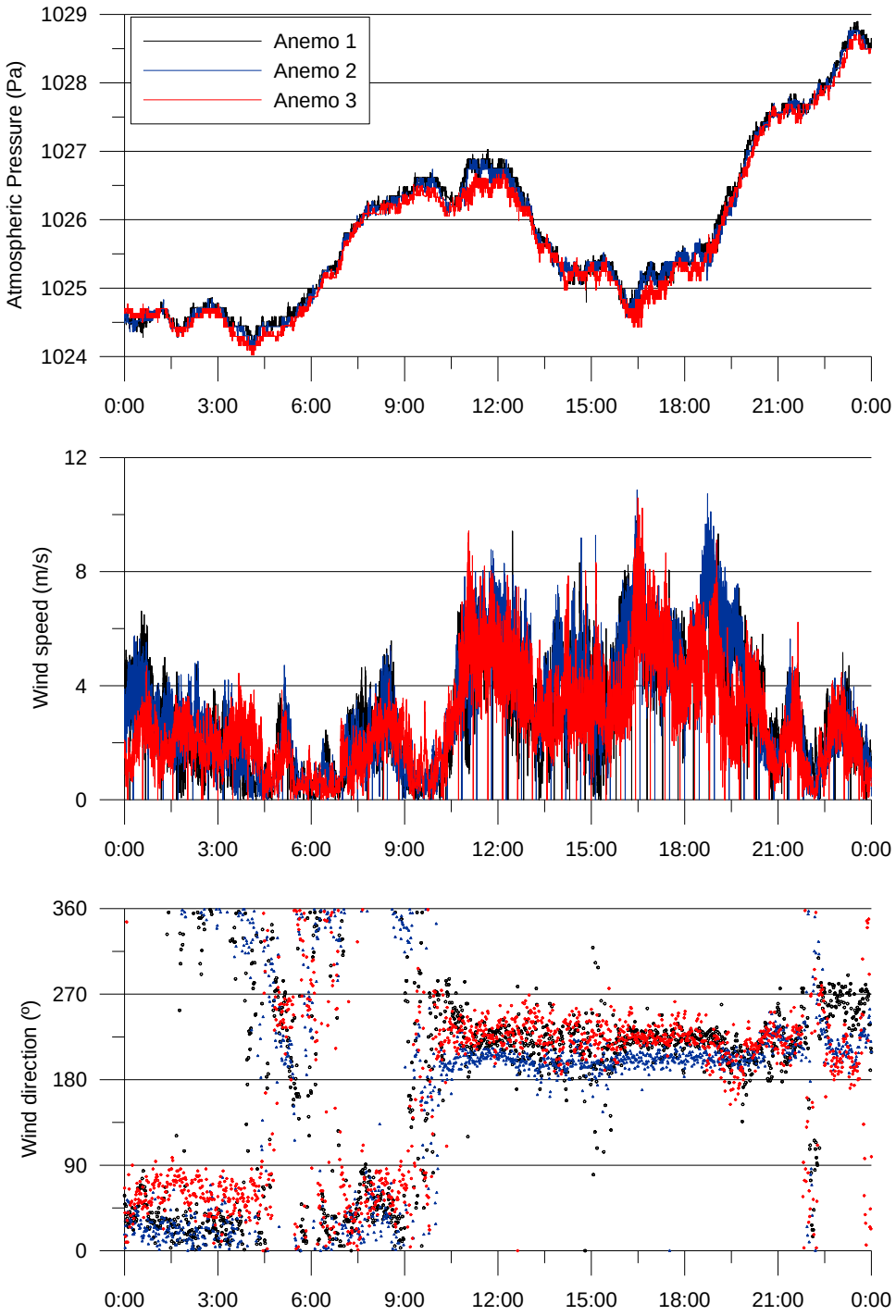

Daily atmospheric conditions. February 21st, 2008.

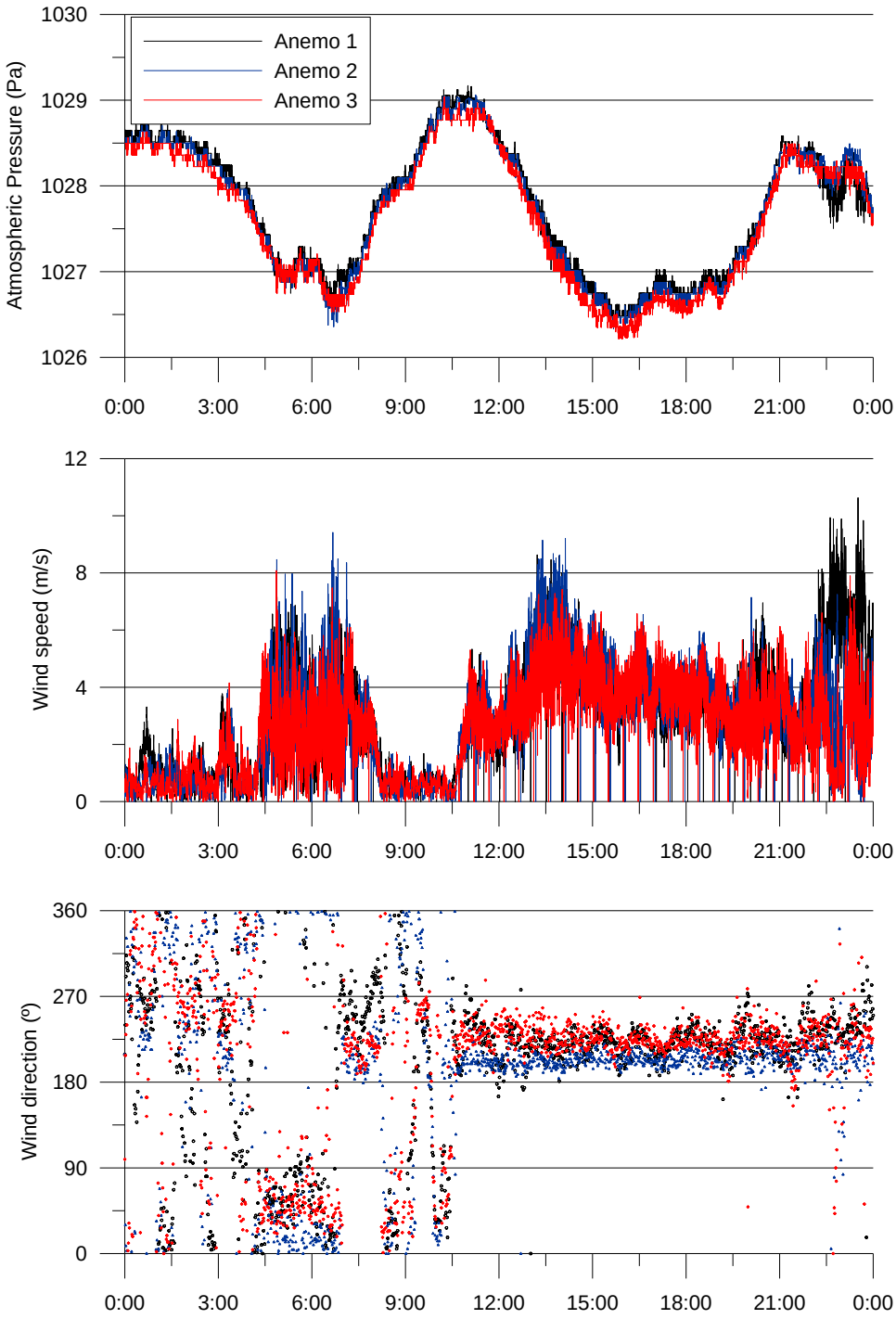

Daily atmospheric conditions. February 22nd, 2008.

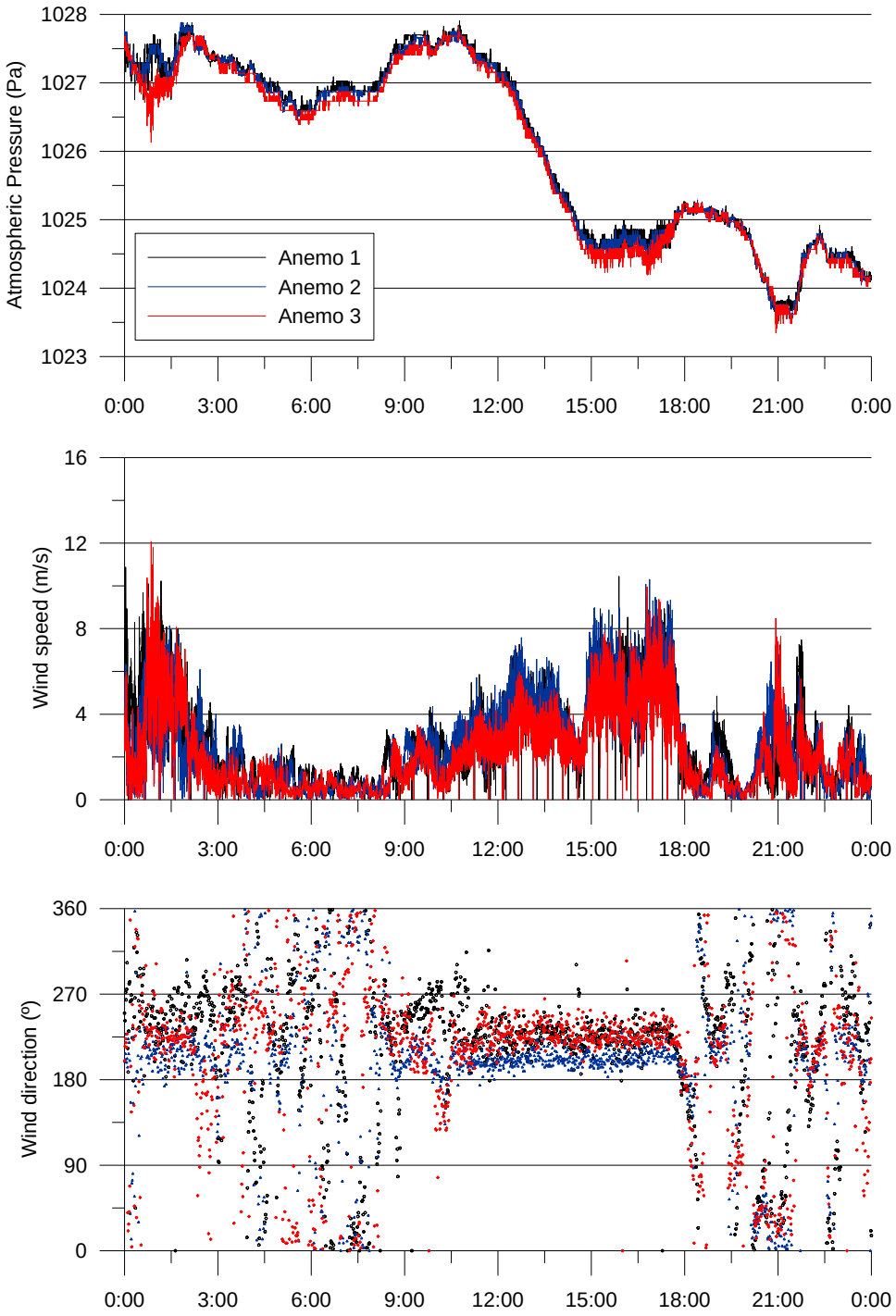

Daily atmospheric conditions. February 23rd, 2008.

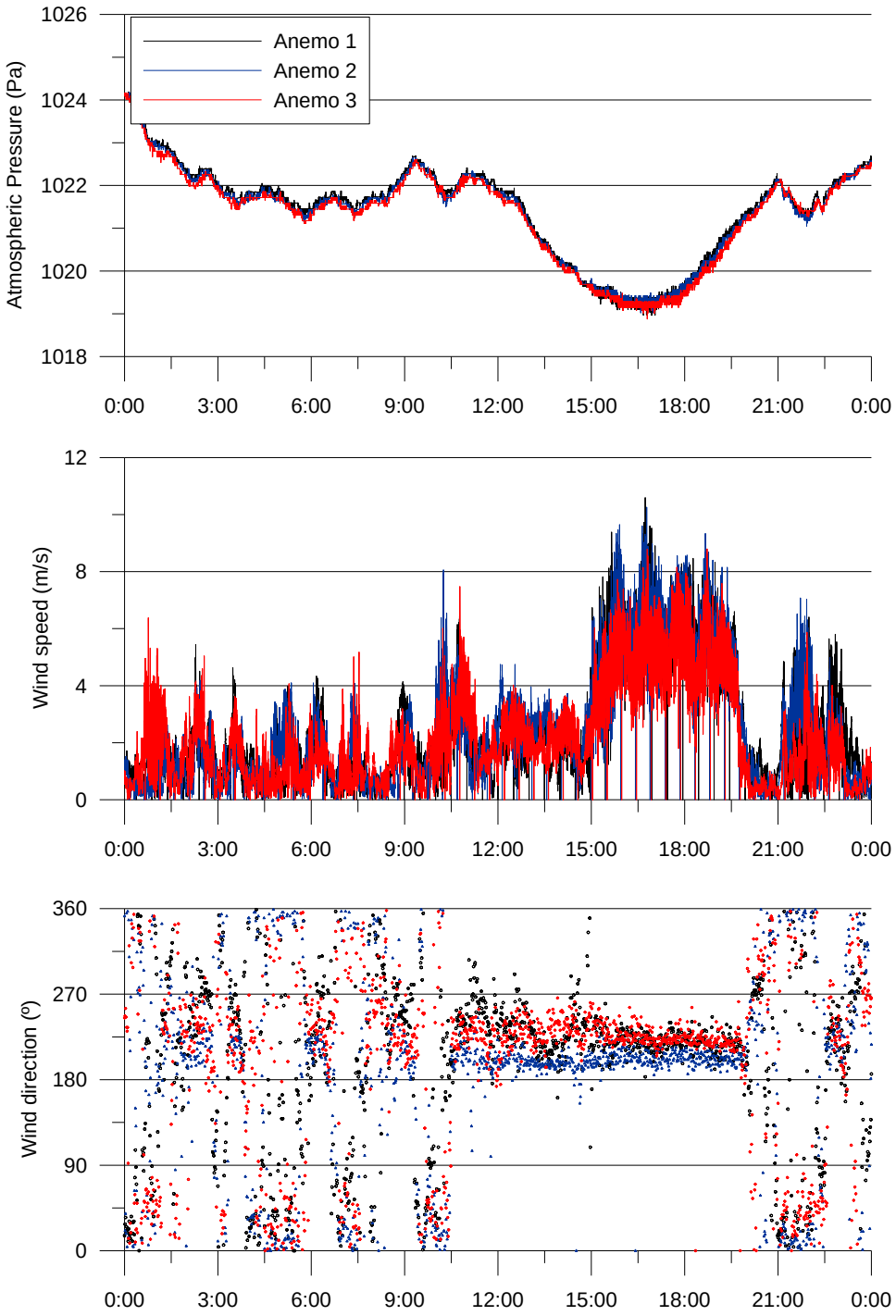

Daily atmospheric conditions. February 24th, 2008.

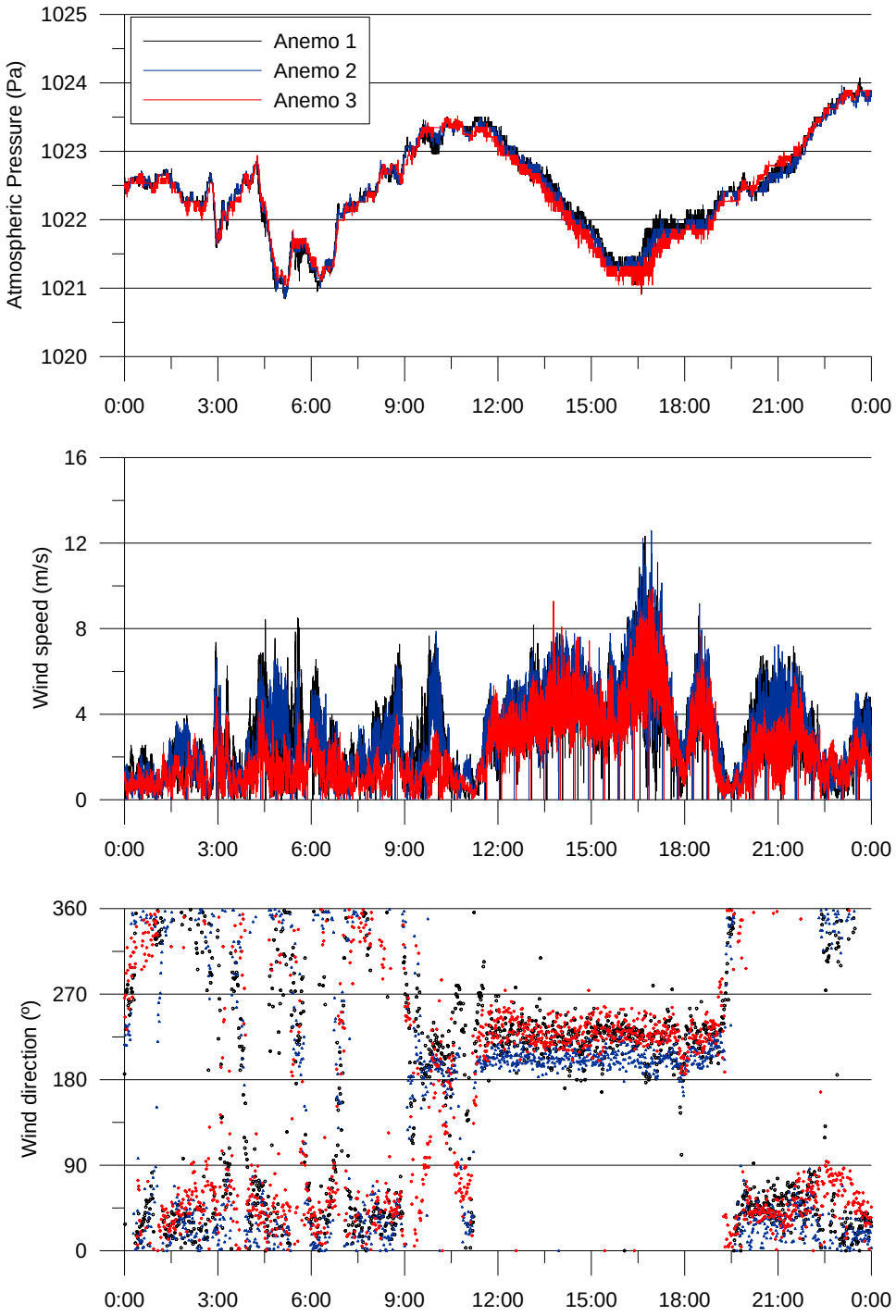

Daily atmospheric conditions. February 25th, 2008.

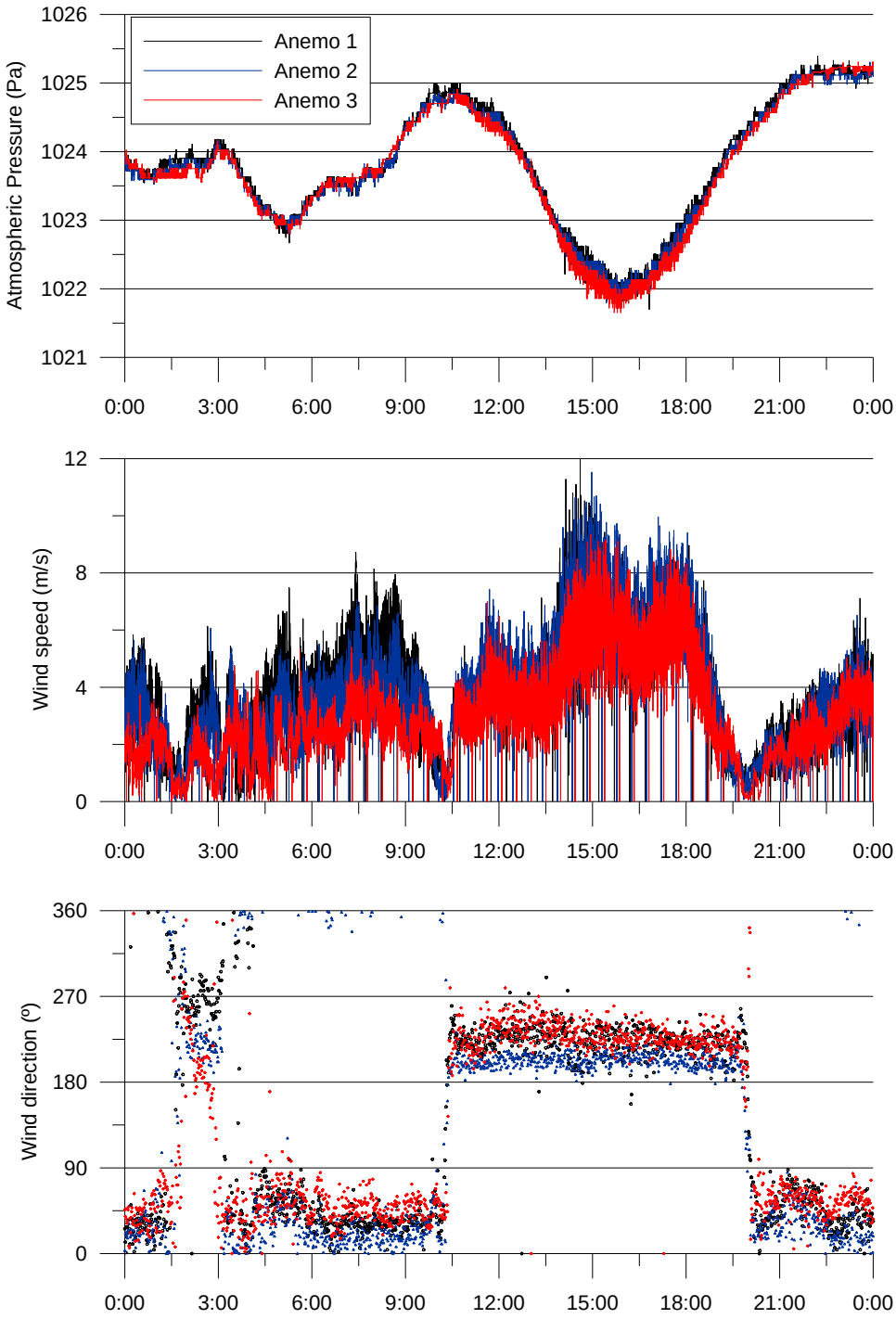

Daily atmospheric conditions. February 26th, 2008.

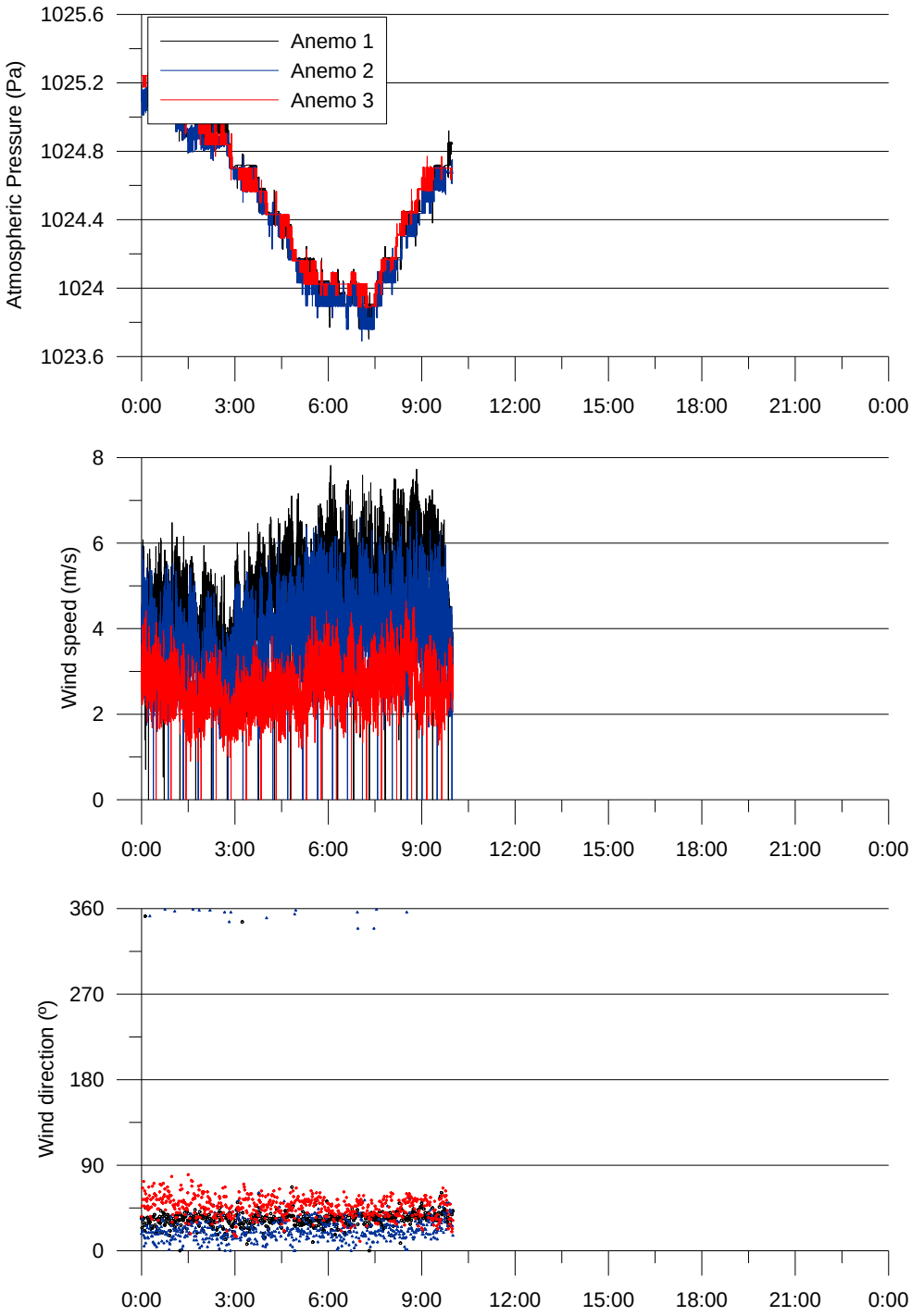

Daily atmospheric conditions. February 27th, 2008.

Appendix D - Hourly FFT of water free surface elevation

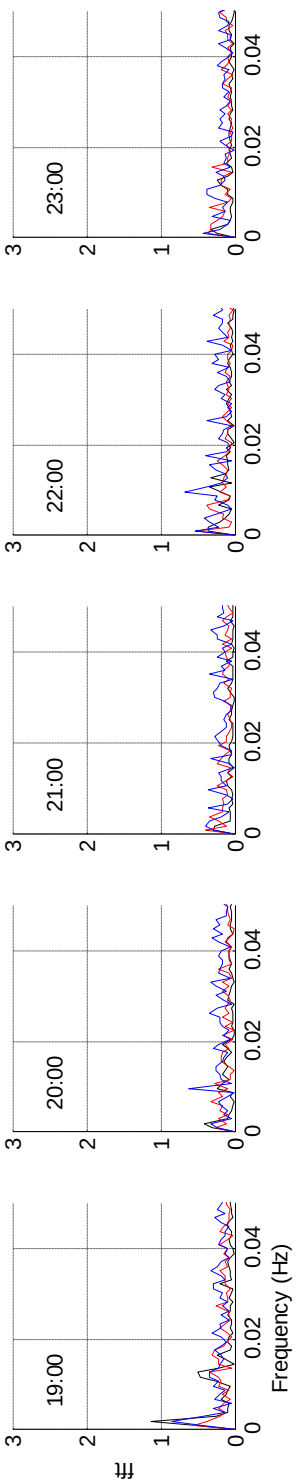

Hourly FFT of water free surface elevation, 14th February, 2008

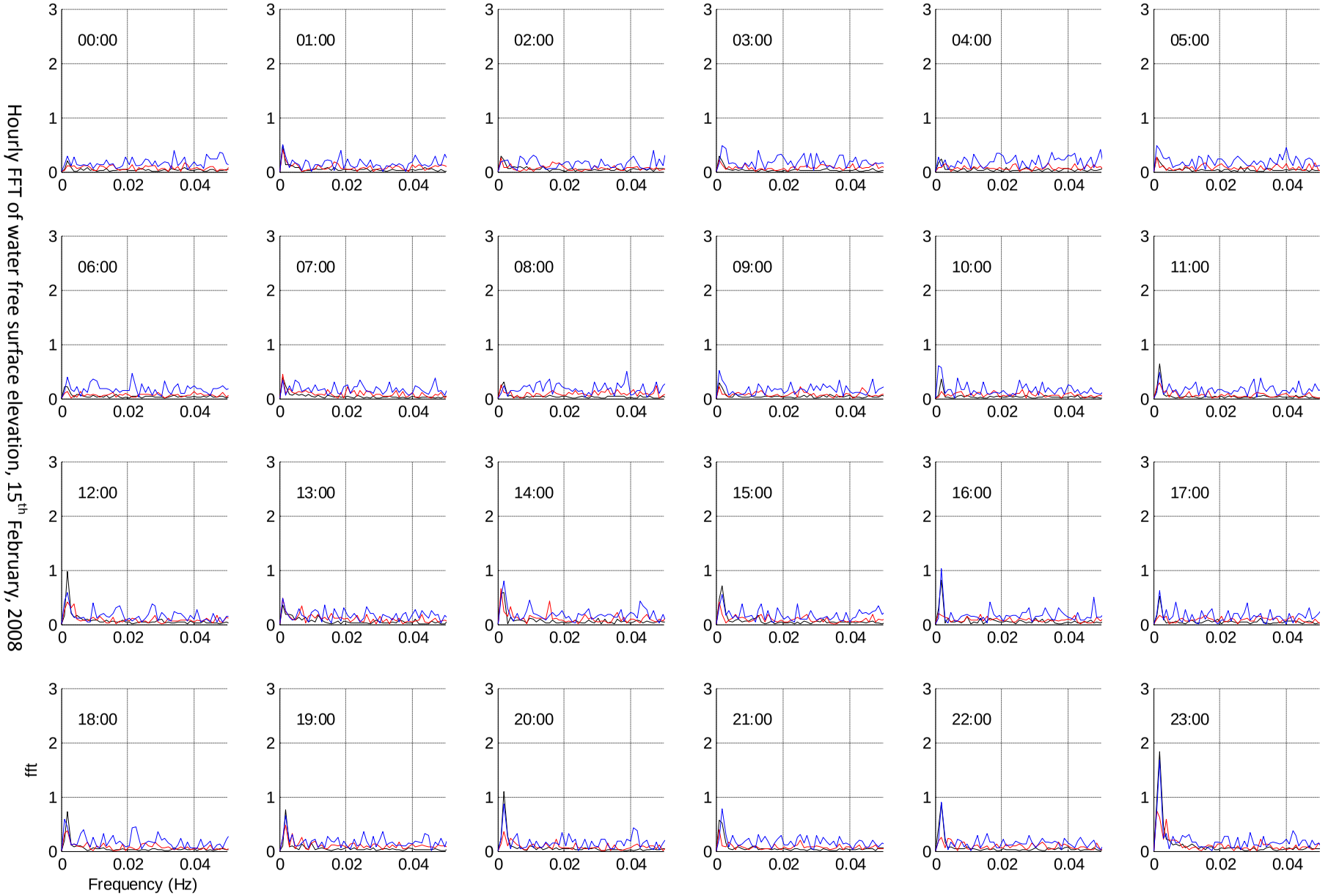
Hourly FFT of water free surface elevation, 15th February, 2008
00:00
01:00
02:00
03:00
04:00
05:00
06:00
07:00
08:00
09:00
10:00
11:00
12:00
13:00
14:00
15:00
16:00
17:00
18:00
19:00
20:00
21:00
22:00
23:00
ff
Frequency (Hz)

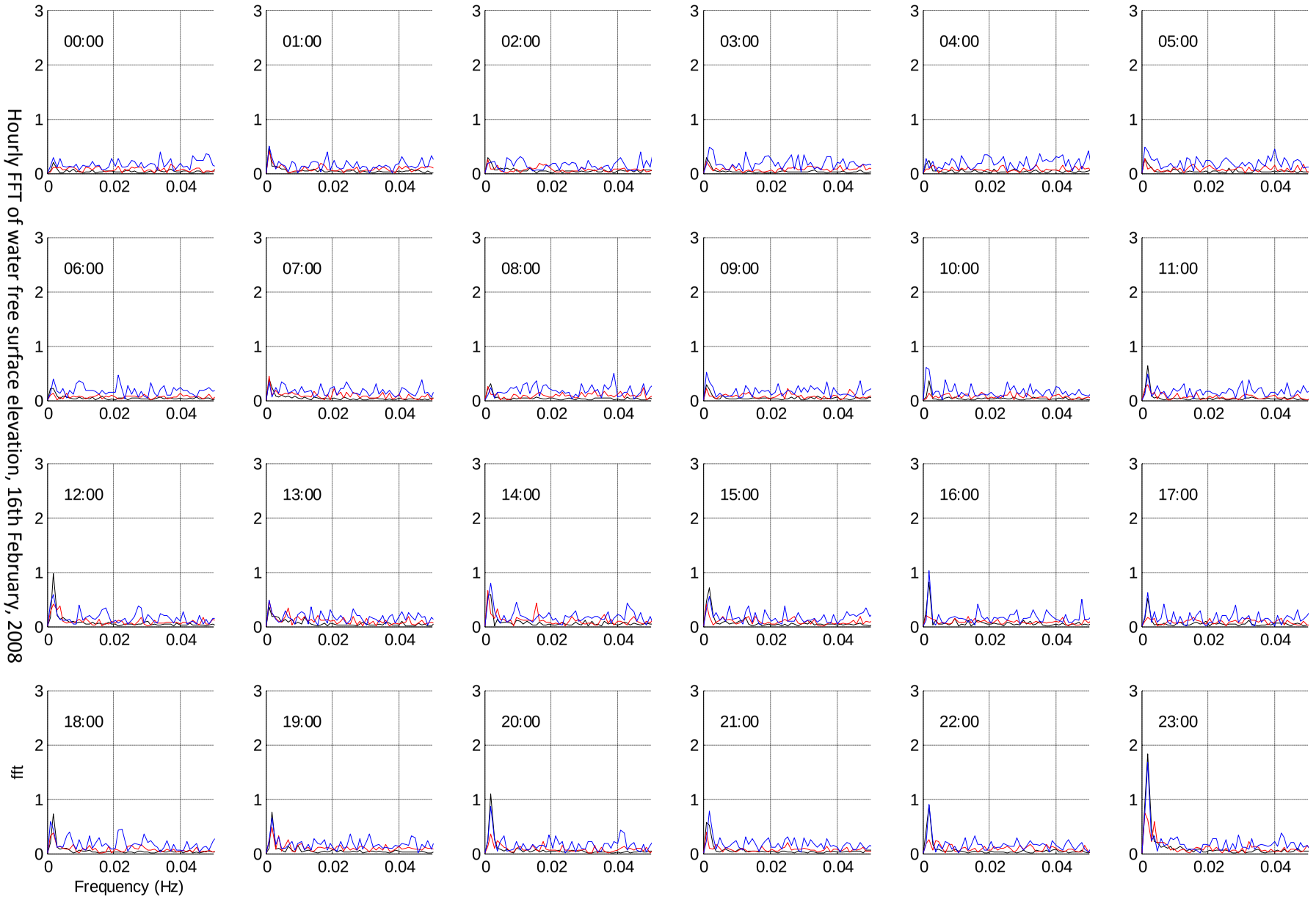
Hourly FFT of water free surface elevation, 16th February, 2008
ft
00:00
01:00
02:00
03:00
04:00
05:00
06:00
07:00
08:00
09:00
10:00
11:00
12:00
13:00
14:00
15:00
16:00
17:00
18:00
19:00
20:00
21:00
22:00
23:00
0
1
2
3
0
0.02
0.04
Frequency (Hz)

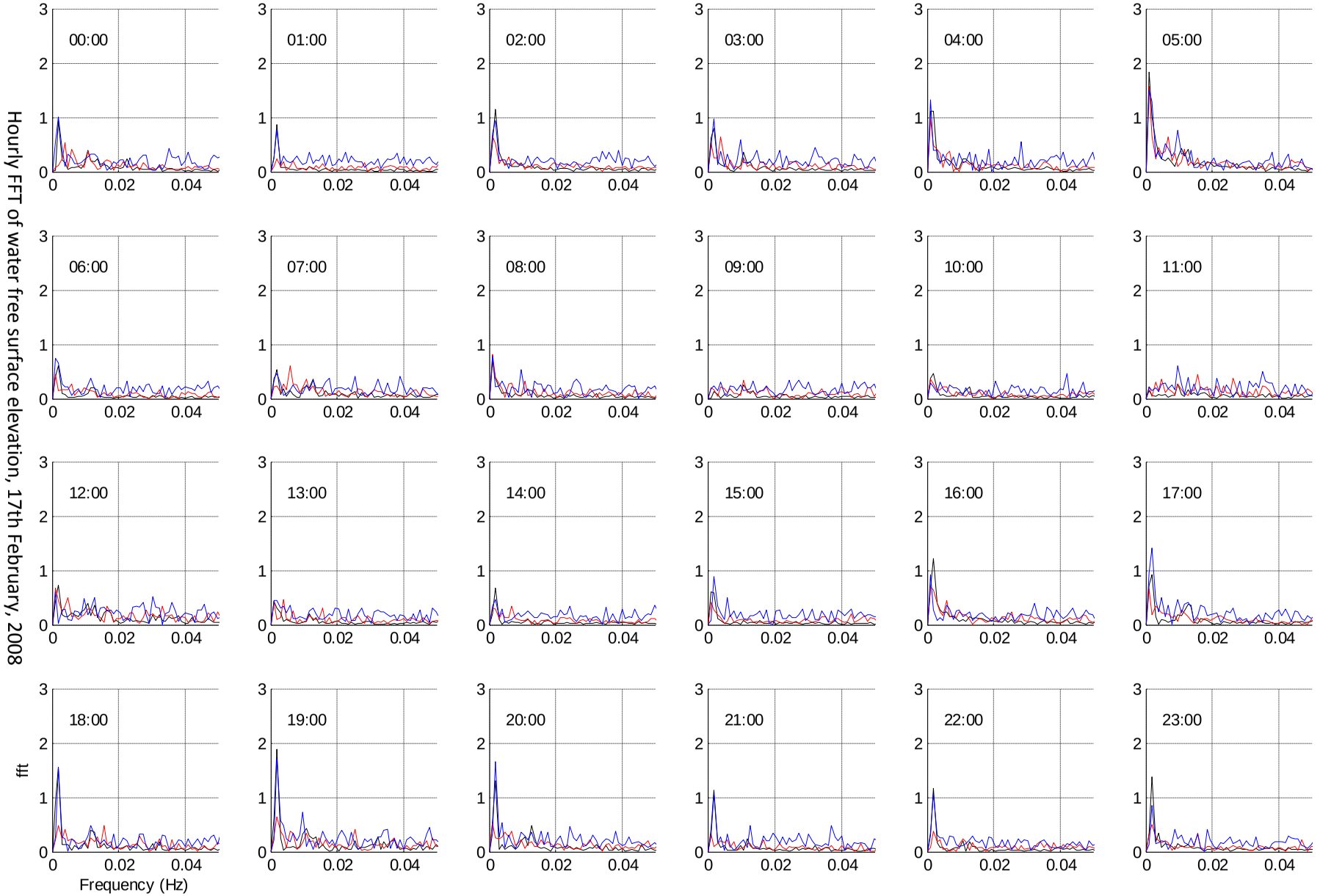
Hourly FFT of water free surface elevation, 17th February, 2008
ff
Frequency (Hz)
00:00
01:00
02:00
03:00
04:00
05:00
06:00
07:00
08:00
09:00
10:00
11:00
12:00
13:00
14:00
15:00
16:00
17:00
18:00
19:00
20:00
21:00
22:00
23:00
0
1
2
3
0.02
0.04

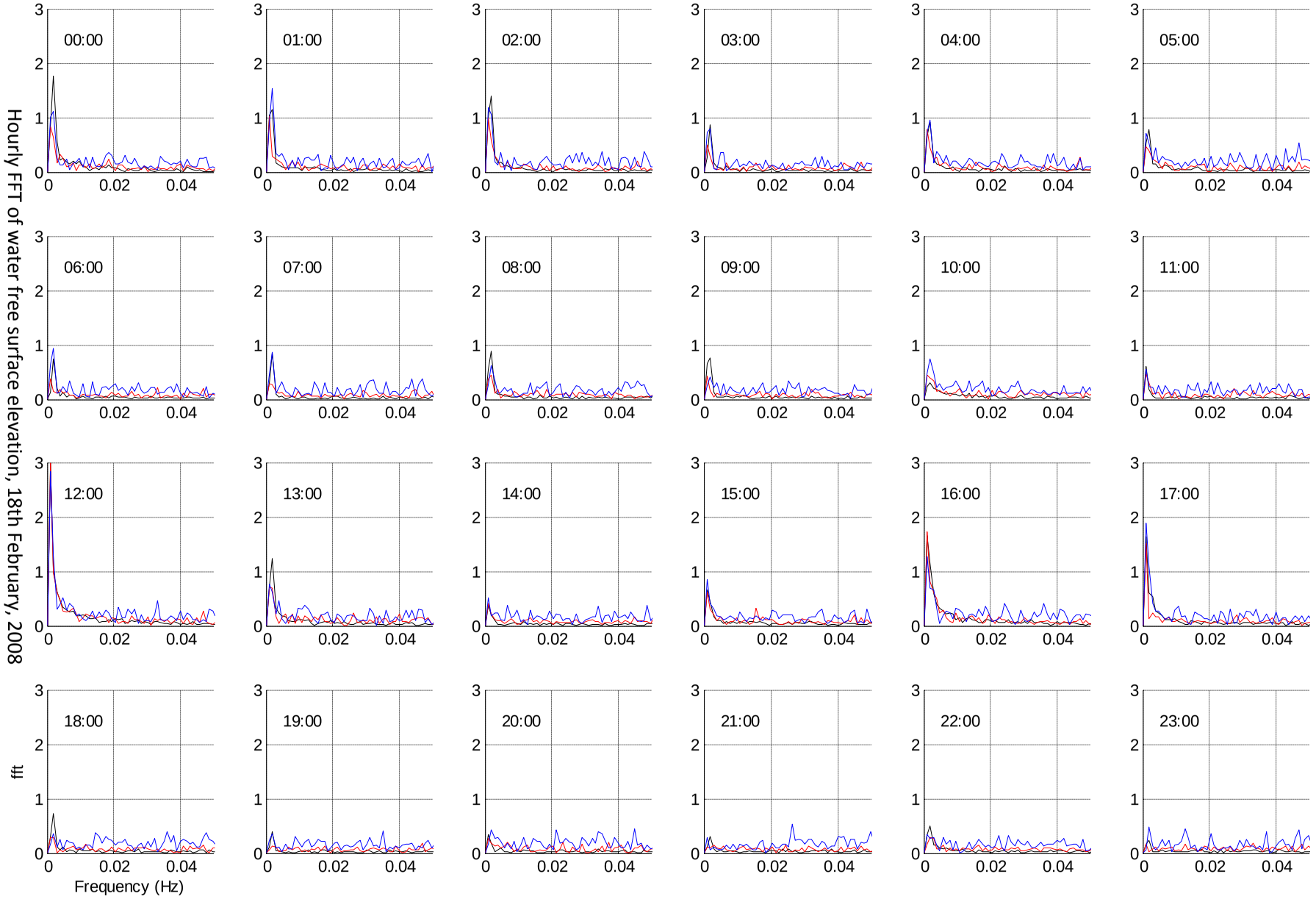
Hourly FFT of water free surface elevation, 18th February, 2008
00:00
01:00
02:00
03:00
04:00
05:00
06:00
07:00
08:00
09:00
10:00
11:00
12:00
13:00
14:00
15:00
16:00
17:00
18:00
19:00
20:00
21:00
22:00
23:00
0
1
2
3
0.02
0.04
ft
Frequency (Hz)

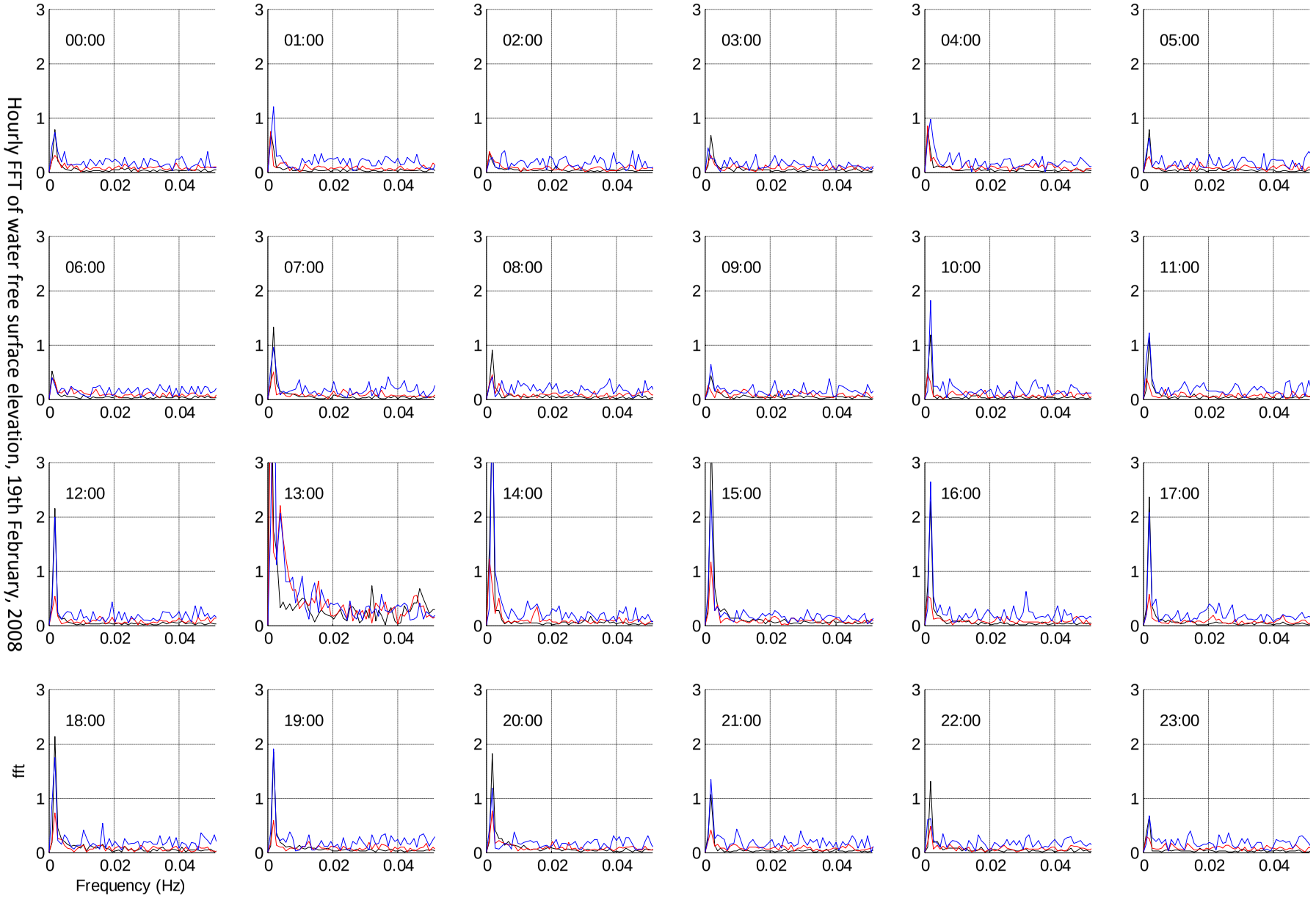
Hourly FFT of water free surface elevation, 19th February, 2008
00:00
01:00
02:00
03:00
04:00
05:00
06:00
07:00
08:00
09:00
10:00
11:00
12:00
13:00
14:00
15:00
16:00
17:00
18:00
19:00
20:00
21:00
22:00
23:00
0
1
2
3
0.02
0.04
Frequency (Hz)
ff

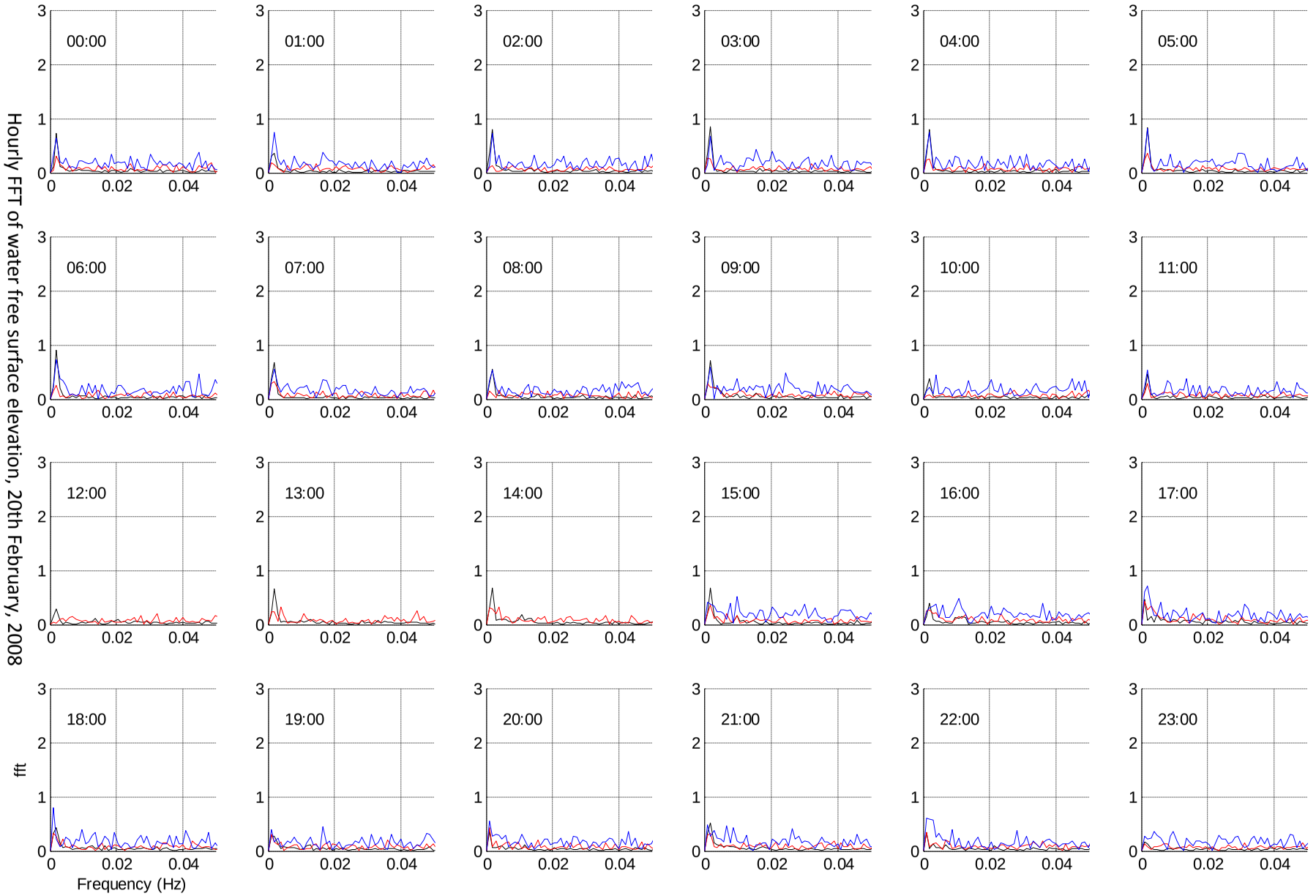
Hourly FFT of water free surface elevation, 20th February, 2008
ft
00:00
01:00
02:00
03:00
04:00
05:00
06:00
07:00
08:00
09:00
10:00
11:00
12:00
13:00
14:00
15:00
16:00
17:00
18:00
19:00
20:00
21:00
22:00
23:00
0
1
2
3
0
0.02
0.04
Frequency (Hz)

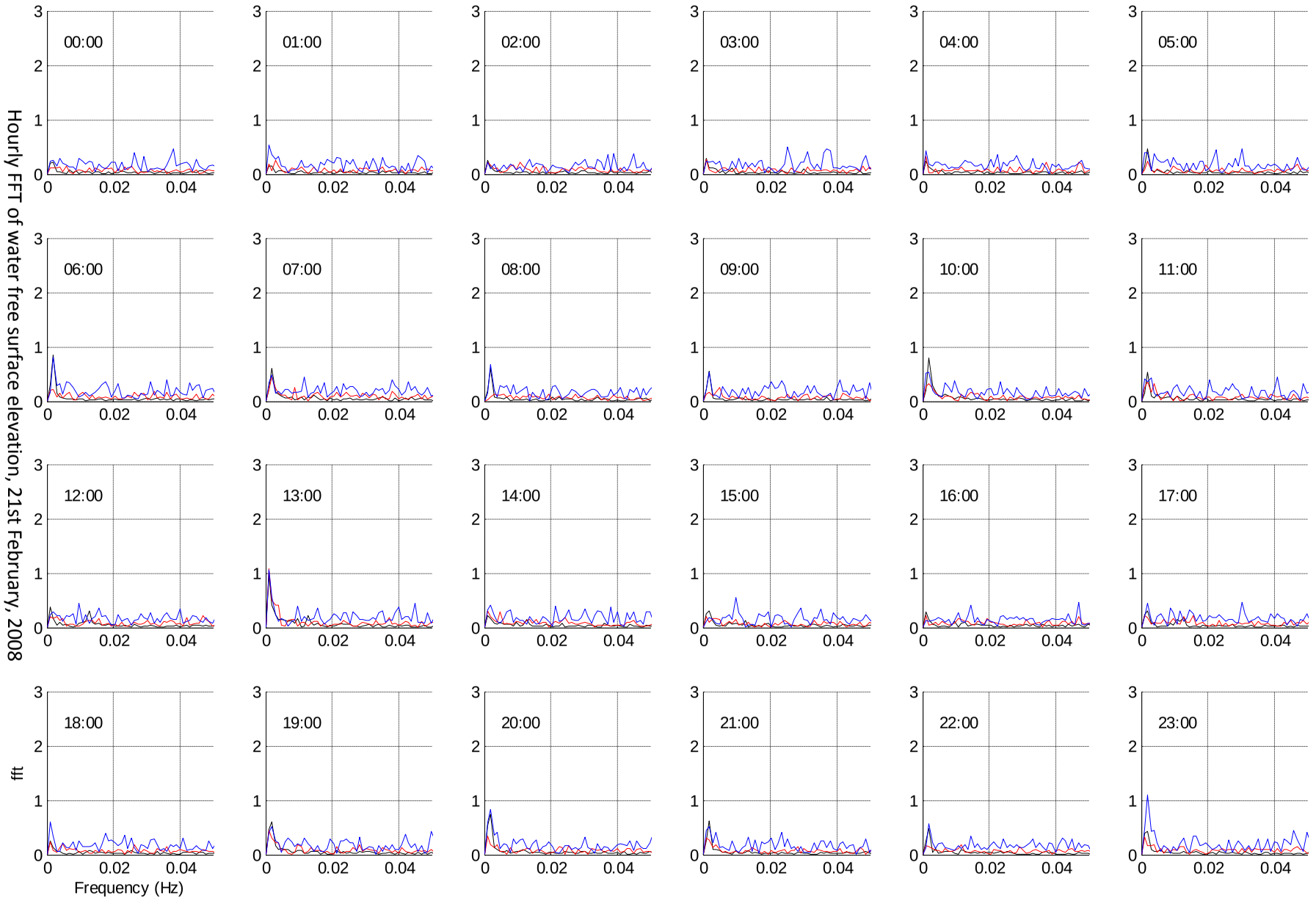
Hourly FFT of water free surface elevation, 21st February, 2008
ff
Frequency (Hz)
00:00
01:00
02:00
03:00
04:00
05:00
06:00
07:00
08:00
09:00
10:00
11:00
12:00
13:00
14:00
15:00
16:00
17:00
18:00
19:00
20:00
21:00
22:00
23:00
0
1
2
3
0.02
0.04

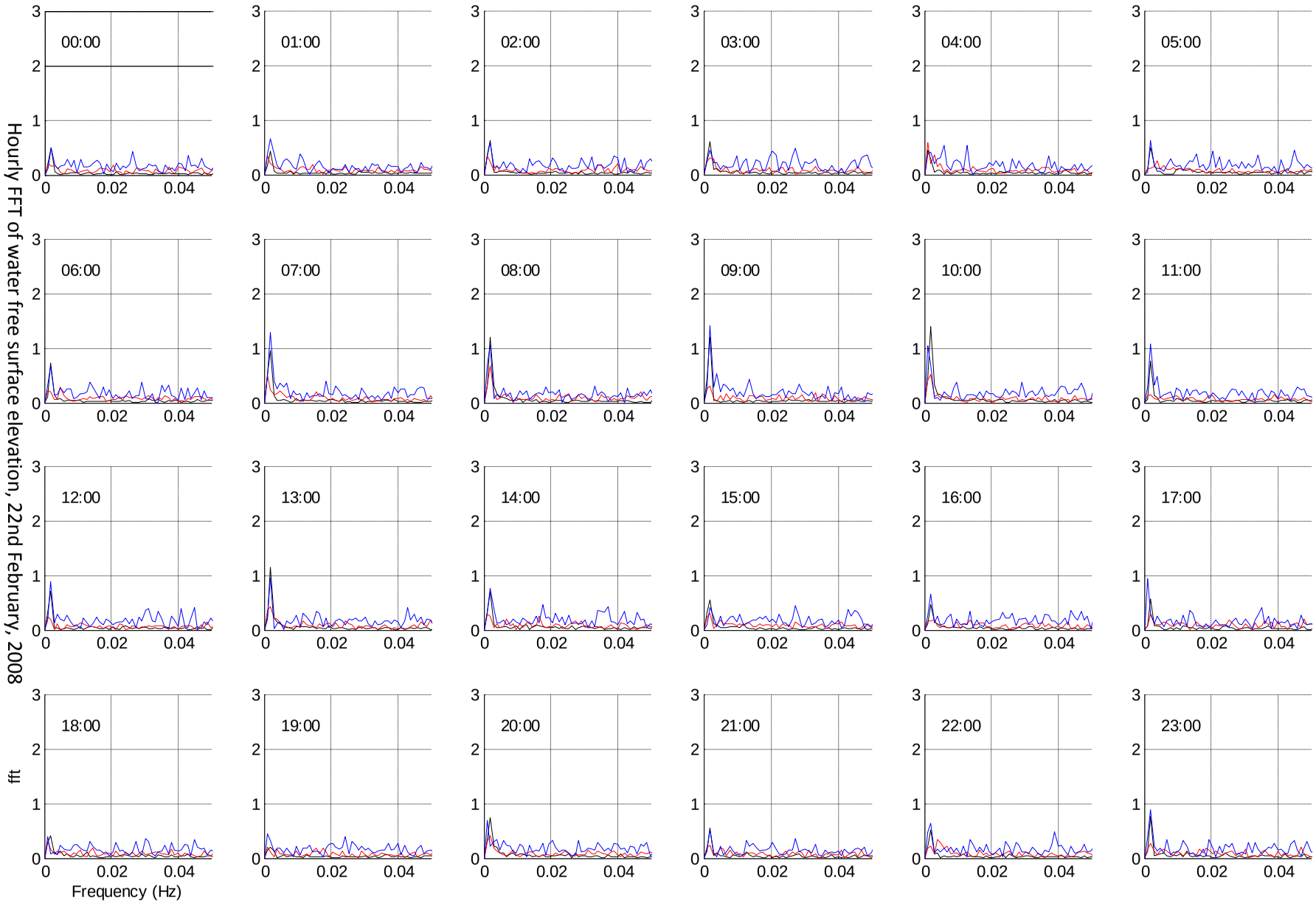
Hourly FFT of water free surface elevation, 22nd February, 2008
ft
00:00
01:00
02:00
03:00
04:00
05:00
06:00
07:00
08:00
09:00
10:00
11:00
12:00
13:00
14:00
15:00
16:00
17:00
18:00
19:00
20:00
21:00
22:00
23:00
0
1
2
3
0
0.02
0.04
Frequency (Hz)

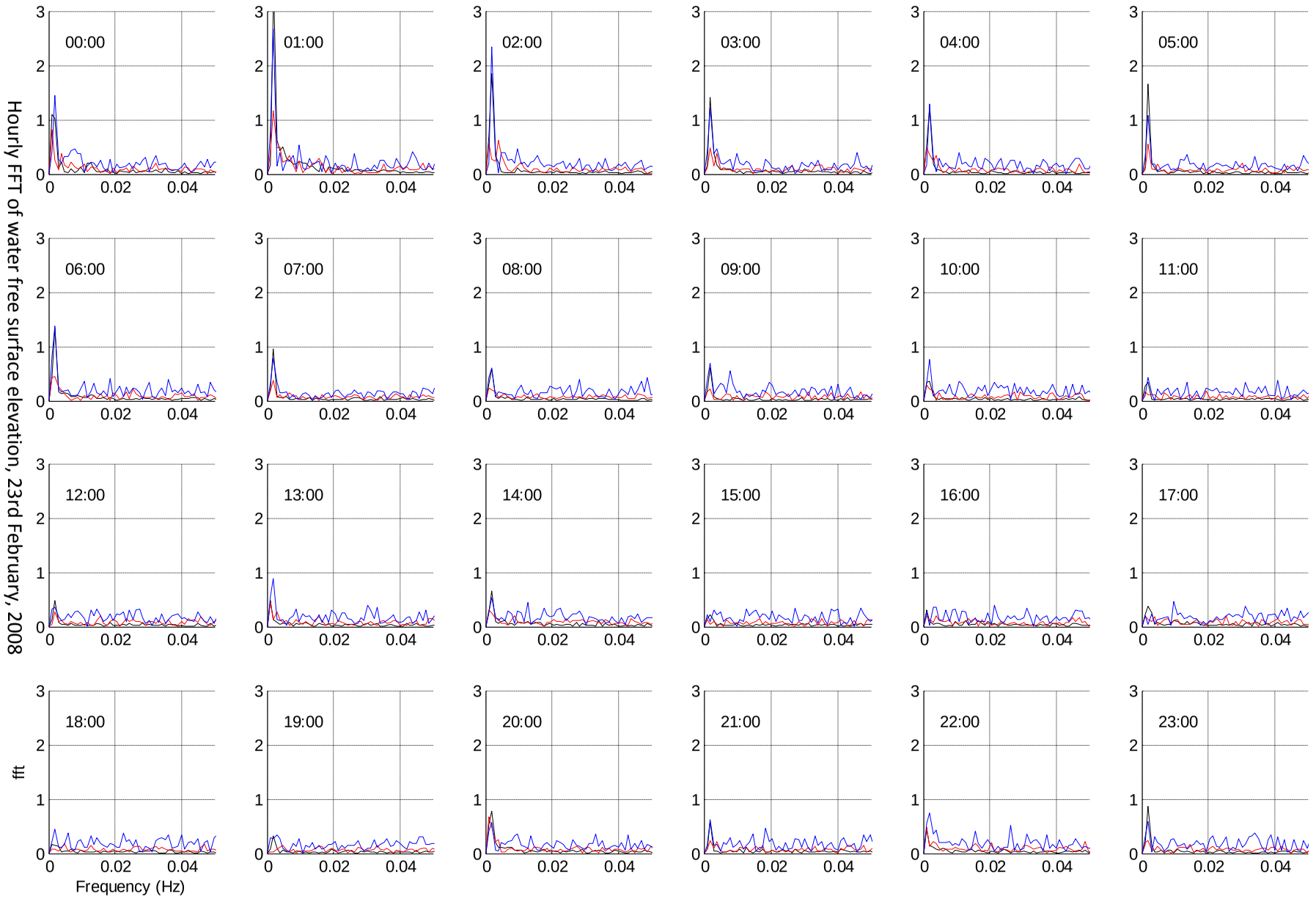
Hourly FFT of water free surface elevation, 23rd February, 2008
00:00
01:00
02:00
03:00
04:00
05:00
06:00
07:00
08:00
09:00
10:00
11:00
12:00
13:00
14:00
15:00
16:00
17:00
18:00
19:00
20:00
21:00
22:00
23:00
0
1
2
3
0.02
0.04
Frequency (Hz)
fft

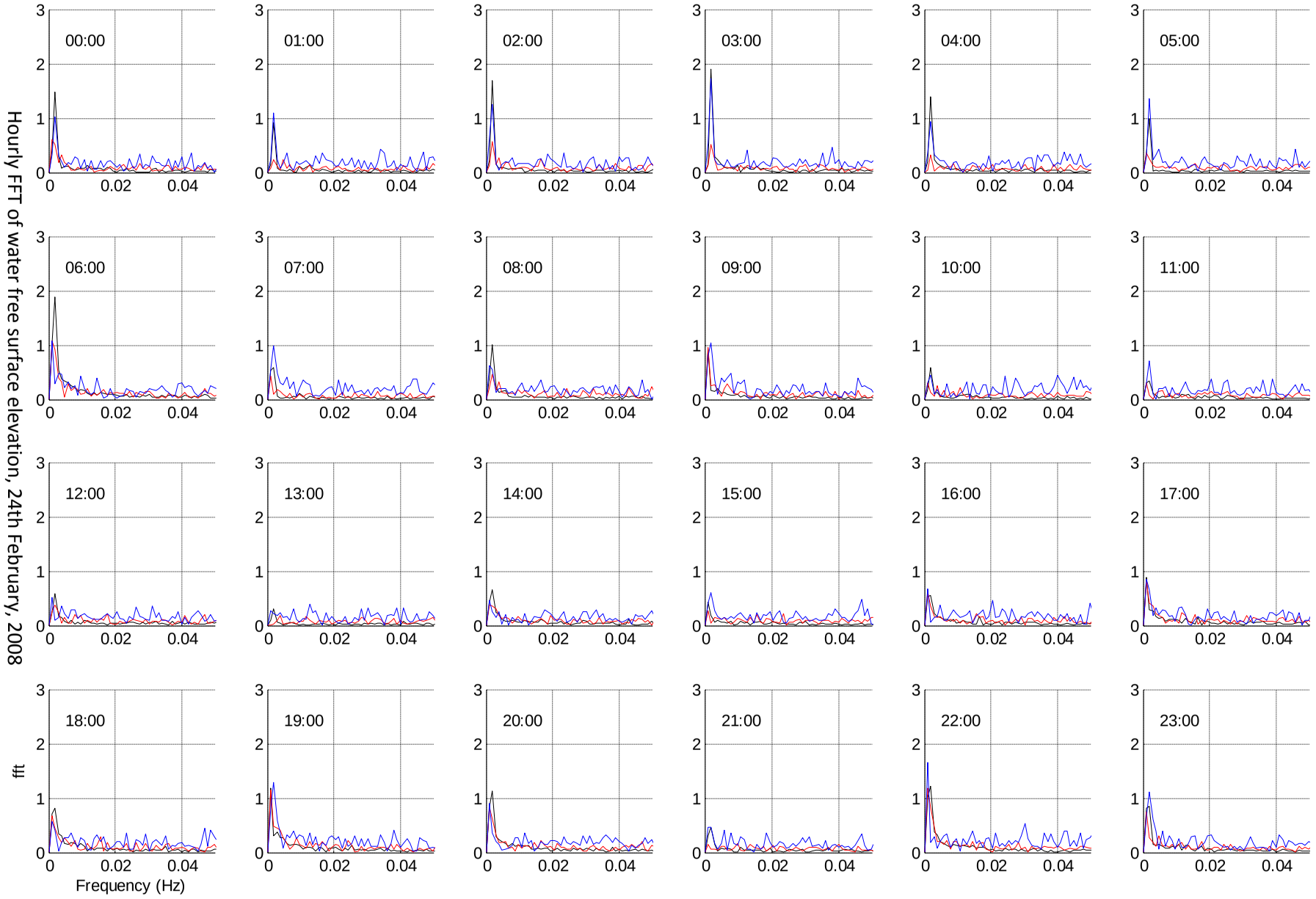
Hourly FFT of water free surface elevation, 24th February, 2008
ft
00:00
01:00
02:00
03:00
04:00
05:00
06:00
07:00
08:00
09:00
10:00
11:00
12:00
13:00
14:00
15:00
16:00
17:00
18:00
19:00
20:00
21:00
22:00
23:00
0
1
2
3
0
0.02
0.04
Frequency (Hz)

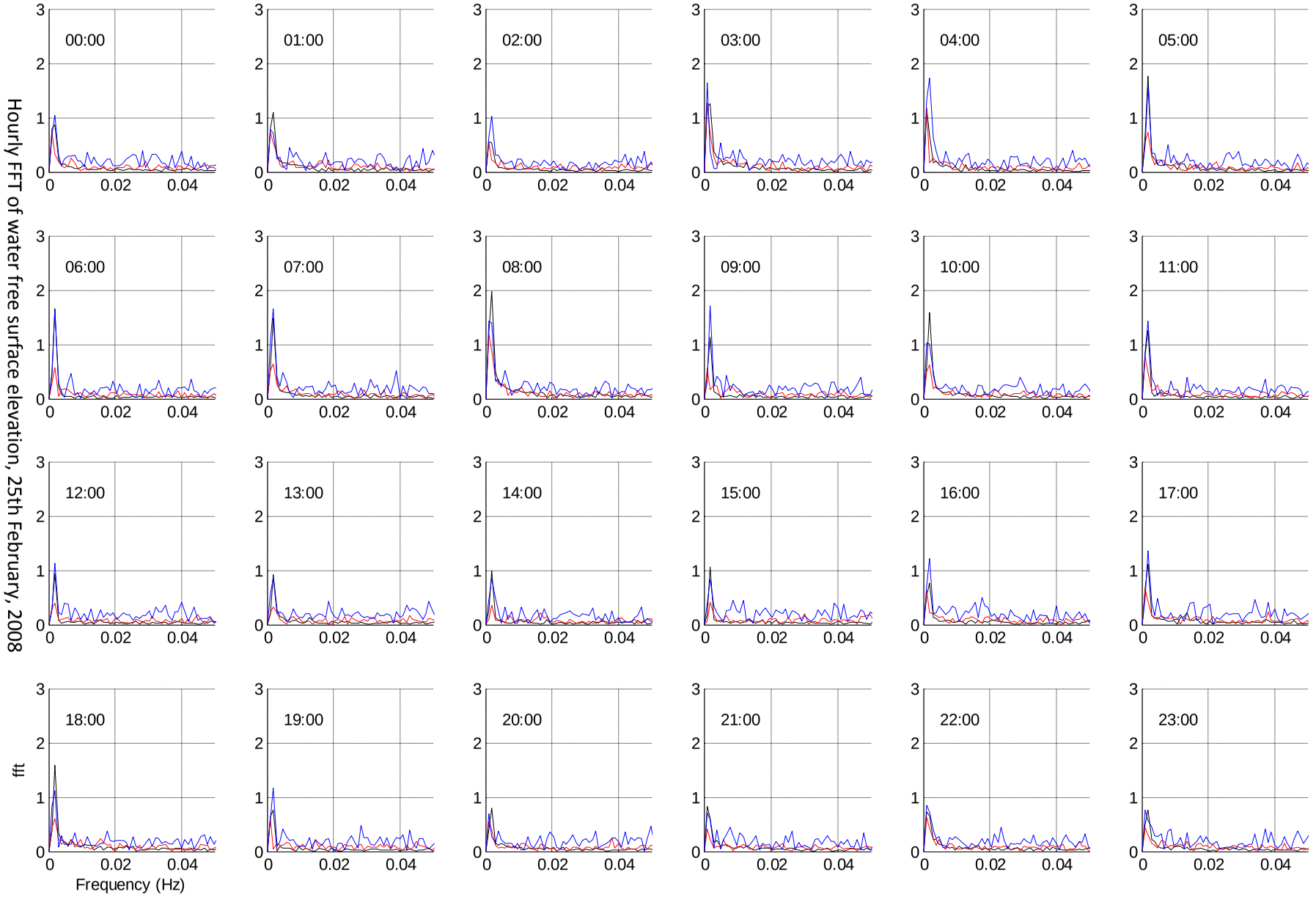
Hourly FFT of water free surface elevation, 25th February, 2008
00:00
01:00
02:00
03:00
04:00
05:00
06:00
07:00
08:00
09:00
10:00
11:00
12:00
13:00
14:00
15:00
16:00
17:00
18:00
19:00
20:00
21:00
22:00
23:00
0
1
2
3
0.02
0.04
Frequency (Hz)
fft

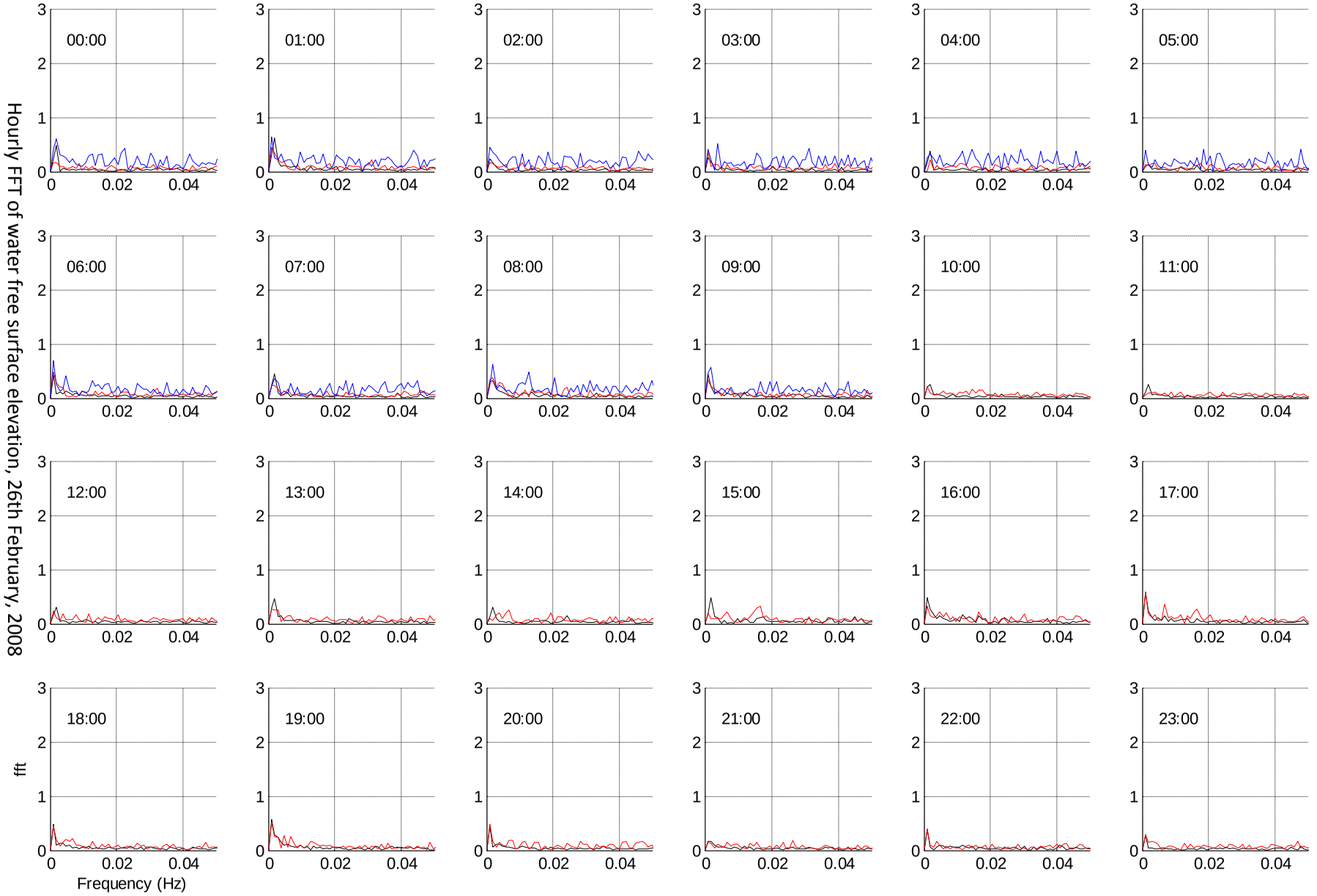
Hourly FFT of water free surface elevation, 26th February, 2008
ft
00:00
01:00
02:00
03:00
04:00
05:00
06:00
07:00
08:00
09:00
10:00
11:00
12:00
13:00
14:00
15:00
16:00
17:00
18:00
19:00
20:00
21:00
22:00
23:00
0
1
2
3
0.02
0.04
Frequency (Hz)

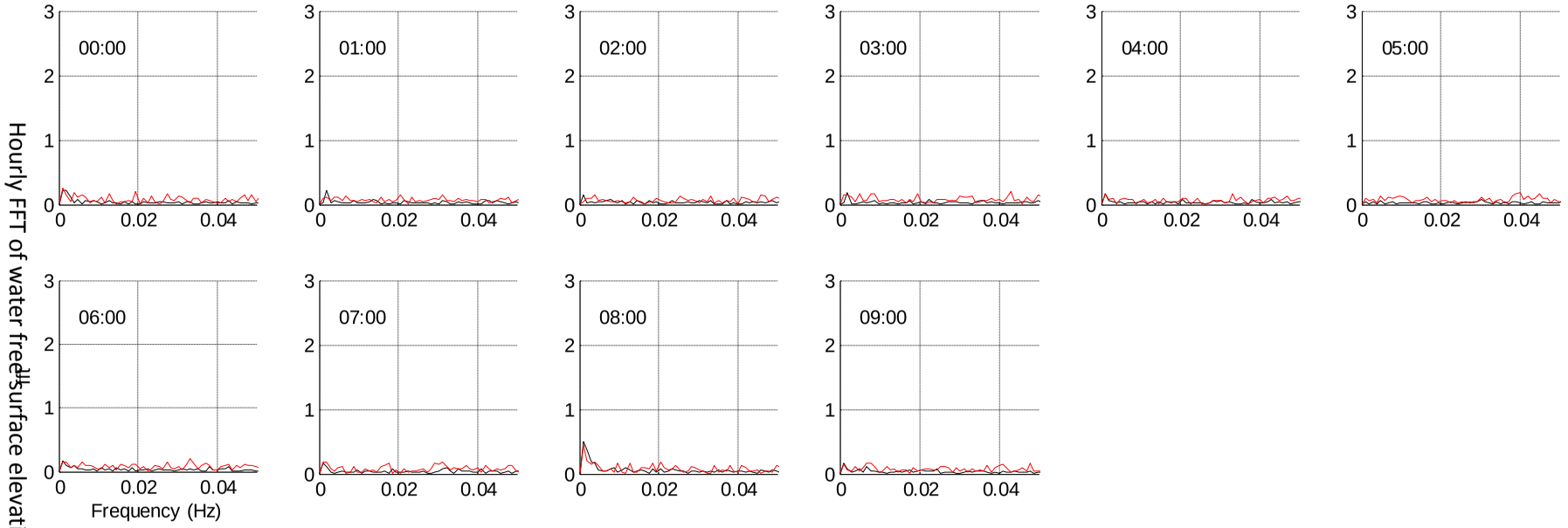
Hourly FFT of water free surface elevation, 27th February, 2008
00:00
01:00
02:00
03:00
04:00
05:00
06:00
07:00
08:00
09:00
0
1
2
3
0.02
0.04
Frequency (Hz)

Appendix E – Wind tunnel mean horizontal and vertical velocity profiles

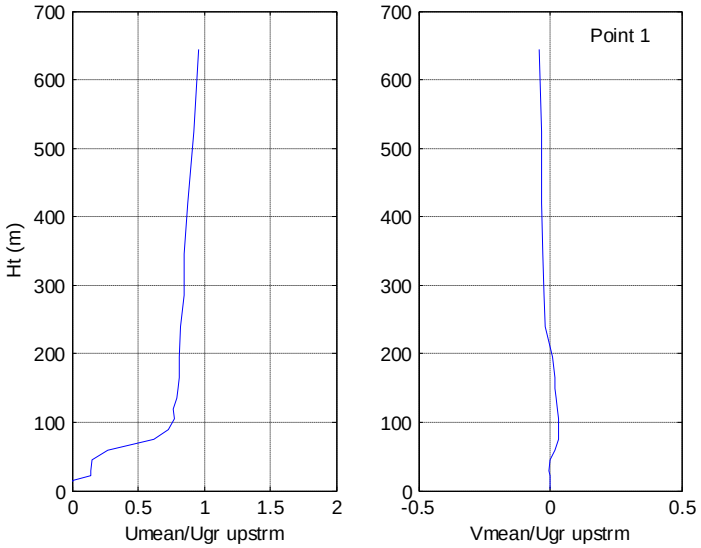
Ht (m)
Umean/Ugr upstrm
Vmean/Ugr upstrm
Point 1

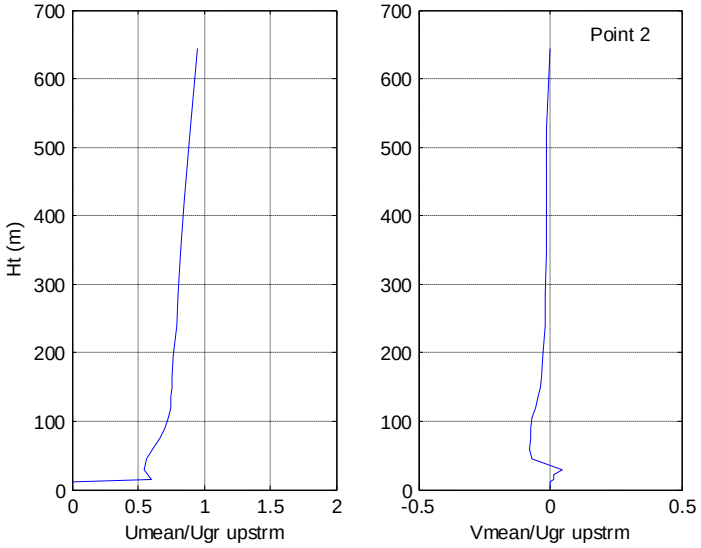
Ht (m)
Umean/Ugr upstrm
Vmean/Ugr upstrm
Point 2

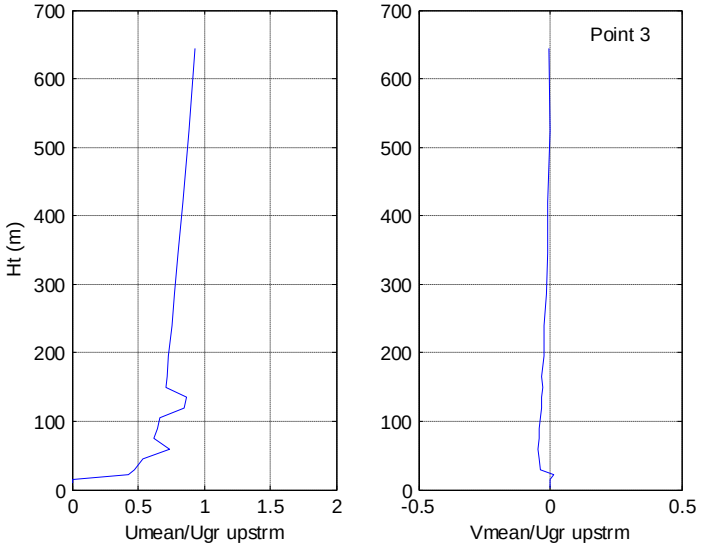
Ht (m)
Umean/Ugr upstrm
Vmean/Ugr upstrm
Point 3

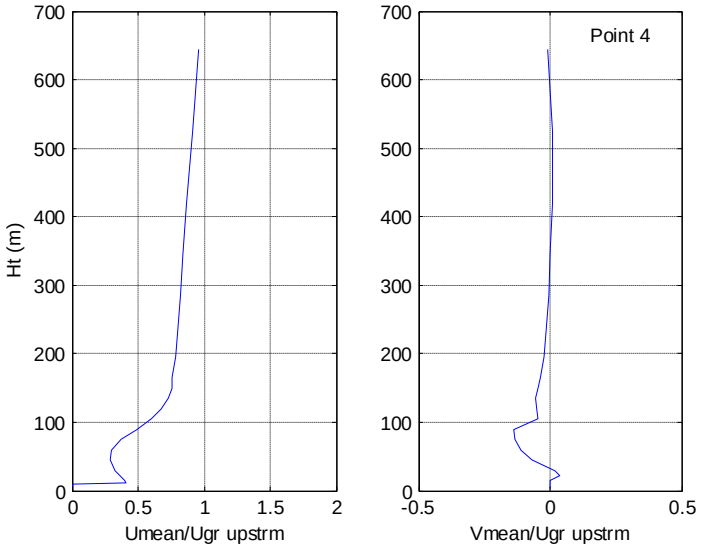
Ht (m)
Umean/Ugr upstrm
Vmean/Ugr upstrm
Point 4

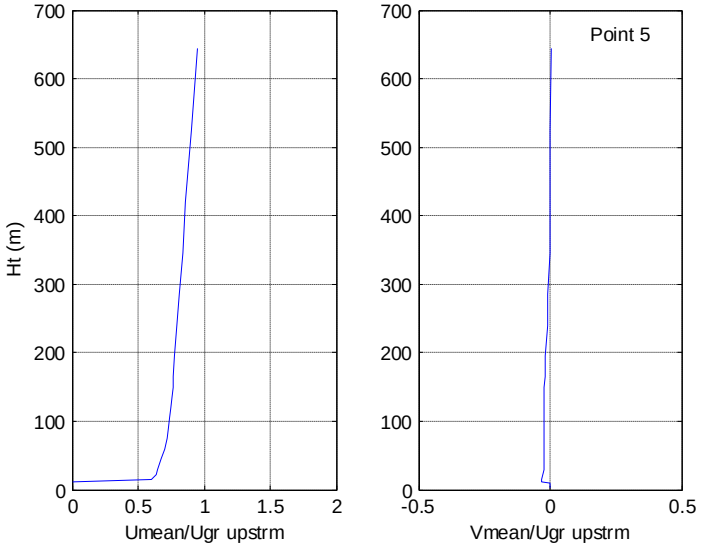
Ht (m)
Umean/Ugr upstrm
Vmean/Ugr upstrm
Point 5

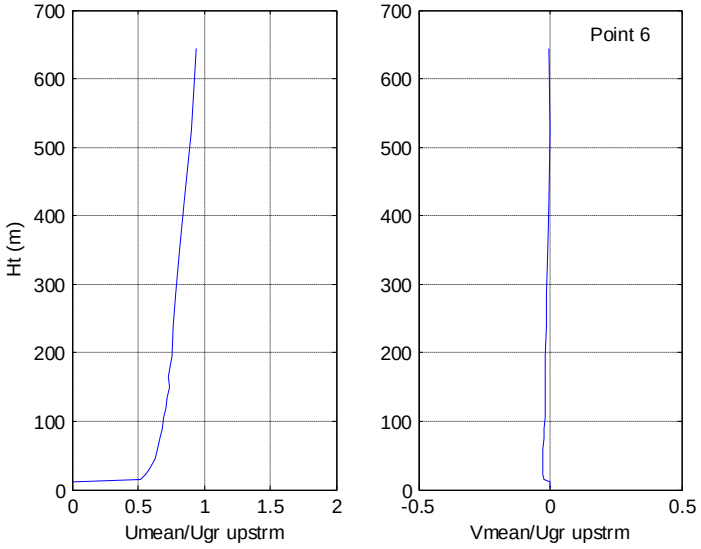
Ht (m)
Umean/Ugr upstrm
Vmean/Ugr upstrm
Point 6

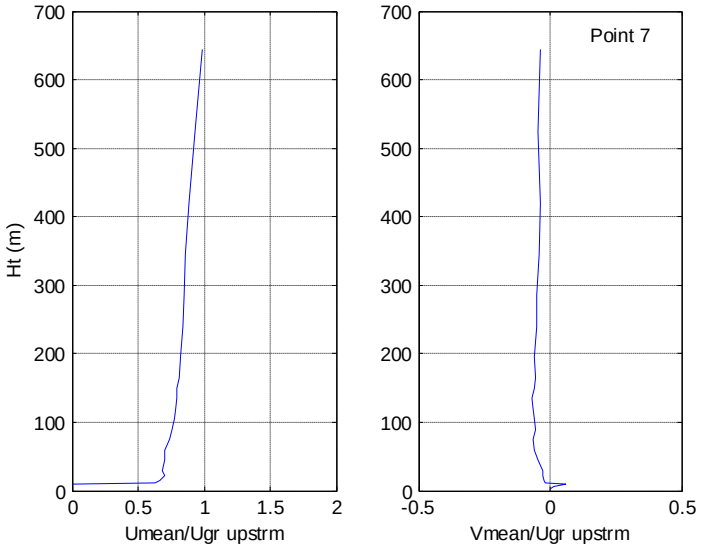
Ht (m)
Umean/Ugr upstrm
Vmean/Ugr upstrm
Point 7

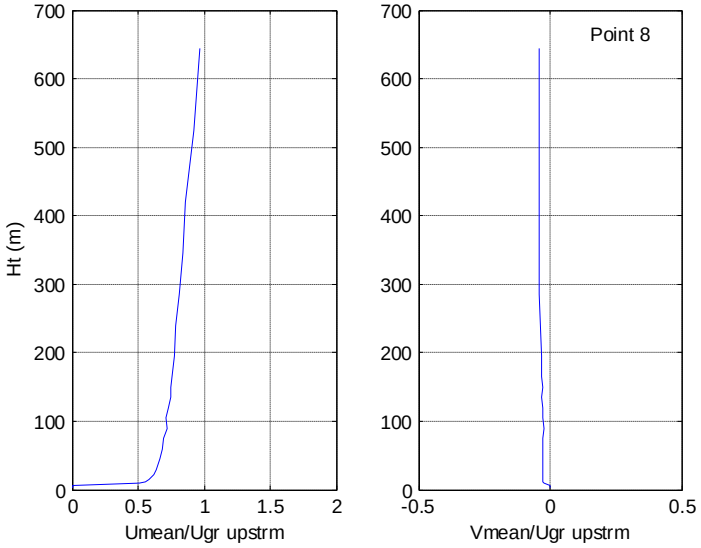
Ht (m)
Umean/Ugr upstrm
Vmean/Ugr upstrm
Point 8

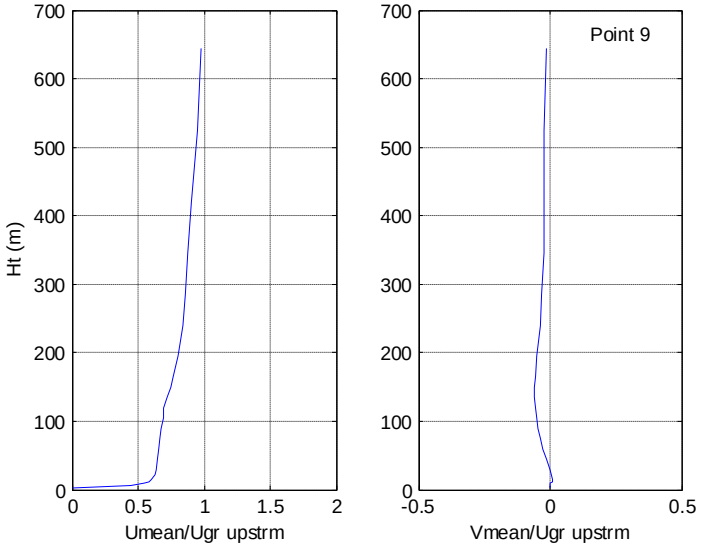
Ht (m)
Umean/Ugr upstrm
Vmean/Ugr upstrm
Point 9

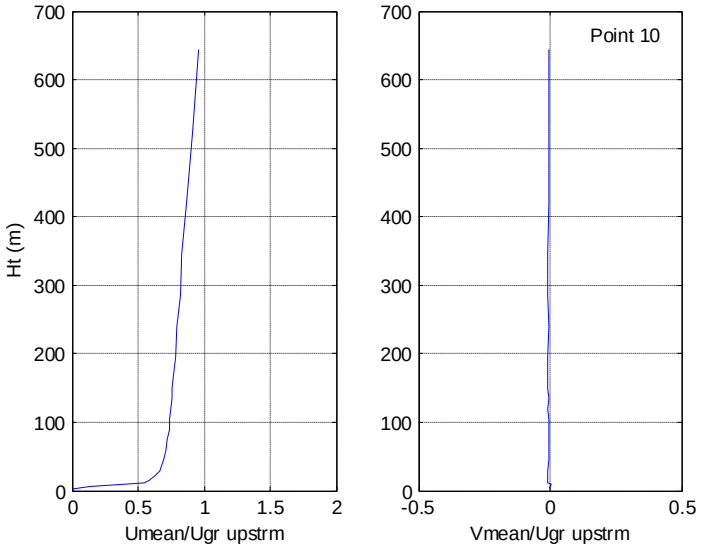
Ht (m)
Umean/Ugr upstrm
Vmean/Ugr upstrm
Point 10

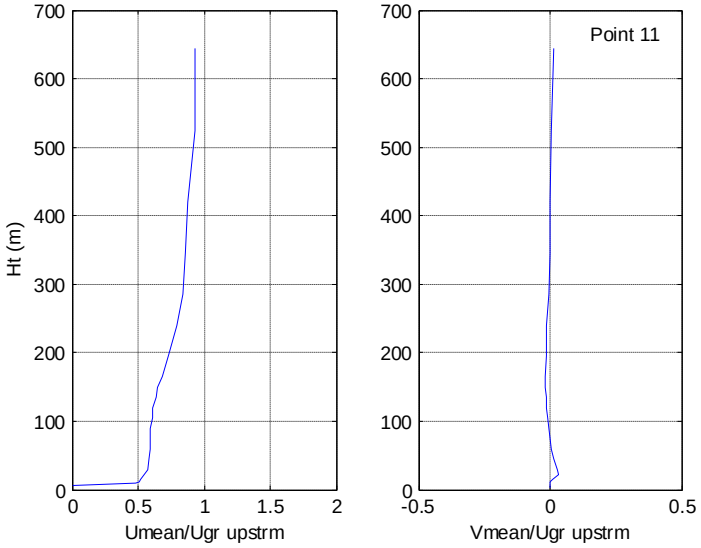
Ht (m)
Umean/Ugr upstrm
Vmean/Ugr upstrm
Point 11

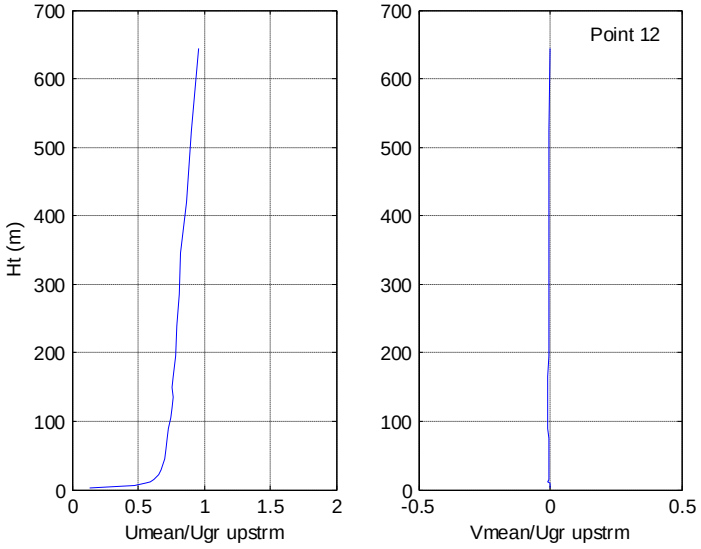
Ht (m)
Umean/Ugr upstrm
Vmean/Ugr upstrm
Point 12

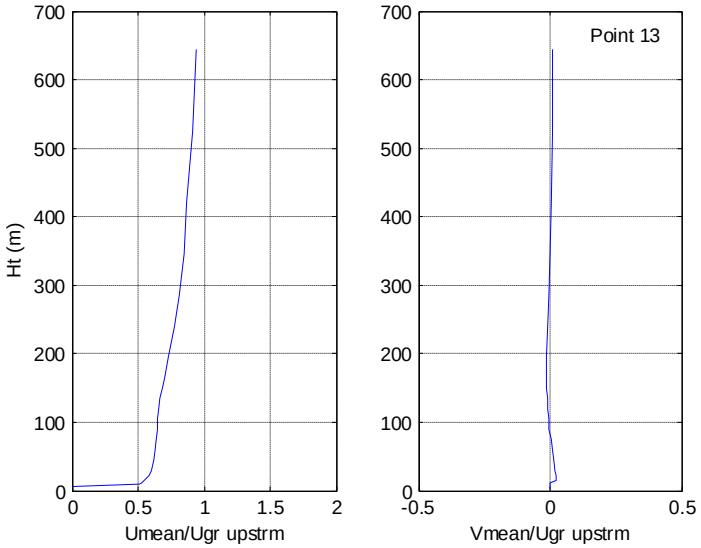
Ht (m)
Umean/Ugr upstrm
Vmean/Ugr upstrm
Point 13

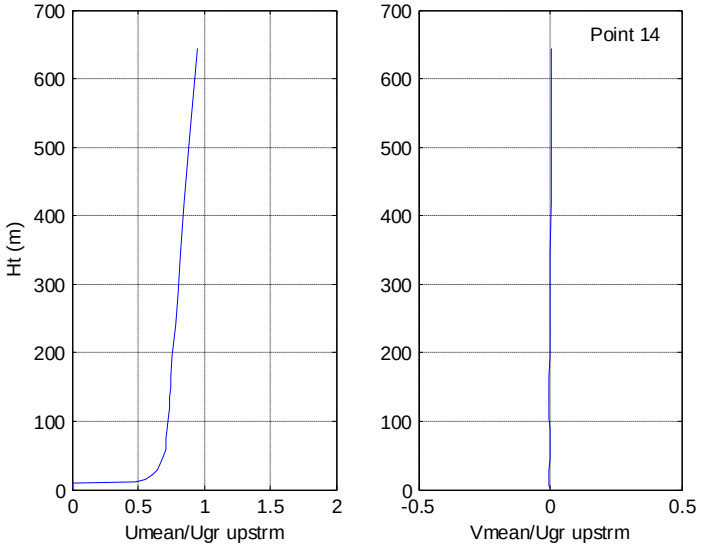
Ht (m)
Umean/Ugr upstrm
Vmean/Ugr upstrm
Point 14

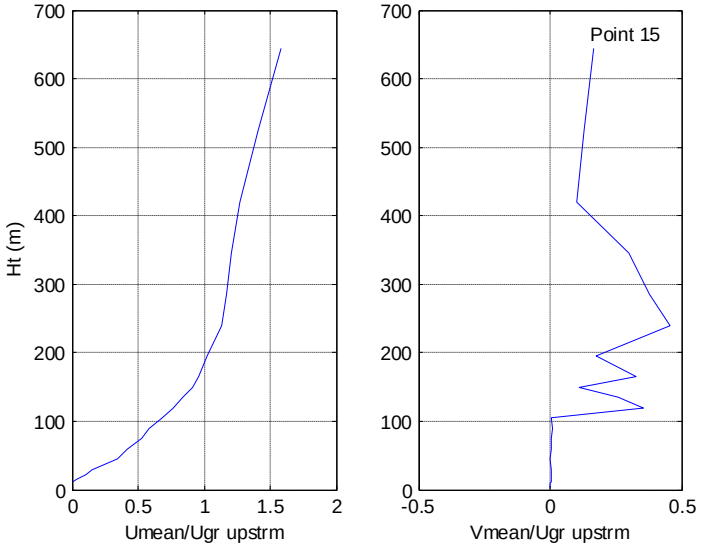
Ht (m)
Umean/Ugr upstrm
Vmean/Ugr upstrm
Point 15

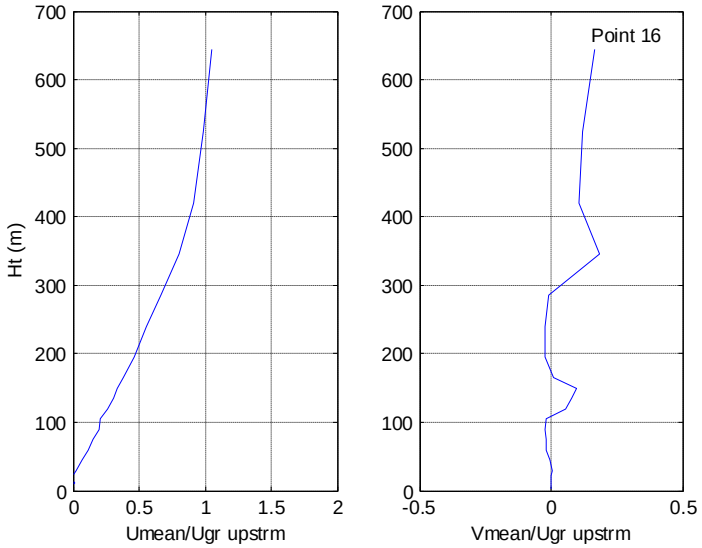
Ht (m)
Umean/Ugr upstrm
Vmean/Ugr upstrm
Point 16

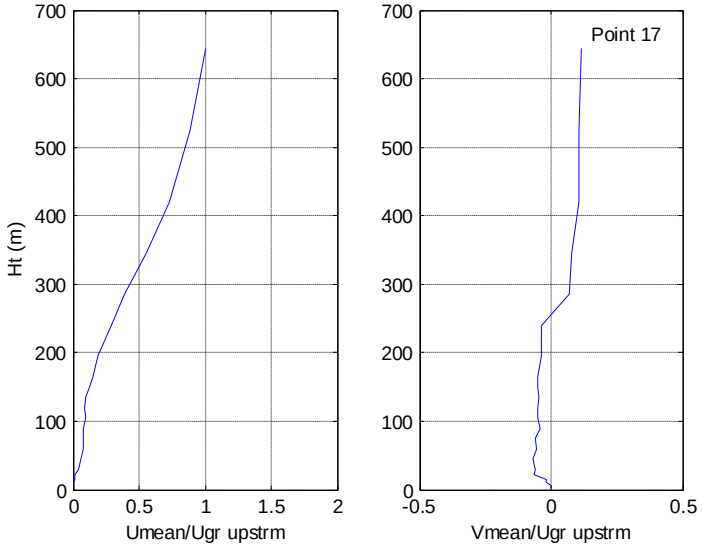
Ht (m)
Umean/Ugr upstrm
Vmean/Ugr upstrm
Point 17

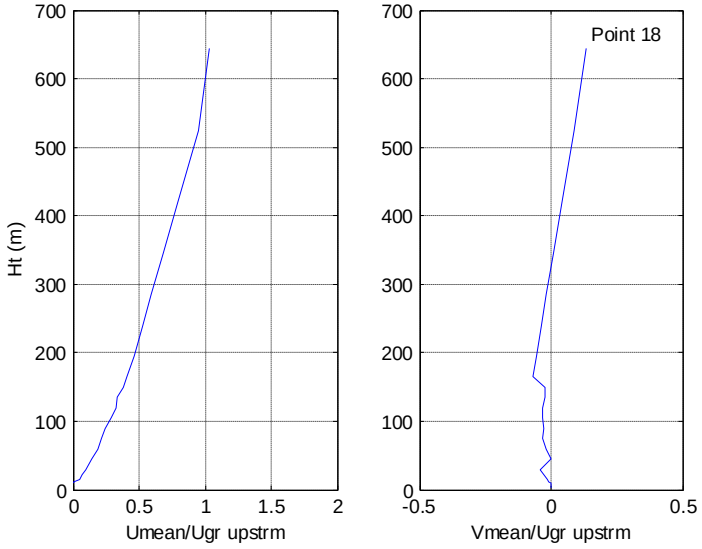
Ht (m)
Umean/Ugr upstrm
Vmean/Ugr upstrm
Point 18

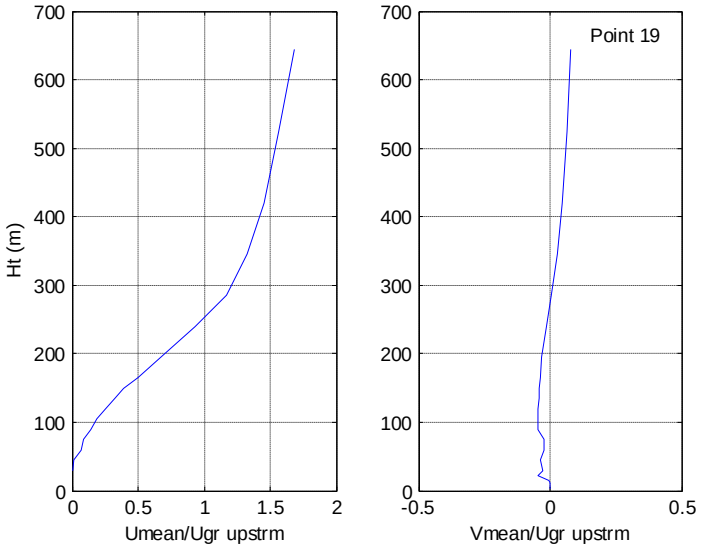
Ht (m)
Umean/Ugr upstrm
Vmean/Ugr upstrm
Point 19

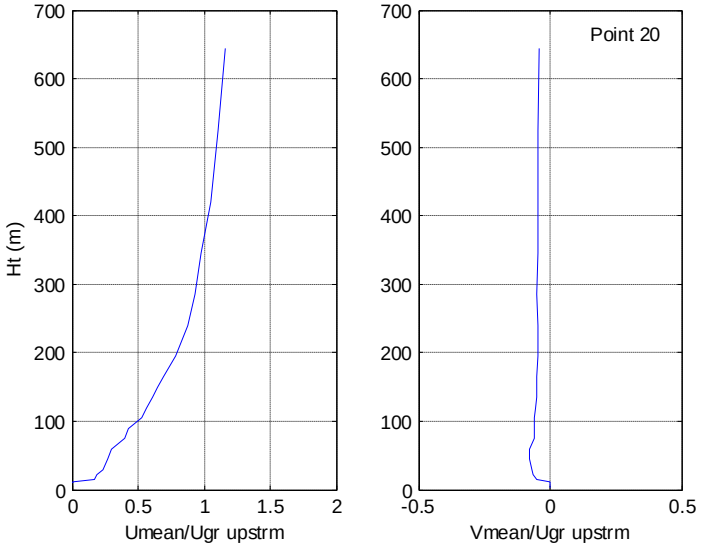
Ht (m)
Umean/Ugr upstrm
Vmean/Ugr upstrm
Point 20

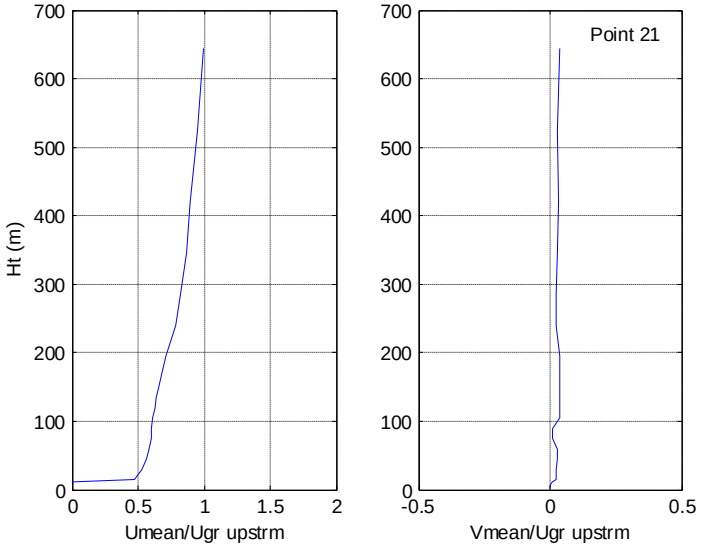
Ht (m)
Umean/Ugr upstrm
Vmean/Ugr upstrm
Point 21

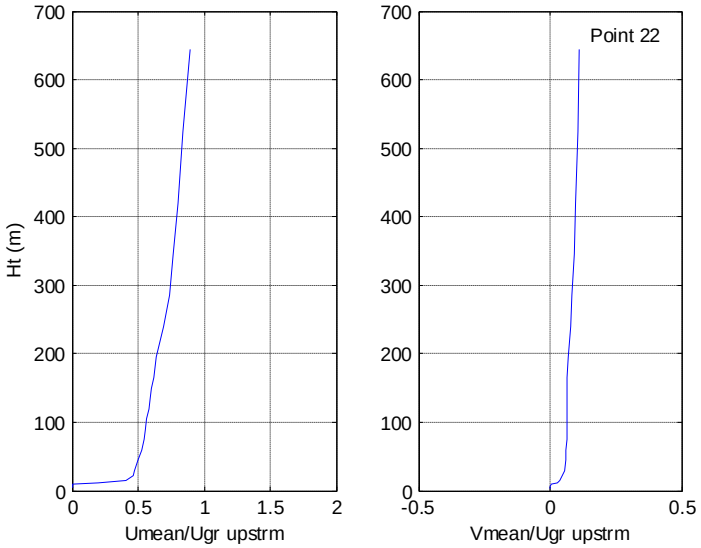
Ht (m)
Umean/Ugr upstrm
Vmean/Ugr upstrm
Point 22

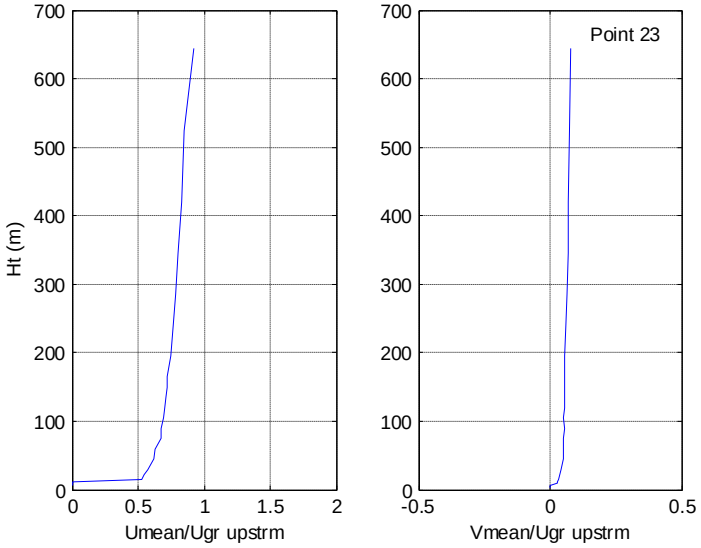
Ht (m)
Umean/Ugr upstrm
Vmean/Ugr upstrm
Point 23

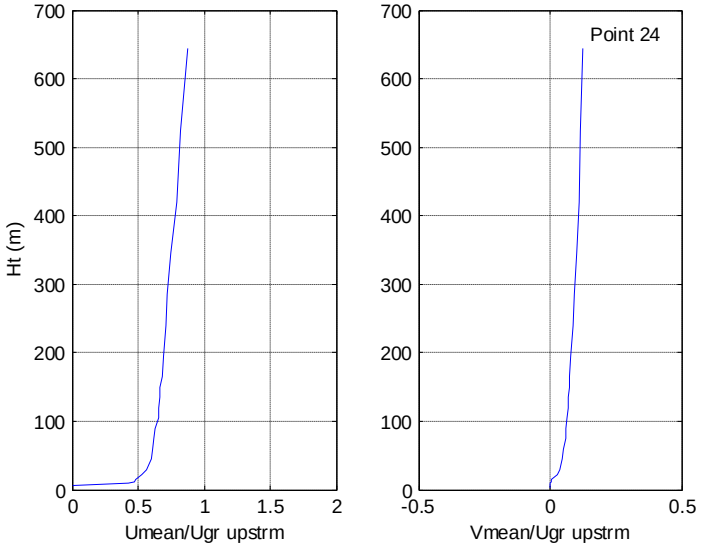
Ht (m)
Umean/Ugr upstrm
Vmean/Ugr upstrm
Point 24

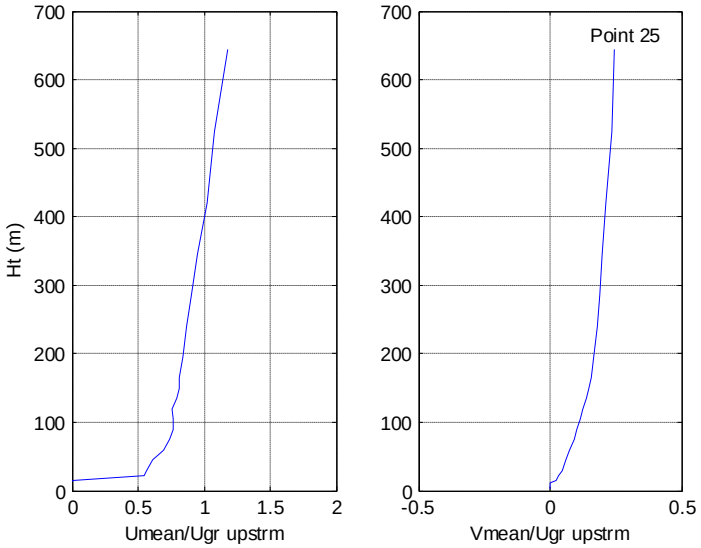
Ht (m)
Umean/Ugr upstrm
Vmean/Ugr upstrm
Point 25

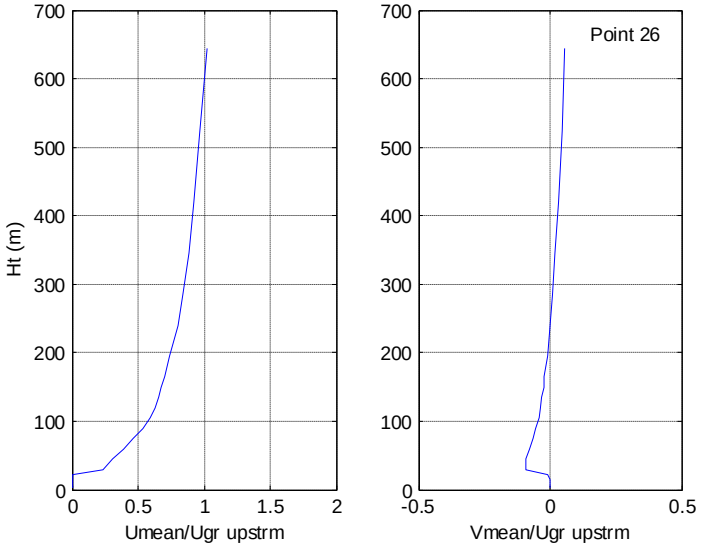
Ht (m)
Umean/Ugr upstrm
Vmean/Ugr upstrm
Point 26

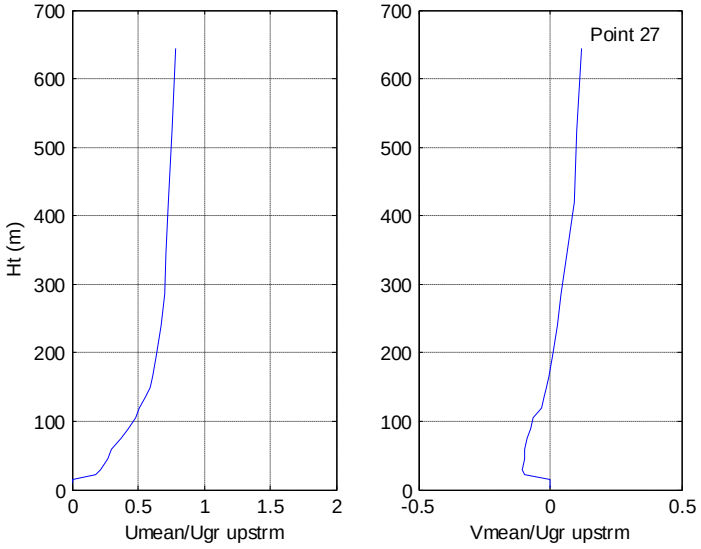
Ht (m)
Umean/Ugr upstrm
Vmean/Ugr upstrm
Point 27

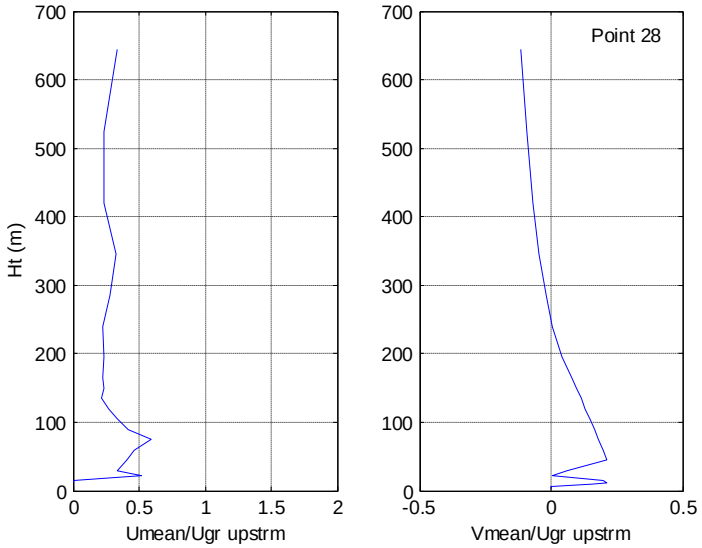
Ht (m)
Umean/Ugr upstrm
Vmean/Ugr upstrm
Point 28

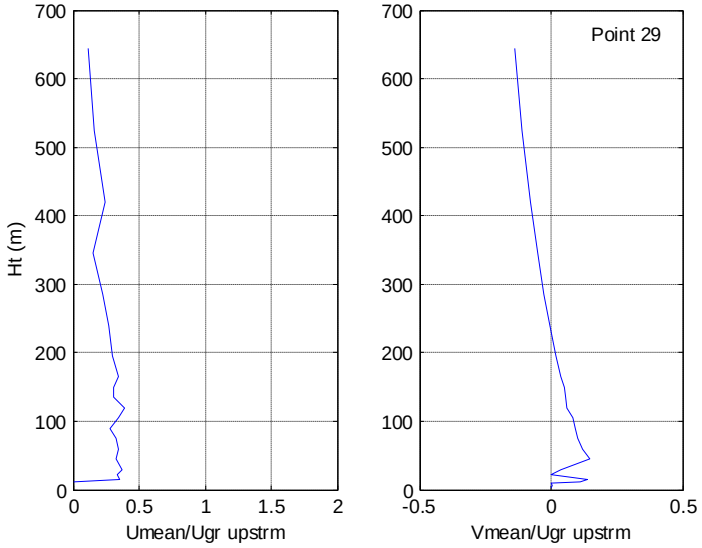
Ht (m)
Umean/Ugr upstrm
Vmean/Ugr upstrm
Point 29

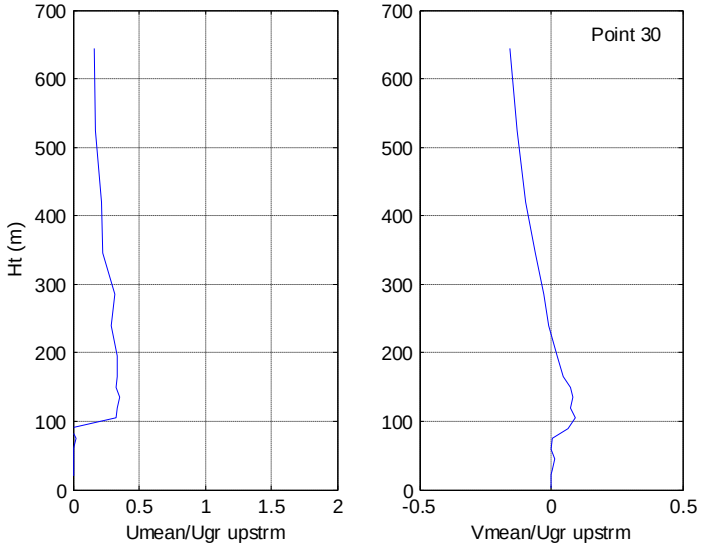
Ht (m)
Umean/Ugr upstrm
Vmean/Ugr upstrm
Point 30

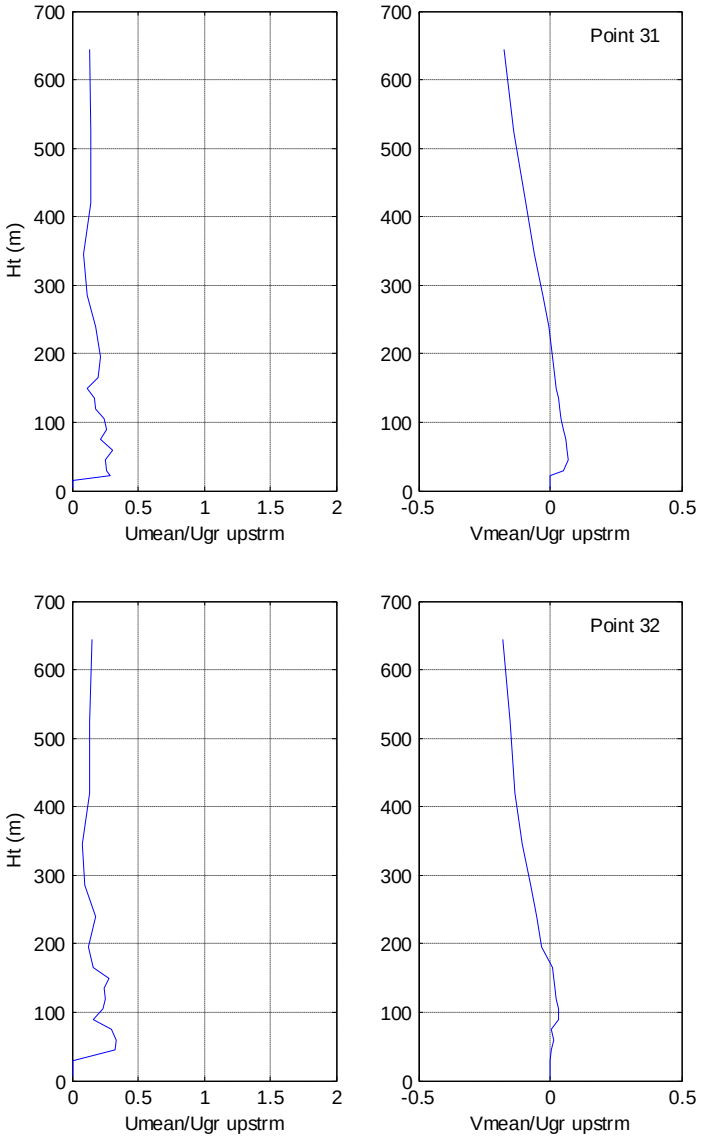
Point 31
Ht (m)
Umean/Ugr upstrm
Vmean/Ugr upstrm
Point 32
Ht (m)
Umean/Ugr upstrm
Vmean/Ugr upstrm